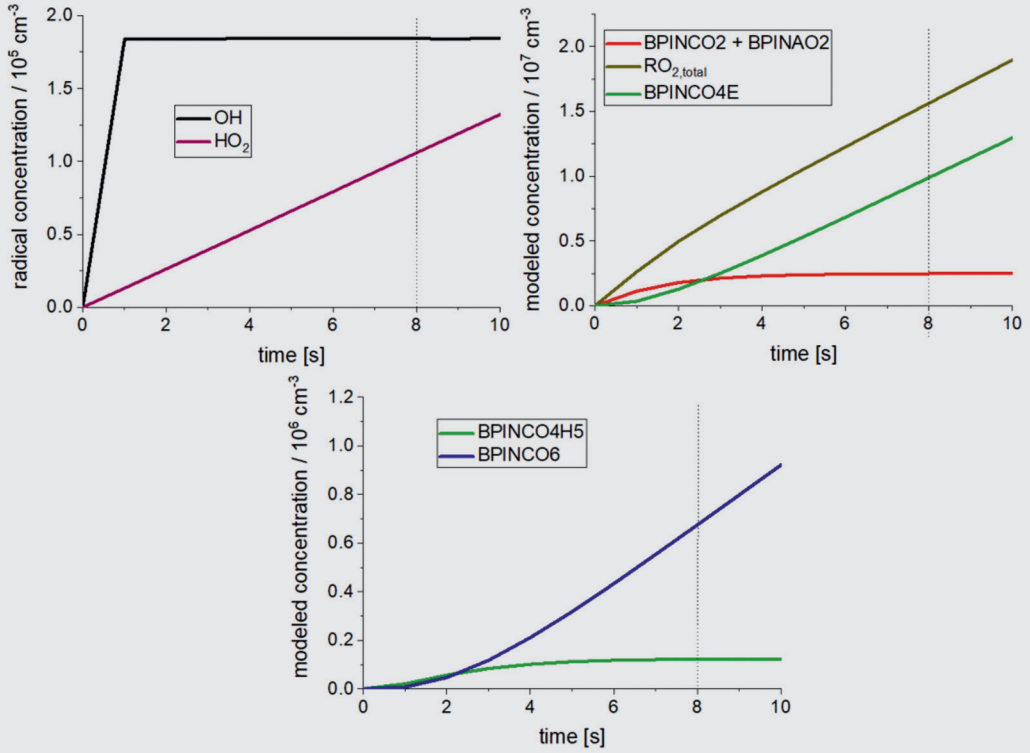

Oxidation of monoterpenes studied in atmospheric simulation chambers

Luisa Lamberta Hantschke

Energie & Umwelt / Energy & Environment
Band / Volume 589
ISBN 978-3-95806-653-3

Mitglied der Helmholtz-Gemeinschaft

JÜLICH
Forschungszentrum

Oxidation of monoterpenes studied in atmospheric simulation chambers

Inaugural-Dissertation
zur
Erlangung des Doktorgrades
an der Mathematisch-Naturwissenschaftlichen Fakultät
der Universität zu Köln

vorgelegt von

Luisa Lamberta Hantschke

aus

Wiesbaden

2022

Berichterstatter: PD Dr. Andreas Hofzumahaus

Prof. Dr. Andreas Wahner

Tag der mündlichen Prüfung: 26.08.2022

Forschungszentrum Jülich GmbH
Institut für Energie- und Klimaforschung
Troposphäre (IEK-8)

Oxidation of monoterpenes studied in atmospheric simulation chambers

Luisa Lamberta Hantschke

Schriften des Forschungszentrums Jülich
Reihe Energie & Umwelt / Energy & Environment Band / Volume 589

ISSN 1866-1793 ISBN 978-3-95806-653-3

Bibliografische Information der Deutschen Nationalbibliothek.
Die Deutsche Nationalbibliothek verzeichnet diese Publikation in der
Deutschen Nationalbibliografie; detaillierte Bibliografische Daten
sind im Internet über http://dnb.d-nb.de abrufbar.

Herausgeber und Vertrieb:	Forschungszentrum Jülich GmbH Zentralbibliothek, Verlag 52425 Jülich Tel.: +49 2461 61-5368 Fax: +49 2461 61-6103 zb-publikation@fz-juelich.de www.fz-juelich.de/zb
Umschlaggestaltung:	Grafische Medien, Forschungszentrum Jülich GmbH
Druck:	Grafische Medien, Forschungszentrum Jülich GmbH
Copyright:	Forschungszentrum Jülich 2022

Schriften des Forschungszentrums Jülich
Reihe Energie & Umwelt / Energy & Environment, Band / Volume 589

D 38 (Diss. Köln, Univ., 2022)

ISSN 1866-1793
ISBN 978-3-95806-653-3

Vollständig frei verfügbar über das Publikationsportal des Forschungszentrums Jülich (JuSER)
unter www.fz-juelich.de/zb/openaccess.

Abstract

Monoterpenes are volatile organic compounds (VOC) that are emitted into the atmosphere from biogenic sources, such as trees and vegetation, or from anthropogenic sources, such as consumer care products. The mean global emission of monoterpenes is estimated to be 160 Tg a year. In the atmosphere, the monoterpenes react with the main oxidants, the OH radical, ozone (O_3), or nitrate radicals (NO_3). Products of these oxidation reactions influence the atmospheric composition. Especially formation and growth of organic aerosols and the formation of ozone can have effects on air quality, human health and climate warming. The oxidation of atmospheric organic compounds by the OH radical initiates a radical chain reaction that involves hydroperoxy radicals (HO_2) and organic peroxy radicals (RO_2, R=organic group). Depending on the environment, the RO_2 radicals can either undergo bimolecular reactions with NO, HO_2 or other RO_2, or unimolecular reactions. Unimolecular reactions of RO_2 include H-shift reactions and endocyclizations. From these autoxidation reactions, higher oxidized species can be formed rapidly. Whether unimolecular reactions of RO_2 are competitive with bimolecular reactions is also highly dependent on the molecules structure. Detailed knowledge about the oxidation mechanism of atmospherically relevant species is crucial for understanding the atmospheres' oxidation capability.

This thesis aims to elucidate some key aspects of the oxidation mechanism of three monoterpenes, β-pinene, myrcene and Δ^3-carene. The oxidation mechanisms of myrcene, Δ^3-carene and caronaldehyde, a main daytime product of the oxidation of Δ^3-carene, were investigated in a total of 10 experiments conducted in the atmospheric simulation chamber SAPHIR (Simulation of Atmospheric PHotochemistry In a large Reaction chamber). A large set of analytical instruments was used in every experiment, allowing the measurement of the concentrations of OH, HO_2 and RO_2 radicals as well as OH reactivity, VOC mixing ratios and mixing ratios of NO, NO_2, HONO and oxidation products. Physical parameters such as the temperature, relative humidity and radiation parameters were also measured. The analysis of the experimental results included the determination of reaction rate constants, product yields and radical budgets.

The reaction rate constants determined for the reactions of myrcene and Δ^3-carene with OH and for the ozonolysis of Δ^3-carene were in good agreement with previously reported values. A new method for the determination of organic nitrate yields in experiments in the SAPHIR chamber was developed. Organic nitrates are formed from the reaction of RO_2 with NO. Due to their usually low vapour pressure, they are prone to condense on atmospheric particles, thereby contributing to the growth and

formation of secondary organic aerosols. The nitrate yield of organic nitrates formed in the oxidation of Δ^3-carene was reported in the gas phase for the first time. The measured yields were compared to values obtained from structure-activity relationship (SAR) considerations. The results of these comparisons showed discrepancies between the SAR estimates and the results obtained in the experiments, underlining the importance of the investigations of oxidation mechanisms of individual monoterpenes.

The analysis of the radical budgets revealed that there are no unknown but relevant radical reformation reactions in the oxidation of Δ^3-carene for the experimental conditions in the SAPHIR chamber (298 K, low NO mixing ratios). Contrary, the analysis of the experiments investigating the oxidation of myrcene indicates that there are unknown radical formation reactions for the conditions in the chamber experiments (298 K, low NO mixing ratios). It can be assumed that unimolecular reactions of the RO_2 formed in the oxidation of myrcene may be the source of the missing radical formation processes due to structural similarities of myrcene to isoprene. Unimolecular reactions have been shown to be of high importance in the oxidation of isoprene.

The oxidation of β-pinene was studied in the SAPHIR-STAR chamber at Forschungszentrum Jülich and at the free-jet flow system at the TROPOS institute in Leipzig. The initially formed RO_2 radical and the RO_2 radicals formed in two subsequent unimolecular reactions as well as the bimolecular reaction products of all three RO_2 families were measured by a CIMS (chemical ionization mass spectrometry) instrument applying a recently developed detection scheme using protonated primary amines. The development of the CIMS based detection scheme for the use at the SAPHIR-STAR chamber was realized in this thesis. The RO_2 radical ratios obtained in the experiments in the free-jet flow system were compared to ratios of the RO_2 radicals obtained from a model run using a published β-pinene oxidation mechanism including reaction rate constants of unimolecular reactions. The reaction rate constants of the unimolecular reactions leading to the formation of highly oxidized RO_2 radicals were experimentally determined for the first time.

The results obtained in this thesis contribute to further understand the importance of unimolecular reactions in the oxidation mechanisms of the investigated monoterpenes. Furthermore, the use of newly developed techniques for the measurement of RO_2 radicals, key species in the oxidation of monoterpenes, is shown to be a powerful tool for the further improvement of our understanding of the atmospherically relevant oxidation processes.

Zusammenfassung

Monoterpene sind flüchtige organische Verbindungen (VOC) die aus biogenen und anthropogenen Quellen in die Atmosphäre emittiert werden. Etwa 160 Tg Monoterpene werden pro Jahr in die Atmosphäre emittiert. Dort werden diese meist ungesättigten Verbindungen oxidiert. Die Produkte, die in diesem Reaktionen gebildet werden, beeinflussen die Zusammensetzung der Atmosphäre. Besonders Ozon oder Verbindungen mit niedrigem Dampfdruck, die zur Neubildung von neuen atmosphärischen Aerosolen beitragen, oder auf bereits existierende Partikel kondensieren, können einen starken Einfluss auf die Luftqualität, Gesundheit der Menschen und die Klimaerwärmung haben. Ein Großteil der VOCs wird tagsüber durch die Reaktion mit dem Hydroxylradiakal (OH) abgebaut, aber auch die Reaktion mit Ozon führt zum Abbau dieser Verbindungen. Durch die Reaktion der VOCs mit dem OH Radikal wird eine Kettenreaktion in Gang gesetzt, die die Bildung von Hydroperoxy-Radikalen (HO_2) und organischen Peroxyradikalen (RO_2, R = organischer Rest) beinhaltet.

Abhängig von der Reaktionsumgebung reagieren RO_2 entweder in bimolekularen Reaktionen mit NO, HO_2 oder anderen RO_2, oder können intramolekular reagieren. Bei diesen unimolekularen Reaktionen kommt es innerhalb des Moleküls zum Beispiel zu H-shift-Reaktionen oder Endozyklisierungen und es können höher oxidierte RO_2 entstehen. Ob die unimolekularen Reaktionen mit den bimolekularen Reaktionen konkurrieren können, hängt zudem von der Struktur des RO_2 ab.

Um das Klima und Luftqualität möglichst gut zu modellieren und voraussagen zu können ist ein tiefgreifendes Verständnis der Mechanismen der atmosphärischen Oxidationsprozesse vonnöten.

Das Ziel der vorliegenden Arbeit ist zum Verständnis der Oxidationsmechanismen von drei atmosphärisch relevanten Monoterpenen, β-Pinen, Myrcen und Δ^3-Caren beizutragen.

Die Reaktionen von Myrcen und Δ^3-Caren, sowie von Caronaldehyd, einem der Hauptprodukte der Oxidation von Δ^3-Caren mit dem OH Radikal, wurden in der Atmosphärensimulationskammer SAPHIR am Forschungszentrum Jülich untersucht. Zusätzlich wurden Experimente zur Ozonolyse von Δ^3-Caren und zur Photolyse von Caronaldehyd durchgeführt. Während aller Experimente wurden die Konzentrationen der OH, HO_2 und RO_2 Radikale, sowie von VOCs und deren Reaktionsprodukten und weiteren Spurengasen wie NO, NO_2 und HONO mithilfe vieler verschiedener analytischer Messinstrumente bestimmt. Zusätzlich wurden auch die Temperatur, die relative Feuchte und Strahlungsparameter in der Kammer gemessen.

Die Analyse der Ergebnisse der Experimente umfasst die Bestimmung von Reaktionskonstanten, Produktausbeuten und Radikalbudgets. Die bestimmten Reaktionskonstanten für alle untersuchten Reaktionen waren in guter Übereinstimmung mit publizierten Daten.

Eine neue Methode zur Bestimmung der Ausbeute von Organischen Nitraten wurde für die Experimente in der SAPHIR Kammer entwickelt. Organische Nitrate entstehen durch die Reaktion von RO_2 mit NO. Aufgrund ihrer normalerweise niedrigen Dampfdrücke kondensieren sie leicht auf bestehende Partikel, und tragen so zur Bildung von sekundären organischen Aerosolen bei. Die Ausbeute von organischen Nitraten wurde für die Gasphasenoxidation von Δ^3-Caren zum ersten Mal bestimmt. Die bestimmten Ausbeuten für alle drei untersuchten VOCs wurden mit Ausbeuten verglichen, die durch Struktur-Eigenschafts-Beziehungen geschätzt wurden. Der Vergleich dieser Werte zeigt deutliche Unterschiede in den experimentell und theoretisch bestimmten Daten. Dies unterstreicht die Wichtigkeit der Untersuchung der Oxidationsmechanismen einzelner Monoterpene.

Die Analyse der Radikalbudgets in den Experimenten zur Untersuchung des Oxidationsmechanismus von Δ^3-Caren geben keinen Hinweis auf fehlende Radikalbildungsreaktionen unter den experimentellen Bedingungen in der SAPHIR Kammer (298 K, niedrige NO Konzentration). Bei der Analyse der Radikalbudgets in den Experimenten zur Untersuchung der Oxidation von Myrcen durch das OH Radikal wurden deutliche Hinweise auf eine zusätzliche Radikalquelle unter den experimentellen Bedingungen in der SAPHIR-Kammer gefunden (298 K, niedrige NO Konzentration). Aufgrund von strukturellen Ähnlichkeiten von Myrcen und Isopren wird davon ausgegangen, dass die fehlenden Radikalquellen in unimolekularen Reaktionen der RO_2 liegen könnten. Für die Oxidation von Isopren ist die Wichtigkeit von unimolekularen Reaktionen unter atmosphärischen Bedingungen bereits nachgewiesen worden.

Der Oxidationsmechanismus des Monoterpens β-Pinen wurde in der Atmosphärensimulationskammer SAPHIR-STAR am Forschungszentrum Jülich und in einem Freistrahl-Strömungssystem am TROPOS Institut in Leipzig untersucht. Die hierbei initial gebildeten RO_2, und die hieraus aus zwei aufeinanderfolgenden unimolekularen Reaktionen gebildeten höher oxidierten RO_2 wurden mit einem CIMS Instrument mit einem kürzlich entwickelten, auf Aminium-Ionen basierenden Reaktionsschema detektiert. Die Entwicklung des CIMS basierten Detektionsschemas für die Verwendung an der SAPHIR-STAR Kammer ist ein Teil dieser Arbeit. Die in dem Freistrahl-Strömungssystem gemessenen Verhältnisse der drei Radikalfamilien wurden mit modellierten Radikalverhältnissen verglichen. Für die Modellierung wurden publizierte Mechanismen verwendet, die um unimolekulare Reaktionen und deren verschiedene veröffentlichte Reaktionskonstanten erweitert waren. Die Reak-

tionskonstanten, die sich am besten eignen, um die experimentellen Beobachtungen im Modell zu reproduzieren, wurden bestimmt.

Die im Rahmen dieser Arbeit erzielten Resultate können zum Verständnis um die Wichtigkeit unimolekularer Reaktionen in den Oxidationsmechanismen der untersuchten Monoterpene beitragen.

Inhaltsverzeichnis

1 Introduction

The first 8-15 km, depending on the latitude and time of the year, of air surrounding planet Earth are called troposphere. The main components of the dry atmosphere are nitrogen (79.08%), oxygen (20.95%) and argon (0.93%). An additional 0 to 4% of water vapour can be found in the lower troposphere depending on the location. Small concentrations of trace gases from anthropogenic sources, like industry or use of fossil fuels and biogenic sources, like forests, volcanoes or oceans influence the tropospheric composition. The nature of the emitted species is diverse and their effect on e.g. climate warming or human health differ. According to the World Health Organization (WHO), 4.2 million premature deaths were caused by ambient air pollution. The main contributors are ozone and fine particulate matters with diameters smaller than 2.5 μm ($P.M_{2.5}$). These two pollutants have been shown to cause respiratory and cardiovascular diseases and cancer (WHO, 2021).

In the atmosphere, most of the emitted species are chemically transformed by oxidation processes. These processes are initiated by atmospheric oxidants, such as the hydroxyl radical (OH), ozone (O_3) or the nitrate radical (NO_3) or by light of a certain wavelength.

One of the few exceptions is carbon dioxide (CO_2) that therefore has a long atmospheric lifetime. Its permanent loss is driven by uptake in the Earth's oceans. At the same time, CO_2 is also the most prominent example for man-made greenhouse gas emissions from combustion processes. The atmospheric CO_2 concentrations are now higher than they have ever been in the last two million years (Masson-Delmotte et al., 2021).

Reactive trace gases emitted from anthropogenic and biogenic sources like volatile organic compounds (VOC) have lower atmospheric lifetimes in the range of only a few hours to several weeks depending how rapidly they react with the atmospheric oxidants. The atmospheric oxidation processes lead to the formation of a myriad of oxidation products, for example organic radicals, organic nitrates, aldehydes or acids. Exploring the formation mechanisms and reactions in which these species are formed from their parent compounds is crucial for improving the knowledge about the composition of the atmosphere.

To elucidate the chemical transformation processes in the atmosphere, highly sensitive instruments are required for the detection of reactive trace gases that generally

have low concentrations. Starting in the middle of the 20th century, many instruments based on spectroscopic, mass spectrometric or electrochemical techniques have been developed for the detection of trace gases and radical species (e.g. Heard (2006)). Due to these developments, it is now possible to measure volume mixing ratios of trace gases in the parts per billion (ppb) to parts per trillion (ppt) range. Through the use of these sensitive measurement techniques, the field of atmospheric chemistry aims, inter alia, to clarify the mechanisms of the many (oxidation) reactions occurring in the atmosphere as detailed as possible. The information obtained about the atmospheric reactions and processes can then be fed into models to better predict air quality, weather phenomena and the climate. Experimental field studies, simulation chamber experiments and laboratory investigations present powerful tools to investigate the oxidation mechanisms of atmospherically relevant species.

Simulation chamber experiments provide a controllable and well-defined environment to investigate findings from field studies or to test predictions made by atmospheric models or theoretical quantum chemistry calculations. They allow for the measurement of product yields and rate constants of the reaction of a single reactive species. Complex chemical degradation mechanisms of single species or mixtures of different substances can be investigated at atmospheric conditions.

In this thesis, two atmospheric simulation chambers of different size and a free-jet flow system were used to investigate the oxidation mechanisms of the three monoterpenes myrcene, Δ^3-carene and β-pinene that are understudied to date. The studies aim to improve the understanding of fundamental chemical properties of the degradation mechanisms such as reaction rate constants, photolysis frequencies, types of product and product yields. A special focus was laid on the study of organic peroxy radicals that are a key intermediate in the atmospheric oxidation of monoterpenes. Further reactions of the organic peroxy radicals can produce stable oxidation products, such as aldehydes or ketones. They also influence the concentration of hydroxyl radicals that control the oxidation capacity of the atmosphere and are relevant for the photochemical formation of ozone and organic aerosol.

1.1 Emissions of monoterpenes in the atmosphere

Monoterpenes are volatile organic compounds (VOC) that are emitted into the atmosphere mainly by biogenic sources, e.g. trees.

Monoterpenes have the chemical formula $C_{10}H_{16}$ and can be divided in different subgroups, depending on their chemical structure. The local emission rates of these species are highly dependent on the type of plants and trees and time of year. Around 1000 Tg of biogenic volatile organic compounds (BVOC) are emitted into the atmosphere per year, and around 160 Tg of these emissions are accounted for by

monoterpenes (Guenther et al. (2012)).

Table 1.1: Simulated global annual emissions of biogenic VOC (BVOC) for the year 2000 (Guenther et al. (2012)). The monoterpenes investigated in this work are highlighted in bold.

BVOC	**Emissions /** Tg year^{-1}
Isoprene	535
α-Pinene	66.1
t-β-Ocimene	19.4
β-Pinene	18.9
Limonene	11.4
Sabinene	9.0
Myrcene	8.7
Δ^3-Carene	7.1

Globally, the most abundant monoterpenes are α- and β-pinene with emission rates of up to 66 Tg year^{-1} (Guenther et al. (2012)). Other monoterpenes, like Δ^3-carene, are less important on a global scale, but gain in importance over certain regions like boreal forests, as they are primarily emitted by certain pine trees that are typically found in these areas. In the plants, the monoterpenes are stored in resin ducts in the leaves or trunks. Their emissions are influenced by temperature and also depend on other external stressors such as droughts (e.g. Lüpke et al. (2017) and references therein). It has been shown that stored monoterpenes are used by plants as a defense mechanism against herbivorous insects (e.g. Mumm and Hilker (2006)) and that monoterpenes have an inhibitory effect on the growth of airborne pathogenic microorganisms (Gao et al. (2005)). Additionally, monoterpenes can be newly synthesized by the plants as a response to oxidative stress (Graßmann et al. (2005)).

Due to their olfactoric characteristics, they are also often used in scents and consumer care products. Recent studies show that half of the VOC emissions in industrialized cities are coming from volatile chemical products used for example in cleaning and personal care products (McDonald et al. (2018)). Their oxidation products therefore influence rural and urban environments.

The structures of monoterpenes are diverse. There are bicyclic monoterpenes with either endo- or exocyclic bonds (e.g. Δ^3-carene and β-pinene, respectively), monocyclic monoterpenes with several double bonds (e.g. limonene) or non-cyclic monoterpenes with several double bonds (e.g.myrcene). The structures of the monoterpenes investigated in this work are shown in Figure 1.1.

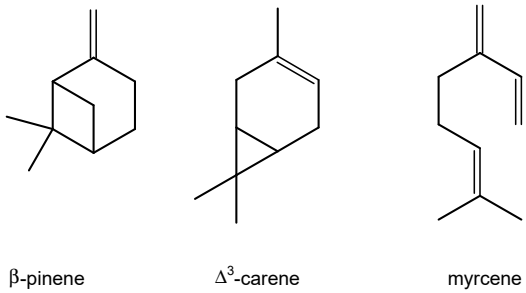

Figure 1.1: Chemical structures of the bicyclic monoterpenes β-pinene and Δ^3-carene, and the linear monoterpene myrcene.

Δ^3-carene is mainly emitted by Scots pine trees and maritime pine (Komenda and Koppmann (2002)) and therefore gains in importance over boreal forests. Carenaldehyde is one of the main oxidation products of the reaction of Δ^3-carene with OH radicals and ozone. Myrcene emissions globally contribute about 2 to 10% to monoterpene emissions (Guenther et al. (2012)), but are also gaining in importance depending on the studied region and the dominating tree species.

Monoterpenes are unsaturated compounds. Therefore, they exhibit a high reactivity towards the main oxidants in the atmosphere, OH, O_3 and NO_3. The products formed from the reaction of monoterpenes with these oxidants, for example organic nitrates or aldehydes, are often less volatile than their parent compounds and thereby influence the formation of secondary organic aerosol (SOA). Additionally, ozone is known to be a by-product of those oxidation reaction in areas where also nitrogen oxides (NOx = NO + NO_2) and light are abundant. Knowing the atmospheric fate of monoterpenes is therefore crucial to understand organic aerosol and ozone formation.

1.2 Tropospheric oxidation chemistry

Oxidation processes play a crucial role in the troposphere, as most biogenically or anthropogenically emitted trace gases are chemically transformed by oxidation. In the following section, the tropospheric oxidation chemistry in regard to the two main oxidants, OH and O_3, is described. The following paragraphs are based on the works of Finnlayson-Pitts and Pitts (2000) and Seinfeld and Pandis (2006).

The most important oxidizing agent in the atmosphere is the hydroxyl radical (OH, Ehhalt (1999)). OH is mainly produced by the photolytic decomposition of O_3 by UV radiation with a wavelength below 340 nm (Reaction R1.1). The electronically excited oxygen atom $O(^1D)$ that is formed in this process subsequently either reacts

with water vapour to form two OH radicals (Reaction R1.2), or is quenched to its non-excited state $O(^3P)$ by the collision with a neutral molecule M (Reaction R1.3), typically either molecular nitrogen or oxygen in the atmosphere.

$$O_3 + h\nu \longrightarrow O_2(^1\Delta) + O(^1D) \quad \text{(R1.1)}$$

$$O(^1D) + H_2O \longrightarrow 2\,OH \quad \text{(R1.2)}$$

$$O(^1D) + M \longrightarrow O(^3P) + M \quad \text{(R1.3)}$$

In polluted (urban) environments, another OH formation process gains in importance. The emissions of nitrogen oxides is typically enhanced in these regions due to traffic or industrial activities. Nitrous acid (HONO) formation that occurs mainly from heterogeneous processes involving nitrogen oxides at surfaces is therefore also higher in polluted environments. As HONO can be photolyzed at UV radiation wavelengths below 390 nm, the formation of OH radicals from HONO photolysis is also important (Kleffmann (2007)). Another source of OH radicals is the ozonolysis of VOC (Atkinson et al. (1992)). The OH radical reacts with almost all the trace gases abundant in the troposphere, and thereby plays a significant role in the atmosphere self cleaning ability.

In many cases, reactions with OH initiate fast radical chain reactions that produce hydroperoxy radicals (HO_2) and organic peroxy radicals (RO_2). Here, R represents an organic group. RO_2 radicals are formed in the reaction of VOCs with the OH radical or ozone and are important intermediates in the further atmospheric degradation of VOCs. The three radicals that are often referenced to as the ROx radical family (ROx = OH + HO_2 + RO_2) dominate the radical chemistry in the troposphere during daytime. The reactions of the ROx radicals can be divided into radical propagating and radical termination reactions. Radical propagation reactions occur when the reaction of a radical with a reaction partner leads to the formation of another radical species. In radical termination reactions, two radicals combine to form a closed-shell molecule.

OH radicals react with methane and higher alkanes by H-abstraction. The subsequent rapid addition of molecular oxygen leads to the formation of organic peroxy radicals (RO_2). Monoterpenes are unsaturated alkenes and react with OH in two different ways. Usually, an OH radical is added to a double bond. The position of the attack varies depending on the exact chemical structure of the VOC, but typically an attack at the least substituted C atom of the double bond is favoured (Jenkin et al. (2018)). In this process, an hydroxy substituted alkyl radical is formed that subsequently quickly adds molecular oxygen at the beta position, forming a hydroxy

peroxy radical ($R(OH)O_2$, Reactions R1.4 and R1.5).

$$R{-}C{=}C{-}R + OH + M \longrightarrow R{-}C(OH){-}C{\cdot}{-}R + M \quad \text{(R1.4)}$$

$$R{-}C(OH){-}C{\cdot}{-}R + O_2 + M \longrightarrow R{-}C(OH){-}C(O_2){\cdot}{-}R + M \quad \text{(R1.5)}$$

An alternative initial pathway is the abstraction of an H-atom usually from one of the monoterpenes C atoms adjacent to the double bond. This results in the formation of an alkyl radical and water. The alkyl radical formed in this reaction then also reacts quickly with molecular oxygen, forming a peroxy radical. For most monoterpenes, this is only a minor pathway. For example, only 10% of the oxidation of Δ^3-carene by the OH radical proceeds via H-abstraction estimated by structure-activity relationship (SAR, Jenkin et al. (2018)). In many parts of this work, both substituted and unsubstituted organic peroxy radicals are summarized as RO_2 radicals for simplicity.

The peroxy radical formed after the addition of OH and subsequent reaction with O_2 can undergo a number of different reactions (e.g. Goldman et al. (2021)), depending on the chemical conditions of the environment:

(i) reaction with NO is dominant in polluted environments, e.g. close to cities or industrial sites
(ii) reactions with HO_2 radicals
(iii) reaction with another peroxy radical (R'O_2), with a different organic rest R' that become more relevant in remote atmosphere
(iv) autoxidation reaction (e.g. intramolecular H-shifts), often leading to the formation of highly oxygenated molecules (HOM).

For the reaction of RO_2 with NO, two different reaction pathways are possible: the formation of an organic nitrate ($RONO_2$, Reaction R1.7) or the formation of a alkoxy radical (RO) and NO_2 (Reaction R1.6).

$$RO_2 + NO \longrightarrow RO + NO_2 \quad \text{(R1.6)}$$

$$RO_2 + NO \longrightarrow RONO_2 \quad \text{(R1.7)}$$

The branching ratio of this reaction depends on the chemical structure of the molecule. Besides the degree of substitution of the radical (primary, secondary or tertiary), the size of the molecule also plays a role, since the stabilization of the intermediate reactive complex is stronger in bigger molecules. A theoretical calculation method that takes into consideration the number of C-atoms and the degree of substitution in the molecule (Jenkin et al. (2019)) gives a branching ratio of 19% for the organic nitrate formation (Reaction R1.6) for primary RO_2 radicals derived

from monoterpene species. Experimental studies show that this calculated branching ratio is indeed in the range of what can be expected, but that specific branching ratios differ for different monoterpenes (Noziere et al. (1999), Rollins et al. (2010)). However, the branching ratio of the nitrate formation is usually below 35%, making the formation of the alkoxy radical (RO, Reaction R1.7) the dominant pathway for the RO_2 + NO reaction.

The NO_2 molecule that is formed in Reaction R1.7 is photolyzed, resulting in the formation of O_3 (Reactions R1.8 and R1.9). The formation of NO_2 from the oxidation of NO from Reaction R1.6 and the subsequent photolysis of NO_2 is the only relevant chemical source of ozone in the troposphere.

$$NO_2 + h\nu \longrightarrow NO + O(^3P) \tag{R1.8}$$

$$O_2 + O(^3P) + M \longrightarrow O_3 + M \tag{R1.9}$$

The ozone formed in Reaction R1.9 subsequently reacts with NO, to regenerate NO_2 (Reaction R1.10).

$$O_3 + NO \longrightarrow NO_2 + O_2 \tag{R1.10}$$

NO, NO_2 and O_3 are thus in a photochemical equilibrium. In areas where high NOx concentrations coincide with high VOC mixing ratios, e.g. big metropolitan areas, NO can be oxidized by its reaction with HO_2 or RO_2 radicals (Reactions R1.21 and R1.6), reforming NO_2. Through Reactions R1.8 and R1.9, new ozone is formed leading to photochemical air pollution referred to as summer smog.

The alkoxy (RO) radical formed in Reaction R1.6 can then undergo further reactions: unimolecular decomposition, unimolecular isomerization, or reaction with O_2 (Reaction R1.11). For simple alkenes, unimolecular decomposition of the formed alkoxy radical leads to the formation of an alkyl radical and formaldehyde, as shown exemplary for an alkoxy radical formed in the oxidation of ethene by OH in Reaction R1.12. The alkyl radical further reacts with O_2, giving formaldehyde and HO_2.

$$RO + O_2 \longrightarrow R'CHO + HO_2 \tag{R1.11}$$

$$HO{-}CH_2CH_2O \longrightarrow HCHO + \cdot CH_2OH \tag{R1.12}$$

$$\cdot CH_2OH + O_2 \longrightarrow HCHO + HO_2 \tag{R1.13}$$

In the case of cyclic monoterpenes, the decomposition of the alkoxy radical often leads to the formation of a ring-opened oxidized VOC (OVOC) species, e.g. caronaldehyde in the oxidation of Δ^3-carene or pinonaldehyde in the case of α-pinene. As in the Reaction R1.11, an HO_2 radical is formed. Those aldehydes usually have an atmospheric lifetime of several hours to days and a lower vapour

pressure than their parent compound, and are thereby influencing secondary organic aerosol (SOA) formation and growth (Laaksonen et al. (2008)). OVOCs mainly react with the OH radical, but can also be photolysed. In the photolysis of formaldehyde (Reactions R1.14 and R1.16), the simplest aldehyde, an H atom that subsequently reacts with O_2 resulting in the production of HO_2 radicals, can be formed.

$$HCHO + h\nu \longrightarrow H + CHO \tag{R1.14}$$
$$CHO + O_2 \longrightarrow HO_2 + CO \tag{R1.15}$$
$$HCHO + h\nu \longrightarrow H_2 + CO \tag{R1.16}$$

The reaction of RO_2 radicals with HO_2 leads to the formation of hydroperoxides (ROOH, Reaction R1.17a). They can be photolyzed, thereby forming an OH radical and an alkoxy radical. Alternatively, H-abstraction by an OH radical can occur, forming a peroxy radical and water molecules. The chain-terminating formation of ROH (Reaction R1.17b) or the chain-propagating formation of an alkoxy radical (Reaction R1.17c) gain in importance depending on the structure of the initial peroxy radical (Iyer et al. (2018)). It was speculated that Reactions R1.17b and R1.17c are of higher importance for monoterpene derived RO_2 that are able to stabilize the transition state of these reactions by strong hydrogen bonding interactions (Iyer et al. (2018)).

$$RO_2 + HO_2 \longrightarrow ROOH + O_2 \tag{R1.17a}$$
$$\longrightarrow ROH + O_3 \tag{R1.17b}$$
$$\longrightarrow RO + OH + O_2 \tag{R1.17c}$$

The reaction of RO_2 with other RO_2 radicals either terminates the ROx radical chain forming of a carbonyl compound and an alcohol (Reaction R1.18a), a dimer (R1.18b) or leads to the formation of two alkoxy radicals (Reaction R1.18c), propagating the radical chain. However, Reaction R1.18b is usually negligible.

$$RO_2 + RO_2 \longrightarrow R'CHO + ROH + O_2 \tag{R1.18a}$$
$$\longrightarrow ROOR + O_2 \tag{R1.18b}$$
$$\longrightarrow RO + RO + O_2 \tag{R1.18c}$$

Unimolecular reactions of the RO_2 radicals have received special attention in the past years. As a consequence of the unimolecular reactions, oxygen (O_2) is added to the organic molecules, and therefore these reactions are often referred to as autoxidation reactions. Autoxidation processes have been known to occur in high-

temperature combustion processes, but it has long been believed that they are of little importance in the atmosphere. Only in the last three decades, their importance for the atmospheric oxidation processes has been discovered and their reaction pathways determined (e.g. Perrin et al. (1998), Vereecken et al. (2007), Crounse et al. (2013)). Autoxidation processes have since been found to be an important reaction pathway for RO_2 with a double bond retained in the structure. These unimolecular reactions can even be competitive with bimolecular reaction in remote atmospheres (Moller et al. (2020)).

An intramolecular H-shift rearranges the RO_2 structure to form an hydroperoxyalkyl radical (QOOH) that then reacts with molecular oxygen, forming a hydroperoxyalkylperoxy radical(O_2QOOH). The newly formed peroxy radical can then react with NO, HO_2, RO_2, as discussed above, or undergo another intramolecular H-shift reaction. Figure 1.2 exemplary shows an autoxidation process.

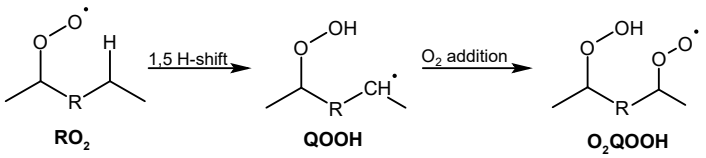

Figure 1.2: Simplified autoxidation scheme, adapted according to Ehn et al. (2014).

Depending on the molecules size and structure, several H-migration and O_2 addition reactions occur subsequently, leading to the formation of RO_2 with a high O:C ratio. The barrier height for H-shift reactions is lowered by the presence of certain functional groups (Moller et al. (2020), Vereecken and Noziere (2020)). From these highly oxidized radicals, highly oxidized closed-shell products can be formed. Due to their low vapour pressure compared to the parent compound, these molecules are likely condensing efficiently on existing particles, or even form new particles, thereby contributing to SOA formation and growth (Bianchi et al. (2019)).

Other reactions of the OH radical in the atmosphere that do not form a RO_2 radical but an HO_2 radical include the OH reaction with CO or formaldehyde. In the case of the reaction of OH with CO, this leads to the formation of CO_2 and an H radical that subsequently reacts with molecular oxygen, forming a HO_2 radical.

$$OH + CO \longrightarrow H + CO_2 \quad \text{(R1.19)}$$

$$H + O_2 + M \longrightarrow HO_2 + M \quad \text{(R1.20)}$$

An OH radical is then reformed from the HO_2 radical by its reaction with NO, also forming NO_2, completing the quasi-catalytic oxidation cycle.

$$HO_2 + NO \longrightarrow OH + NO_2 \qquad \text{(R1.21)}$$

The reaction cycle of the radicals of the ROx family can be summed up as shown in Figure 1.3. They are interconnected by cyclic chain reactions. Due to this radical recycling reactions, every primary formed OH can oxidise several reactants as the radical is regenerated before the radical chain terminates. In environments where sufficient NO is present as a reaction partner for RO_2 and HO_2 radicals, at least one O_3 molecule is formed per reaction cycle. Since RO_2 are less reactive than the OH radical, their concentration exceeds the OH radical concentration by up to two orders of magnitude for typical atmospheric conditions. OH radicals have an atmospheric lifetime of only fractions of a second and typically observed concentrations are in the range of $10^6\,cm^{-3}$. Typical atmospheric lifetimes of RO_2 are in the range of seconds to minutes, and typically observed concentrations are in the range of $10^8\,cm^{-3}$.

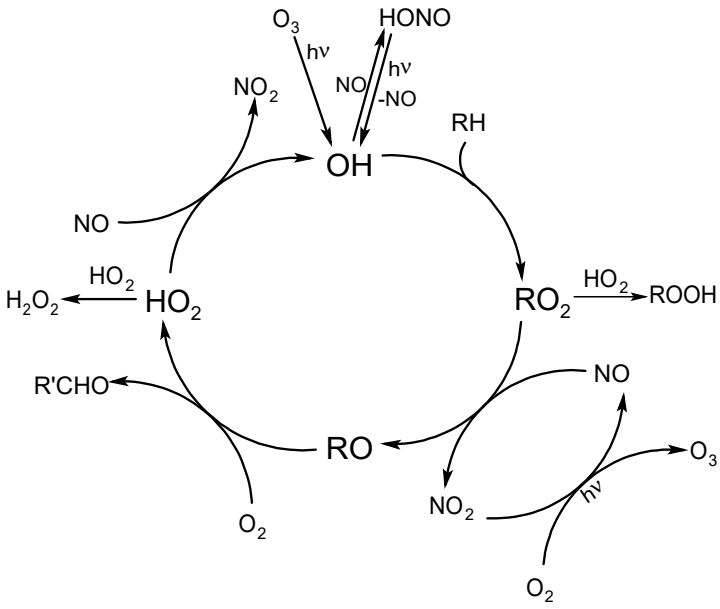

Figure 1.3: Simplified scheme of the daytime radical chemistry in the atmosphere.

The second most important oxidizing agent in the troposphere is ozone. The atmospheric lifetime of ozone is in the range of days, whereas the lifetime of OH

is a fraction of a second. In the atmosphere, alkanes and aromatic compounds do not react with ozone, but are only oxidized by the reaction with the OH radical. Since alkenes such as the monoterpenes are unsaturated compounds with at least one C-C double bond, they are prone to be oxidized by ozonolysis. The molecular structure of the VOC is important for the rate of this reaction. However, reaction rates of ozonolysis of VOC are usually smaller than those of the reaction of VOC with the OH radical, making oxidation by the OH radical the dominant oxidation process during daytime.

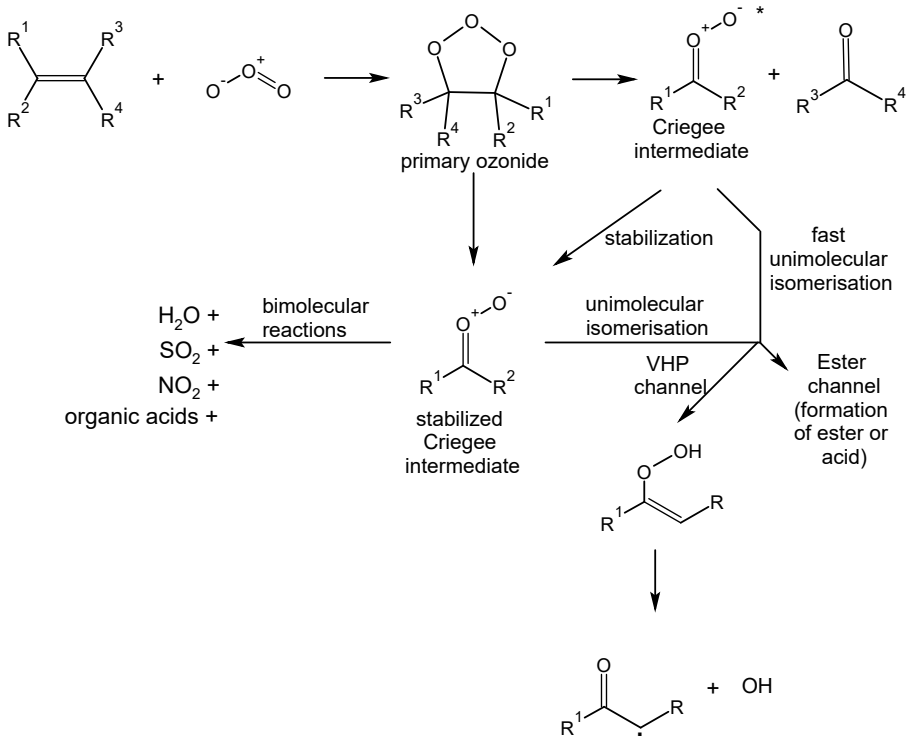

Figure 1.4: Ozonolysis of an unsaturated compound. OH radicals and a carbonyl compound are formed from a vinyl hydroxy peroxide (VHP) by decomposition of the -O-OH bond. Another possible pathway of the (stabilized) Criegee intermediate is the ester channel. Many different molecules with an acidic or ester functionalization are formed through this pathway.

For example, the atmospheric lifetime of β-pinene to oxidation by O_3 is nearly 30 hours for typical atmospheric O_3 mixing ratios of 30 ppbv while it is only 3.5 hours to the reaction with the OH radical at typical atmospheric OH concentrations of $1{\times}10^6\,\mathrm{cm}^{-3}$.

The ozonolysis of monoterpenes in the atmosphere follows the Criegee mechanism (Criegee (1975)) and is initiated by an attack to the unsaturated C-C double bond, resulting in the formation of an energy-rich primary ozonide (Figure 1.4). The primary ozonide rapidly decomposes to form a Criegee intermediate and a carbonyl compound. In the case of some cyclic monoterpenes like Δ^3-carene, one structure is retained and the carbonyl functional group and Criegee intermediate are on the opposite sites of the molecule. The Criegee intermediate subsequently forms dioxiranes, secondary ozonides or vinyl hydroperoxides in an isomerization reaction. A collisional stabilization of the Criegee intermediate to form stabilized Criegee intermediates is also possible. The formation yields of the aforementioned species differ for different monoterpenes. Isomerisation of the excited or stabilized Criegee intermediate leads to the formation of a vinyl hydroxy peroxide through a 1,4-H shift. The vinyl hydroxy peroxide subsequently decomposes, forming OH and an alkoxy radical. The ozonolyis of alkenes is one of the main sources of the OH radicals at night-time (Paulson and Orlando (1996)), thereby adding to the total oxidizing capacity of the atmosphere.

1.3 Objectives of this thesis

Monoterpenes are emitted in high quantities into the atmosphere from both biogenic and anthropogenic sources. As they are unsaturated compounds, bearing at least one C-C double bond, they rapidly react with the major oxidants in the atmosphere, the OH radical and ozone, thereby contributing to the formation of organic aerosol and ozone and impacting the oxidation capacity of the atmosphere. Therefore, understanding the exact degradation mechanism of specific monoterpene species, including the reaction rate constants of their reactions with OH radicals and ozone and the yields of organic oxidation products, such as aldehydes and nitrates, is crucial to understand the composition of the atmosphere, especially over forested areas, where monoterpene emissions are often dominating and NOx concentrations are low.

The reaction mechanisms of the most abundant monoterpenes, α- and β-pinene have been investigated in numerous studies (e.g. Arey et al. (1990), Hakola et al. (1994), Vereecken and Peeters (2012), Kaminski et al. (2017), Rolletter et al. (2020) and references therein) and their detailed degradation mechanisms have been published in the Master Chemical Mechanism (MCM, Saunders et al. (2003)), a near-explicit mechanism describing the gas-phase chemical processes involved in the tropospheric degradation of these species. However, many experimental studies were conducted at precursor concentrations higher than several hundred ppbv (e.g. Arey et al. (1990); Hakola et al. (1994)). Since bimolecular reactions depend on the con-

centration of the reaction partners, they are more likely to dominate the product formation reactions for conditions with high precursor concentrations. Experiments in the SAPHIR chamber, like the experiments investigating the oxidation of β-pinene by Kaminski et al. (2017) and the oxidation of α-pinene by Rolletter et al. (2020) as well as the experiments analysed in this work, investigating myrcene and Δ^3-carene oxidation, are conducted at precursor concentrations of 3 to 10 ppbv. Those concentrations are close to mixing ratios of monoterpenes observed in field studies (e.g. Hakola et al. (2012)).

In the monoterpene oxidation studies conducted in the SAPHIR chamber by Kaminski et al. (2017) and Rolletter et al. (2020), it was found that the respective oxidation mechanism reported in the MCM (version 3.2 in Kaminski et al. (2017) and version 3.3.1 in Rolletter et al. (2020)) was not able to reproduce the experimental findings, especially in regard to measured OH and HO_2 concentrations that were underpredicted by up to a factor of 2 by the model. In the same experiments, the model overpredicted the measured yields of the oxidation products, nopinone and pinonaldehyde, by up to a factor of 3-4, respectively. A better model to measurement agreement of the radical and oxidation product concentrations was achieved in both cases when implementing reaction pathways from quantum chemical calculations by Vereecken et al. (2007) in the case of α-pinene and by Vereecken and Peeters (2012) in the case of β-pinene. For both molecules, the main differences between the mechanism reported in the MCM and by Vereecken et al. (2007) or Vereecken and Peeters (2012) were the branching ratio of the formation of the first generation RO_2 and the inclusion of unimolecular reaction pathways for the RO_2 in the mechanisms published by Vereecken et al. (2007) or Vereecken and Peeters (2012).

Discrepancies between measured and modelled radical concentrations were also found in field measurements conducted in monoterpene rich environments over boreal forests. A field study conducted in a forest in Hyytiälä, Finland, where mostly pine trees grow, (Hens et al. (2014)) found that it is possible to explain measured OH concentrations, while HO_2 concentrations and the OH reactivity (k_{OH}) were significantly underpredicted by chemical models. The authors concluded that this must be due to an unaccounted HO_2 source. Similar conclusions can be drawn from a field study conducted by Kim et al. (2013). OH radicals were measured during a field campaign in the monoterpene rich environment at the Manitou Forest Observatory, in Colorado, US. While it was found that the measured OH radical concentrations were in good agreement with results from steady-state calculations, a chemical box model severely underpredicted the measured HO_2 and OH radical concentrations. It was concluded that an unknown HO_2 source may be the cause. Because both studies were conducted in monoterpene-rich environments, it is likely that the additional HO_2 source is due to unaccounted processes in the oxidation of monoterpenes.

For some monoterpenes whose abundance is globally less important, but whose emissions are high in certain areas, few experimental studies have reported specific information of the chemical degradation reactions and their products. For that reason, no detailed and tested mechanisms existed so far for the degradation of Δ^3-carene and myrcene in the atmosphere, two monoterpenes that have significant emissions over boreal forests, where the studies by Hens et al. (2014) and Kim et al. (2013) were conducted. It can be assumed that the oxidation mechanisms of structurally similar molecules are usually comparable. Structure-activity relationship (SAR) make use of existing experimental and theoretical data of reactions of well-studied molecules in the atmosphere to obtain trends and extrapolating them to the reactions of less studied compounds (Vereecken et al. (2018)). While this often gives a good approximation of one possible reaction mechanism of an understudied species, the real oxidation mechanism could be different. This is especially true for highly functionalized molecules. For example, it has recently been shown that even though α-pinene and Δ^3-carene are structurally very similar, reaction rates of unimolecular reactions of the RO_2 formed in the OH oxidation of both species show significant differences (Moller et al. (2020)). The sole structural difference between the two molecules is the nature of the bicyclus that is a four-membered ring for α-pinene and a three-membered ring for Δ^3-carene.

To clarify the source of the additional HO_2 found in field studies, it is necessary to know the oxidation mechanism of all involved species as detailed as possible. This includes knowledge about reaction rate constants, branching ratios and product yields as well as the radical regeneration efficiency and the importance of unimolecular RO_2 radical reactions that can be determined from experiments conducted in atmospheric simulation chambers. Besides helping to understand the discrepancies in model and measurement results found when comparing field measurements of HO_2 concentrations, this also helps understanding the processes leading to the formation of e.g. aerosol particles.

Ameliorating and testing the mechanistic understanding of the degradation of monoterpenes can be challenging, since it requires the measurement of the individual intermediates and products. Different experimental timeframes are needed to determine the product distribution and concentration at different stages of the oxidation processes. Additionally, a large set of instrumentation is required to measure all necessary trace gases, radicals and physical parameters such as solar actinic radiation. The comparison of experimentally determined values for reaction rate constants, product yields and branching ratios to theoretical predictions can be a useful tool to test postulated mechanisms, to determine missing processes and distinguish possible needed reaction pathways.

Experiments in atmospheric simulation chambers and flow tubes are often the

method of choice to determine reaction mechanisms and reaction rate constants. In the 270 m^3 atmospheric simulation chamber SAPHIR at Forschungszentrum Jülich (Rohrer et al. (2005), Chapter 2.1), a special focus is put on reproducing atmospheric conditions as close as possible, by adding reactants and oxidants in atmospherically relevant concentrations. A large set of analytical instrument is used to measure radical concentrations, VOC and NOx mixing ratios and other important parameters. This allows to determine reaction rate constants, products yields and whether there are missing radical sources. In the smaller SAPHIR-STAR chamber, oxidation reactions can be observed at steady-state conditions. Experiments in the free-jet flow tube system are conducted with reaction times of 8 seconds, allowing to observe the formation of early oxidation products and to determine the rates of possible unimolecular reactions of the formed peroxy radicals. The development of new measurement techniques for the detection of species formed in the oxidation of atmospherically relevant monoterpenes, like the detection of specific peroxy radical families by mass spectrometric methods, is another step towards a better understanding of the composition of the atmosphere as it helps to develop chemical oxidation mechanisms for VOCs emitted in both rural and urban environments.

This thesis aims to elucidate key aspects of the oxidation mechanisms of three monoterpenes and one monoterpene oxidation product. The oxidation of Δ^3-carene by the OH radical and ozone, the oxidation of myrcene by OH and the oxidation of caronaldehyde were studied in the large atmospheric simulation chamber SAPHIR, with special regard to the determination of reaction rate constants, yields of organic nitrates and other reaction products and to the analysis of the OH, HO_2 and RO_2 radical concentrations observed in the chamber study.

The oxidation of β-pinene was studied in a free-jet flow system and in the atmospheric simulation chamber SAPHIR-STAR. The main focus of these investigations was the measurement of specific peroxy radicals, using a recently developed detection scheme based on chemical ionization mass spectrometry. The further development of this detection scheme for its use at the SAPHIR-STAR chamber was a part of this work. The investigations of the β-pinene oxdiation by the OH radical are based on recent studies by Vereecken and Peeters (2012) and Kaminski et al. (2017) that revealed that the product distribution determined from chemical models like the Master Chemical Mechanism (MCM, Saunders et al. (2003)) fail to match experimental observations.

This thesis has the following objectives:

(i) using and further developing analytical detection techniques that can be used to clarify chemical mechanisms through the direct detection of organic peroxy radicals by mass spectrometric methods, such as chemical ionization mass spec-

trometry (CIMS, Chapter 3)
(ii) determine the importance of unimolecular reactions in the photooxidation of the investigated monoterpenes
(iii) contributing to the understanding of the oxidation mechanism of the studied monoterpenes by determining product yields, reaction rate constants and branching ratios.

The results of the experiments investigating the oxidation mechanisms of Δ^3-carene and myrcene in the atmospheric simulation chamber SAPHIR were published in two peer-reviewed publications (Hantschke et al. (2021) and Tan et al. (2021)) that can be found in Chapters 5 and 6 respectively. Experiments conducted in a small flow tube and in the atmospheric simulation chamber SAPHIR-STAR investigating the oxidation mechanism of β-pinene are discussed in regard to the observed peroxy radical formation in Chapter 7.

A team of people has been involved in both the measurements at the SAPHIR and the SAPHIR-STAR chamber. In this work, the data obtained from these measurements as provided by the measurement teams are used to analyse the VOC oxidation experiments. Contributions of each team member can be found in the respective publications. Individual contributions are also described in Appendix B.1. The experiments conducted in the free-jet flow system were supported by Dr. Torsten Berndt, who provided the experimental facilities and the initial development of the CIMS-based detection scheme for the measurement of specific peroxy radicals.

2 Atmospheric Simulation chambers

In this thesis, three different chemical reactors, the atmospheric simulation chambers SAPHIR (Simulation of Atmospheric PHotochemistry In a large Reaction chamber) and SAPHIR-STAR (Stirred Atmospheric flow Reactor) at the Forschungszentrum Jülich, and a free-jet flow system at the TROPOS Institute in Leipzig, were used to study different aspects of the oxidation mechanisms of the three monoterpenes Δ^3-carene, myrcene and β-pinene at atmospherically relevant temperature, pressure and concentration conditions. The three reactors offer benefits for the investigations of different aspects of chemical oxidation mechanisms on different time scales.

In the SAPHIR chamber, a starting mixture of VOC is injected into the chamber, and the VOC decay and the radical chemistry is observed over the course of several hours. Natural sunlight is used as a light source in the chamber. A big variety of different analytical instruments is used to simultaneously measure concentrations of trace gases and radicals. In this thesis, experiments investigating the oxidation of myrcene and Δ^3-carene were conducted in the SAPHIR chamber.

Table 2.1: Overview of the properties of the three different chemical reactors used in this thesis.

	SAPHIR	**SAPHIR-STAR**	**free-jet flow system**
size / m^{-3}	270	2	/
material	FEP	glass	glass
light source	natural	artificial	artificial
wavelength	solar UV-vis	254 and 365 nm	360 nm
radical source	photolysis	photolysis	ozonolysis/photolysis
T / K	ambient	293	293-298
p / K	1000	1000	1000
residence time	several hours	1 hour	1-8 seconds
measured species	Chapter 5+6	(O)VOC, NOx, O_3	(O)VOC, O_3

The SAPHIR-STAR chamber is a newly built atmospheric simulation chamber at Forschungszentrum Jülich and allows for studies of atmospheric chemistry reactions. The SAPHIR-STAR chamber is significantly smaller than the SAPHIR chamber and is operated in steady-state conditions. In the SAPHIR chamber, reactants are only injected once into the chamber, and their temporal behaviour is observed. In the SAPHIR-STAR chamber, reactants are added continuously so

that the chemistry in the chamber is assumed to be in steady-state. Artificial light sources are used in the SAPHIR-STAR chamber, and the reaction time is about 1 h. The concept of the SAPHIR-STAR chamber is similar to JPAC (Jülich Plant Atmosphere Chamber) previously used at the Forschungszentrum Jülich to study e.g. the formation of organic aerosol or highly oxidized molecules (HOM) at different experimental conditions (Mentel et al. (2009), Sarrafzadeh et al. (2016), Pullinen et al. (2020)). In this study, SAPHIR-STAR was used to investigate the oxidation mechanism of β-pinene.

In the free-jet flow system at the TROPOS institute, the kinetics and product distribution of the oxidation of VOC species can be observed on a time scale of only a few seconds without the influence of secondary chemistry. In this thesis, the first steps of the oxidation of β-pinene by the OH radical were investigated in the free-jet flow system.

2.1 The atmospheric simulation chamber SAPHIR at Forschungszentrum Jülich

The SAPHIR chamber is one of the atmospheric simulation chambers used for experiments at the IEK-8 at Forschungszentrum Jülich. In this work, it was used to examine the oxidation mechanism and product formation from oxidation reactions of Δ^3-carene and myrcene.

As it has been described in detail in many publications, e.g. Rohrer et al. (2005), only a short overview of its characteristics is given here.

SAPHIR is a double-walled atmospheric simulation chamber of cylindrical shape. It is made of an inert Fluorinated Ethylene Propylene (FEP) film and has a volume of 270 m^3. The chamber has a length of 18 m and an inner diameter of 5 m. The volume to surface ratio is about 1 m^{-1}, which is beneficial for studying reactions at nearly atmospheric conditions, as the influence of heterogeneous reaction on the walls and wall losses on observed reactive species is kept small. To mix the synthetic air for the experiments, ultrapure oxygen and nitrogen (Linde, <99.9999%) are used.

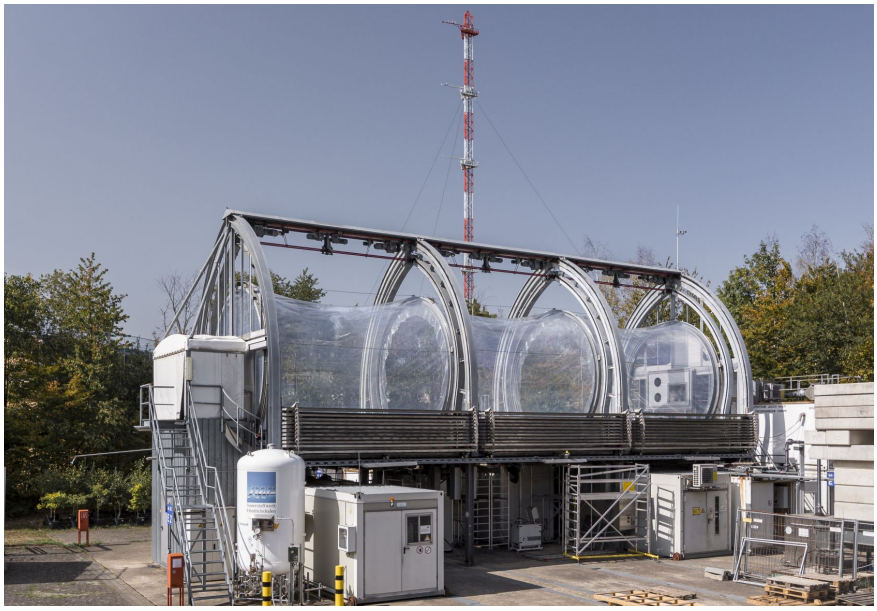

Figure 2.1: The SAPHIR chamber at Forschungszentrum Jülich with opened roof. Copyright „Forschungszentrum Jülich / Sascha Kreklau“

The chamber is kept at an overpressure of 35 Pa compared to the outside pressure and the space between the two FEP films is continuously flushed with ultrapure nitrogen to avoid leaking of outside air into the reaction chamber. During experiments, a flow of synthetic air is constantly introduced into the chamber to compensate for air loss due to instrument sampling and small leakages. This leads to a dilution of trace gases in the chamber of about 4% per hour. Since the chamber foil has a transmittance of 85% for solar radiation, natural sunlight can be used as a light source. A shutter system allows the experiments to be conducted in both a sunlit (shutters open) or a dark (shutters closed) chamber to simulation e.g. night-to-day transitions even during daytime. Two fans that are installed at opposite ends of the chamber ensure that the air in the chamber is well mixed. The instruments measuring the trace gases and particle properties are usually mounted outside of the chamber in containers to avoid additional surfaces inside the chamber. For some instruments, short sampling lines are used to minimize wall losses in the sampling lines.

2.1.1 Instrumentation

In the SAPHIR chamber, two different instruments are available for the detection of the OH radical: differential optical absorption spectroscopy (DOAS) and laser

induced fluorescence (LIF). With LIF, HO_2 and RO_2 radicals can be measured additionally.

The DOAS technique (Dorn et al. (1995)) provides a calibration-free detection of the OH radical by measuring the absorption of UV light by OH radicals at 308 nm. To obtain a sufficient signal to noise ratio, a long path is required. For the instrument measuring in the SAPHIR chamber, this is realised by using a modified multiple-reflection cell with a base length of 20 m. A total path length of 2240 m is achieved after 112 travels (Schlosser et al. (2007)). The DOAS technique relies on the separation of broad- and narrowband spectral structures. Using a mathematical fit procedure, the 'slow' changes e.g. caused by Mie or Rayleigh scattering are separated from the 'fast' changes caused by absorption by a molecule of interest, and a differential spectrum is obtained (Platt and Stutz (2008)). Applying the Lambert Beer's law, concentrations of absorbers like the OH radical can be calculated from the optical density using the differential absorption cross sections by fitting the measured spectra to a linear superposition of reference spectra.

In the LIF instrument, OH radicals are detected directly, whereas HO_2 and RO_2 radicals have to be chemically converted to OH prior to the detection in the instrument (Fuchs et al. (2008)). OH radicals are excited at 308 nm by laser radiation from a pulsed laser. The resulting resonance fluorescence is measured by gated photon counting. A radical calibration source generating OH radicals by water photolysis at 185 nm with a mercury vapour lamp is used for calibration of the measured fluorescence intensity. Comparison of the two measurement techniques for the OH radical, DOAS and LIF, generally shows a good agreement within their combined 1σ accuracies of 6.5% and 18.5%, respectively (e.g. Fuchs et al. (2012), Cho et al. (2021)).

A second low-pressure measurement cell is used in the LIF instrument to measure HO_2 radical concentrations. The sampled air containing HO_2 radicals is mixed with NO, thereby converting HO_2 to OH through its reaction with NO (Reaction R1.13, $HO_2 + NO \rightarrow OH + NO_2$). The sum of OH and HO_2 radicals is measured, and the actual HO_2 concentration can be determined by subtracting the OH concentration measured in the first fluorescence cell.

A third measurement cell is used to determine the RO_2 concentration in a two-stage system. In a first step, the RO_2 radicals are chemically converted into HO_2 radicals through their reaction with NO, which also leads to the formation of OH from the reaction of formed HO_2 radicals with NO, since both reactions happen on the same time scale. To avoid wall loss reactions and loss of the radicals through radical termination reactions (e.g. HONO formation) an excess of CO is also added in this first step, reconverting formed OH radicals to HO_2. The air is then sucked into a second detection chamber where HO_2 is converted to OH by excess NO and

detected subsequently. The detection sensitivity of the LIF-RO_2 measurements is optimized and calibrated for the CH_3O_2 radical produced from methane oxidation with OH. The detection sensitivity was also tested for other peroxy radicals (Fuchs et al. (2008)) derived from the oxidation of other VOC, e.g. monoterpenes. In most cases, the detection sensitivity differed less than 20% from the value determined for the CH_3O_2 peroxy radical (master thesis of C. Lakshmisha). For some radicals, a lower detection sensitivity was found, which hints to an incomplete conversion of the RO_2 radicals to OH and needs to be taken into account in the analysis.

OH reactivity (k_{OH}) is measured with a laser flash photolysis - laser induced fluorescence instrument (Lou et al. (2010), Fuchs et al. (2017)). k_{OH} is the inverse OH lifetime and describes the sum of OH reactant concentrations [X_i] weighted by their bimolecular reaction rate coefficients with OH, k_{OH+X_i} (Equation 2.1).

$$k_{OH} = \sum_i k_{OH+X_i}[X_i] \tag{2.1}$$

Parent VOCs injected into the chamber and some of their reaction products were measured by proton-transfer time-of-flight mass spectrometers (PTR-TOF-MS, and (VOCUS)-PTR-MS, Aerodyne). During some experiments described in this work, GC-FID (gas chromatography with flame ionization detection) is used additionally to detect VOCs. A custom-built long-path absorption photometer was used to detect nitrous acid (HONO) (Kleffmann et al. (2002), Li et al. (2014)). NO and NO_2 are measured by a chemiluminescence instrument (Eco Physics), equipped with a blue light converter for the conversion of NO_2 to NO. CH_4, CO and water vapour are measured with a cavity ring-down instrument (G2401, Picarro) and O_3 with an UV absorption instrument (Ansyco). A model is used for calculating the mean spectral actinic flux density F_λ using the spectral radiometer measurements as an input. Photolysis frequencies (j) are calculated from total and diffuse spectral actinic flux measurements outside of the SAPHIR chamber (Equation 2.2) with σ the absorption cross section, ϕ the quantum yield, and F the actinic flux.

$$j = \int \sigma(\lambda)\phi(\lambda)F_\lambda(\lambda)\mathrm{d}\lambda \tag{2.2}$$

Conversion to photolysis frequencies applicable inside the chamber is described in detail by Bohn et al. (2005) and Bohn and Zilken (2005).

2.1.2 Experiment procedure

The experiments in SAPHIR were all conducted following a similar procedure. Before the start of each experiment, the chamber was flushed with synthetic air until trace gas concentrations were below the detection limits of the instrument to ensure

a clean chamber. The chamber air was humidified by adding water vapour obtained from boiling Milli-Q water and supplying it together with a high flow of synthetic air into the chamber. The humidity ranges were different for different experiments. For photooxidation experiments, the relative humidity was up to 80% at the beginning of the experiment, while for ozonolysis experiments, relative humidities were only in the range of 20 to 30%. Over the course of the experiment day, the relative humidity in the chamber decreases, mostly due to a rise in temperature inside of the chamber. After the humidification, the chamber roof was opened if the experiment required sunlit conditions. OH radicals are mainly produced in the chamber from photolysis of HONO when the roof is opened and from photolysis of ozone that can be either injected or is photochemically produced. After the opening of the roof, no reactive trace gases were added into the chamber for the next two to three hours. This so-called 'zero-air' phase is needed to determine the strength of small chamber sources of HONO, HCHO and acetone and to determine the background OH reactivity from further undetected contaminations for the respective day. The reason for these chamber impurities are likely due to some contaminants that remain in the chamber film even after flushing out the chamber after an experiment. Upon humidification or irradiation of the chamber, these contaminants are desorbed from the chamber film. The OH reactivity observed during that time is seen as background reactivity as it is caused by the background contaminants in the chamber.

After the 'zero-air' phase, VOCs are injected up to three times into the chamber, together with NO or CO, depending on the experiment. For chamber experiments in the dark, the respective VOC is injected into the chamber directly after the end of the humidification phase, since no desorption from the chamber walls caused by irradiation are expected. VOC mixing ratios in the chamber depend on the goal of the experiment, but are usually in the range of several ppbv. The VOCs are injected as a liquid into a heated volume and transported into the chamber with the replenishment flow of synthetic air that is constantly provided. Using the rate constant of the reaction of the injected VOC with OH, the VOC concentration in the SAPHIR chamber can be determined. Changes in the OH reactivity in the SAPHIR chamber are due to the injection of traces gases in the chamber. For experiments conducted in the sunlit chamber, the experiments are concluded by closing the roof of the chamber, usually several hours after the last injection of the investigated VOC species.

2.2 The atmospheric simulation chamber SAPHIR-STAR at Forschungszentrum Jülich

SAPHIR-STAR is a continuously stirred flow reactor made out of borosilicate glass of cylindrical shape. It has a volume of 2 m^3. SAPHIR-STAR is placed inside of a temperature-controlled chamber, making a distinct control of the reaction temperature in a range between 10°C and 50°C possible. A residence time of approximately one hour is reached by supplying a constant flow of synthetic air or nitrogen with a rate of 30 l min^{-1}. The air is provided by mixing ultrapure oxygen and nitrogen (Linde, <99.9999%) as for the SAPHIR chamber. Air enters the chamber through two inlet lines at opposite ends to ensure a homogeneous mixing of trace gases. Additionally, the chamber air can be stirred by a fan to ensure better mixing. Controlled Evaporation Mixing (CEM) systems (Bronkhorst) are used to humidify the synthetic air.

Figure 2.2: The SAPHIR-STAR chamber at Forschungszentrum Jülich. Copyright „Forschungszentrum Jülich / Sascha Kreklau“

Several additional lines attached to the main lines for supplying air to the chamber allow the introduction of trace gases. One additional inlet line is used for the introduction of aerosols produced by an aerosol generator. Ozone is produced by an ozone generator (UVP OG-2, Fisher scientific). Organic compounds that are liquids at room temperature can be continuously added into the gas stream by using a syringe pump system. The liquid provided by the pump evaporates in a heated glass

bulb and is then transported by a small flow of nitrogen to the inlet line.

Artificial light sources are used in the SAPHIR-STAR chamber to initiate photolysis reactions. Two lamps provide light in the UV-C range with peak emissions at 254 nm. They are equipped with a shutter system, consisting of two bellows that can be opened and closed by a motor. Additionally, UV-A lamps are installed in the chamber with peak emissions at 365 nm.

Temperature and humidity of the air are measured by sensors in all inlet lines, inside the chamber, and in the main outflow line. Ozone concentrations inside the chambers are measured by an UV absorption instrument. A PTR-MS instrument is used for the detection of the primary VOC and some reaction products. A chemical-ionization-atmospheric-pressure-interface-time-of-flight (CI-API-TOF-CIMS, Chapter 3.2) instrument (Aerodyne) is used with protonated propylamine primary ions for the detection of oxidation products.

OH radicals are produced in the chamber either by photolysis of hydrogen peroxide (H_2O_2) or by ozone photolysis in the presence of water. OH is formed from the H_2O_2 photolysis by Reaction R2.1a.

$$\begin{aligned}
H_2O_2 + h\nu &\longrightarrow 2\,OH && (\lambda < 555\text{ nm}) && \text{(R2.1a)}\\
&\longrightarrow H + HO_2 && (\lambda < 325\text{ nm}) && \text{(R2.1b)}\\
&\longrightarrow 2\,H + O_2 && (\lambda < 209\text{ nm}) && \text{(R2.1c)}\\
&\longrightarrow H_2 + O_2 && (\lambda < 555\text{ nm}) && \text{(R2.1d)}
\end{aligned}$$

$$OH + H_2O_2 \longrightarrow H_2O + HO_2 \qquad \text{(R2.2)}$$

Additionally, the photolysis of H_2O_2 leads to the formation of HO_2 radicals (Lockhart et al. (2018)), through either the direct formation of HO_2 from photolysis by UV light ($\lambda < 325$nm) (Reaction R2.1b), the reaction of the H atoms formed in Reactions R2.1b and R2.1c with O_2 or its formation from the H_2O_2 + OH reaction (Reaction R2.2).

2.3 The free-jet flow system at the TROPOS institute in Leipzig

Experiments investigating the reaction mechanism of β-pinene were also conducted in a flow tube at the TROPOS institute in Leipzig. The flow tube is best described as a free-jet flow system. As its features have been detailed in previous publications (e.g. Berndt (2005), Berndt et al. (2018)) only a brief overview is given here. The

flow tube is operated at a temperature of (297±1) K and at atmospheric pressure (1010 hPa).

Figure 2.3: Schematics of the free-jet flow system used at TROPOS. Adapted from Berndt et al. (2015b).

The system consists of a tube with a length of 2 m and an inner diameter of 16 cm. In the tube, there is a movable injector tube with a 3 mm nozzle. Dry synthetic air is flowed through the flow tube with a flow rate of 95 $l\,min^{-1}$. It is laminarized by passing a grid. In a typical experiment, the reactant whose reaction mechanism is to be investigated and other trace gases are continuously injected. The main reactant, normally a VOC, is injected with the main gas stream. An additional $5\,l\,min^{-1}$ of air, containing the other reactants, usually ozone or isopropylnitrite, is introduced through the injector into the main gas stream. Ozone is produced by a ozone generator upstream of the injector tube. The air leaving the nozzle has a high velocity of $15.9\,m\,s^{-1}$, whereas the gas velocity of the main gas flow is only $0.13\,m\,s^{-1}$ (Berndt et al. (2015a)). The large difference of the gas velocities ensures rapid mixing of trace gases downstream of the nozzle (Berndt et al. (2015a)). The reactants are almost completely mixed 0.25 m downstream of the nozzle, as numerically simulated by computational fluid dynamics calculations by Berndt et al. (2015a).

No significant wall losses are expected, as for these flow conditions at atmospheric pressure diffusion processes transporting reaction products out of the center of the stream are negligible due to the laminarization of the main gas flow (Berndt et al. (2015a)). The position of the injector tube can be changed. If the injector tube is moved closer to the end of the tube, the residence time of the reactants introduced into the system is shortened. In this way, the reaction time can be varied from 1 to 8 s. Photolysis of reactants is carried out by using eight 36 W blacklight blue tube lamps (NARVA), emitting light in the UV-A range with a peak emission at 360 nm.

In the experiments in this work, OH radicals were produced by either the photolysis of isopropylnitrite (IPN, Reactions R2.6 to R2.8) or by the ozonolysis of tetramethylethylene (TME, Reactions R2.3 to R2.5). IPN and TME were introduced into the system together with the main gas stream in the flow tube, so that

a homogeneous distribution can be assumed.

$$\mathrm{TME + O_3 \longrightarrow CH_3C(O)CH_3 + CH_3C(OO)CH_3} \quad \text{(R2.3)}$$

$$\mathrm{CH_3C(OO)CH_3 \longrightarrow CH_3C(OOH)CH_2} \quad \text{(R2.4)}$$

$$\mathrm{CH_3C(OOH)CH_2 + O_2 \longrightarrow OH + CH_3C(O)CH_2(OO)} \quad \text{(R2.5)}$$

The ozonolysis of TME leads to the formation of acetone and a Criegee intermediate (Reaction R2.3). Through a 1,4-H-shift (Reaction R2.4), a vinyl hydroxy peroxide (VHP) is formed from the Criegee intermediate (Figure 1.4). OH is formed through the decomposition of the hydroperoxide bond (-OOH, Reaction R2.5). The amount of OH formed by this reaction in the free-jet flow system is controlled by adding different amounts of O_3. The higher the O_3 concentration in the chamber, the higher the turnover rate of the TME ozonolysis, and the more OH is produced.

The photolysis of IPN results in the production of NO and an isopropyl alkoxy radical (Reaction R2.6).

$$\mathrm{IPN + h\nu \longrightarrow NO + i{-}C_3H_7O} \quad \text{(R2.6)}$$

$$\mathrm{i{-}C_3H_7O + O_2 \longrightarrow CH_3C(O)CH_3 + HO_2} \quad \text{(R2.7)}$$

$$\mathrm{HO_2 + NO \longrightarrow NO_2 + OH} \quad \text{(R2.8)}$$

The alkoxy radical then forms acetone and an HO_2 radical (Reaction R2.7), which subsequently can react with the NO formed in the previous step (Reaction R2.6) to form OH (Reaction R2.8). The concentration of OH in the system increases with increasing concentration of IPN.

Oxidation products are sampled from the center of the flow by a CI-API-TOF mass spectrometer (Chapter 3.2). VOC mixing ratios are measured by a proton-transfer time-of-flight mass spectrometer (PTR-TOF-MS, Ionicon) also sampling from the center of the flow tube. The ozone mixing ratio is monitored by a gas monitor (Thermo Environmental Instruments 49C).

3 Chemical Ionization Mass Spectrometry

Mass spectrometry is a very versatile and powerful tool that is used to solve analytical problems in many different disciplines. In the context of atmospheric chemistry, mass spectrometric methods are often used to determine the concentrations of volatile organic compounds (VOCs). Especially chemical ionization mass spectrometry (CIMS) is well established in the atmospheric sciences. It provides a soft ionization scheme that in many cases does not lead to fragmentation of the analyte ions and allows the sensitive detection of many different atmospherically relevant compounds from small inorganic acids to oxidation products of bigger organic compounds such as monoterpenes with a high time resolution and limits of detection in the range of several pptv (Huey (2007)). In chemical ionization mass spectrometry, analytes cluster with a primary ion. The primary ion-analyte clusters are subsequently separated according to their mass to charge ratio (m/z). In this work, Th (Thomson) is used as a unit of mass to charge ratio.

3.1 ROx radical detection by CIMS

In the last three decades, it has been shown that the detection of ROx radicals with mass spectrometric methods is possible, though some challenges remain, especially with regard to the detection of specific peroxy radicals. Different ionization schemes partly combined with chemical conversion methods have been applied to individually detect OH, HO_2 and RO_2 radicals.

As demonstrated by e.g. Eisele and Tanner (1991) and Berresheim et al. (2000), OH radicals can be measured by an API-CIMS (atmospheric pressure interface CIMS) by converting them to sulfuric acid (H_2SO_4) that can be detected by a CIMS instrument with nitrate (NO_3^-) as primary ions. The chemical conversion is achieved through a titration of OH radicals with SO_2, which leads to the formation of H_2SO_4

through the following reactions (Reactions R3.1 to R3.3):

$$SO_2 + OH + M \longrightarrow HSO_3 + M \quad \text{(R3.1)}$$

$$HSO_3 + O_2 \longrightarrow SO_3 + HO_2 \quad \text{(R3.2)}$$

$$SO_3 + H_2O + M \longrightarrow H_2SO_4 + M \quad \text{(R3.3)}$$

H_2SO_4 is then detected in the CIMS instrument by both cluster formation with the nitrate primary ion ($(H_2SO_4)NO_3^-$) and as (HSO_4^-) ion formed by charge transfer. The OH measurement by the CIMS needs to be calibrated using a calibration source that produces OH radicals in known concentrations by photolyzing water vapour (Reaction R3.4).

$$H_2O + h\nu \longrightarrow H + OH \quad \text{(R3.4)}$$

$$H + O_2 \longrightarrow HO_2 \quad \text{(R3.5)}$$

The photolyzing radiation at 185 nm is produced by a mercury pen-ray lamp (Berresheim et al. (2000)). The produced OH is then titrated with SO_2 and a calibration curve is obtained.

Chemical conversion can also be used to measure HO_2 radical concentrations and sum RO_2 concentrations as shown by Reiner et al. (1997). In their ROxMAS system, a chain reaction with NO and SO_2 converts the gaseous peroxy radicals to sulfuric acid that is detected by the mass spectrometer. In a first step, RO_2 radicals are converted to HO_2 radicals by their reaction with NO and O_2. The HO_2 radicals are converted to OH radicals that subsequently react with SO_2 forming H_2SO_4. To only detect HO_2 radicals, the conversion of RO_2 to HO_2 in the first is hindered by using N_2 instead of O_2 as a buffer gas (Reiner et al. (1997), Hanke et al. (2002)). A similar approach was used by Edwards et al. (2003) for the detection of peroxy radicals in the PerCIMS instrument.

Veres et al. (2015) showed that the HO_2 radical can directly be measured by CIMS using iodide as primary ions by the formation of analyte-ion clusters ($(HO_2)I^-$). Sanchez et al. (2016) demonstrated that bromide ions can also be used to form $(HO_2)Br^-$ clusters that are detectable by CIMS. Albrecht et al. (2019) used a CIMS instrument with bromide as primary ions to measure the HO_2 radical concentration in experiments in the atmospheric simulation chamber SAPHIR at Forschungszentrum Jülich. For the calibration of the CIMS instrument, a calibration source producing HO_2 radicals by water photolysis is used. Like in the calibration source used by Berresheim et al. (2000), water vapour is photolyzed by radiation at 185 nm provided by a mercury pen-ray lamp. The H atom that is formed in this reaction together with OH (Reaction R3.4) immediately reacts with O_2 forming an HO_2 radical (Reaction R3.5). Albrecht et al. (2019) found that the sensitivity of the Br^--CIMS

instrument depends on the water vapour in the sampled air. The sensitivity is increased by a factor of 2, if the water vapour mixing ratio increases from 0.1% to 1%. An instrumental background signal equivalent to an HO_2 concentration of 1 $\times 10^8$ cm^{-3} when overflowing the inlet with pure nitrogen that needs to be accounted for in the data analysis was determined (Albrecht et al. (2019)).

The HO_2 concentrations measured by the CIMS instrument were compared to the HO_2 concentrations from a LIF instrument measuring at the SAPHIR chamber simultaneously. A good agreement between the two measurement techniques was found (Albrecht et al. (2019)). For some experiments in the SAPHIR chamber, an increased background signal was observed when O_3 was added into the chamber. The exact reason for that interference is yet to be determined, as O_3 interference tests in the laboratory did not show an interference under these conditions. However, a reliable and precise measurement of HO_2 radicals is possible by chemical ionization mass spectrometry.

In the laboratory, specific RO_2 radicals have been detected (Nozière and Hanson (2017), and references therein). However, the sensitivity of the measurement was too low for the detection of peroxy radicals at atmospheric conditions. The detection of specific, highly oxidized RO_2 in both the lab and in the atmosphere has only been successful in recent years (Bianchi et al. (2019) and references therein). Nitrate ions have a high probability to cluster with highly functionalized organic compounds (Hyttinen et al. (2015)) and are therefore well suited for the detection of highly oxidized peroxy radicals. Highly oxidized peroxy radicals are formed in several subsequent autoxidation reactions of peroxy radicals formed in the oxidation of volatile organic compounds (Chapter 1.2). The possibility of their gas-phase detection by CIMS instruments has inspired many studies investigating their formation and their effect on the formation of new particles and secondary organic aerosols (Bianchi et al. (2019) and references therein).

Due to the lack of calibration standards, the knowledge about the atmospheric concentration of these highly oxidized compounds is still limited. Also, since mass spectrometry can only provide sum formulas, information about the structure of these molecules is at the moment mostly derived from theoretical calculations. The use of different primary ions, such as nitrate, bromide, acetate or lactate is possible for the detection of highly oxidized peroxy radicals with CIMS instruments in the negative ionization mode, but the nitrate ionization scheme is most often used.

A study by Berndt et al. (2018) demonstrated that the first generation RO_2 from the ozonolysis of α-pinene form stable clusters with protonated primary amines, and can be detected in the positive ion mode by a CIMS instrument. This method of detection has recently also been applied to the detection of peroxy radicals from the α-pinene + OH reaction system by Berndt et al. (2021a) and Berndt (2021b), demon-

strating that the concentrations of individual peroxy radicals formed in the oxidation of monoterpenes can be determined from CIMS measurements. An instrument-specific calibration factor is used to determine the peroxy radical concentrations (Chapter 3.4.1).

These recent instrumental developments demonstrate the power and versatility of mass spectrometry for the detection of radicals in atmospheric sciences and encourage the further development of ionization schemes and techniques for the detection of ROx radicals with CIMS. An application of the technique developed by Berndt et al. (2021a) and Berndt (2021b) and its optimization for the use at an atmospheric simulation chamber is presented in this work.

3.2 Principle of Chemical Ionization Mass Spectrometry

The use of an atmospheric pressure interface time of flight mass spectrometer combined with a chemical ionization inlet (CI-API-TOF-MS) is common in atmospheric sciences as it allows to measure in both field studies and chamber experiments without the requirement of a further pumping stage.

The CI-API-TOF-MS consists of two parts (Junninen et al. (2010)). Molecules are ionized in the chemical ionization-inlet (CI-inlet) through the use of radioactive sources, X-Ray sources or corona-discharge. The produced ions are then focused and separated according to their mass to charge ratio (m/z) in the API-TOF (Tofwerk AG).

In chemical ionization mass spectrometry, a precursor molecule that is easily ionized is used to generate primary ions. The ionization of analytes occurs through primary ion-molecule reactions. Ion-analyte cluster formation is usually the dominant formation process (Reaction R3.6).

$$X^+ + A \longrightarrow [XA]^+ \tag{R3.6}$$

The formation of the ion-analyte clusters is proportional to the abundance of the primary ion. Therefore, all detected mass signals are usually normalized to the signal of the primary ion for comparability. Different ionization schemes can be applied depending on the type of molecule that is to be detected.

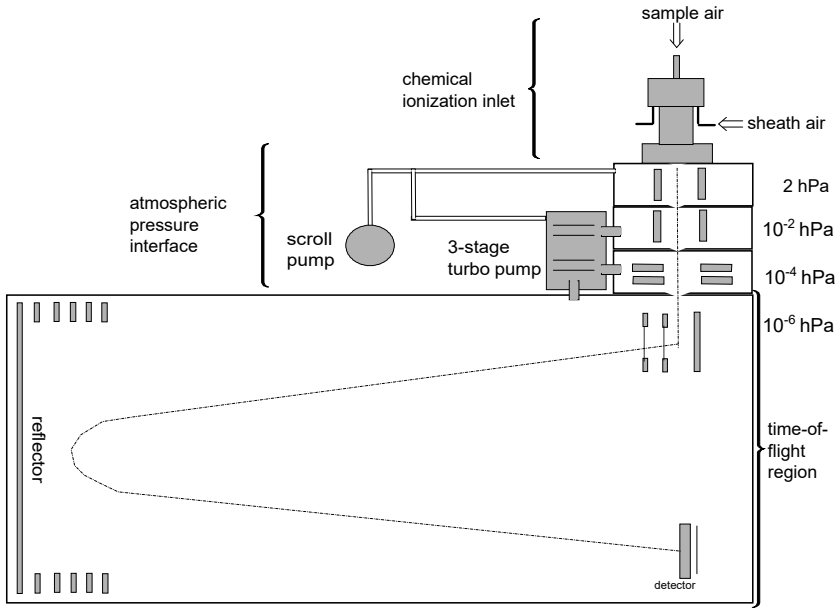

Figure 3.1: The atmospheric pressure interface time-of-flight mass spectrometer (API-TOF-MS), consisting of a three-stage API and the TOF region with a chemical ionization inlet (Junninen et al. (2010)). The three API chambers and the TOF-region are differentially pumped by a scroll pump and a three-stage turbo pump. Air containing analyte-ion clusters enters the first chamber through a critical orifice, and is guided into the TOF region by two segmented quadrupoles and a stack of electrical lenses. In the TOF region, ion molecule clusters are separated according to their mass to charge ratio and detected by a microchannel plate detector.

In this work, a CI-inlet initially described by Eisele and Tanner (1993) is used (Figure 3.2). Originally designed for the measurement of atmospheric sulfuric acid with nitrate (NO_3^-) as reagent ion, the CI-inlet has been used to measure a wide range of compounds with different primary ions in the past years. In this CI-inlet, $10\,\mathrm{l\,min^{-1}}$ of sample air enters the inlet tube at atmospheric pressure. Several ppbv of neutral reagent ion precursors are introduced into the CI-inlet together with a $30\,\mathrm{l\,min^{-1}}$ flow of nitrogen that enters the CI-inlet at the upper end. The ionization of the primary ion precursor vapour is realized through the exposure of the entering gas flow to α-radiation from a radioactive ^{241}Am source. Depending on the nature of the primary ion precursor, either positively charged ions or negatively charged ions are obtained through ionization by the alpha particles emitted by the ^{241}Am source. If, e.g., HNO_3 is used as a precursor for the primary ions, negatively charged NO_3^- ions are formed. In the case of propylamine ($C_3H_7NH_2$), positively charged $C_3H_7NH_3^+$ ions are formed.

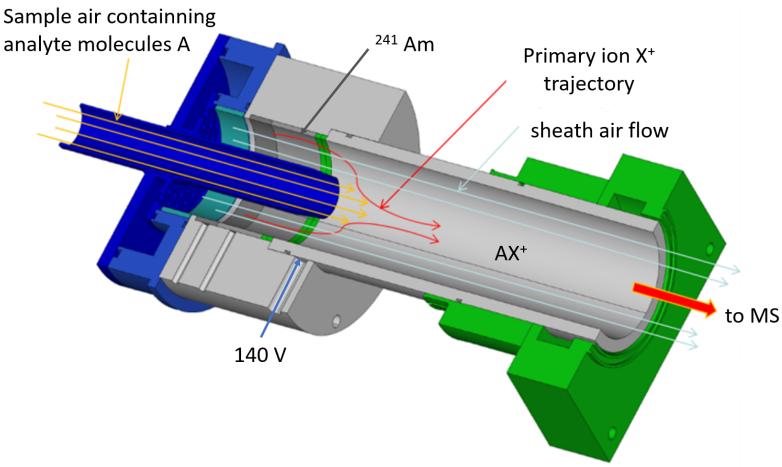

Figure 3.2: The CI-inlet based on an initial design by Eisele and Tanner (1993). 30 l min^{-1} of purified nitrogen containing the primary ion precursor (propylamine) enter the CI-inlet on the side (not shown). Primary ions X^+ are formed by exposing the gas flow to α-radiation from a ^{241}Am source. Downstream of the radioactive source, the 30 l min^{-1} nitrogen flow enters the CI-inlet tube as a sheath flow. The primary ions are pushed into the center of the CI-inlet by applying a voltage of 140 V to the walls. At the center of the tube, the primary ions react with analytes A contained in the sampled air, forming primary ion-analyte clusters, XA^+.

The 30 l min^{-1} nitrogen flow is then directed towards the walls of the tube, creating a sheath air flow. The ions are pushed into the center of the tube by applying a voltage to the walls of the inlet tube. A voltage of +140 V is applied when measuring with positively charged primary ions and a voltage of -140 V when measuring with negatively charged primary ions. The sample air flow and the primary ions are mixed at the center of the tube in the ion-molecule-reaction zone. The many different chemical molecules contained in the sample air, for example organic species or water molecules, form clusters with the primary ions that are then transported into the API-TOF. There, they are pre-selected through declustering. Weakly bound clusters are declustered by the voltages applied in the API. The residence time of the ions in the ion-molecule-reaction zone is about 200 ms.

0.8 l min^{-1} of air containing the ion-molecule clusters enter the atmospheric pressure interface transfer stage through a 0.3 μm critical orifice. The API stage provides a link between the atmospheric pressure at the CI-inlet and the low pressure required in the TOF mass analyzer (Tofwerk AG, Switzerland), where the ion molecule clusters are separated according to their mass to charge ratio and detected by a microchannel plate (MCP) detector.

The separation of the analyte ion clusters requires a high vacuum of at least 1.0×10^{-6} hPa in the TOF analyzer region. This vacuum is reached in three steps in

the API. Simultaneously, the carrier gas and neutral molecules are removed from the ion beam through the reduction of the pressure. The API consists of two segmented quadrupole ion guides in separate chambers and a third chamber with a stack of electrical lenses, the primary beam chamber. These three differentially pumped chambers serve to guide the ions into the TOF analyzer region. This is made possible by several individually controlled voltages applied to the quadrupoles and the lenses. The voltages that are applied at the different stages determine the focusing and filtering of the ions.

The chamber housing the first segmented quadrupole is operated at a pressure of about 2 hPa. At this stage of the API, collisional decomposition of clusters of the analyte ion with water occurs, as the water clusters are usually weaker bound than the analyte ion clusters. The chamber housing the second segmented quadrupole is operated at a pressure of 1×10^{-2} hPa. Through the voltages applied to this quadrupole, declustering processes can be controlled. The applied voltages impart energy to the ions via the electrical fields (Lopez-Hilfiker et al. (2016)). If there is a big difference between the voltages applied to the top and the bottom of this quadrupole, weakly bound clusters may undergo declustering, i.e collision-induced dissociation processes. However, a certain voltage difference is needed to pull the ion beam through the quadrupole, therefore the applied voltages need to be optimized carefully, depending on the target molecule to be measured with high sensitivity. The primary beam chamber houses a stack of electrical lenses that ensure that the ion beam is focused. Additionally, the ion clusters are accelerated into the time-of-flight region. The primary beam chamber is operated at a pressure of 1×10^{-5} hPa. A scroll pump and a three-stage turbo pump ensure that the pressures are reached at all times.

In the TOF analyzer region, the preselected ions are accelerated by an electrical pulser perpendicular to their previous flight path. The separation of the ions occurs due to their different time of flight based on their individual mass to charge ratio (m/z). The individual time of flight of an ion is proportional to the root square of its mass to charge ratio. Since all ions are accelerated with the same energy from the high voltage pulse of the electric pulser, molecules with a small mass to charge ratio arrive at the detector earlier than molecules with a higher mass to charge ratio. Prolonging the flight path leads to a higher resolution of the resulting mass spectrum. At the end opposite to the electrical pulser, an ion-mirror (reflectron) is installed. Small differences in the speed of ions of the same mass to charge ratio can be balanced by the use of the reflectron. The direction of the flight path of the ions is reversed. The ions are then detected by a MCP. The typical resolving power, defined as the ratio of the mass to charge ratio m/z divided by the width of the peak at its half maximum, achieved for the instrument in this work is 3000-4000 Th/Th.

3.3 Optimization of the CIMS instrument for measurements of RO_2 radicals

In this work, a CIMS instrument operated with the Eisele CI-inlet (Chapter 3.2) is used in positive ion mode with protonated primary amines as reagent ion. At the end of the CI-inlet, a pump is removing a total air flow of $40\,\mathrm{l\,min^{-1}}$. A sheath flow of purified nitrogen of $30\,\mathrm{l\ min^{-1}}$ containing the vapour of propylamine ($C_3H_7NH_2$, Sigma-Aldrich, purity $\geq$99%) is introduced into the CI-inlet. This results in a sample air flow of $10\,\mathrm{l\,min^{-1}}$.

The detection of peroxy radicals and some of their reaction products by a CIMS instrument with protonated amines as primary ions was developed for and established at the free-jet flow system, where reaction times are in the range of several seconds, by Torsten Berndt. Based on his studies (Berndt et al. (2018), Berndt et al. (2021a), Berndt (2021b)) and experiments conducted at the free-jet flow system in cooperation with Torsten Berndt as a part of this work, a similar detection scheme was developed for the use in atmospheric simulation chambers at Forschungszentrum Jülich in this work. The general set-up of the CIMS instrument is similar to the instrument shown in Figure 3.1.

The addition of the amines into the sheath air flow of the CI-inlet is optimized for the measurement of peroxy radicals. The main focus of the optimization is the reduction of unwanted peaks caused by contaminations in the amine or secondary chemistry in the sample air. The presence of such peaks may interfere with the detection of the peroxy radical signals. In total, four steps have been taken to optimize the cleanliness of the mass spectrum: cleaning of the amine prior to its addition to the sheath air flow of the CIMS, optimization of the amount of the amine added into the sheath air flow, addition of water vapour to the sheath air flow and the dilution of the sample air flow. While the latter focuses on the reduction of secondary chemistry occurring in the CI-inlet, the first three optimization steps aim to reduce the intensity of contamination peaks.

3.3.1 Preparation of purified amine-N_2 mixtures

In order to obtain meaningful product spectra from the experiments, a very clean initial primary ion spectrum is needed. A crucial factor is the purity of the precursor species for the primary ions. There are two different possibilities how to prepare the amines for the addition into the sheath flow of the CIMS.

One is to directly connect a glass bulb containing the liquid amine to the sheath air line of the CI-inlet. The mass spectra obtained using this method in test experiments in Jülich contain several peaks that indicate contaminations. The contamination peaks may be related to contaminants in the liquid amine sample, but their exact nature could not be determined. The addition of the amine to the main flow of the CI-inlet is diffusion controlled, so that the exact concentration of the amine entering the CI-inlet cannot be easily controlled.

An alternative way to add the amine into the CI-inlet gas stream is the use of pre-mixed gas mixtures containing a defined amount of amine. At the free-jet flow system in Leipzig, gas mixtures containing the amines are prepared in a gas metering unit similar to the vacuum line installed at Forschungszentrum Jülich described in the following. The gas mixtures are added to the main gas stream by calibrated mass flow controllers (Berndt et al. (2018)).

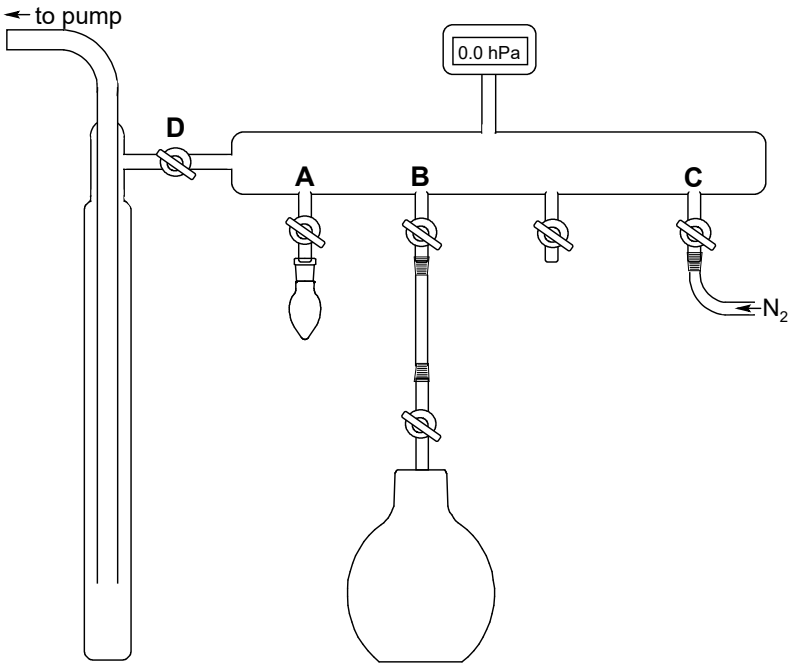

Figure 3.3: Vacuum line set-up at the Forschungszentrum Jülich for the preparation of gas mixtures containing the amine for use as primary ions in the CIMS instrument. The vacuum line is equipped with Young stopcocks. The amine vial is connected via a glass joint. The connection of the Restek canister and the nitrogen supply to the vacuum line are realized through Swagelok Ultra Torr vacuum fittings. The set-up was done as a part of this work.

At Forschungszentrum Jülich, a vacuum line is set up for the preparation of the gas mixtures. The vacuum line is evacuated using a scroll pump to pressures of 2×10^{-1} hPa. A 10 ml glass vial containing the amine is attached to the line and closed with a valve. Possible contaminations caused by the manufacturing process of the amine are removed from the liquid sample by first freezing the amine at liquid nitrogen temperature. For that purpose, the vial is moved into a Dewar vessel containing liquid nitrogen. After the amine has been completely frozen, the Dewar is removed and the valve (A, Figure 3.3) is opened to the vacuum line for several seconds allowing to remove gaseous contaminants that have a higher vapour pressure than the amine from the sample. This process is repeated three to five times.

After the amine is cleaned and the valve connecting the vial and the vacuum line is closed, an air-sampling canister (Restek 2 l), is evacuated at the vacuum line. The air sampling canister is made of stainless steel and its interior is coated with inert Silktec. Prior to use, the canister is heated to remove possible contaminations. After the evacuation of the canister, the valve to the pump evacuating the vacuum line (D, Figure 3.3) is closed, and the valve to the evacuated air-sampling canister (B, Figure 3.3) was opened. By carefully opening the valve of the vial holding the liquid amine to the vacuum line (A, Figure 3.3), the canister is filled with the gaseous amine until a pressure of 2 to 8 hPa is reached. The canister is then pressurized with nitrogen (Linde, <99.9999%) to approximately 2000 hPa (C, Figure 3.3). The mixing ratio of the amine in the canister is derived from its partial pressure in the canister.

3.3.2 Dosing of the amine-N_2 mixture to the CI-inlet

From the canister containing the propylamine-nitrogen mixture, a 0.1 - 0.5 ml min^{-1} flow controlled by a mass flow controller (Bronkhorst EL-Flow) is added to the sheath air flow providing the 30 l min^{-1} nitrogen sheath flow for the CIMS instrument. Several test experiments were conducted to determine the optimal concentration of the propylamine in the sheath air flow to obtain a clean mass spectrum. In these experiments, the CIMS instrument was sampling from the SAPHIR-STAR chamber that was filled with pure nitrogen (Linde, <99.9999%) All mass peaks occurring in the spectrum can be attributed to species such as the protonated propylamine and its dimer that are injected in the inlet system of the CIMS instrument.

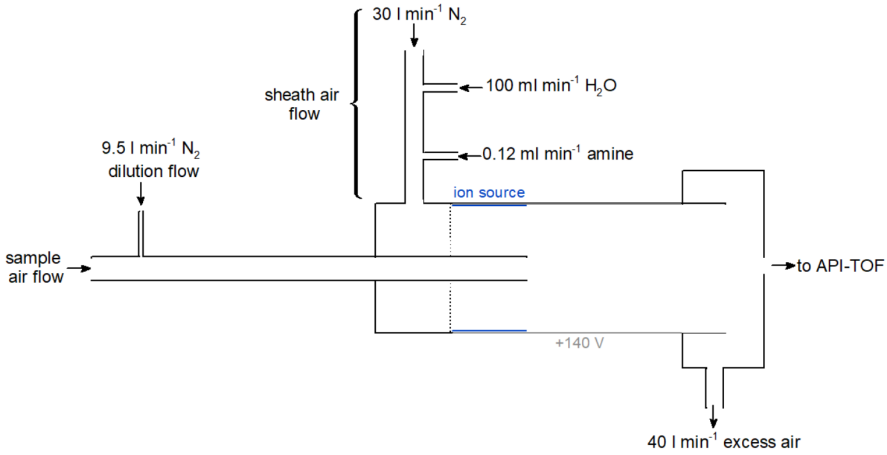

Figure 3.4: Schematics of the CI-inlet. The flows of propylamine and water entering the CI-inlet and the dilution flow have been optimized as described in the text.

As a first test, a propylamine nitrogen mixture (6 hPa : 1982 hPa) was prepared in a sample canister and added into the sheath air flow at a flow rate of 0.5 ml min^{-1} to achieve an amine concentrations of about 7.8×10^{11} cm^{-3} in the CI-inlet. In the resulting mass spectrum, propylamine primary ions and their dimers are detected at the expected mass to charge ratio of 60 Th ($C_3H_7NH_3^+$) and 119 Th ($(C_3H_7NH_2)C_3H_7NH_3^+$), respectively. Additionally, two unexpected signals are detected at m/z 100 and m/z 130 at about half the intensity of the primary ion (Figure 3.5). The source of these peaks are related to the gas mixture in the propylamine sample canister, as they disappear when the addition of the amine to the sheath air flow is stopped. If the addition of the propylamine nitrogen mixture to the sheath air flow of the CIMS instrument is stopped and only nitrogen is flowing to the CI-inlet, these peaks are also not observed. It is not clear whether the two signals at m/z 100 and m/z 130 are clusters with the propylamine ions or ions independently formed at the radioactive source, since their sum formula could not be unambiguously determined. Another peak is observed at m/z 29. The peak was identified to likely be CHO^+. The exact source for this ion is not clear. One hypothesis is that it is due to contaminations in either the CI-inlet or the tubing in which the gas mixture was provided to the CI-inlet, as it is always present in the spectrum when using CIMS instruments in positive ionization mode and does not depend on the flow of the amine. The intensity of the peak at m/z 29 does not significantly increase or decrease over time, so that a constant source of the contamination can be assumed. One hypothetical formation pathway for the CHO^+ is the dissociation of aldehydes by radioactive radiation from the radioactive source in the CI-inlet.

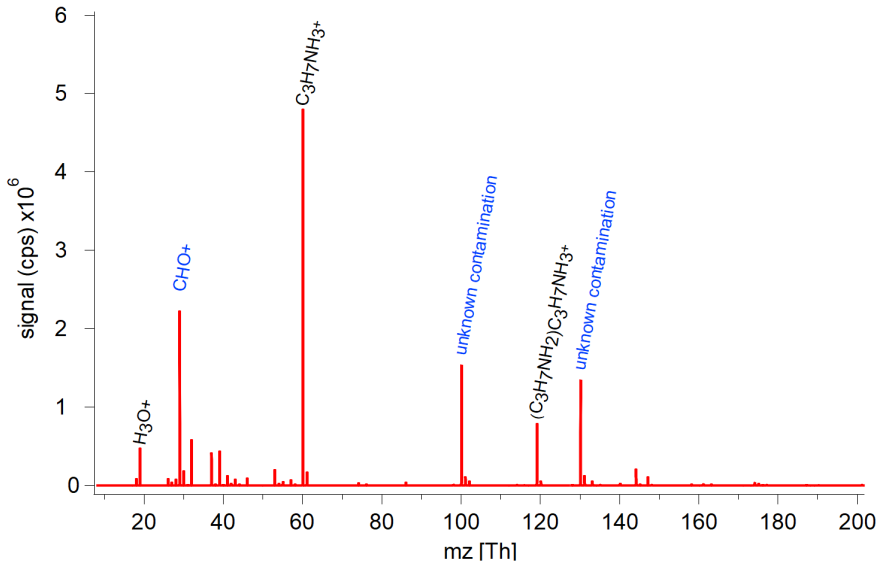

Figure 3.5: Mass spectrum from m/z 0-200 obtained with an addition of 0.5 ml min^{-1} of a (6 hPa : 1982 hPa) propylamine-nitrogen mixture to the sheath air flow in an experiment in which only nitrogen was sampled from the SAPHIR-STAR chamber. The propylamine is detected at a mass to charge ratio of 60 Th ($C_3H_7NH_3^+$) and as a dimer in significantly smaller intensity at a mass to charge ratio of 119 Th ($(C_3H_7NH_2)C_3H_7NH_3^+$). The signals at mass to charge ratios 100 Th and 130 Th are peaks from contaminations whose origin could not be unambiguously determined.

To reduce the contaminations coming from the propylamine-nitrogen gas mixture, the concentration of the amine in the gas mixture can be reduced. Additionally, the flow adding the amine to the main flow to the CI-inlet can be reduced. In a test experiment, a propylamine nitrogen mixture was prepared with a slightly lower amine mixing ratio (2 hPa : 1990 hPa). Furthermore, the flow rate of the amine mixture was reduced to 0.12 ml min^{-1}, resulting in a propylamine concentration of 1.1×10^{11} cm^{-3} in the sheath air flow. It is expected that the intensity of the primary ion signal scales with the amount of propylamine added to the sheath air flow. The intensity of the primary ion peak (m/z 60 Th) is reduced by about a factor of 5 compared to the intensity observed with higher propylamine concentrations added to the main gas stream (Figure 3.6). The concentration of the amine in the sheath air flow of the CI-inlet is reduced by a factor of 7. The observed reduction in the peak intensity is lower than that. This discrepancy is most likely caused by the uncertainty of the given concentration. The intensities of the impurities detected at mass to charge ratios of 100 Th and 130 Th are significantly reduced. A lower propylamine concentration in the sheath air flow is therefore beneficial to obtain a clean mass spectrum. A comparable concentration of the primary amines in the

sheath air flow is also used by Torsten Berndt for experiments in the free-jet flow system.

3.3.3 Addition of water vapour to the sheath flow

To further enhance the cleanliness of the mass spectrum, a small stream (100 $ml\,min^{-1}$) of nitrogen saturated with MilliQ-water vapour is added to the sheath air flow. A small increase of the primary ion intensity and a small reduction in the intensity if the impurity peaks is observed. Due to the addition of water vapour saturated nitrogen into the sheath air flow, protonated water (H_3O^+), its water dimer ($(H_2O)H_3O^+$) and water trimer ($(H_2O)_2H_3O^+$) are detected as additional peaks at m/z 19, 37 and 55, respectively (Figure 3.6).

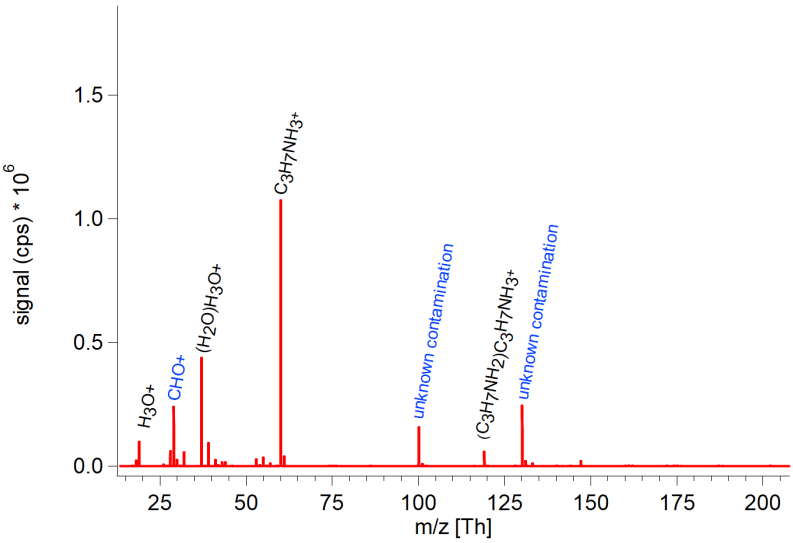

Figure 3.6: Mass spectrum from m/z 0-200 obtained after the optimization of the initial propylamine concentration (0.12 ml min^{-1} of a (2 hPa : 1990 hPa) propylamine-nitrogen mixture) in an experiment in which only nitrogen was sampled from the SAPHIR-STAR chamber. The propylamine is detected at a mass to charge ratio of 60 Th ($C_3H_7NH_3^+$) and as a dimer in significantly smaller intensity at a mass to charge ratio of 119 Th ($(C_3H_7NH_2)C_3H_7NH_3^+$). The signals at mass to charge ratios 100 Th and 130 Th are peaks from contaminations whose origin could not be unambiguously determined. Since a small amount of water-saturated nitrogen is added into the sheath air flow of the CIMS, protonized water and its dimer and trimer are detected as H_3O^+, $(H_2O)H_3O^+$ and $(H_2O)_2H_3O^+$ at mass to charge ratios of 19, 37 and 55, respectively.

One reason for the increase of the primary ion peak and the decrease in the

contamination ions could be that the ionization of the amine is more efficient in the presence of a few water molecules.

The mass spectrum obtained after the three optimization steps aimed to increase the cleanliness of the mass spectrum - purification of the used amine, dosing of the amine-N_2 mixture into the CI-inlet and addition of water vapour - is sufficiently clean to obtain meaningful mass spectra from experiments in the SAPHIR-STAR chamber as described in Chapter 7. The quality of the mass spectrum is comparable to those of mass spectra recorded by Berndt (2021b).

3.3.4 Dilution of the sampled air flow

Bimolecular reactions of the peroxy radicals in the CI-inlet can lead to an additional formation of reaction products that may potentially change the product distribution originally observed in the experiment (Berndt (2021b)). To avoid the formation of such products in the CI-inlet, a dilution of the gas sample downstream of the sampling point of the CIMS instrument has been used successfully by Berndt (2021b). In the dilution setup used by Berndt (2021b), nitrogen is introduced into the sample air flow of the CI-inlet through small capillaries about 10 cm downstream of the sampling point of the CIMS to dilute the sample air (Figure 3.4).

Berndt (2021b) performed two experiments investigating the oxidation of α-pinene by OH in the presence of NOx, one with and one without the use of a dilution setup. Other than the use of the dilution setup, all other experiment conditions were similar. In the experiments with the dilution setup, the sample air was diluted with pure nitrogen by a factor of 7. The products formed from the unwanted bimolecular RO_2 + NO reaction in the CI-inlet were reduced by a factor of 50 (Berndt (2021b)), consistent with a reduction of both reaction partners of the bimolecular reaction by a factor of 7. The reduction of the analyte peaks of the RO_2 radicals was consistent with the applied dilution factor. Considering the dilution factor, the concentration of the peroxy radicals found in the experiments with and without the dilution setup were similar (Berndt (2021b)).

A dilution setup similar to the one used by Berndt (2021b) was used for the experiments in the SAPHIR-STAR chamber. In the dilution set-up, nitrogen is mixed into the sample air stream through two capillaries with a high flow of $9.5\,\mathrm{l\,min^{-1}}$ (Figure 3.4). This ensured fast mixing of the dilution and the sampling flow, and laminarization of the joined flows thereafter. The sample air coming from the chamber is diluted by a factor of 9, theoretically reducing unwanted bimolecular reactions in the CI-inlet by a factor of 80.

3.4 Detection of peroxy radicals from the OH reaction with β-pinene by CIMS using amine as primary ions

In the free-jet flow system and the SAPHIR-STAR chamber, the oxidation of β-pinene by the OH radical was investigated. In the radical reaction chain subsequent to the OH addition to β-pinene, organic peroxy radicals RO_2 with sum formulas $OH-C_{10}H_{16}O_2$, $OH-C_{10}H_{16}O_4$ and $OH-C_{10}H_{16}O_6$ that include several different isomeric RO_2 species were produced (Chapter 7.1). Details about the respective experiments are discussed in Chapters 7.2.2 and 2.3.

In the experiments in this work at the TROPOS free-jet flow system, a CI-API-TOF-MS was operated with protonated ethylamine as primary ion ($C_2H_5NH_3^+$). At the SAPHIR-STAR chamber in Jülich, a CI-API-TOF-MS was operated with protonated propylamine as primary ions ($C_3H_7NH_3^+$) in the experiments in this work. In the experiments conducted in the free-jet flow system, the peroxy radicals with the sum formulas $OH-C_{10}H_{16}O_2$, $OH-C_{10}H_{16}O_4$ and $OH-C_{10}H_{16}O_6$ were detected as clusters with the protonated ethylamine primary ions at mass to charge ratios of 231, 263, 295, respectively. This corresponds to their molecular mass plus 46 Th, the molecular mass of protonated ethylamine.

In the experiments in the SAPHIR-STAR chamber, the peroxy radicals with the sum formulas $OH-C_{10}H_{16}O_2$, $OH-C_{10}H_{16}O_4$ and $OH-C_{10}H_{16}O_6$ were detected as clusters with the protonated propylamine primary ion at mass to charge ratios of 245, 277 and 309, respectively, their molecular mass plus 60 Th, the molecular mass of protonated propylamine.

A further validation of the assignment of the signals at m/z 231, 263 and 295 to the peroxy radicals is the detection of reaction products of these peroxy radical, for example hydroperoxides from the reaction of the peroxy radicals with HO_2 radicals or organic nitrates from the reaction of the peroxy radicals with NO. The detection of hydroperoxides and organic nitrates is possible with the CIMS instrument. The experimental conditions are adapted to enhance the formation of the RO_2 reaction products.

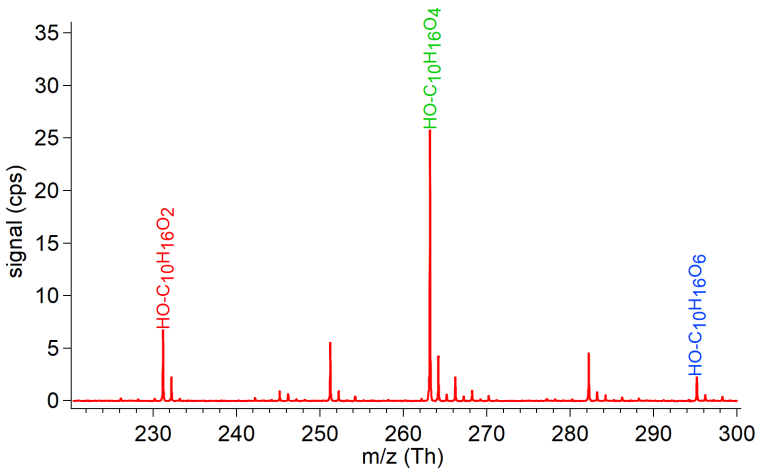

Figure 3.7: Mass spectrum showing non-normalized signals from peroxy radicals with the sum formulas OH−$C_{10}H_{16}O_2$, OH−$C_{10}H_{16}O_4$ and $C_{10}H_{16}O_6$ produced from the reaction of β-pinene with OH (Figure 7.1) in the experiment in the free-jet flow system. Ozonolysis of tetramethylethylene was used as an OH source. Peroxy radicals are detected as clusters with ethylaminium ions ($C_2H_5NH_3^+$). The peroxy radical intensities are given in counts per second (cps).

In a test experiment where isopropylnitrate photolysis is used as an OH source, organic nitrates are formed from the RO_2 + NO pathway, as NO is produced in the photolysis of IPN. To push the system towards the formation of hydroperoxides, H_2 is added to the system in the experiments in the free-jet flow system. In the SAPHIR-STAR chamber, HO_2 radicals are produced by using H_2O_2 photolysis. Other reaction products that are formed in these bimolecular reaction, e.g. alkoxy radicals in the RO_2 + NO reaction cannot be detected by the CIMS instrument, as they do not form stable clusters with the protonated amines.

In the experiments in the free-jet flow system where NO is added to the system, peaks with mass to charge ratios corresponding to the organic nitrates formed from the reaction of RO_2 + NO (Chapter 7.1) with the sum formula OH−$C_{10}H_{16}NO_3$, OH−$C_{10}H_{16}O_2NO_3$ and OH−$C_{10}H_{16}O_4NO_3$ were detected. The signals of the organic nitrates were detected at mass to charge ratios of 261, 293 and 325, respectively (Figure 3.8), together with the peroxy radical signals at m/z 231, 263 and 295. In this reaction system, the formation of the organic nitrates was not possible through a pathway other than the reaction of the peroxy radicals with NO.

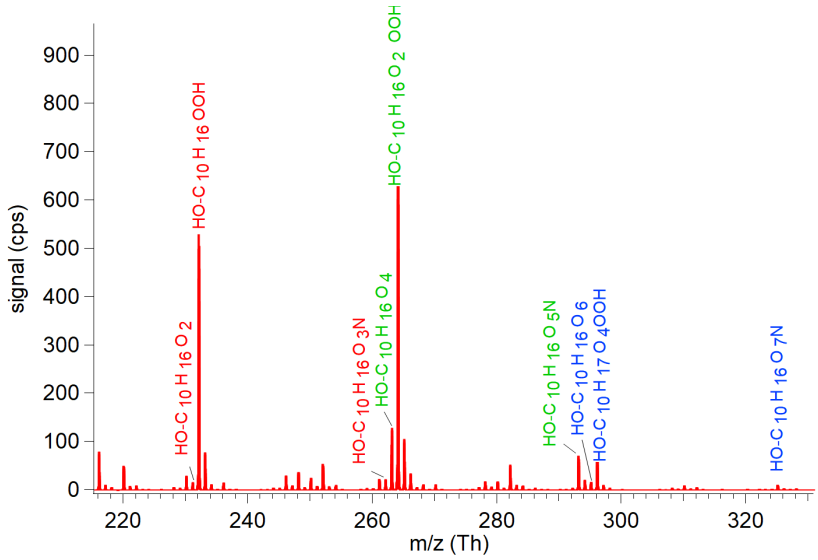

Figure 3.8: Mass spectrum showing signals from peroxy radicals produced from the reaction of β-pinene with OH, organic nitrates formed from the reaction of the peroxy radicals with NO and hydroperoxides formed from the reaction of the peroxy radicals with HO_2 for an experiment in the free-jet flow system at the TROPOS institute in Leipzig. Isopropylnitrate photolyis was used as an OH source. NO is formed in the photolysis of IPN, HO_2 is a product of the reaction of H_2 with OH (Chapters 2.3

In the test experiment where H_2 was added to the main gas stream of the free-jet flow system signals at mass to charge ratios of 232, 264 and 296 were detected that can be assigned to the hydroperoxides with the sum formula $OH-C_{10}H_{16}OOH$, $OH-C_{10}H_{16}O_2OOH$ and $OH-C_{10}H_{16}O_4OOH$, respectively. The formation of species with these sum formulas other than the hydroperoxides is not expected from the oxidation of β-pinene. The detection of the organic nitrates and the hydroperoxides together with the peroxy radicals therefore further validated the assignment of the peaks at m/z 231, 263 and 295 to the peroxy radicals. Without the occurrence of all three peroxy radical species, the organic nitrates and hydroperoxides could not be formed.

Test experiments with conditions where the formation of organic nitrates and hydroperoxides was enhanced were also conducted in the SAPHIR-STAR chamber. The organic nitrates and hydroperoxides were also detected in these experiments.

The results of the presented experiments demonstrate that the detection of peroxy radicals formed in the oxidation of β-pinene by the OH radicals, as well as some of the reaction products is possible by means of chemical ionization mass spectrometry, using protonated amines as primary ions. Due to the structural similarities

between the monoterpenes and the peroxy radicals formed in their oxidation, it can be assumed that the detection of most peroxy radicals formed in the oxidation of monoterpenes is possible.

3.4.1 Determination of the sensitivity of the CIMS instrument for RO_2 radical detection

The peroxy radical concentration [RO_2] can be determined from CIMS measurements by multiplying the measured signal with a calibration factor f_{RO_2} (Equation 3.1). The measured peroxy radical signal ($I_{m/z=RO_2}$) is normalized to the sum of the measured protonated amine signal and its dimer ($I_{m/z=\text{reagent ion}}$).

$$[RO_2] = f_{RO_2} \cdot \frac{I_{m/z=RO_2}}{I_{m/z=\text{reagent ion}}} \tag{3.1}$$

To determine an absolute value for the calibration factor, calibration standards can be used. To calibrate other instruments, such as LIF instruments for the measurement of peroxy radicals, radical sources developed for the calibration of OH measurements, based on the photolysis of water vapour (Reaction R3.4) in air at 185 nm are used (Fuchs et al. (2008)). The generation of specific peroxy radicals is achieved by scavenging the OH radicals with a hydrocarbon. The transport time from the addition of the hydrocarbon to the entrance of the LIF instrument is only 25 ms (Fuchs et al. (2008)). A calibration source based on the same principle, producing OH through the photolysis of water vapour, is also used to calibrate the PerCIMS (Edwards et al. (2003)). The calibration sources have an accuracy of 20%. However, these radical sources only produce relatively low calibration gas flows in the range of a few $1\,l\,min^{-1}$ that are not suitable for the high sample air flows of $10\,l\,min^{-1}$ required by the CIMS instrument. Additionally, the residence time in the calibration sources is short (25 ms) to avoid loss of the radicals to the walls of the calibration source. Autoxidation reactions that lead to the formation of higher oxidized peroxy radicals are not expected to occur on these time scales. Therefore, the known radical sources cannot be used for the calibration of the CIMS instrument used in this work for the detection of specific peroxy radicals from the oxidation of β-pinene.

An alternative way to approximate the sensitivity of the CIMS instrument for the detection of RO_2 radicals is to calculate the calibration factor f_{RO_2}. This method is applied in this work to calibrate the RO_2 data obtained from the experiments in the free-jet flow system at the TROPOS institute in Leipzig. The same method can also be applied to calibrate the RO_2 data from the experiments in the SAPHIR-STAR chamber.

The peroxy radicals are detected as clusters with the primary ion in the CIMS instrument. For the calculation of the calibration factor, it is assumed that the formed RO_2-protonated amine clusters are stable and do not decluster in the instrument. The sensitivity of the CIMS instrument for the detection of peroxy radicals is therefore assumed to be proportional to the rate at which the analyte-primary ion clusters are formed multiplied by the reaction time for the cluster formation. Additionally, certain loss processes of the analyte-primary ion clusters have to be taken into account. Therefore, the rate coefficient k of the ion-molecule reactions, the reaction time t, and an inlet-specific transmission factor l_{inlet}, accounting for loss of products in the sampling tube need to be known (e.g. Ehn et al. (2014), Berndt et al. (2016), Berndt et al. (2018)). The peroxy radical concentrations that are determined with this method are lower limit concentrations as it is possible that the RO_2-protonated amine clusters are not formed at the collision limit and that they are less strongly bound than assumed, and therefore undergo declustering during the transmission from the CI-inlet to the TOF analyzer. This would result in a lower detection efficiency and therefore a higher calculated radical concentration (Ehn et al. (2014)).

$$f_{\mathrm{RO_2}} = 1/(k \cdot t \cdot l_{inlet}) \tag{3.2}$$

A typical value for the reaction rate constant k of the ion-molecule reaction is (2-3) $\times 10^{-9}$ cm^3 s^{-1}(Viggiano et al. (1997), Mackay and Bohme (1978)). This value is close to the collision limit. The reaction time of the ion-molecule reactions in the CI-inlet is about 200 ms for the flow rates applied in this work. The loss of the products in the CI-inlet wall is assumed to be diffusion-controlled. A diffusion coefficient of D=0.08 cm^2 s^{-1} is estimated to calculate the diffusion of the ion-molecule clusters to the inlet walls. It is assumed that every contact of an ion with the inlet wall results in a loss of the ion (Berndt et al. (2016)). This results in a 12% wall loss of the ion-molecule clusters in the sampling tube. Assuming that this is the only loss process, the value of l_{inlet} is 0.88 (Berndt et al. (2016)). Using these values, the calibration factor f is in the range of (1.3 - 2.8) $\times 10^9$ molecules cm^{-3} (Berndt et al. (2016), Berndt et al. (2019)).

This approximation of a calibration factor range can be compared to one available absolute experimental calibration factor for the CIMS instrument determined for the detection of sulfuric acid by CIMS with nitrate as primary ions (Berndt et al. (2014)). It has been found that the $H_2SO_4(NO_3-)$ clusters are very strongly bound (Viggiano et al. (1997)) and that they therefore do not undergo declustering in the transmission from the CI-inlet to the detector. The calibration was performed as described in Chapter 3.1. The experimentally determined calibration factor $f_{\mathrm{H_2SO_4}} = 1.85 \times 10^9$ molecules cm^{-3} (Berndt et al. (2014)) is in the range of

the calculated calibration factor.

It is believed that the peroxy radicals are detected with a similar sensitivity as H_2SO_4 and that their behaviour in the mass spectrometer is comparable. Therefore, the calibration factor determined for the detection of H_2SO_4 that is in good agreement with the calculations, is used (Berndt et al. (2016)). For the detection of the peroxy radicals with the CIMS instrument, it is assumed that the clusters of RO_2 with the protonated amines also form at the collision limit, and that once formed, the clusters are strongly bound. Using the determined calibration factor f, the lower limit concentration of the RO_2 radicals are calculated using the measured signal intensities of the respective clusters of RO_2 with the protonated amines ($I_{\text{product}-\text{reagent ion}}$) normalized to the intensity of the primary ion ($C_2H_5NH_3^+$) and its dimer ($(C_2H_5NH_2)C_2H_5NH_3^+$) ($I_{\text{reagent ion}}$, Berndt et al. (2019) and Berndt et al. (2016)).

The uncertainty of the lower limit concentrations for RO_2 radicals is less than a factor of two (Berndt et al. (2016), Berndt et al. (2019)). The comparison of the range of the calibration factor f determined from Equation 3.2 to the value of the calibration factor $f_{H_2SO_4}$ contributes to the uncertainty.

This method of calibration is applied with the same values for k, t and l_{inlet} to determine lower limit concentrations for all species detected by the CIMS instrument, e.g. peroxy nitrates, hydroperoxides and carbonyl products.

4 Box models for chamber experiments

To determine the reaction rate constant and some of the product yields from the experiments conducted in the SAPHIR chamber, the SAPHIR-STAR chamber and the free-jet flow system, a zero dimensional chemical box model was used. Since no transport processes have to be considered in the chamber experiments, but only chemical reactions, sources and sinks, the box model is an adequate choice to describe the chamber experiments.

The chemical mechanisms used in the model can be separated into basic chemistry reactions as described in Chapter 1.2, such as photolysis of O_3 or HONO, and monoterpene specific reactions. Reaction rate constants of the basic chemistry reactions are taken from the NASA/JPL evaluation (Burkholder et al. (2020)). The monoterpene specific mechanisms are either taken from the Master Chemical Mechanism, version 3.3.1 (http://mcm.york.ac.uk/) or, where complete explicit mechanisms are not published yet, constructed from published partial mechanisms for the purpose of this work.

The EASY interface (Easy AtmoSpheric chemistrY, Brauers and Rohrer (1999)) is used to assign a set of differential equations describing the time dependent reaction rate constants of the chemical reactants to the used chemical mechanism. The differential equation system is numerically integrated by the Facsimile solver (AEA Technology). For given boundary conditions, concentration time series of all reactants are obtained that can be further analysed. Chamber specific boundary conditions include e.g. the measured temperature, pressure and radiation data. Using these conditions, the temporal behaviour of concentrations of the investigated species, Δ^3-carene, myrcene and β-pinene, was simulated. The output data obtained from the model runs was processed in IDL (Interactive Data Language, Harris Geospatial Solutions).

4.1 Modelling of experiments in the SAPHIR chamber

The modelling of the needed parameters in the chamber requires the input of a reaction mechanism detailing the processes involved. There are no explicit complete mechanisms for the oxidation of Δ^3-carene and myrcene published as of yet. Therefore, mechanisms were developed for both oxidation processes. The mechanisms are based on the radical chemistry described in Chapter 1.2, and include previously published reaction rate constants and partial mechanisms.

For the oxidation mechanism developed for the modelling of the experiments investigating the oxidation of Δ^3-carene, studies by Colville and Griffin (2004), Baptista et al. (2014) and Chen et al. (2015) were used to compose the mechanism. For some specific branching ratios, a structure-activity relationship by Jenkin et al. (2018) has been used. Fundamental reaction rate constants for the reaction of Δ^3-carene with OH and O_3 were determined in this work (Chapter 5).

For the oxidation of myrcene, the mechanism is developed using published experimental studies by Orlando et al. (2000), Reissell et al. (2002), Lee et al. (2006) and Boge et al. (2013). Furthermore, reaction rate constants obtained from SAR considerations by Vereecken and Peeters (2009), Vereecken and Peeters (2010), and Vereecken and Noziere (2020) are used. Since myrcene bears structural similarities to isoprene, it can be assumed that unimolecular reactions that are of importance in the oxidation of isoprene (Peeters et al. (2009, 2014), Novelli et al. (2020), Vereecken et al. (2021)) also play an important role in the oxidation mechanism of myrcene. Their reaction rate constants are therefore also used to construct the mechanism and are taken from the respective publications. A more detailed description of the reactions considered for the oxidation of myrcene is given in Chapter 6.

In addition to the oxidation mechanism of the investigated monoterpene and the basic chemistry reactions described in Chapter 1.2, SAPHIR specific reactions have to be taken into account in the model. This includes trace gas sources from the chamber (described in Chapter 2.1) and their oxidation reactions and photolysis reactions. The model is constrained to the OH and/or O_3 concentrations measured in the chamber and the measured NO and VOC concentration. Additionally, the measured temperature, pressure, status of the roof (open/closed), calculated solar zenith angle, relative humidity and determined chamber sources are set as boundary conditions.

4.2 Modelling of experiments in the free-jet flow system

For the modelling of the experimental results in the free-jet flow system, the model included the mechanism of the β-pinene oxidation as described by the Master Chemical mechanism (MCM, version 3.3.1, http://mcm.york.ac.uk/, last access January 2022), adapted with the reaction rates and unimolecular reaction rates published by Vereecken and Peeters (2012) and Xu et al. (2019). In the future, the same model can also be used to model experiments in the SAPHIR-STAR chamber. Also included are some other reactions, like the ozonolysis of TME, leading to the formation of OH radicals. The reaction rate constants of the ozonolysis of TME is taken from Copeland et al. (2011). The model is constrained to the concentrations of β-pinene, NO and TME used in the experiment at the free-jet flow system. A temperature of 24°C and ambient pressure are also set as boundary conditions. The reaction time in the model is set to 8 s. No wall loss reactions or additional system-specific reactions are expected to occur in the free-jet flow system. An overview of the reactions and rate constants used in the model is given in Appendix A3.

5 Oxidation of $\triangle^3$-carene

The content of this chapter was published as "Atmospheric photooxidation and ozonolysis of Δ^3-carene and 3-caronaldehyde: Rate constants and product yields" by L. Hantschke, A. Novelli, B. Bohn, C. Cho, D. Reimer, F. Rohrer, R. Tillmann, M. Glowania,A. Hofzumahaus, A. Kiendler-Scharr, A. Wahner and H.Fuchs in Atmospheric Chemistry and Physics, 21, 12665–12685, https://doi.org/10.5194/acp-21-12665-2021, 2021, under the Creative Commons Attribution 4.0 License. The Supplementary material is provided in Appendix A.1.

Atmos. Chem. Phys., 21, 12665–12685, 2021
https://doi.org/10.5194/acp-21-12665-2021

Atmospheric Chemistry and Physics
Open Access
EGU

Atmospheric photooxidation and ozonolysis of Δ^3-carene and 3-caronaldehyde: rate constants and product yields

Luisa Hantschke, Anna Novelli, Birger Bohn, Changmin Cho, David Reimer, Franz Rohrer, Ralf Tillmann, Marvin Glowania, Andreas Hofzumahaus, Astrid Kiendler-Scharr, Andreas Wahner, and Hendrik Fuchs

Institute of Energy and Climate Research, IEK-8: Troposphere, Forschungszentrum Jülich GmbH, Jülich, Germany

Correspondence: Hendrik Fuchs (h.fuchs@fz-juelich.de)

Received: 22 April 2021 – Discussion started: 30 April 2021
Revised: 27 July 2021 – Accepted: 29 July 2021 – Published: 26 August 2021

Abstract. The oxidation of Δ^3-carene and one of its main oxidation products, caronaldehyde, by the OH radical and O_3 was investigated in the atmospheric simulation chamber SAPHIR under atmospheric conditions for NO_x mixing ratios below 2 ppbv. Within this study, the rate constants of the reaction of Δ^3-carene with OH and O_3 and of the reaction of caronaldehyde with OH were determined to be $(8.0 \pm 0.5) \times 10^{-11}$ cm^3 s^{-1} at 304 K, $(4.4 \pm 0.2) \times 10^{-17}$ cm^3 s^{-1} at 300 K and $(4.6 \pm 1.6) \times 10^{-11}$ cm^3 s^{-1} at 300 K, in agreement with previously published values. The yields of caronaldehyde from the reaction of OH and ozone with Δ^3-carene were determined to be 0.30 ± 0.05 and 0.06 ± 0.02, respectively. Both values are in reasonably good agreement with reported literature values. An organic nitrate ($RONO_2$) yield from the reaction of NO with RO_2 derived from Δ^3-carene of 0.25 ± 0.04 was determined from the analysis of the reactive nitrogen species (NO_y) in the SAPHIR chamber. The $RONO_2$ yield of the reaction of NO with RO_2 derived from the reaction of caronaldehyde with OH was found to be 0.10 ± 0.02. The organic nitrate yields of Δ^3-carene and caronaldehyde oxidation with OH are reported here for the first time in the gas phase. An OH yield of 0.65 ± 0.10 was determined from the ozonolysis of Δ^3-carene. Calculations of production and destruction rates of the sum of hydroxyl and peroxy radicals ($RO_x = OH + HO_2 + RO_2$) demonstrated that there were no unaccounted production or loss processes of radicals in the oxidation of Δ^3-carene for conditions of the chamber experiments. In an OH-free experiment with added OH scavenger, the photolysis frequency of caronaldehyde was obtained from its photolytical decay. The experimental photolysis frequency was a factor of 7 higher than the value calculated from the measured solar actinic flux density, an absorption cross section from the literature and an assumed effective quantum yield of unity for photodissociation.

1 Introduction

On a global scale, the emission of carbon from biogenic volatile organic compounds (BVOCs) exceeds 1000 Tg per year (Guenther et al., 2012). Among all BVOC emissions, monoterpenes are the second most important class of species, contributing up to 16 % to the total emissions. As they are unsaturated and highly reactive, knowledge of their atmospheric chemistry is crucial to understand the formation of secondary pollutants such as ozone (O_3) and particles (e.g. Seinfeld and Pandis, 2006; Zhang et al., 2018).

Of the total global annual monoterpene emissions, Δ^3-carene contributes 4.5 %, making it the seventh most abundant monoterpene species (Geron et al., 2000). Δ^3-Carene is primarily emitted by pine trees. Measured emission rates are up to (85 ± 17) ng g(dw)$^{-1}$ h^{-1} (nanograms monoterpenes per gram dry weight (dw) of needles and hour) from Scots pine trees (Komenda and Koppmann, 2002) and 57 ng g(dw)$^{-1}$ h^{-1} from maritime pine. Therefore, Δ^3-carene regionally gains in importance, for example, in boreal forests and the Mediterranean region. Hakola et al. (2012) measured the mixing ratios of monoterpenes over a boreal forest in Hyytiälä, Finland, and found Δ^3-carene to be the second most abundant monoterpene after α-pinene. However, while the atmospheric chemistry of some monoterpenes such as α-pinene or β-pinene has been investigated in a number of experimental and theoretical studies (e.g. Peeters et al., 2001; Aschmann et al., 2002b; Eddingsaas et al., 2012; Rol-

Published by Copernicus Publications on behalf of the European Geosciences Union.

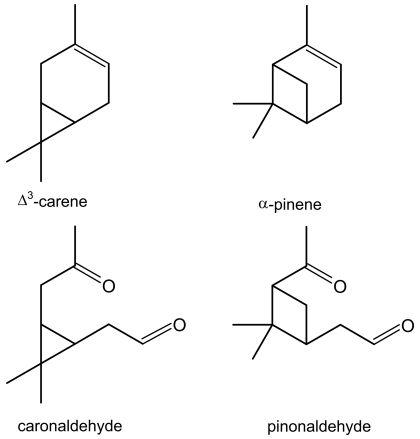

Figure 1. Structures of Δ^3-carene and its oxidation product caronaldehyde, as well as α-pinene and its oxidation product pinonaldehyde.

letter et al., 2019, and references therein), only few studies exist investigating the photooxidation of Δ^3-carene.

The similarity of its structure and type of products, e.g. caronaldehyde and pinonaldehyde that have been reported in literature (e.g. Arey et al., 1990; Hakola et al., 1994; Yu et al., 1999), suggest that Δ^3-carene behaves similarly to α-pinene (Colville and Griffin, 2004) regarding its oxidation mechanism. The structural relations between Δ^3-carene and α-pinene as well as their oxidation products caronaldehyde and pinonaldehyde are shown in Fig. 1. However, recent theoretical and experimental studies show that while the structural differences between the two molecules may be small, they may have an impact on the oxidation mechanism, e.g. due to the impact of unimolecular peroxy radical reactions (Draper et al., 2019; Moller et al., 2020).

In the atmosphere, monoterpenes mainly react with the hydroxyl radical (OH) and ozone (O_3) during daytime and O_3 and the nitrate radical (NO_3) during nighttime. From the reaction of Δ^3-carene with OH, organic peroxy radicals (RO_2) are formed that can subsequently react with NO regenerating either eventually OH or forming organic nitrates ($RONO_2$). Organic nitrates terminate the radical chain. They are typically less volatile and more hydrophilic than their parent organic compound, making them important for secondary organic aerosol (SOA) formation. Recent measurements suggest that 17 % to 23 % of organic aerosols contain molecules with nitrate functional groups (Rollins et al., 2013). $RONO_2$ species serve also as NO_x ($NO_x = NO_2 + NO$) reservoirs, hereby influencing, for example, O_3 formation (Farmer et al., 2011).

In oxidation product studies, caronaldehyde was found to be the main daytime organic oxidation product from the oxidation of Δ^3-carene (Arey et al., 1990; Reissell et al., 1999). The vapor pressure of this compound is lower than the vapor pressure of Δ^3-carene, possibly making it a contributor to particle formation in the atmosphere (Yokouchi and Ambe, 1985; Hallquist et al., 1997).

In the present study, the following reactions of Δ^3-carene were investigated in a series of experiments in the atmospheric simulation chamber SAPHIR:

$$\Delta^3\text{-carene} + \text{OH} \rightarrow \text{product}, \quad \text{(R1)}$$

$$\Delta^3\text{-carene} + \text{O}_3 \rightarrow \text{product} + \text{OH}, \quad \text{(R2)}$$

$$\text{caronaldehyde} + \text{OH} \rightarrow \text{product}, \quad \text{(R3)}$$

$$\text{caronaldehyde} + h\nu \rightarrow \text{product}. \quad \text{(R4)}$$

The reaction rate constants of Reactions (R1)–(R3) and the photolysis frequency of Reaction (R4) are determined from the experimental decay of the respective VOC and compared to previously published values. Furthermore, the OH yield of Reaction (R2) and the caronaldehyde yield of Reactions (R1) and (R2) are determined under atmospheric conditions. The organic nitrate yields of the reactions of NO with RO_2 radicals formed in Reactions (R1) and (R3) are obtained for the first time in the gas phase. Radical and trace gas measurements are used for analysis if unaccounted radical reactions are of importance in the oxidation mechanism of Δ^3-carene.

2 Methods

2.1 Experiments in the SAPHIR chamber

SAPHIR is a double-walled atmospheric simulation chamber made of Teflon (FEP) film. It is of cylindrical shape (5 m diameter, 18 m length) with an inner volume of 270 m^3. A shutter system allows for experiments to be conducted both in the dark (shutters closed) and the sunlit (shutters opened) chamber. With the shutters opened, the chamber is exposed to sunlight, therefore allowing for natural photooxidation conditions. The pressure of the chamber is kept 35 Pa higher than the outside pressure to avoid leakage from ambient air into the chamber. Ultrapure nitrogen and oxygen (Linde, purity 99.99990 %) are used to mix the synthetic air for the experiments. The space between the two FEP films is permanently flushed with ultrapure nitrogen. In order to compensate for the air lost to small leakages and sampling from the instruments, a flow of synthetic air is continuously introduced into the chamber leading to a dilution of trace gases of about 4 % per hour. OH radicals are produced mainly from nitrous acid (HONO) photolysis. HONO is formed on the chamber walls upon illumination of the chamber. The photolysis of HONO also leads to the formation of nitric oxide (NO), so the NO_x concentration increases continuously over the course of an experiment. A more detailed description of

Table 1. Experimental conditions for all discussed oxidation experiments. Concentrations are given for the conditions in the SAPHIR chamber at the time of the first VOC injection; VOC concentrations refer to the first injection.

Expt. no.	Date	Type of experiment	RH / %	NO / ppbv	O_3 / ppbv	VOC / ppbv	T / K
E1	13 June 2019	Δ^3-carene, OH oxidation, low NO_x	60	0.8	35	5	303
E2	21 May 2020	Δ^3-carene, OH oxidation, low NO_x	40	0.3	90	6	305
E3	31 May 2020	Δ^3-carene, ozonolysis, dark chamber	20	0.1	120	7	300
E4	31 May 2020	Δ^3-carene, ozonolysis, dark chamber[a]	20	0.1	120	7	300
E5	27 May 2020	caronaldehyde, photolysis[a]	40	≤ 1.5	80	17	300
E6	27 May 2020	caronaldehyde, OH oxidation	40	≤ 1.5	80	17	300

[a] ~ 100 ppmv CO added as OH scavenger

the SAPHIR chamber and its features can be found elsewhere (e.g. Rohrer et al., 2005).

In total, six experiments were conducted to study the OH-induced photochemical degradation and ozonolysis of Δ^3-carene as well as the photolysis and photooxidation of caronaldehyde under different conditions. Experimental conditions for each experiment are summarized in Table 1.

Two experiments, experiment E1 and experiment E2, were conducted to investigate the OH reaction of Δ^3-carene with NO mixing ratios of less than 0.8 ppbv. Additionally, the ozonolysis of Δ^3-carene was studied under dark conditions (chamber roof closed) in two experiments, one without (experiment E3) and one with (experiment E4) the addition of an OH scavenger. Two experiments focused on the photolysis (experiment E5) and reaction with OH (experiment E6) of caronaldehyde with NO mixing ratios below 2 ppbv.

Before each experiment, the chamber was flushed with synthetic air until the concentrations of trace gases were below the detection limit of the instruments. Experiments E3 and E4 as well as Experiments E5 and E6 were conducted on the same day, and flushing of the chamber was only done overnight prior to experiments E3 and E5, respectively. At the beginning of the experiments, the chamber air was humidified by boiling Milli-Q water and adding the water vapor together with a high flow of synthetic air into the chamber. Relative humidity (RH) for the photooxidation experiments was around 80 % at the beginning of the experiment (water vapor mixing ratio ~ 2 %) but decreased during the day mostly due to a rise in temperature inside the chamber. RH values at the end of the experiment were typically 35 % (water vapor mixing ratio ~ 0.7 %). For the ozonolysis experiment, relative humidity was 20 % at the beginning of the experiment. For some of the photooxidation experiments, ozone produced by a discharge ozonizer was injected into the chamber to reach mixing ratios of up to 60 ppbv to suppress NO in its reaction with O_3. Up to 100 ppmv of CO was injected into the chamber as an OH scavenger for experiments E4 and E5 to study the ozonolysis of Δ^3-carene and the photolysis of caronaldehyde under OH-free conditions.

During the first 2 h after opening the roof, the "zero-air" phase, no further reactive species were added, allowing for characterizing chamber sources of, for example, nitrous acid (HONO), formaldehyde (HCHO) and acetone, and to quantify the background OH reactivity. The sum of OH reactant concentrations ([X]) weighted by their reaction rate coefficient with OH (k_{OH+X}) is called OH reactivity (k_{OH}). OH reactivity observed in the SAPHIR chamber in the zero-air phase cannot be attributed to a specific species and is therefore seen as background reactivity. Background OH reactivity in the range of $0.5\,s^{-1}$ is commonly observed in the SAPHIR chamber due to contaminants coming from the chamber wall upon humidification or irradiation. For the experiments in this study, a higher background reactivity of up to $5\,s^{-1}$ was observed possibly due to a higher contamination of the chamber caused by previous experiments. Specific contaminants can remain in the chamber even after flushing the chamber with a high flow of ultrapure synthetic air, because they are adsorbed on the chamber's Teflon film. Upon humidification or illumination of the chamber, these contaminants can be desorbed resulting in a higher than usual background OH reactivity. After the injections of the VOCs, OH reactivity was dominated by their reaction with OH, and the background reactivity could be well described from measurements in the zero-air phase, so its influence is negligible for the analysis in this work, which concentrates on the times right after the injection of the VOC, when the total OH reactivity was dominated by the VOC.

Following the zero-air phase, Δ^3-carene (Fluka, purity 99 %) was injected two to three times as a liquid into a heated volume. The vapor was transported into the SAPHIR chamber with the abovementioned replenishment flow of synthetic air. Δ^3-Carene mixing ratios ranged from 3.1 to 6.0 ppbv in the chamber right after the injections.

Caronaldehyde was synthesized by ChiroBlock GmbH (Wolfen, Germany) as an enantiomeric mixture of (+)- and (−)-caronaldehyde with a purity of > 95 % determined by ^{1}H-NMR measurements. The liquid was dissolved in dichloromethane (DCM) for stability reasons. The concentration of caronaldehyde in DCM was $0.5\,mol\,L^{-1}$. To ex-

clude influences of the solvent on the chemistry observed in the experiments, additional test experiments were conducted in which only DCM was injected into the chamber. It was found that DCM did not interfere with the measurements and that DCM chemistry did not play a role for the analysis here. Caronaldehyde was injected as a liquid dissolved in DCM and evaporated as done for liquid Δ^3-carene. Caronaldehyde mixing ratios in the chamber were 5 to 9 ppbv right after the injections. Potential wall loss of caronaldehyde was determined in a test experiment and was found to be negligible on the timescale of the experiments. Therefore, wall loss of caronaldehyde was not considered in the analysis of experiments.

2.2 Instrumentation

Δ^3-Carene and caronaldehyde were detected by proton-transfer-reaction time-of-flight mass spectrometer instruments (VOCUS-PTR-MS, Aerodyne). Both instruments were calibrated for Δ^3-carene. The measured concentrations were compared to the rise of the OH reactivity measurements when Δ^3-carene was injected. It was found that the Δ^3-carene concentration was underestimated by the VOCUS by a factor of 3 throughout all experiments. Therefore, the concentrations were scaled, so the measured rise of Δ^3-carene by these mass spectrometric methods matched the increase in the measured OH reactivity at the time of the injections using a Δ^3-carene + OH reaction rate constant of 8.0×10^{-11} cm^3 s^{-1}. The uncertainty of this calibration correction is given by the uncertainty in the Δ^3-carene + OH reaction rate constant and the uncertainty in the OH reactivity measurements that is 10 % (Fuchs et al., 2017a). Pinonaldehyde was used as a substituent to calibrate the instrument for caronaldehyde, as there is no calibration standard for caronaldehyde. The concentrations obtained from this calibration were in good agreement with the rise of the OH reactivity during caronaldehyde photooxidation experiments using a reaction rate constant of 4.1×10^{-11} cm^3 s^{-1}.

Formaldehyde (HCHO) was measured by a Hantzsch monitor (AL4021, AeroLaser GmbH) and with a cavity ring-down instrument (G2307, Picarro). On average, the concentrations measured by both instruments agreed within 15 % (Glowania et al., 2021). HONO concentrations were measured by a custom-built long-path absorption photometer (LOPAP) (Kleffmann et al., 2002; Li et al., 2014). NO and NO_2 were measured using a chemiluminescence instrument (Eco Physics) equipped with a blue-light photolytic converter for the conversion of NO_2 to NO. CO and water vapor were measured with a cavity ring-down instrument (G2401, Picarro) and O_3 with an UV absorption instrument (Ansyco). Total and diffuse spectral actinic flux densities measured by a spectral radiometer outside of the chamber were used to calculate photolysis frequencies (j) following Eq. (1):

$$j = \int \sigma(\lambda)\phi(\lambda)F_\lambda(\lambda)\mathrm{d}\lambda, \quad (1)$$

with σ being the absorption cross section, ϕ the quantum yield and F_λ the mean spectral actinic flux density inside the chamber. Absorption cross sections and quantum yields were taken from recommendations in literature. The actinic flux spectra within the chamber were calculated in a model using the spectral radiometer measurements as input. As explained in more detail in Bohn et al. (2005) and Bohn and Zilken (2005), this model takes into account chamber-specific parameters such as the time-dependent effects of shadings of the chamber steel frame and the transmittance of the Teflon film. RO_x radicals (OH, HO_2, RO_2) were measured by laser-induced fluorescence (LIF), in which OH is excited at 308 nm (Holland et al., 1995; Fuchs et al., 2011). HO_2 and RO_2 are chemically converted to OH so that the sum of radicals could be detected as OH in separate measurement cells (Fuchs et al., 2008, 2011). In the experiments in 2019, HO_2 was additionally measured by bromide chemical ionization mass spectrometry (Br-CIMS) as described by Albrecht et al. (2019). The measurements usually agreed within 15 %. The detection sensitivity for RO_2 from Δ^3-carene was found to be in the range of the detection sensitivity for methyl peroxy radicals. For some experiments in this work, the fraction of RO_2 formed from Δ^3-carene ($RO_{2,\mathrm{carene}}$) is used and calculated as described in the following section. In all experiments, OH reactivity (k_{OH}) was measured using a pump–probe instrument (Lou et al., 2010; Fuchs et al., 2017b). An overview of the instrumentation including their accuracies is given in the Supplement (Table S1).

2.3 OH reactivity and peroxy radical distribution

The OH reactivity measured in the SAPHIR chamber represents the sum of all species that react with OH. It can be separated into a fraction attributed to inorganic species (NO, CO, NO_2) and formaldehyde (here named $k\mathrm{OH}_{\mathrm{inorg}}$), as well as a fraction contributed to by VOC species ($k\mathrm{OH}_{\mathrm{VOC}}$). This allows us to distinguish between reactions forming RO_2 and those that do not. Equation (2) allows us to calculate the fraction contributed to by VOC species by subtracting $k\mathrm{OH}_{\mathrm{inorg}}$ from the total measured reactivity. $k_{(\mathrm{OH+X})}$ represents the reaction rate constant of the respective compound X with OH.

$$\begin{aligned} k\mathrm{OH}_{\mathrm{VOC}} = & k\mathrm{OH}_{\mathrm{obs}} - (k_{\mathrm{OH+NO}}[\mathrm{NO}] + k_{\mathrm{OH+NO_2}}[\mathrm{NO_2}] \\ & + k_{\mathrm{OH+CO}}[\mathrm{CO}] + k_{\mathrm{OH+HCHO}}[\mathrm{HCHO}]) \end{aligned} \quad (2)$$

Included in $k\mathrm{OH}_{\mathrm{VOC}}$ is the reactivity from Δ^3-carene but also from reaction products like oxygenated VOCs (OVOCs). $k\mathrm{OH}_{\mathrm{carene}}$, the fraction of OH reactivity from Δ^3-carene, can be calculated using its OH reaction rate constant and measured concentrations (Eq. 3).

$$k\mathrm{OH}_{\mathrm{carene}} = k_{\mathrm{OH+carene}}[\mathrm{carene}] \quad (3)$$

Since the RO_2 measurement is the sum of all RO_2 produced in the chamber, it can be assumed that the fraction of

RO_2 radicals produced by Δ^3-carene to the total RO_2 concentration is equal to the ratio of OH reactivity from the Δ^3-carene + OH reaction to the total measured OH reactivity, assuming that every VOC + OH reaction leads to the formation of an RO_2 radical and that all RO_2 species have similar chemical lifetimes. The concentration of RO_2 formed by Δ^3-carene oxidation can therefore be estimated using Eq. (4).

$$[RO_{2,\mathrm{carene}}] = \frac{k\mathrm{OH}_{\mathrm{carene}}}{k\mathrm{OH}_{\mathrm{VOC}}}[RO_{2,\mathrm{obs}}] \quad (4)$$

2.4 Determination of reaction rate constants and OH yield from ozonolysis

Reaction rate constants for the reaction of OH with Δ^3-carene as well as its oxidation product caronaldehyde and for the ozonolysis of Δ^3-carene are determined by minimizing the root-mean-square error (RMSE) between measured VOC concentration time series and results from a simplified box model while the reaction rate constant is varied. The box model includes a minimum number of reactions required to describe the loss of the VOC. For the ozonoylsis and OH oxidation of Δ^3-carene, the model consists of Reactions (R1), (R2) and the dilution of the trace gases from the chamber replenishment flow. The model for the reaction of caronaldehyde with OH consists of Reactions (R3) and (R4) and the dilution of trace gases. The model is constrained to measured oxidant concentrations (OH and O_3), temperature, pressure and dilution rates. For the determination of the caronaldehyde + OH reaction rate constant, the model is additionally constrained to the measured photolysis frequency.

To determine the OH yield of the ozonolysis of Δ^3-carene, the same method is applied, but the model is constrained to the determined reaction rate constants while the OH yield is varied. When ozonolysis experiments are conducted in the dark chamber, it is assumed that OH production only occurs through the ozonolysis of Δ^3-carene and that there are no other photolytic sources (see Sect. 3.1). For this analysis, it is of no importance whether the correct absolute concentration of Δ^3-carene or caronaldehyde is used in the box model, as the relative decay of modeled and measured Δ^3-carene or caronaldehyde are compared.

2.5 Determination of product yields – organic nitrate $RONO_2$

The yield of nitrates ($RONO_2$) from the reaction of $RO_{2,\mathrm{carene}} + NO$ can be determined from the analysis of the concentrations of reactive nitrogen species in the chamber. NO, NO_2 and HONO were directly measured in the experiments, and their sum is called NO_y^* for the analysis in this work (Eq. 5):

$$[NO_y^*] = [\mathrm{HONO}] + [NO_2] + [\mathrm{NO}]. \quad (5)$$

The source of all reactive nitrogen species in the experiment is the chamber source of HONO in the sunlit chamber. Its variable source strength $Q(\mathrm{HONO})$ depends on temperature, relative humidity and solar ultraviolet radiation (Rohrer et al., 2005). HONO photolysis leads to the production of NO that is further oxidized to higher nitrogen oxides over the course of the experiment.

As HONO can be reformed by the reaction of NO with OH, a photostationary state between HONO, NO and OH is usually reached within several minutes. Therefore, measurements of NO, OH, j_{HONO} and HONO can be used to calculate the source strength of HONO (Eq. 7).

$$\frac{\mathrm{d}[\mathrm{HONO}]}{\mathrm{d}t} = Q(\mathrm{HONO}) - j_{\mathrm{HONO}}[\mathrm{HONO}] + k_{\mathrm{OH+NO}}[\mathrm{OH}][\mathrm{NO}] \approx 0, \quad (6)$$

$$Q(\mathrm{HONO}) = j_{\mathrm{HONO}}[\mathrm{HONO}] - k_{\mathrm{OH+NO}}[\mathrm{OH}][\mathrm{NO}]. \quad (7)$$

For the experimental conditions in this work ($j_{\mathrm{HONO}} \approx 8 \times 10^{-4}\ \mathrm{s}^{-1}$) photostationarity is reached within 20 min. Chemical loss of NO_y^* in the chamber occurs due to the formation of $RONO_2$ (R6, Table 2) and HNO_3 (R2, Table 2). Additionally, NO_y^* species are lost due to replenishment flow that compensates for chamber leakage and gas sampling of analytical instruments. The difference between the time-integrated production and loss terms can then be used to determine the concentration of NO_y^* at a given time t.

$$[NO_y^*]_t = \int_t (Q[\mathrm{HONO}] - k_{\mathrm{OH+NO_2}}[\mathrm{OH}][NO_2] - k_{\mathrm{RO_2,carene+NO,R10}}[RO_{2,\mathrm{carene}}][\mathrm{NO}] - L_{\mathrm{dil}})\mathrm{d}t', \quad (8)$$

where L_{dil} is the loss due to the replenishment flow, diluting the chamber air with the first-order rate coefficient $k_d = 1.6 \times 10^{-5}\ \mathrm{s}^{-1}$. L_{dil} is calculated by Eq. (9).

$$L_{\mathrm{dil}} = ([\mathrm{NO}] + [NO_2] + [\mathrm{HONO}])k_d \quad (9)$$

With respect to analysis of total nitrogen oxide concentration in the chamber, Eq. (8) assumes that HNO_3 and $RONO_2$ formation are effective sinks for NO_x and that it does not play a role, if nitrates remain as HNO_3 or $RONO_2$ in the gas-phase or if they are, for example, deposited on the chamber wall as long as neither NO nor NO_2 are reformed. Possible decomposition pathways could be, for example, due to photolysis, which would lead to a reformation of NO_2. However, reported atmospheric lifetimes of $RONO_2$ species are in the range of several days due to their small absorption cross sections (Roberts and Fajer, 1989), much longer than the duration of the chamber experiment. NO_2 loss due to the formation of nitrate radicals (NO_3) from the reaction of NO_2 with ozone is also neglected in Eq. (6). For the experimental conditions in this work, the photolytic back-reactions, reforming NO_2 from NO_3, are fast enough such that the NO_3 concentration in the sunlit chamber remains negligibly small. The formation of other oxidized nitrogen species such as acetyl per-

oxy nitrate (PAN) is also assumed to be negligible. The thermally unstable PAN species are formed from reaction of acyl peroxy radicals with NO_2. For experiments in the SAPHIR chamber with comparable temperature conditions, the mixing ratios of PAN formed in the oxidation of acetaldehyde emitted by chamber sources are typically less than 100 pptv. Combining Eqs. (5) and (8), the amount of $RONO_2$ formed can be calculated as follows.

$$\begin{aligned}[RONO_2]_t &= \int_t k_{NO+RO_2(R10)}[RO_{2,carene}][NO]dt' \\ &= \phi_{RONO_2} \times \int_t k_{RO_2+NO}[RO_{2,carene}][NO]dt' \\ &= \int_t (Q[HONO] - k_{OH\times NO_2}[OH][NO_2] - L_{dil})dt' \\ &\quad - ([NO] + [NO_2] + [HONO]) \end{aligned} \tag{10}$$

Applying Eq. (10), the reaction yield of organic nitrates (ϕ_{RONO_2}) can be derived from the calculated $\Delta[RONO_2]$ and measured $RO_{2,carene}$ concentrations.

To prove this concept of calculating organic nitrate yields, reference experiments with CH_4 were performed. An upper limit of 0.001 was found for the nitrate yield. Within the uncertainty of the measurements, this value is in good agreement with literature (Scholtens et al., 1999; Butkovskaya et al., 2012). To exclude possible errors in the analysis for larger molecules for which nitrate formation is significant, such as unknown chamber sources of reactive nitrate species, a similar analysis was performed for an α-pinene experiment conducted in the SAPHIR chamber. For this experiment, an organic nitrate yield of (32 ± 6) % was found, which is in reasonable agreement with the reported literature values. A detailed description of the reference experiments with CH_4 and α-pinene will be given in a publication currently in preparation.

2.6 Determination of product yields

The experiments conducted in SAPHIR allow us to determine the product yields of caronaldehyde from the reaction of Δ^3-carene with OH and O_3. The product yield determination for caronaldehyde is done using measured caronaldehyde concentrations and relating them to the concentration of Δ^3-carene consumed by OH or O_3. The concentrations of Δ^3-carene and caronaldehyde were measured by VOCUS or PTR-TOF-MS. A correction was applied to the Δ^3-carene and caronaldehyde concentrations similar to corrections described by Galloway et al. (2011) and Kaminski et al. (2017). To derive the concentration of Δ^3-carene that reacted with OH or O_3, measured Δ^3-carene concentrations were corrected for dilution in the chamber and the reaction with O_3 or OH, respectively. The measured product concentrations of caronaldehyde were corrected for loss due to photolysis and dilution.

2.7 Determination of radical sources and sinks

The experiments performed in the SAPHIR chamber that investigated the OH oxidation of Δ^3-carene allow us to calculate production and destruction rates of the total RO_x concentration. The atmospheric lifetimes of the RO_x radicals range from only a few seconds for the OH radical to minutes for HO_2 and RO_2 radicals. Therefore, steady-state conditions of RO_x concentrations can be assumed, so radical production and destruction rates are always balanced for the timescale of the chamber experiments. If there are imbalances between the calculated production and destruction rates, chemical reactions leading to the formation or destruction of radicals must be missing in the calculations. Table 2 gives an overview of the formation and loss reactions considered in the analysis including the respective reaction rate constants used. The reaction rate constants of the individual reactions were either taken from recent experimental studies, from measurements in this study or from calculations applying structure–activity relationship (SAR) as described in Jenkin et al. (2019).

The main RO_x formation processes include the photolysis of ozone (Reaction R11), HONO (Reaction R12) and HCHO (Reaction R13) as well as the ozonolysis of Δ^3-carene (Reaction R14). The formation of RO_x radicals from the photolysis of caronaldehyde (R4) was also considered. The formation rate of RO_x radicals $P(RO_x)$ can be calculated by Eq. (11).

$$\begin{aligned} P(RO_x) = &j_{HONO}[HONO] + \Phi_{OH-R11} \times j_{O(^1D)}[O_3] \\ &+ 2j_{HCHO}[HCHO] \\ &+ \Phi_{OH+RO_x} \times k_{14}[\Delta^3\text{-carene}][O_3] \\ &+ \Phi_{RO_x-R4} \times j_{caronal}[caronal] \end{aligned} \tag{11}$$

Φ_X indicates the yield of the respective radical X from the given reaction. Loss processes include the reactions of radicals with NO_x that lead to the formation of HONO from the reaction of OH with NO (Reaction R5), nitric acid (HNO_3) from the reaction of OH with NO_2 (Reaction R6) or organic nitrates ($RONO_2$) from the reaction of $RO_{2,carene}$ and NO (Reaction R10). Depending on the experimental conditions, radical loss through radical self-reactions becomes more important, leading to the formation of hydrogen peroxide (H_2O_2) from the reaction of two HO_2 radicals (Reaction R7), the formation of peroxides (ROOH) from the reaction of HO_2 with RO_2 (Reaction R8) and the self-reaction of RO_2 (Reaction R9). The loss rate of RO_x radicals $L(RO_x)$ is calculated by Eq. (12).

$$\begin{aligned} L(RO_x) = &(k_6[NO_2] + k_5[NO])[OH] + (k_8[HO_2] \\ &+ 2 \times k_9[RO_2] + k_{10}[NO])[RO_2] \\ &+ 2k_7[HO_2]^2 \end{aligned} \tag{12}$$

Direct measurements of all relevant species allow us to calculate the total formation and loss rates for the RO_x radicals.

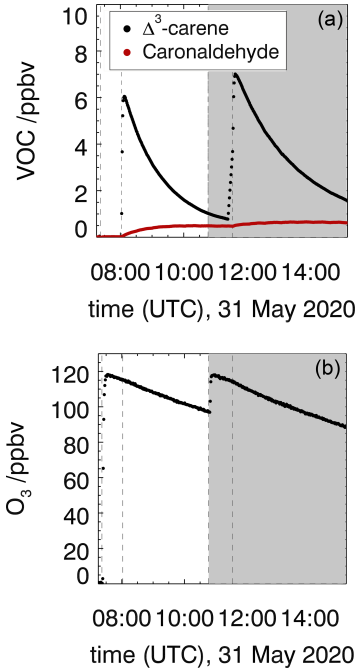

Figure 2. Measured Δ^3-carene, caronaldehyde **(a)** and O_3 **(b)** mixing ratios in the experiment investigating the ozonolysis of Δ^3-carene (experiment E3). The shaded area indicates the time where CO was injected as an OH scavenger (experiment E4). Vertical lines give the times when trace gases were injected.

The error of the loss and production rates of the RO_x radicals is determined by error propagation, taking uncertainties in the measurements and kinetic parameters into account.

3 Results and discussion

3.1 Ozonolysis of Δ^3-carene

The ozonolysis of Δ^3-carene was investigated in the dark SAPHIR chamber in two experiments in order to determine the rate constant (experiment E3) and OH yield (experiment E4) of the ozonolysis reaction, as well as the yield of caronaldehyde. Measured time series of O_3, Δ^3-carene and caronaldehyde are shown in Fig. 2. In total, 6.5 ppbv of Δ^3-carene was consumed in experiment E3, and 7 ppbv was consumed in experiment E4. The roof of the chamber was closed for the whole duration of both experiments, to eliminate photolytical OH production. Since there was no OH scavenger present in experiment E3, the reaction system was also influenced by OH that is formed from ozonolysis

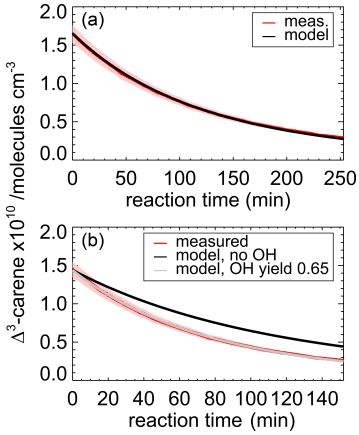

Figure 3. Measured and modeled Δ^3-carene concentrations for the ozonolysis experiment E4. During the second part of the experiment **(a)**, 90 ppmv of an OH scavenger (CO) was injected to suppress OH so that Δ^3-carene reacted only with ozone. The modeled decay is fitted with a rate constant of $(4.4 \pm 0.2) \times 10^{-17}$ cm^3 s^{-1}. During the first part of the experiment **(b)**, when no CO was present, the measured decay of Δ^3-carene is significantly faster than expected from ozonolysis alone. The measured time series of Δ^3-carene can be best matched if an OH yield of 0.65 ± 0.10 from its ozonolysis reaction is assumed. Red colored areas indicate the accuracy of the measured Δ^3-carene concentrations.

(Sect. 3.1.2). OH concentrations were in the range of 1.0 to 2.0×10^6 cm^{-3}. CO was injected into the chamber as an OH scavenger prior to the beginning of experiment E4.

3.1.1 Rate constant of the ozonolysis reaction of Δ^3-carene

Optimization of the ozonolysis reaction rate constants as described in Sect. 2.4 results in a value of $(4.4 \pm 0.2) \times 10^{-17}$ cm^3 s^{-1}. The stated error arises from the accuracy of the O_3 and Δ^3-carene measurements. The average temperature inside the SAPHIR chamber during the experiment was 300 K. The value reported in this study is slightly higher than values reported by Atkinson et al. (1990) and Chen et al. (2015) but still agrees within the stated errors (Table 3).

Reaction rate constants determined by Atkinson et al. (1990) and Chen et al. (2015) were $(4.05 \pm 0.4) \times 10^{-17}$ and $(3.7 \pm 0.4) \times 10^{-17}$ cm^3 s^{-1}, respectively. Both values were obtained from relative reaction rate measurements by comparing the rate of decay of Δ^3-carene from ozonolysis to the rate of decay of a well-known reference compound (α-pinene in Atkinson et al., 1990, and cyclohexene in Chen et al., 2015). Additionally both studies also determined the reaction rate constant with an absolute rate technique using a pseudo-first-order approach. In Atkinson et al. (1990), reactive im-

Table 2. Formation and loss reactions of the RO_x radicals considered in the budget analysis (Fig. 11). Reaction rate constants are given for 298 K and 1 atm. The reaction rate constants in the actual analysis are calculated using temperature and pressure data measured during the experiments in SAPHIR.

		Reaction	k (298 K, 1 atm) $cm^3\,s^{-1}$	Reference
Radical loss	R5	$OH + NO \rightarrow HONO$	7.5×10^{-12}	Burkholder et al. (2020)
	R6	$OH + NO_2 \rightarrow HNO_3$	1.1×10^{-11}	Burkholder et al. (2020)
	R7	$HO_2 + HO_2 \rightarrow H_2O_2 + O_2$	1.4×10^{-12}	Burkholder et al. (2020)
		$HO_2 + HO_2 + M \rightarrow H_2O_2 + O_2$	1.1×10^{-12} [a]	Burkholder et al. (2020)
	R8	$HO_2 + RO_{2,obs.} \rightarrow ROOH + O_2$	2.3×10^{-11}	Jenkin et al. (2019)
	R9	$RO_{2,obs.} + RO_{2,obs.} \rightarrow$ products	1.3×10^{-13}	Jenkin et al. (2019)
	R10	$RO_{2,carene} + NO \rightarrow RONO_2$	Φ[b] 9.0×10^{-12}	Jenkin et al. (2019)
Radical formation	R11	$O_3 + h\nu\,(< 340\,nm) \rightarrow O(^1D) + O_2$	$j_{O(^1D)}$	measured
		$O(^1D) + H_2O \rightarrow 2OH$	2.1×10^{-10}	Atkinson et al. (2004)
		$O(^1D) + M \rightarrow O(^3P) + M$	3.3×10^{-11}	Atkinson et al. (2004)
	R12	$HONO + h\nu\,(< 340) \rightarrow OH + NO$	j_{HONO}	measured
	R13	$HCHO + h\nu\,(< 335) + O_2 \rightarrow 2HO_2 + CO$	j_{HCHO}	measured
	R14	Δ^3-carene $+ O_3 \rightarrow 0.65 \times OH + RO_2 +$ products	4.4×10^{-17}	Table 3, this work
	R4	caronaldehyde $+ h\nu \rightarrow HO_2 + RO_2 +$ products	$j_{caronal}$	measured

[a] pressure dependent value given as $4.6 \times 10^{-32} \times (M)$ in Burkholder et al. (2020); [b] the yield Φ of this reaction is determined in Sect. 3.2.3.

Table 3. Rate constants of the reaction of Δ^3-carene with O_3 and OH as well as of the reaction of caronaldehyde with OH. Experimental values obtained in this study are compared to reported literature values.

Reaction	Reaction rate constant / $cm^3\,s^{-1}$	Technique	Temperature / K	Reference
Δ^3-carene $+ O_3$	$(4.4 \pm 0.2) \times 10^{-17}$	absolute rate	300	this study
	$(5.9 \pm 1) \times 10^{-17}$	relative rate	295	Witter et al. (2002)
	$(3.7 \pm 0.2) \times 10^{-17}$	relative rate	299	Chen et al. (2015)
	$(4.9 \pm 0.8) \times 10^{-17}$	absolute rate[b]	299	Chen et al. (2015)
	$(3.5 \pm 0.2) \times 10^{-17}$	absolute rate[c]	299	Chen et al. (2015)
	$(3.7 \pm 0.2) \times 10^{-17}$	absolute rate[d]	299	Chen et al. (2015)
	$(3.8 \pm 0.2) \times 10^{-17}$	relative rate	296	Atkinson et al. (1990)
	$(5.2 \pm 0.6) \times 10^{-17}$	absolute rate	296	Atkinson et al. (1990)
	4.8×10^{-17}	SAR[e]	298	Jenkin et al. (2020)
Δ^3-carene + OH	$(8.0 \pm 0.5) \times 10^{-11}$	absolute rate	304	this study
	$(8.0 \pm 0.1) \times 10^{-11}$ [a]	relative rate	304	Dillon et al. (2017)
	$(8.7 \pm 0.4) \times 10^{-11}$	relative rate	294	Atkinson et al. (1986)
	8.5×10^{-11}	SAR	298	Peeters et al. (2007)
Caronaldehyde + OH	$(4.1 \pm 0.3) \times 10^{-11}$	absolute rate	300	this study
	$(4.8 \pm 0.8) \times 10^{-11}$	relative rate	296	Alvarado et al. (1998)
	$(12.1 \pm 0.8) \times 10^{-11}$	relative rate	298	Hallquist et al. (1997)
	$(2.9 \pm 0.8) \times 10^{-11}$	SAR	298	Jenkin et al. (2018)

[a] temperature-dependent reaction rate coefficient given by Dillon et al. (2017): $(2.48 \pm 0.14) \times \exp(357 \pm 17)/T \times 10^{-17}\,cm^3\,s^{-1}$; [b] measured in a flow reactor; [c] measured in a 7.3 m^3 Teflon chamber; [d] measured in a 90 m^3 Teflon chamber; [e] structure–activity relationship

purities in the used Δ^3-carene sample were reported, whose presence would reduce the initially measured reaction rate constant from the absolute technique from $(5.2 \pm 0.6) \times 10^{-17}$ to $(4.1 \pm 0.6) \times 10^{-17}\,cm^3\,s^{-1}$. Chen et al. (2015) used three different set-ups to determine the reaction rate constant with an absolute rate technique: two simulation chambers with volumes of 90 m^3 (HELIOS) and 7.3 m^3 and a laminar flow reactor. The values determined in the simulation chambers were $(3.5 \pm 0.2) \times 10^{-17}\,cm^3\,s^{-1}$ in the smaller simulation chamber and $(3.7 \pm 0.2) \times 10^{-17}\,cm^3\,s^{-1}$ in HELIOS. A rate

Table 4. OH yield of the reaction of Δ^3-carene with O_3. Experimental values obtained in this study are compared to reported literature values.

OH yield	Technique	Reference
0.65 ± 0.10	absolute rate	this study
1.1 ± 1.0	OH scavenging with c-hexane	Atkinson et al. (1992)
0.6 ± 1.0	OH scavenging with c-hexane[a]	Atkinson et al. (1992)
0.86 ± 0.11	OH scavenging with 2-butanol	Aschmann et al. (2002b)
0.56 to 0.59	theoretical calculations	Wang et al. (2019)

[a] with revisited yields of c-hexanone and c-hexanol by Berndt et al. (2003) as explained in the text

Table 5. Caronaldehyde yields for the reaction of Δ^3-carene with OH and OH as well as caronaldehyde yields for the reaction of Δ^3-carene with O_3 obtained from this study compared to literature values. Given Δ^3-carene concentrations are initial concentrations.

Reaction	Yield / % caronaldehyde	Expt. conditions Δ^3-carene / ppbv	NO / ppbv	RH / %	Product quantification	Reference
Δ^3-carene + OH	30 ± 5	5	0.8	45	PTR-MS	this study
	31	975	9756	0	GC-FID[a]	Arey et al. (1990)
	34 ± 0.8	9800	0	0	GC-FID	Hakola et al. (1994)
Δ^3-carene + O_3	5.5 ± 2	6	0.1	18	PTR-MS	this study
	8.5[b]	89.9	n/a[c]	n/a[c]	GC–MS	Yu et al. (1999)
	≤ 8[d]	9800	0	0	GC-FID/GC–MS	Hakola et al. (1994)
	0.47 ± 0.05[e]	15000	0	0	GC-FID/GC–MS	Ma et al. (2009)

[a] GC-FID: gas chromatograph with flame ionization detector, GC–MS: gas chromatograph with mass spectrometer; [b] combined yield for gas and aerosol phase; [c] no values given in the publication; [d] yield obtained in the absence of an OH scavenger; [e] obtained from filter samples.

constant of $(4.9 \pm 0.8) \times 10^{-17}$ cm^3 s^{-1} was determined in the flow reactor. The 30 % discrepancy between the determined reaction rate constant is explained by interferences in the O_3 measurements and increased uncertainties due to higher wall losses in the flow reactor. Witter et al. (2002) reported a faster reaction rate constant of $(5.9 \pm 1.0) \times 10^{-17}$ cm^3 s^{-1}, obtained with a relative rate technique using 2-methyl-2-butene as reference compound. The value reported by Witter et al. (2002) is higher than the other reported values. Although the reason for this discrepancy is not clear, in their study Witter et al. (2002) also determined the ozonolysis reaction rate constants for other monoterpenes, e.g. limonene, α-terpinene and α-pinene, and the determined values were mostly on the upper end of reported literature values. The rate constants were on average 20 % higher than comparable values, which may point to a general overestimation of monoterpene reaction rate constants. The IUPAC Task Group on Atmospheric Chemical Kinetic Data Evaluation recommend to use a value of $(4.9 \pm 0.2) \times 10^{-17}$ cm^3 s^{-1} (Atkinson et al., 2004), which is an average of the relative rate constants determined by Atkinson et al. (1990) and Witter et al. (2002) and is in good agreement with the value determined in this work. Using the SAR published by Jenkin et al. (2020), a reaction rate constant of 4.7×10^{-17} cm^3 s^{-1} can be calculated. The value reported in this study is in relatively good agreement with this theory-derived value.

3.1.2 Determination of the OH yield from the ozonolysis of Δ^3-carene

During experiment E3, when no OH scavenger was present, Δ^3-carene was not only consumed by O_3 but also by OH that is produced from the ozonolysis reaction. Because OH production from the ozonolysis was the only OH source, the OH yield from ozonolysis of Δ^3-carene can be determined from this experiment. The chamber roof was closed for the whole experiment, and there are no photolytic sources for OH formation. The reaction rate constant determined in the previous section for the period, when an OH scavenger was present in the SAPHIR chamber, is used in the box model to determine the OH yield of the ozonolysis as explained in Sect. 2.4. The OH yield from ozonolysis is optimized until the measured decay of Δ^3-carene matches the modeled decay (Fig. 3). A comparison of the experimental decay to model runs with different OH yields is shown in Fig. S1.

The OH yield is found to be 0.65 ± 0.10 in the experiment in this work. The error is mainly due to the uncertainties in the reaction rate constants and the accuracies of the O_3 measurement. Reported literature values for the OH yield from the ozonolysis of Δ^3-carene determined in experiments are 1.1 ± 1.0 (Atkinson et al., 1992) and 0.86 ± 0.11 (Aschmann et al., 2002a). Wang et al. (2019) theoretically calculated the OH yield to be 0.56 to 0.59. Table 4 shows the value de-

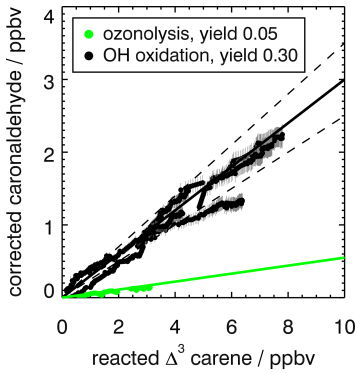

Figure 4. Yield of caronaldehyde for Reactions (R1) ($OH + \Delta^3$-carene) and (R2) (O_3+ Δ^3-carene) determined from the slope of the relation between consumed Δ^3-carene and measured caronaldehyde concentrations. For Reaction (R1), the result from experiments E1 and E2 are shown. Concentrations were corrected for dilution and chemical loss (see text for details). Caronaldehyde yields from the oxidation of Δ^3-carene are determined as the slopes of the shown solid linear regression lines (black: OH oxidation R1, green: ozonolysis R2). Dashed lines indicate the error of the regression analysis.

termined here compared with reported literature values. The value reported here is closer to the theoretical than to the other measured values, but it agrees with the yield reported by Aschmann et al. (2002a) within the reported uncertainties. As discussed in Wang et al. (2019), the high OH yield reported in Atkinson et al. (1992) could have been overestimated because of the high uncertainty in the determination of the OH yield. Atkinson et al. (1992) derived the OH yield by measuring the concentration of cyclohexanol and cyclohexanone produced in the reaction of OH and cyclohexane that was used as OH scavenger in their experiments. More recent investigations of the yield of cyclohexanol and cyclohexanone from the reaction of cyclohexane and OH indicate a larger yield of 0.88 (Berndt et al., 2003), as compared to the value of 0.5 used by Atkinson et al. (1992). This higher value would reduce the OH yield in the ozonolysis of Δ^3-carene in the experiments by Atkinson et al. (1992) to 0.6, which would agree well with the OH yield determined in this work and the value calculated by Wang et al. (2019).

The ozonolysis of Δ^3-carene is initiated by O_3 attacking the C=C double bond, forming an energy-rich primary ozonide (POZ). Mostly, the energy retained in the POZ leads to a decomposition into Criegee intermediates, retaining one structure bearing a carbonyl functionality on one side of the molecule and the Criegee functionality on the other. These Criegee intermediates then isomerize to form dioxiranes, secondary ozonides (SOZs) or vinyl hydroperoxides. A theoretical study of the ozonolysis of Δ^3-carene by Wang et al. (2019) found the formation yields dioxiranes, SOZ and vinyl hydroperoxides to be 0.16, 0.24 and 0.56, respectively. Collisional stabilization of the Criegee intermediates was found to be of minor importance with a yield of only 0.04 in the same study. OH (and an alkoxy radical) is formed from the vinyl hydroperoxide (ROOH) by breakage of the −O−OH bond (Aschmann et al., 2002a; Ma et al., 2009). The fate of the alkoxy radical formed from this reaction has yet to be investigated, but it might result in the formation of highly oxidized molecules (HOMs) (Wang et al., 2019).

3.1.3 Caronaldehyde yield from ozonolysis

The caronaldehyde yield for the Δ^3-carene $+ O_3$ reaction was determined from experiment E4, where an OH scavenger was injected into the chamber so that caronaldehyde is exclusively formed form the ozonolysis reaction. The corrections described in Sect. 2.5 were applied. Caronaldehyde was formed from the ozonolysis of Δ^3-carene with a yield of (5.5 ± 2) % as shown in Fig. 4. The uncertainty is derived from measurements and errors of the applied corrections (Sect. 2.6) for the respective experiment.

The determined caronaldehyde yields from this study and reported literature values are given in Table 5. The obtained value is in reasonably good agreement with most of the reported literature values. Yu et al. (1999) reported a caronaldehyde yield of 8 %, using 2-butanol to scavenge OH radicals. Hakola et al. (1994) determined the caronaldehyde yield to be ≤ 8 %. In the presence of cyclohexane as an OH scavenger, caronaldehyde was not detected in the ozonolysis of Δ^3-carene in the experiments conducted by Hakola et al. (1994). Ma et al. (2009) reported a caronaldehyde yield of (0.47 ± 0.05) % from filter samples, using cyclohexane, methanol or ethanol to scavenge OH radicals. However, due to its relatively high vapor pressure, it is likely that caronaldehyde was mainly present in the gas phase, so only a small fraction of the formed caronaldehyde was collected on the filters.

The formation of caronaldehyde from Δ^3-carene ozonolysis most likely results from the stabilization and subsequent reaction with water of one of the Criegee intermediates; the formation mechanism of caronaldehyde in the absence of water has yet to be clarified (Ma et al., 2009). The stabilization of the Criegee intermediate is found to be a minor pathway by Wang et al. (2019), possibly explaining the small caronaldehyde yield found for the ozonolysis of Δ^3-carene. Further reaction products that have not been measured in this study include a range of multifunctional organic acids according to studies conducted by, for example, Ma et al. (2009).

3.2 OH reaction of Δ^3-carene

The first oxidation steps of the OH-induced photochemical oxidation of Δ^3-carene relevant for this study are shown in Fig. 5 (Colville and Griffin, 2004). The OH oxidation is ini-

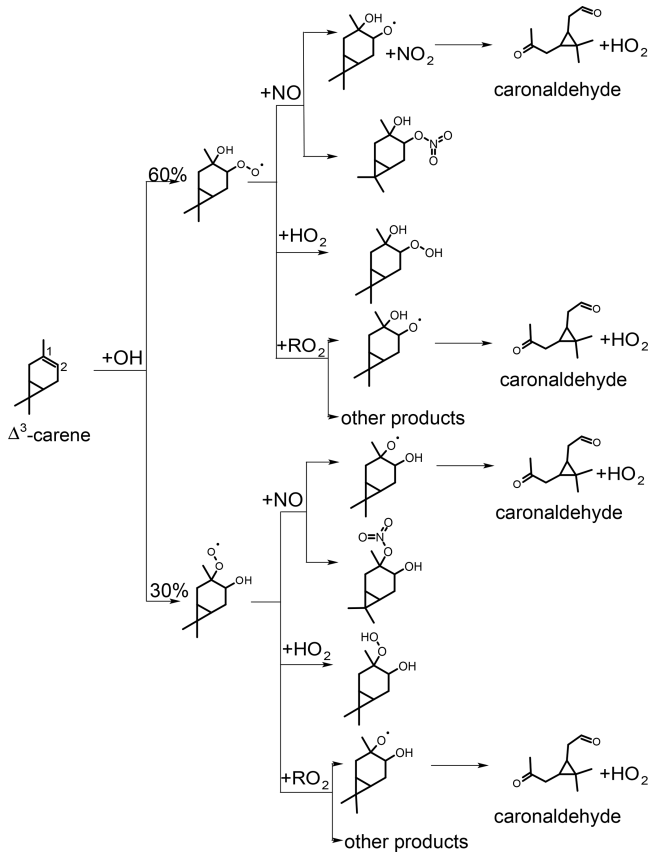

Figure 5. Simplified scheme of the first reaction steps of the OH photooxidation of Δ^3-carene (adapted from Colville and Griffin, 2004). Yields shown in black are from SAR by Jenkin et al. (2018). H abstraction has only little influence on the presented product yields. $RO_2 + RO_2$ reactions could lead to other products than the formation of the alkoxy radical that produces caronaldehyde + HO_2, so the yield of caronaldehyde from $RO_2 + RO_2$ reactions is expected to be less than 1.

tiated by addition of OH to the C=C double bond or by the abstraction of an H atom rapidly followed by addition of O_2. From the OH addition, two peroxy radical isomers are formed. The branching ratios of the specific attack on the C=C double bond (Fig. 5) and the H abstraction are estimated using the structure–activity relationship (SAR) method described in Jenkin et al. (2018). Branching ratios are 10 % for H abstraction, 30 % for OH addition to C1 and 60 % for OH addition to C2 of the double bond. Due to the small fraction of H abstraction, a relatively small influence of these reactions on the results of the following analysis can be expected.

Peroxy radicals (RO_2) can react with NO, HO_2 or undergo radical self-reactions with RO_2. The reaction of Δ^3-carene-derived $RO_{2,carene}$ with NO and possible reaction products are discussed in Sect. 3.2.2 and 3.2.3. $RO_2 + RO_2$ and $RO_2 + HO_2$ reactions are discussed in Sect. 3.2.4.

OH-induced photooxidation of Δ^3-carene was investigated in the SAPHIR chamber during two experiments with NO_x mixing ratios below 1 ppbv (Table 1). Figure 6 shows an overview of all measured species in experiment E1 that are representative for experiments at low NO_x mixing ratios. Time series of concentration measurements for the other experiment are shown in the Supplement (Figs. S2 and S3). For all experiments, Δ^3-carene was injected three times into the chamber, increasing the mixing ratio by approximately 5 ppbv each injection.

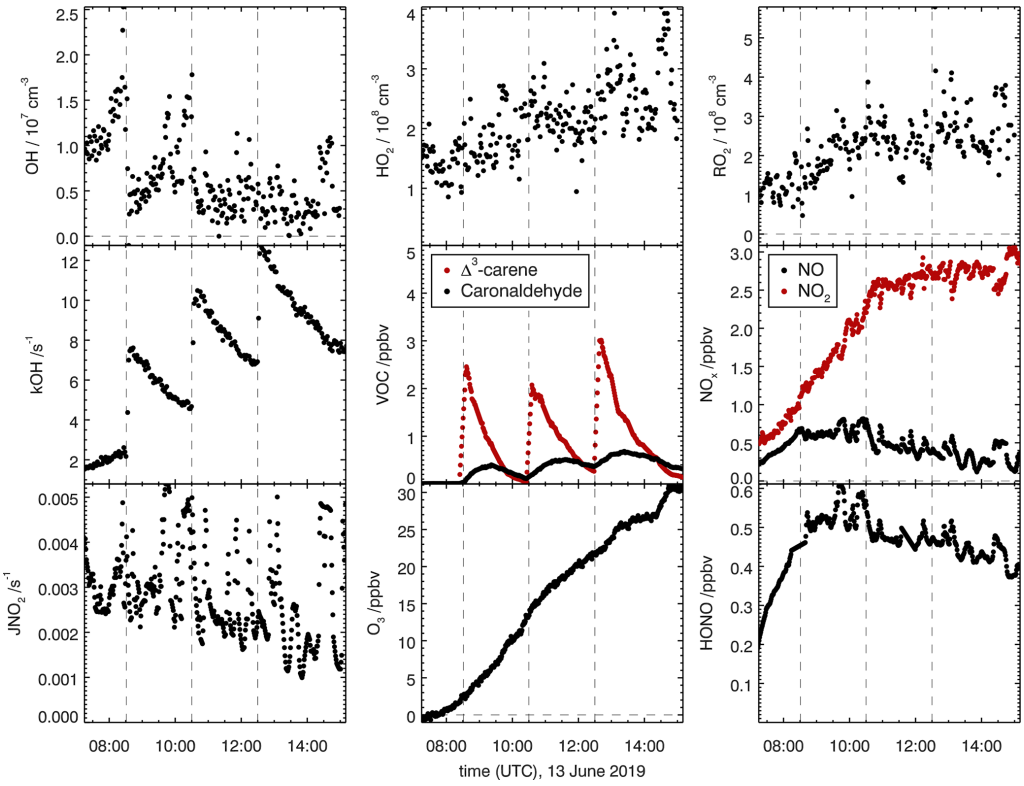

Figure 6. Overview of measured concentrations for selected species in the SAPHIR chamber for the Δ^3-carene + OH oxidation experiment E1. Dashed lines indicate times when Δ^3-carene was injected into the chamber. Measured concentrations are shown in the illuminated chamber only starting with the opening of the roof (zero-air phase).

3.2.1 Rate constant of the OH + Δ^3-carene reaction

In order to determine the rate constant of the reaction of Δ^3-carene with OH, measured time series were compared to model results from a box model, in which OH and O_3 concentrations were constrained to the measurements. A reaction rate constant was determined from all experiments. The determined value represents the mean value from all experiments. The given error is the standard error of the mean. The optimization error was much smaller than the variability of the results in different experiments. On average, the temperature inside the SAPHIR chamber was 304 K during the experiments. OH concentrations usually ranged from 5 to 8×10^6 cm^{-3}. Ozonolysis only played a minor role in the experiments, contributing to a maximum of 5 % to the Δ^3-carene consumption. The reaction rate constant for the ozonolysis reaction was taken from this work (Sect. 3.1.1).

The optimized rate constant of the OH reaction with Δ^3-carene is $(8.0 \pm 0.5) \times 10^{-11}$ cm^3 s^{-1} as shown in Fig. 7.

Table 3 shows a comparison of reported literature values to the reaction rate constants obtained in this study. The determined value for the OH + Δ^3-carene reaction rate constant from this study agrees well with both experimentally and theoretically derived literature values. Dillon et al. (2017) determined a temperature-dependent rate coefficient; for comparability with data in this work, only the rate coefficient determined at 304 K is used. Dillon et al. (2017) determined a reaction rate constant of $(8.1 \pm 0.1) \times 10^{-11}$ cm^3 s^{-1} using an absolute rate approach, and Atkinson et al. (1986) reported a value of $(8.7 \pm 0.4) \times 10^{-11}$ cm^3 s^{-1} at 294 K using a relative rate determination approach. From a site-specific structure–activity relationship (SAR), Peeters et al. (2007) predict the reaction rate constant to be 8.5×10^{-11} cm^3 s^{-1} at 298 K. In

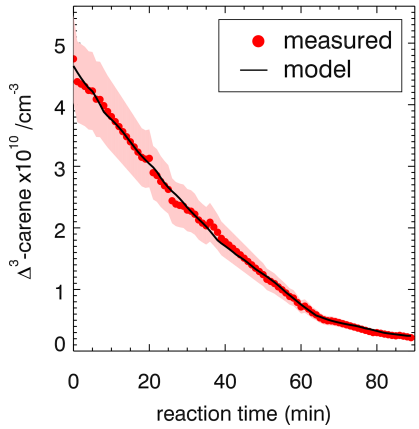

Figure 7. Comparison of the modeled and measured Δ^3-carene decay for the OH-oxidation experiment E2. Shown is the result of optimization of the rate constant of the OH reaction with Δ^3-carene in the model calculations resulting in a reaction rate constant of 7.9×10^{-11} cm^3 s^{-1}.

this reaction rate constant, the contribution of H abstraction is not considered.

3.2.2 Caronaldehyde yield from the reaction of Δ^3-carene with OH

Table 5 compares the product yields of the Δ^3-carene + OH reaction obtained in this study to reported literature values. The caronaldehyde yield of (30 ± 5) % determined in this study as shown in Fig. 4 in good agreement with reported literature values within the range of the uncertainty of the measurements. The given error reflects the range of values determined in the considered experiments. Arey et al. (1990) reported a yield of 31 % and Hakola et al. (1994) a yield of (34 ± 0.8) %. In both studies, caronaldehyde was quantified using GC-FID. Hakola et al. (1994) additionally used GC–MS and ^{1}H NMR to verify the structure and purity of the measured compound.

As shown in Fig. 5, caronaldehyde is mainly formed from the decomposition of alkoxy radicals (RO). These alkoxy radicals are mainly formed from the reaction of RO_2 with NO. A similar RO radical is also formed from the RO_2+RO_2 reaction, as well as from the photolysis of hydroperoxides (ROOH) that result from the $RO_2 + HO_2$ reaction. Since the $RO_2 + NO$ reaction mainly leads to the formation of RO (the branching ratio of an alternative pathway is discussed in Sect. 3.2.3), yields of caronaldehyde as found in this and previous studies can be expected. Other reaction products of the Δ^3-carene + OH reaction determined in previous studies include formaldehyde with a yield of 20 % (Orlando et al., 2000) and acetone with a yield of 15 % (Reissell et al., 1999; Orlando et al., 2000). Caronic acid, hydroxy-caronic acid isomers and hydroxy-caronaldehyde isomers have additionally been found in the aerosol phase of smog chamber experiments investigating the Δ^3-carene + OH reaction by Larsen et al. (2001).

3.2.3 Determination of alkyl nitrate yield for the reaction of Δ^3-carene + OH

Organic nitrates are formed from the reaction of RO_2 radicals with NO as shown in Fig. 5 for the reaction of the RO_2 formed in the first oxidation step of Δ^3-carene. An alternative pathway for the NO+RO_2 reaction is the formation of an alkoxy radical and NO_2 that ultimately leads to the formation of caronaldehyde (Sect. 3.2.2). The nitrate yield Φ_{RONO_2} for the reaction of Δ^3-carene + OH is determined following the procedure described in Sect. 2.4 using $RO_{2,carene}$. Figure 8 shows the accumulation of reactive NO_y species over the course of experiment E2. In total, 8.1 ppbv of reactive nitrogen species were formed over the course of the experiment. The contributions of NO, NO_2 and HONO are almost constant with 2.2 ppbv, while the contributions of $RONO_2$ and HNO_3 increase continuously over the course of the experiments due to their continuous production from the reaction of $RO_{2,carene}$ with NO and OH with NO_2. The formation of HNO_3 and $RONO_2$ before the injection of Δ^3-carene is not relevant for the analysis and therefore not shown in Fig. 8.

An organic nitrate yield of (25 ± 4) % was found from experiments E1 and E2. To our knowledge, only one other study investigated the organic nitrate yield of Δ^3-carene. Based on $RONO_2$ measurements in the aerosol phase using a TD-LIF instrument (thermal dissociation laser-induced fluorescence), Rollins et al. (2010) calculated an organic nitrate yield of 25 % for the photooxidation of Δ^3-carene in experiments with high NO_x conditions (100 ppbv of Δ^3-carene and 500 ppbv of NO). This yield represents the fraction of SOA molecules that are hydroxynitrates, and Rollins et al. (2010) suggest that the organic nitrate fraction of SOA molecules produced in photooxidation are similar to the total yield of $RONO_2$ from $RO_2 + NO$. The SAR by Jenkin et al. (2019) predicts an organic nitrate yield of 19 %. This calculation is based on the number of C atoms in the peroxy radical and therefore possibly has a relatively high uncertainty. The value obtained in this study for experiments with NO_x mixing ratios below 1 ppbv is in good agreement with both the experimental and the SAR-derived values. Due to their structural similarities, it can be assumed that organic nitrate yields for Δ^3-carene could be comparable to reported determined organic nitrate yields of α-pinene. Noziere et al. (1999) report an organic nitrate yield of (18 ± 9) % and Rindelaub et al. (2015) (26 ± 7) % for the reaction of α-pinene with OH. The organic nitrate yield of 1 % by Aschmann et al. (2002b) was not measured directly but approximated from API-MS measurements. This leads to a high uncertainty and likely ex-

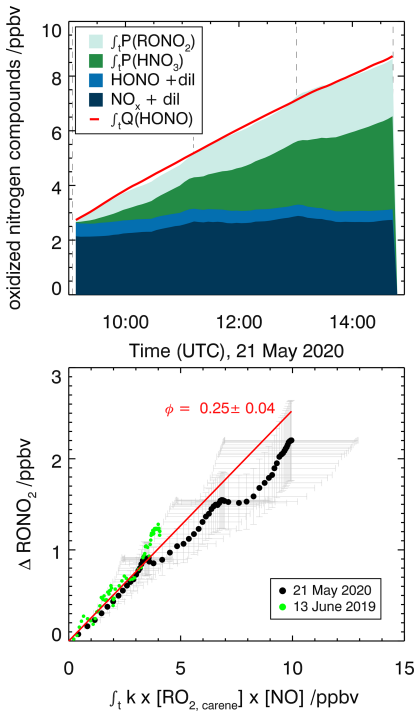

Figure 8. Determination of the organic nitrate yield for the Δ^3-carene + OH oxidation experiment E2. The red line shows the time-integrated HONO emission calculated as described in the text. NO_x and HONO concentrations were measured, while the time-integrated NO_2 loss by HNO_3 formation and time-integrated NO loss by $RONO_2$ formation are calculated as described in the text. The yield of (25 ± 4) % for alkyl nitrates is optimized such that the total NO_y produced over the course of both experiments, E1 and E2, is accounted for.

plains the difference with the values by Noziere et al. (1999) and Rindelaub et al. (2015). The nitrate yield obtained in this study for Δ^3-carene is in reasonable agreement with the values reported for α-pinene, as can be expected due to their structural similarities.

3.3 Photooxidation of caronaldehyde

A simplified reaction scheme for caronaldehyde degradation chemistry is shown in Fig. 9. Caronaldehyde can be oxidized by the reaction with OH, forming RO_2 radicals through H abstraction and fast subsequent addition of O_2. The formed peroxy radicals can then undergo reactions with NO, HO_2 and RO_2, resulting in similar product species such as explained before. Photolysis of caronaldehyde is an additional loss path. Due to their structural similarities, it can be assumed that caronaldehyde photolyzes in a similar way like pinonaldehyde. Photolysis leads to the C−C bond scission next to the aldehydic functional unit of the molecule, leading to the formation of HCO and an alkyl radical. Both species subsequently react with O_2, forming CO, HO_2 and a peroxy radical.

The reaction of caronaldehyde with OH was investigated in experiment E6. Caronaldehyde was injected twice into the chamber to reach mixing ratios of 5 ppbv directly after the first and 6 ppbv directly after the second injection. The OH concentration was 7×10^6 cm^{-3} for the period after the first injection. Prior to the second injection, 50 ppmv of CO was injected into the chamber as an OH scavenger to study the photolysis of caronaldehyde separately. The temperature in the chamber ranged from 295 to 305 K during the experiment.

3.3.1 Photolysis frequency of caronaldehyde

As CO was injected into the chamber as an OH scavenger and as wall loss was found to be negligible in the timeframe of the experiment, the decay of caronaldehyde measured can only be due to photolysis and dilution. The absorption spectrum of caronaldehyde was measured by Hallquist et al. (1997) in the range from 275 to 340 nm at 300 K. This spectrum and an assumed quantum yield for dissociation of 1 was used to calculate the photolysis frequency for the conditions of the experiment in the sunlit chamber using Eq. (1) (Sect. 2.2), resulting in a mean loss of caronaldehyde due to photolysis of 1.3×10^{-5} s^{-1}. The calculated photolysis frequency was included in a model to compare the measured to the modeled decay. The modeled decay was found to be too slow and requires a photolysis frequency that is larger by a factor of 7 to match the experimental decay. The absorption cross section by Hallquist et al. (1997) used in this work is the only reported measurement. It was measured in a 0.48 m^3 borosilicate reactor at low pressure. During their experiments, dichloromethane and methanol solvents used in the synthesis of caronaldehyde were present in the reactor. Even though the authors corrected for possible interferences caused by these two species regarding the caronaldehyde concentration measured by IR spectroscopy, potential errors in the measurement of caronaldehyde concentrations might explain the discrepancy. Although there is no mechanistic explanation, it cannot be fully excluded that the faster decay observed in the experiments in this work compared to that by Hallquist et al. (1997) is the result of an alternative OH independent loss process occurring in the illuminated chamber. The absorption cross sections that have to be applied to explain the decay of caronaldehyde in photolysis experiments in SAPHIR suggest further investigation of this reaction and the absorption cross section of caronaldehyde.

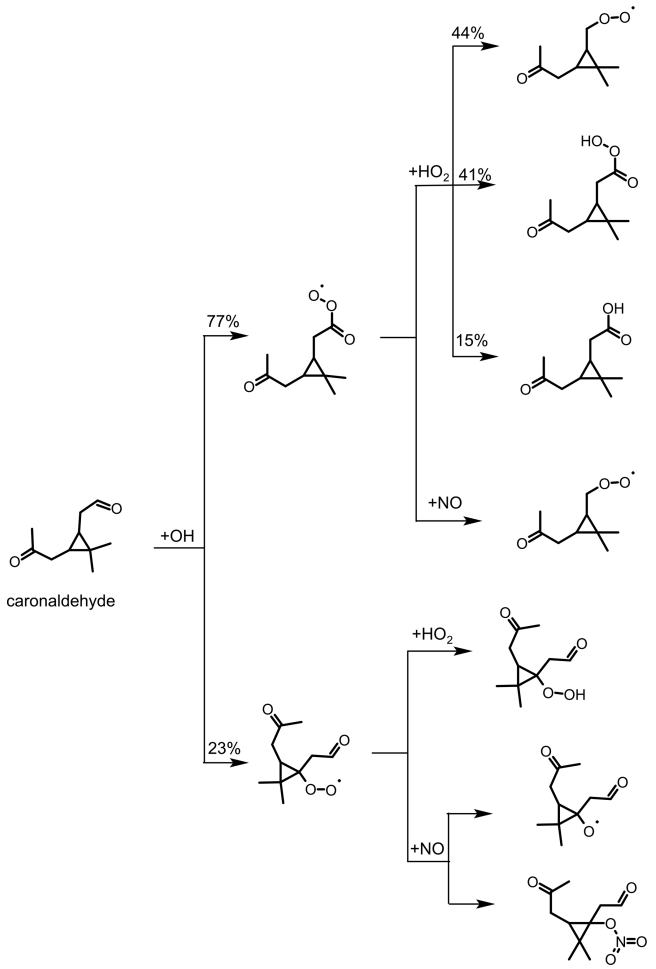

Figure 9. Simplified scheme of the first reaction steps of the OH photooxidation of caronaldehyde, adapted from the oxidation mechanism of pinonaldehyde. Yields shown in black are from SAR by Jenkin et al. (2018). Additional reactions like, for example, the formation of carbonic acids from RO_2 with HO_2 are not shown in the scheme.

3.3.2 Rate constant of the caronaldehyde + OH reaction

The measured decay of caronaldehyde was compared to the results from the box model constraining the photolysis frequency to the value with a correction by a factor of 7 calculated as explained above. The temperature inside the SAPHIR chamber was 300 K, and the OH concentration was $8 \times 10^6\,\mathrm{cm}^{-3}$. The optimum OH reaction rate constant is $(3.6 \pm 0.7) \times 10^{-11}\,\mathrm{cm}^3\,\mathrm{s}^{-1}$. The reaction rate constant was also optimized with the model constrained to the photolysis frequency as calculated with the absorption spectrum measured by Hallquist and a quantum yield of 1. This yields an OH reaction rate constant of $(5.5 \pm 0.7) \times 10^{-11}\,\mathrm{cm}^3\,\mathrm{s}^{-1}$. Both values agree reasonably well with the reaction rate constant of $(4.8 \pm 0.8) \times 10^{-11}\,\mathrm{cm}^3\,\mathrm{s}^{-1}$ measured by Alvarado et al. (1998) within the error. The structure–activity relationship by Jenkin et al. (2018) predicts a total reaction rate constant of $2.9 \times 10^{-11}\,\mathrm{cm}^3\,\mathrm{s}^{-1}$ which is consistent with the two measured values within the uncertainty

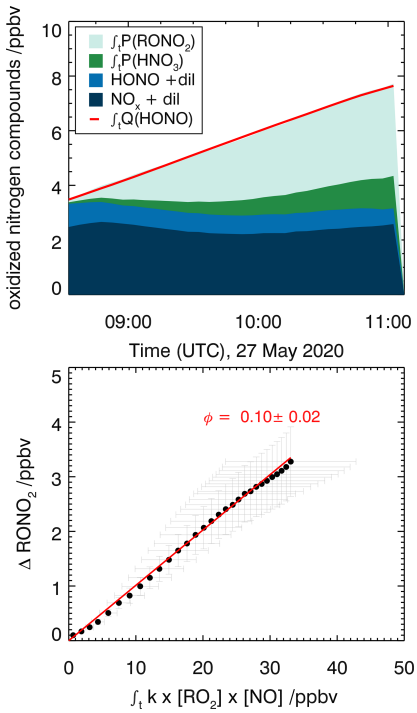

Figure 10. Determination of the organic nitrate yield for the reaction of caronaldehyde with OH for experiment E6. HONO and NO_x concentrations are measured, while $RONO_2$ and HNO_3 concentrations are calculated as described in the text.

of SAR. Hallquist et al. (1997) also determined the reaction rate constant of caronaldehyde with OH resulting in a value of $(12.1 \pm 3.6) \times 10^{-11}$ cm^3 s^{-1}. This value is significantly higher than both values reported here and by Alvarado et al. (1998). Both Alvarado et al. (1998) and Hallquist et al. (1997) determined the reaction rate constant using a relative rate technique, and both studies were performed in smaller reaction volumes than the 270 m^3 SAPHIR chamber. The measurements by Hallquist et al. (1997) were performed in a 0.153 m^3 borosilicate glass reactor, while the studies by Alvarado et al. (1998) were performed in an 7.9 m^3 Teflon chamber. Wall losses of caronaldehyde in the range of (4–7) $\times 10^{-5}$ s^{-1} were observed in the borosilicate chamber in the dark and further increased when the chamber was irradiated. Even though the determined reaction rate constant is corrected for the measured wall loss, it causes further uncertainty. Additionally, the initial caronaldehyde mixing ratio in the experiments in this work and the study performed by Alvarado et al. (1998) were significantly lower than those used by Hallquist et al. (1997) (20 ppbv, this study; 113 ppbv, Alvarado et al., 1998; 3252 ppbv, Hallquist et al., 1997). The reason for the high reaction rate constant reported by Hallquist et al. (1997) is not entirely clear, but it may arise from enhanced wall losses in the irradiated chamber unaccounted for in the experiments by Hallquist et al. (1997).

3.3.3 Determination of alkyl nitrate yields for the reaction of caronaldehyde + OH

The nitrate yield from the reaction of caronaldehyde with OH is determined for experiment E6. The organic nitrate yield Φ_{RONO_2} is found to be (10 ± 2) %, following the procedure described in Sect. 2.5. As shown in Fig. 10, 3.5 ppbv of $RONO_2$ was formed in the chamber during experiment E6 along with 1.2 ppbv of HNO_3. NO_x and HONO concentrations were 2 and 1 ppbv, respectively. The error is derived from the accuracies of measured concentrations. To our knowledge, this is the first report of a measured organic nitrate yield for the caronaldehyde + OH reaction.

Generally, the nitrate yields from aldehydes are typically smaller than those of monoterpenes. Organic nitrate yields for other aldehydes used in current chemical models like the MCM3.3.1 are 5 % for pinonaldehyde, the main daytime oxidation product of α-pinene, and 12 % for pentanal. Calculation of the organic nitrate yield from the caronaldehyde oxidation according to Jenkin et al. (2019) is 5.5 %. The value determined in this study is within the range of nitrate yields reported in the literature but somewhat higher than values reported for similar aldehydes and calculations from SAR.

3.4 Production and destruction rates of RO_x radicals in the oxidation of Δ^3-carene

Field studies in forested environments, where Δ^3-carene was one of the main monoterpenes emitted, found that both measured OH and HO_2 concentrations cannot be reproduced by models (Kim et al., 2013; Hens et al., 2014). The analysis of radical formation and loss reactions for those environments revealed that a photolytic HO_2 source missing in the model calculations is one possible explanation for the observed discrepancies. In the following, radical formation and loss rates of the sum of radicals (RO_x) and their differences are determined according to Eqs. (6) and (7). The results of this analysis for experiment E1 with NO_x mixing ratios below 1 ppbv are shown in Fig. 11.

The turnover rates in this experiment reach maximum values between 2 and 3 ppbv h^{-1}. The main radical formation process is HONO photolysis, contributing more than 70 % to the average formation rate. Assuming that the photolysis frequency is higher by a factor of 7 (see Sect. 3.3.1), the formation of one HO_2 and one RO_2 radical per photolyzed caronaldehyde molecule would have a higher influence on the radical budgets of the Δ^3-carene + OH reaction than previously assumed. This may therefore help to reduce

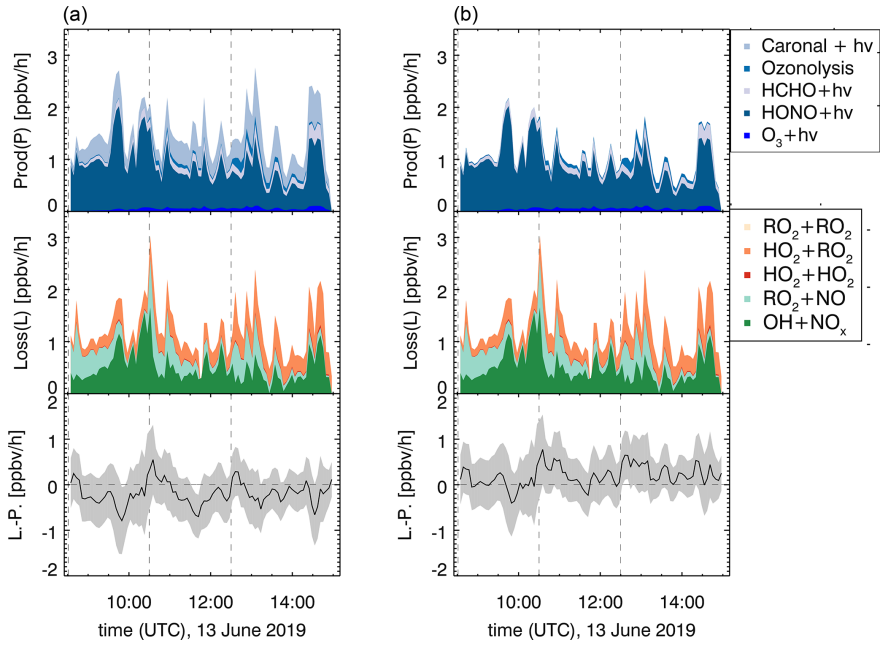

Figure 11. RO_x production and destruction rates for the OH-induced photooxidation in experiment E1, excluding **(a)** and including **(b)** the higher photolysis frequency determined in this work. Dashed lines indicate times when trace gases were injected.

the discrepancies between measured and modeled HO_2 concentrations in field studies. The photolysis of caronaldehyde contributes on average 0.3 ppbv h^{-1}; 60 % of the average loss rate is due to the reaction of RO_x with NO_x species. The remaining RO_x losses can be explained by radical self-reactions, as can be expected for the experimental conditions because the reaction of the peroxy radical with HO_2 (35 %) or RO_2 radicals becomes competitive.

For experiments with NO_x mixing ratios below 1 ppbv in the experiments in this work, the RO_x budgets are closed within the uncertainty. It can therefore be assumed that there are no primary radical production or loss processes that are unaccounted for in this analysis. The contribution of the photolysis of caronaldehyde to the radical formation is in the range of the error of the analysis, and the loss and formation of radicals would also be closed if this process was not considered. In the scope of this work, it is therefore not possible to distinguish whether the caronaldehyde photolysis will contribute significantly to reduce the previously observed discrepancies between measured and modeled HO_2 concentration in field studies. Possible reaction pathways leading to the formation and loss of radicals in the Δ^3-carene oxidation are shown in Fig. 5. The reaction of RO_2 with HO_2 proceeds with a reaction rate constant of 1.9×10^{-11} cm^3 s^{-1} (Jenkin et al., 2019), mainly leading the formation of hydroperoxide species ROOH. The reaction of RO_2 with RO_2 results in the formation of either a diol or an alkoxy radical RO, which again most likely decomposes forming caronaldehyde. The reaction rate constant of this reaction is calculated to be 1.2×10^{-13} cm^3 s^{-1} (Jenkin et al., 2019). In the experiments presented here, this reaction only contributes < 1 % to the loss of total RO_x radicals. Isomerization reactions like intramolecular H shifts as investigated by Vereecken and Noziere (2020) can form a new pathway to product formation from RO_2. For the RO_2 described here, an intramolecular 1,5-H-shift from the OH functional group to the peroxy radical unit $-OO$ would be the fastest of the possible isomerization reactions with a reaction rate constant of 3.5×10^{-5} s^{-1} expected from the SAR in (Vereecken and Noziere, 2020). Compared to the other described RO_2 loss rates, especially the loss in the reaction with NO (0.07 s^{-1} at 0.3 ppbv NO) and HO_2 (1.9×10^{-3} s^{-1} at 1.0×10^8 cm^{-3} HO_2), this isomerization reaction is too slow to be significant for atmospheric conditions like in the experiments here.

4 Summary and conclusion

The photooxidation of Δ^3-carene was investigated for NO_x mixing ratios below 1.5 ppbv in the atmospheric simulation chamber SAPHIR. Photooxidation experiments were performed under atmospheric conditions with Δ^3-carene mixing ratios in the range of 5 to 7 ppbv. In this study, the gas-phase organic nitrate yield of the Δ^3-carene + OH reaction was determined for the first time and found to be (25 ± 4) %. The comparison of the obtained organic nitrate yield to yields obtained in the aerosol phase (Rollins et al., 2010) and to the organic nitrate yield of the structurally similar monoterpene α-pinene shows that the determined value is in accordance with the reported values. The reaction rate constant of the reaction of Δ^3-carene with OH was determined to be $(8.0 \pm 0.5) \times 10^{-11}$ cm^3 s^{-1} using an absolute rate technique approach. The obtained value was found to be in good agreement with reaction rate constants reported in the literature within the stated error. Additionally, the ozonolysis of Δ^3-carene was studied. A reaction rate constant of $(4.4 \pm 0.2) \times 10^{-17}$ cm^3 s^{-1} was found, with an OH yield of 0.65 ± 0.10. The yield of the oxidation products caronaldehyde was determined for the Δ^3-carene + OH and Δ^3-carene + O_3 reactions and found to be (0.33 ± 0.03) and (0.055 ± 0.02), respectively, in good agreement with reported literature values. The photolysis and OH-induced photooxidation of caronaldehyde were also studied. The photolysis frequency was calculated using the absorption spectrum measured by Hallquist et al. (1997), but it was found that to explain the observed caronaldehyde decay the absorption cross section would need to be higher by a factor of 7 assuming a maximum quantum yield of 1. The caronaldehyde + OH reaction rate constant was found to be $(3.6 \pm 0.7) \times 10^{-11}$ cm^3 s^{-1}, in relatively good agreement with reported literature values. The experimental budget analysis of the loss and production processes of RO_x radicals for the Δ^3-carene + OH reaction shows that primary loss and production reactions are balanced within the uncertainty of the experiment of ± 0.5 ppbv h^{-1}. The formation of HO_2 and RO_2 radicals from the photolysis of caronaldehyde was considered an additional radical source with the photolysis frequency determined in this work. The contribution of the photolysis reaction to the radical formation was about 10 %. The fact that radical formation and loss reactions are well balanced indicates that there are no primary formation or loss processes unaccounted for in this analysis.

Data availability. Data from the experiments in the SAPHIR chamber used in this work are available on the EUROCHAMP data home page. 13 June 2019: https://doi.org/10.25326/BQNH-P286 (Hantschke et al., 2021a), 21 May 2020: https://doi.org/10.25326/AGPD-MP70 (Hantschke et al., 2021b), 27 May 2020: https://doi.org/10.25326/8K59-JC53 (Hantschke et al., 2021c), 30 May 2020: https://doi.org/10.25326/PXFM-3967 (Hantschke et al., 2021d), 31 May 2020: https://doi.org/10.25326/QACC-KJ83 (Hantschke et al., 2021e).

Supplement. The supplement related to this article is available online at: https://doi.org/10.5194/acp-21-12665-2021-supplement.

Author contributions. LH and HF designed the experiments. AN and CC conducted the RO_x radical measurements and the OH reactivity measurements. MG conducted the HONO measurements. RT, DR and SW were responsible for the PTR-TOF-MS and VOCUS measurements. BB conducted the radiation measurements. FR was responsible for the NO_x and O_3 data. LH analyzed the data and wrote the paper with the help of HF. All co-authors commented and discussed the article.

Competing interests. Astrid Kiendler-Scharr and Andreas Hofzumahaus are editors of *ACP*.

Disclaimer. Publisher's note: Copernicus Publications remains neutral with regard to jurisdictional claims in published maps and institutional affiliations.

Special issue statement. This article is part of the special issue "Simulation chambers as tools in atmospheric research (AMT/ACP/GMD inter-journal SI)". It is not associated with a conference.

Financial support. This research has been supported by the European Research Council, H2020 European Research Council (SARLEP (grant no. 681529)) and the European Commission, Horizon 2020 Framework Programme (EUROCHAMP-2020 (grant no. 730997)).

The article processing charges for this open-access publication were covered by the Forschungszentrum Jülich.

Review statement. This paper was edited by Hang Su and reviewed by two anonymous referees.

References

Albrecht, S. R., Novelli, A., Hofzumahaus, A., Kang, S., Baker, Y., Mentel, T., Wahner, A., and Fuchs, H.: Measurements of hydroperoxy radicals (HO_2) at atmospheric concentrations using bromide chemical ionisation mass spectrometry, Atmos. Meas. Tech., 12, 891–902, https://doi.org/10.5194/amt-12-891-2019, 2019.

Alvarado, A., Arey, J., and Atkinson, R.: Kinetics of the gas-phase reactions of OH and NO_3 radicals and O_3 with

the monoterpene reaction products pinonaldehyde, caronaldehyde, and sabinaketone, J. Atmos. Chem., 31, 281–297, https://doi.org/10.1023/a:1006010915971, 1998.

Arey, J., Atkinson, R., and Aschmann, S. M.: Product study of the gas-phase reaction of monoterpenes with the OH radical in the presence of NO_x, J. Geophys. Res.-Atmos., 95, 18539–18546, https://doi.org/10.1029/JD095iD11p18539, 1990.

Aschmann, S. M., Arey, J., and Atkinson, R.: OH radical formation from the gas-phase reactions of O_3 with a series of terpenes, Atmos. Environ., 36, 4347–4355, https://doi.org/10.1016/s1352-2310(02)00355-2, 2002a.

Aschmann, S. M., Atkinson, R., and Arey, J.: Products of reaction of OH radicals with α-pinene, J. Geophys. Res.-Atmos., 107, 7, https://doi.org/10.1029/2001jd001098, 2002b.

Atkinson, R., Aschmann, S. M., and Pitts, J. N.: Rate constants for the gas-phase reactions of the OH – radical with a series of monoterpenes (294 ± 1) K, Int. J. Chem. Kinet., 18, 287–299, https://doi.org/10.1002/kin.550180303, 1986.

Atkinson, R., Hasegawa, D., and Aschmann, S. M.: Rate constants for the gas-phase reactions of O_3 with a series of monoterpenes and related compounds at 296 ± 2 K, Int. J. Chem. Kinet., 22, 871–887, https://doi.org/10.1002/kin.550220807, 1990.

Atkinson, R., Aschmann, S. M., Arey, J., and Shorees, B.: Formation of OH radicals in the gas-phase reaction of O_3 with a series of terpenes, J. Geophys. Res.-Atmos., 97, 6065–6073, https://doi.org/10.1029/92jd00062, 1992.

Atkinson, R., Baulch, D. L., Cox, R. A., Crowley, J. N., Hampson, R. F., Hynes, R. G., Jenkin, M. E., Rossi, M. J., and Troe, J.: Evaluated kinetic and photochemical data for atmospheric chemistry: Volume I - gas phase reactions of O_x, HO_x, NO_x and SO_x species, Atmos. Chem. Phys., 4, 1461–1738, https://doi.org/10.5194/acp-4-1461-2004, 2004.

Berndt, T., Boge, O., and Stratmann, F.: Gas-phase ozonolysis of α-pinene: gaseous products and particle formation, Atmos. Environ., 37, 3933–3945, https://doi.org/10.1016/s1352-2310(03)00501-6, 2003.

Bohn, B. and Zilken, H.: Model-aided radiometric determination of photolysis frequencies in a sunlit atmosphere simulation chamber, Atmos. Chem. Phys., 5, 191–206, https://doi.org/10.5194/acp-5-191-2005, 2005.

Bohn, B., Rohrer, F., Brauers, T., and Wahner, A.: Actinometric measurements of NO_2 photolysis frequencies in the atmosphere simulation chamber SAPHIR, Atmos. Chem. Phys., 5, 493–503, https://doi.org/10.5194/acp-5-493-2005, 2005.

Burkholder, J. B., Sander, S. P., Abbatt, J., Barker, J. R., Cappa, C., Crounse, J. D., Dibble, T. S., Huie, R. E., Kolb, C. E., Kurylo, M. J., Orkin, V. L., Percival, C. J., Wilmouth, D. M., and Wine, P. H.: Chemical Kinetics and Photochemical Data for Use in Atmospheric Studies, Evaluation No. 19, JPL Publication 19-5, Jet Propulsion Laboratory, Pasadena, available at: http://jpldataeval.jpl.nasa.gov/ (last access: 16 April 2021), 2020.

Butkovskaya, N., Kukui, A., and Le Bras, G.: Pressure and Temperature Dependence of Methyl Nitrate Formation in the $CH_3O_2 + NO$ Reaction, J. Phys. Chem. A, 116, 5972–5980, https://doi.org/10.1021/jp210710d, 2012.

Chen, H., Ren, Y., Cazaunau, M., Daële, V., Hua, Y., Chena, J., and Mellouki, A.: Rate coefficients for the reaction of ozone with 2- and 3-carene, Chem. Phys. Lett., 621, 71–77, https://doi.org/10.1016/j.cplett.2014.12.056, 2015.

Colville, C. J. and Griffin, R. J.: The roles of individual oxidants in secondary organic aerosol formation from Δ-3-carene: 1. gas-phase chemical mechanism, Atmos. Environ., 38, 4001–4012, https://doi.org/10.1016/j.atmosenv.2004.03.064, 2004.

Dillon, T. J., Dulitz, K., Groß, C. B. M., and Crowley, J. N.: Temperature-dependent rate coefficients for the reactions of the hydroxyl radical with the atmospheric biogenics isoprene, alpha-pinene and delta-3-carene, Atmos. Chem. Phys., 17, 15137–15150, https://doi.org/10.5194/acp-17-15137-2017, 2017.

Draper, D. C., Myllys, N., Hyttinen, N., Moller, K. H., Kjaergaard, H. G., Fry, J. L., Smith, J. N., and Kurten, T.: Formation of Highly Oxidized Molecules from NO_3 Radical Initiated Oxidation of Δ-3-Carene: A Mechanistic Study, ACS Earth Space Chem., 3, 1460–1470, https://doi.org/10.1021/acsearthspacechem.9b00143, 2019.

Eddingsaas, N. C., Loza, C. L., Yee, L. D., Seinfeld, J. H., and Wennberg, P. O.: α-pinene photooxidation under controlled chemical conditions – Part 1: Gas-phase composition in low- and high$-NO_x$ environments, Atmos. Chem. Phys., 12, 6489–6504, https://doi.org/10.5194/acp-12-6489-2012, 2012.

Farmer, D. K., Perring, A. E., Wooldridge, P. J., Blake, D. R., Baker, A., Meinardi, S., Huey, L. G., Tanner, D., Vargas, O., and Cohen, R. C.: Impact of organic nitrates on urban ozone production, Atmos. Chem. Phys., 11, 4085–4094, https://doi.org/10.5194/acp-11-4085-2011, 2011.

Fuchs, H., Holland, F., and Hofzumahaus, A.: Measurement of tropospheric RO_2 and HO_2 radicals by a laser-induced fluorescence instrument, Rev. Sci. Instrum., 79, 12, https://doi.org/10.1063/1.2968712, 2008.

Fuchs, H., Bohn, B., Hofzumahaus, A., Holland, F., Lu, K. D., Nehr, S., Rohrer, F., and Wahner, A.: Detection of HO_2 by laser-induced fluorescence: calibration and interferences from RO_2 radicals, Atmos. Meas. Tech., 4, 1209–1225, https://doi.org/10.5194/amt-4-1209-2011, 2011.

Fuchs, H., Novelli, A., Rolletter, M., Hofzumahaus, A., Pfannerstill, E. Y., Kessel, S., Edtbauer, A., Williams, J., Michoud, V., Dusanter, S., Locoge, N., Zannoni, N., Gros, V., Truong, F., Sarda-Esteve, R., Cryer, D. R., Brumby, C. A., Whalley, L. K., Stone, D., Seakins, P. W., Heard, D. E., Schoemaecker, C., Blocquet, M., Coudert, S., Batut, S., Fittschen, C., Thames, A. B., Brune, W. H., Ernest, C., Harder, H., Muller, J. B. A., Elste, T., Kubistin, D., Andres, S., Bohn, B., Hohaus, T., Holland, F., Li, X., Rohrer, F., Kiendler-Scharr, A., Tillmann, R., Wegener, R., Yu, Z., Zou, Q., and Wahner, A.: Comparison of OH reactivity measurements in the atmospheric simulation chamber SAPHIR, Atmos. Meas. Tech., 10, 4023–4053, https://doi.org/10.5194/amt-10-4023-2017, 2017a.

Fuchs, H., Tan, Z., Lu, K., Bohn, B., Broch, S., Brown, S. S., Dong, H., Gomm, S., Häseler, R., He, L., Hofzumahaus, A., Holland, F., Li, X., Liu, Y., Lu, S., Min, K.-E., Rohrer, F., Shao, M., Wang, B., Wang, M., Wu, Y., Zeng, L., Zhang, Y., Wahner, A., and Zhang, Y.: OH reactivity at a rural site (Wangdu) in the North China Plain: contributions from OH reactants and experimental OH budget, Atmos. Chem. Phys., 17, 645–661, https://doi.org/10.5194/acp-17-645-2017, 2017b.

Galloway, M. M., Huisman, A. J., Yee, L. D., Chan, A. W. H., Loza, C. L., Seinfeld, J. H., and Keutsch, F. N.: Yields of oxidized volatile organic compounds during the OH radical initiated oxidation of isoprene, methyl vinyl ketone, and methacrolein under

high−NO_x conditions, Atmos. Chem. Phys., 11, 10779–10790, https://doi.org/10.5194/acp-11-10779-2011, 2011.

Geron, C., Rasmussen, R., Arnts, R. R., and Guenther, A.: A review and synthesis of monoterpene speciation from forests in the United States, Atmos. Environ., 34, 1761–1781, https://doi.org/10.1016/s1352-2310(99)00364-7, 2000.

Glowania, M., Rohrer, F., Dorn, H.-P., Hofzumahaus, A., Holland, F., Kiendler-Scharr, A., Wahner, A., and Fuchs, H.: Comparison of formaldehyde measurements by Hantzsch, CRDS and DOAS in the SAPHIR chamber, Atmos. Meas. Tech., 14, 4239–4253, https://doi.org/10.5194/amt-14-4239-2021, 2021.

Guenther, A. B., Jiang, X., Heald, C. L., Sakulyanontvittaya, T., Duhl, T., Emmons, L. K., and Wang, X.: The Model of Emissions of Gases and Aerosols from Nature version 2.1 (MEGAN2.1): an extended and updated framework for modeling biogenic emissions, Geosci. Model Dev., 5, 1471–1492, https://doi.org/10.5194/gmd-5-1471-2012, 2012.

Hakola, H., Arey, J., Aschmann, S. M., and Atkinson, R.: Product formation from the gas-phase reactions of OH radicals and O_3 with a series of monoterpenes, J. Atmos. Chem., 18, 75–102, https://doi.org/10.1007/bf00694375, 1994.

Hakola, H., Hellén, H., Hemmilä, M., Rinne, J., and Kulmala, M.: In situ measurements of volatile organic compounds in a boreal forest, Atmos. Chem. Phys., 12, 11665–11678, https://doi.org/10.5194/acp-12-11665-2012, 2012.

Hallquist, M., Wangberg, I., and Ljungstrom, E.: Atmospheric fate of carbonyl oxidation products originating from α-pinene and Δ-(3)-carene: Determination of rate of reaction with OH and NO_3radicals, UV absorption cross sections, and vapor pressures, Environ. Sci. Technol., 31, 3166–3172, https://doi.org/10.1021/es970151a, 1997.

Hantschke, L., Fuchs, H., Novelli, A., Bohn, B., Cho, C., Reimer, D., Rohrer, F., Tillmann, R., and Glowania, M.: Atmospheric simulation chamber study: delta-carene + OH – Gas-phase oxidation – product study, AERIS [data set], https://doi.org/10.25326/BQNH-P286, 2021a.

Hantschke, L., Fuchs, H., Novelli, A., Bohn, B., Cho, C., Reimer, D., Rohrer, F., Tillmann, R., and Glowania, M.: Atmospheric simulation chamber study: delta-carene + OH – Gas-phase oxidation – product study, AERIS [data set], https://doi.org/10.25326/AGPD-MP70, 2021b.

Hantschke, L., Fuchs, H., Novelli, A., Bohn, B., Cho, C., Reimer, D., Rohrer, F., Tillmann, R., and Glowania, M.: Atmospheric simulation chamber study: caronaldehyde + OH – Gas-phase oxidation – product study, AERIS [data set], https://doi.org/10.25326/8K59-JC53, 2021c.

Hantschke, L., Fuchs, H., Novelli, A., Bohn, B., Cho, C., Reimer, D., Rohrer, F., Tillmann, R., and Glowania, M.: Atmospheric simulation chamber study: caronaldehyde + OH – Gas-phase oxidation – product study, AERIS [data set], https://doi.org/10.25326/PXFM-3967, 2021d.

Hantschke, L., Fuchs, H., Novelli, A., Bohn, B., Cho, C., Reimer, D., Rohrer, F., Tillmann, R., and Glowania, M.: Atmospheric simulation chamber study: delta-carene + OH – Gas-phase oxidation – product study, AERIS [data set], https://doi.org/10.25326/QACC-KJ83, 2021e.

Hens, K., Novelli, A., Martinez, M., Auld, J., Axinte, R., Bohn, B., Fischer, H., Keronen, P., Kubistin, D., Nölscher, A. C., Oswald, R., Paasonen, P., Petäjä, T., Regelin, E., Sander, R., Sinha, V., Sipilä, M., Taraborrelli, D., Tatum Ernest, C., Williams, J., Lelieveld, J., and Harder, H.: Observation and modelling of HO_x radicals in a boreal forest, Atmos. Chem. Phys., 14, 8723–8747, https://doi.org/10.5194/acp-14-8723-2014, 2014.

Holland, F., Hessling, M., and Hofzumahaus, A.: In-situ measurement of tropospheric OH radicals by laser-induced fluorescence – a description of the KFA instrument, J. Atmos. Sci., 52, 3393–3401, https://doi.org/10.1175/1520-0469(1995)052<3393:Ismoto>2.0.Co;2, 1995.

Jenkin, M. E., Valorso, R., Aumont, B., Rickard, A. R., and Wallington, T. J.: Estimation of rate coefficients and branching ratios for gas-phase reactions of OH with aliphatic organic compounds for use in automated mechanism construction, Atmos. Chem. Phys., 18, 9297–9328, https://doi.org/10.5194/acp-18-9297-2018, 2018.

Jenkin, M. E., Valorso, R., Aumont, B., and Rickard, A. R.: Estimation of rate coefficients and branching ratios for reactions of organic peroxy radicals for use in automated mechanism construction, Atmos. Chem. Phys., 19, 7691–7717, https://doi.org/10.5194/acp-19-7691-2019, 2019.

Jenkin, M. E., Valorso, R., Aumont, B., Newland, M. J., and Rickard, A. R.: Estimation of rate coefficients for the reactions of O_3 with unsaturated organic compounds for use in automated mechanism construction, Atmos. Chem. Phys., 20, 12921–12937, https://doi.org/10.5194/acp-20-12921-2020, 2020.

Kaminski, M., Fuchs, H., Acir, I.-H., Bohn, B., Brauers, T., Dorn, H.-P., Häseler, R., Hofzumahaus, A., Li, X., Lutz, A., Nehr, S., Rohrer, F., Tillmann, R., Vereecken, L., Wegener, R., and Wahner, A.: Investigation of the β-pinene photooxidation by OH in the atmosphere simulation chamber SAPHIR, Atmos. Chem. Phys., 17, 6631–6650, https://doi.org/10.5194/acp-17-6631-2017, 2017.

Kim, S., Wolfe, G. M., Mauldin, L., Cantrell, C., Guenther, A., Karl, T., Turnipseed, A., Greenberg, J., Hall, S. R., Ullmann, K., Apel, E., Hornbrook, R., Kajii, Y., Nakashima, Y., Keutsch, F. N., DiGangi, J. P., Henry, S. B., Kaser, L., Schnitzhofer, R., Graus, M., Hansel, A., Zheng, W., and Flocke, F. F.: Evaluation of HO_x sources and cycling using measurement-constrained model calculations in a 2-methyl-3-butene-2-ol (MBO) and monoterpene (MT) dominated ecosystem, Atmos. Chem. Phys., 13, 2031–2044, https://doi.org/10.5194/acp-13-2031-2013, 2013.

Kleffmann, J., Heland, J., Kurtenbach, R., Lorzer, J., and Wiesen, P.: A new instrument (LOPAP) for the detection of nitrous acid (HONO), Environ. Sci. Pollut. R., 4, 48–54, 2002.

Komenda, M. and Koppmann, R.: Monoterpene emissions from Scots pine (*Pinus sylvestris*): Field studies of emission rate variabilities, J. Geophys. Res.-Atmos., 107, 13, https://doi.org/10.1029/2001jd000691, 2002.

Larsen, B. R., Di Bella, D., Glasius, M., Winterhalter, R., Jensen, N. R., and Hjorth, J.: Gas-phase OH oxidation of monoterpenes: Gaseous and particulate products, J. Atmos. Chem., 38, 231–276, https://doi.org/10.1023/a:1006487530903, 2001.

Li, X., Rohrer, F., Hofzumahaus, A., Brauers, T., Haseler, R., Bohn, B., Broch, S., Fuchs, H., Gomm, S., Holland, F., Jager, J., Kaiser, J., Keutsch, F. N., Lohse, I., Lu, K. D., Tillmann, R., Wegener, R., Wolfe, G. M., Mentel, T. F., Kiendler-Scharr, A., and Wahner, A.: Missing Gas-Phase Source of HONO Inferred from

Zeppelin Measurements in the Troposphere, Science, 344, 292–296, https://doi.org/10.1126/science.1248999, 2014.

Lou, S., Holland, F., Rohrer, F., Lu, K., Bohn, B., Brauers, T., Chang, C. C., Fuchs, H., Häseler, R., Kita, K., Kondo, Y., Li, X., Shao, M., Zeng, L., Wahner, A., Zhang, Y., Wang, W., and Hofzumahaus, A.: Atmospheric OH reactivities in the Pearl River Delta – China in summer 2006: measurement and model results, Atmos. Chem. Phys., 10, 11243–11260, https://doi.org/10.5194/acp-10-11243-2010, 2010.

Ma, Y., Porter, R. A., Chappell, D., Russell, A. T., and Marston, G.: Mechanisms for the formation of organic acids in the gas-phase ozonolysis of 3-carene, Phys. Chem. Chem. Phys., 11, 4184–4197, 2009.

Moller, K. H., Otkjaer, R. V., Chen, J., and Kjaergaard, H. G.: Double Bonds Are Key to Fast Unimolecular Reactivity in First-Generation Monoterpene Hydroxy Peroxy Radicals, J. Phys. Chem. A, 124, 2885–2896, https://doi.org/10.1021/acs.jpca.0c01079, 2020.

Noziere, B., Barnes, I., and Becker, K. H.: Product study and mechanisms of the reactions of α-pinene and of pinonaldehyde with OH radicals, J. Geophys. Res.-Atmos., 104, 23645–23656, https://doi.org/10.1029/1999jd900778, 1999.

Orlando, J. J., Noziere, B., Tyndall, G. S., Orzechowska, G. E., Paulson, S. E., and Rudich, Y.: Product studies of the OH- and ozone-initiated oxidation of some monoterpenes, J. Geophys. Res.-Atmos., 105, 11561–11572, https://doi.org/10.1029/2000jd900005, 2000.

Peeters, J., Vereecken, L., and Fantechi, G.: The detailed mechanism of the OH-initiated atmospheric oxidation of α-pinene: a theoretical study, Phys. Chem. Chem. Phys., 3, 5489–5504, https://doi.org/10.1039/b106555f, 2001.

Peeters, J., Boullart, W., Pultau, V., Vandenberk, S., and Vereecken, L.: Structure-activity relationship for the addition of OH to (poly)alkenes: Site-specific and total rate constants, J. Phys. Chem. A, 111, 1618–1631, https://doi.org/10.1021/jp066973o, 2007.

Reissell, A., Harry, C., Aschmann, S. M., Atkinson, R., and Arey, J.: Formation of acetone from the OH radical- and O_3-initiated reactions of a series of monoterpenes, J. Geophys. Res.-Atmos., 104, 13869–13879, https://doi.org/10.1029/1999jd900198, 1999.

Rindelaub, J. D., McAvey, K. M., and Shepson, P. B.: The photochemical production of organic nitrates from α-pinene and loss via acid-dependent particle phase hydrolysis, Atmos. Environ., 100, 193–201, https://doi.org/10.1016/j.atmosenv.2014.11.010, 2015.

Roberts, J. M. and Fajer, R. W.: UV absorption cross sections of organic nitrates of potential atmospheric importance and estimation of atmospheric lifetimes, Environ. Sci. Technol., 23, 945–951, https://doi.org/10.1021/es00066a003, 1989.

Rohrer, F., Bohn, B., Brauers, T., Brüning, D., Johnen, F.-J., Wahner, A., and Kleffmann, J.: Characterisation of the photolytic HONO-source in the atmosphere simulation chamber SAPHIR, Atmos. Chem. Phys., 5, 2189–2201, https://doi.org/10.5194/acp-5-2189-2005, 2005.

Rolletter, M., Kaminski, M., Acir, I.-H., Bohn, B., Dorn, H.-P., Li, X., Lutz, A., Nehr, S., Rohrer, F., Tillmann, R., Wegener, R., Hofzumahaus, A., Kiendler-Scharr, A., Wahner, A., and Fuchs, H.: Investigation of the α-pinene photooxidation by OH in the atmospheric simulation chamber SAPHIR, Atmos. Chem. Phys., 19, 11635–11649, https://doi.org/10.5194/acp-19-11635-2019, 2019.

Rollins, A. W., Smith, J. D., Wilson, K. R., and Cohen, R. C.: Real Time In Situ Detection of Organic Nitrates in Atmospheric Aerosols, Environ. Sci. Technol., 44, 5540–5545, https://doi.org/10.1021/es100926x, 2010.

Rollins, A. W., Pusede, S., Wooldridge, P., Min, K. E., Gentner, D. R., Goldstein, A. H., Liu, S., Day, D. A., Russell, L. M., Rubitschun, C. L., Surratt, J. D., and Cohen, R. C.: Gas/particle partitioning of total alkyl nitrates observed with TD-LIF in Bakersfield, J. Geophys. Res.-Atmos., 118, 6651–6662, https://doi.org/10.1002/jgrd.50522, 2013.

Scholtens, K. W., Messer, B. M., Cappa, C. D., and Elrod, M. J.: Kinetics of the $CH_3O_2 + NO$ reaction: Temperature dependence of the overall rate constant and an improved upper limit for the CH_3ONO_2 branching channel, J. Phys. Chem. A, 103, 4378–4384, https://doi.org/10.1021/jp990469k, 1999.

Seinfeld, J. H. and Pandis, S. N.: Atmospheric Chemistry and Physics From Air Pollution to Climate Change, John Wiley and Sons, Inc., Hoboken, New Jersey, 2nd edn., 2006.

Vereecken, L. and Nozière, B.: H migration in peroxy radicals under atmospheric conditions, Atmos. Chem. Phys., 20, 7429–7458, https://doi.org/10.5194/acp-20-7429-2020, 2020.

Wang, L. Y., Liu, Y. H., and Wang, L. M.: Ozonolysis of 3-carene in the atmosphere. Formation mechanism of hydroxyl radical and secondary ozonides, Phys. Chem. Chem. Phys., 21, 8081–8091, https://doi.org/10.1039/c8cp07195k, 2019.

Witter, M., Berndt, T., Boge, O., Stratmann, F., and Heintzenberg, J.: Gas-phase ozonolysis: Rate coefficients for a series of terpenes and rate coefficients and OH yields for 2-methyl-2-butene and 2,3-dimethyl-2-butene, Int. J. Chem. Kinet., 34, 394–403, https://doi.org/10.1002/kin.10063, 2002.

Yokouchi, Y. and Ambe, Y.: Aersols formed from the chemical reaction of monoterpenes and ozone, Atmos. Environ., 19, 1271–1276, https://doi.org/10.1016/0004-6981(85)90257-4, 1985.

Yu, J. Z., Cocker, D. R., Griffin, R. J., Flagan, R. C., and Seinfeld, J. H.: Gas-phase ozone oxidation of monoterpenes: Gaseous and particulate products, J. Atmos. Chem., 34, 207–258, https://doi.org/10.1023/a:1006254930583, 1999.

Zhang, H. F., Yee, L. D., Lee, B. H., Curtis, M. P., Worton, D. R., Isaacman-VanWertz, G., Offenberg, J. H., Lewandowski, M., Kleindienst, T. E., Beaver, M. R., Holder, A. L., Lonneman, W. A., Docherty, K. S., Jaoui, M., Pye, H. O. T., Hu, W. W., Day, D. A., Campuzano-Jost, P., Jimenez, J. L., Guo, H. Y., Weber, R. J., de Gouw, J., Koss, A. R., Edgerton, E. S., Brune, W., Mohr, C., Lopez-Hilfiker, F. D., Lutz, A., Kreisberg, N. M., Spielman, S. R., Hering, S. V., Wilson, K. R., Thornton, J. A., and Goldstein, A. H.: Monoterpenes are the largest source of summertime organic aerosol in the southeastern United States, P. Natl. Acad. Sci. USA, 115, 2038–2043, https://doi.org/10.1073/pnas.1717513115, 2018.

6 Photooxidation of myrcene

The content of this chapter was published as "Atmospheric photo-oxidation of myrcene: OH reaction rate constant, gas-phase oxidation products and radical budgets" by Z. Tan, L. Hantschke, M. Kaminski, I.-H. Acir, B. Bohn1, C. Cho, H.-P. Dorn, X. Li, A. Novelli, S. Nehr, F. Rohrer, R. Tillmann, R. Wegener, A. Hofzumahaus, A. Kiendler-Scharr, A. Wahner, and H. Fuchs in Atmospheric Chemistry and Physics, 21, 16067–16091, https://doi.org/10.5194/acp-21-16067-2021, 2021, under the Creative Commons Attribution 4.0 License. The Supplementary material is provided in Appendix A.2.

Atmos. Chem. Phys., 21, 16067–16091, 2021
https://doi.org/10.5194/acp-21-16067-2021

Atmospheric Chemistry and Physics
Open Access
EGU

Atmospheric photo-oxidation of myrcene: OH reaction rate constant, gas-phase oxidation products and radical budgets

Zhaofeng Tan[1], Luisa Hantschke[1], Martin Kaminski[1,a], Ismail-Hakki Acir[1,b], Birger Bohn[1], Changmin Cho[1], Hans-Peter Dorn[1], Xin Li[1,c], Anna Novelli[1], Sascha Nehr[1,d], Franz Rohrer[1], Ralf Tillmann[1], Robert Wegener[1], Andreas Hofzumahaus[1], Astrid Kiendler-Scharr[1], Andreas Wahner[1], and Hendrik Fuchs[1]

[1]Institute of Energy and Climate Research, Troposphere (IEK-8), Forschungszentrum Jülich GmbH, Jülich, Germany
[a]now at: Department 5 – Method Standardisation, Reference Laboratories, Resistance to Antibiotics, Federal Office of Consumer Protection and Food Safety, Berlin, Germany
[b]now at: Institute of Nutrition and Food Sciences, Food Science, University of Bonn, Bonn, Germany
[c]now at: State Key Joint Laboratory of Environmental Simulation and Pollution Control, College of Environmental Sciences and Engineering, Peking University, Beijing, China
[d]now at: European University of Applied Sciences, Brühl, Germany

Correspondence: Hendrik Fuchs (h.fuchs@fz-juelich.de)

Received: 1 July 2021 – Discussion started: 20 July 2021
Revised: 27 September 2021 – Accepted: 3 October 2021 – Published: 29 October 2021

Abstract. The photo-oxidation of myrcene, a monoterpene species emitted by plants, was investigated at atmospheric conditions in the outdoor simulation chamber SAPHIR (Simulation of Atmospheric PHotochemistry In a Large Reaction Chamber). The chemical structure of myrcene consists of one moiety that is a conjugated π system (similar to isoprene) and another moiety that is a triple-substituted olefinic unit (similar to 2-methyl-2-butene). Hydrogen shift reactions of organic peroxy radicals (RO_2) formed in the reaction of isoprene with atmospheric OH radicals are known to be of importance for the regeneration of OH. Structure–activity relationships (SARs) suggest that similar hydrogen shift reactions like in isoprene may apply to the isoprenyl part of RO_2 radicals formed during the OH oxidation of myrcene. In addition, SAR predicts further isomerization reactions that would be competitive with bimolecular RO_2 reactions for chemical conditions that are typical for forested environments with low concentrations of nitric oxide. Assuming that OH peroxy radicals can rapidly interconvert by addition and elimination of O_2 like in isoprene, bulk isomerization rate constants of 0.21 and 0.097 s^{-1} ($T = 298$ K) for the three isomers resulting from the 3′-OH and 1-OH addition, respectively, can be derived from SAR. Measurements of radicals and trace gases in the experiments allowed us to calculate radical production and destruction rates, which are expected to be balanced. The largest discrepancies between production and destruction rates were found for RO_2. Additional loss of organic peroxy radicals due to isomerization reactions could explain the observed discrepancies. The uncertainty of the total radical ($RO_x = OH + HO_2 + RO_2$) production rates was high due to the uncertainty in the yield of radicals from myrcene ozonolysis. However, results indicate that radical production can only be balanced if the reaction rate constant of the reaction between hydroperoxy (HO_2) and RO_2 radicals derived from myrcene is lower (0.9 to 1.6×10^{-11} cm^3 s^{-1}) than predicted by SAR. Another explanation of the discrepancies would be that a significant fraction of products (yield: 0.3 to 0.6) from these reactions include OH and HO_2 radicals instead of radical-terminating organic peroxides. Experiments also allowed us to determine the yields of organic oxidation products acetone (yield: 0.45 ± 0.08) and formaldehyde (yield: 0.35 ± 0.08). Acetone and formaldehyde are produced from different oxidation pathways, so that yields of these compounds reflect the branching ratios of the initial OH addition to myrcene. Yields determined in the experiments are consistent with branching ratios expected from SAR. The yield of organic nitrate was determined from the gas-phase budget analysis of reactive oxidized nitrogen in the chamber, giving a value of 0.13 ± 0.03. In addition, the reaction rate constant for myrcene + OH was determined from

Published by Copernicus Publications on behalf of the European Geosciences Union.

the measured myrcene concentration, yielding a value of $(2.3 \pm 0.3) \times 10^{-10}$ cm^3 s^{-1}.

1 Introduction

Monoterpenes are emitted from vegetation accounting for approximately 160 Tg of the 1000 Tg of biogenic volatile organic compounds (VOCs) that are released into the atmosphere per year (Guenther et al., 2012; Sindelarova et al., 2014). Monoterpenes are highly reactive to the major oxidants in the atmosphere, hydroxyl radicals (OH), ozone (O_3), and nitrate radicals (NO_3) (Atkinson and Arey, 2003) and thus play an important role in ozone and secondary organic aerosol formation (Xu et al., 2015; Zhang et al., 2018; Schwantes et al., 2020).

Myrcene emissions contribute to the total biogenic monoterpene emissions in the range of 2 % to 10 % (Guenther et al., 2012). Emission rates highly depend on the type of tree and season of the year (Helmig et al., 2013). In addition, there are hints for anthropogenic sources from the analysis of the composition of indoor air (Kostiainen, 1995). Few studies have been conducted to investigate the oxidation of myrcene (Deng et al., 2018; Atkinson, 1997; Reissell et al., 2002; Kim et al., 2011). In these studies, acetone, formaldehyde and 4-vinyl-pentenal have been identified as major oxidation products from the reaction of myrcene with OH, but yields determined in these studies vary. Lee et al. (2006) reported an organic nitrate yield of 10 % from the oxidation of myrcene by direct measurements using mass spectrometry. The reaction rate constant of myrcene + OH was determined to be $(2.1 \pm 0.2) \times 10^{-10}$ (Atkinson et al., 1986) and $(3.4^{+1.5}_{-1.0}) \times 10^{-10}$ (Hites and Turner, 2009) at room temperature, with a discrepancy of up to 60 %. These results demonstrate the photo-oxidation of myrcene requires further investigation.

There is no detailed chemical mechanism of myrcene degradation by OH in the literature. The acyclic structure of myrcene consists of two parts: an isoprenyl part (CH_2=CH−C(=CH_2)CH_2−moiety) and another part that is structurally similar to 2-methyl-2-butene ((CH_3)$_2$C=CH−CH_2−moiety) (Fig. 1). Recent investigations of the oxidation of isoprene (Fuchs et al., 2013; Peeters et al., 2014; Wennberg et al., 2018; Novelli et al., 2020) revealed that organic peroxy radicals (RO_2) formed after the attack of OH to isoprene can rapidly interconvert, so that fast H-atom migration reactions of specific RO_2 isomers with initially low yield can significantly gain in importance. These reactions impact atmospheric chemistry most if they become competitive with bimolecular loss reactions such as reactions with nitric oxide (NO) and hydroperoxy radicals (HO_2). In the case of isoprene, these isomerization reactions can eventually regenerate OH radicals, so that a high OH regeneration efficiency of 0.5 can be sustained in the atmosphere also in regions where radical termination reactions have been thought to dominate the fate of radicals (Novelli et al., 2020). Therefore, radical regeneration from isomerization reactions helped partly to explain observations of unexpectedly high OH concentrations in field experiments (Lelieveld et al., 2008; Hofzumahaus et al., 2009; Whalley et al., 2011). Radical regeneration from RO_2 isomerization reactions has also been shown to play a role in the oxidation of methacrolein (Fuchs et al., 2014; Crounse et al., 2012), 3-pentanone (Crounse et al., 2013), glyoxal (Lockhart et al., 2013), *n*-hexane and 2-hexanol (Praske et al., 2018), hydroxymethyl hydroperoxides (Allen et al., 2018), and 2-hydroperoxy-2-methylpentane (Praske et al., 2019).

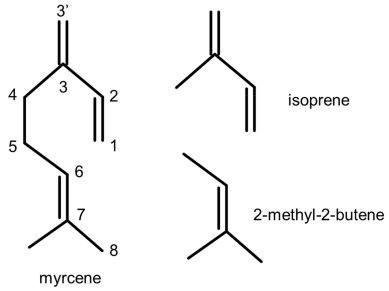

Figure 1. Chemical structures of myrcene, isoprene and 2-methyl-2-butene.

In this study, the oxidation of myrcene by OH was investigated in the atmospheric simulation chamber SAPHIR (Simulation of Atmospheric PHotochemistry In a Large Reaction Chamber) at Forschungszentrum Jülich. Experiments were performed under controlled conditions with concentrations of trace gases and radicals typical for atmospheric conditions. Experiments aim for adding to the determination of a degradation mechanism for myrcene.

2 Oxidation mechanism of myrcene

Myrcene is an acyclic hydrocarbon with three unsaturated carbon double bonds to which OH preferentially adds. One end of the myrcene molecule is structurally similar to isoprene, and the other end is similar to 2-methyl-2-butene (Fig. 1). The myrcene oxidation by OH forms 10 isomers of peroxy radicals (MyO_2) (Fig. 2). Structure–activity relationships (SARs) by Peeters et al. (2007) suggest that OH preferably adds to the double bond of the isolated −CH=C(CH_3)$_2$ moiety producing two peroxy radical species with yields of 17 % (7-OH-6-OO radical) and 31 % (6-OH-7-OO radical) (Fig. 2). When OH adds to the conjugated carbon double bonds, six isomeric hydroxy peroxy radicals are formed like in the OH or NO_3 oxidation of isoprene (Peeters et al., 2009, 2014; Vereecken et al., 2021). Addition to the $C_{3'}$ po-

sition yields two allyl-like hydroxy radical isomers producing E-3′-OH-1-OO, 3′-OH-3-OO and Z-3′-OH-1-OO peroxy radicals after the subsequent addition of O_2. A total yield of 31 % is estimated by SAR (Peeters et al., 2007) for these three isomers. Similarly, OH addition to the C_1 position followed by addition of O_2 to the allyl radical structure leads to the formation of E-1-OH-3′-OO, 1-OH-2-OO and Z-1-OH-3′-OO radicals with a total yield of 17 %. In the isoprene mechanism developed by Peeters et al. (2009, 2014), Novelli et al. (2020) and Vereecken et al. (2021), a central element is the fast interconversion reactions between the OH adducts and corresponding OH peroxy radicals that proceed by addition and elimination of O_2. Similar reactions are expected for the isoprene structure in myrcene (Fig. 2) establishing a coupled equilibrium between MyO_2 isomers.

For OH attack on the C_2 or C_3 position of myrcene, the resulting OH adducts are not resonance stabilized and are hence not as favourable as the allylic-type radicals produced from C_1 or $C_{3'}$ addition. Yields of these MyO_2 radicals are expected to be less than 2 %, and therefore the chemistry of these two minor isomers is not further discussed in this work.

All MyO_2 isomers can undergo bimolecular reactions with NO, HO_2 and other RO_2 species. Specific reaction rate constants have not been measured, but values are expected to be within the range of typical rate constants for organic peroxy radicals. For example, SAR by Jenkin et al. (2019) suggests a value of 2.2×10^{-11} cm^3 s^{-1} ($T = 298$ K) of the reaction rate constants for the reaction of monoterpene-derived RO_2 (including MyO_2) with HO_2. Reaction products of the reaction of RO_2 with HO_2 are expected to be organic peroxides.

The reaction of the 6-OH-7-OO and 7-OH-6-OO radicals with NO produces mainly 4-vinyl-4-pentenal, acetone and HO_2 (Fig. 3) as shown in experimental studies (Orlando et al., 2000; Reissell et al., 2002; Lee et al., 2006) as well as predicted by SAR (Vereecken and Peeters, 2009, 2010). Reissell et al. (2002) and Lee et al. (2006) suggested additional pathways for the alkoxy radical that is formed in the reaction with NO of these two MyO_2 species. These pathways would include rearrangement reactions followed by reaction with NO and fragmentation. This was suggested to explain the observation of organic species with various masses ($m/z = 71$, $m/z = 113$, $m/z = 115$) detected by the proton-transfer-reaction mass spectrometry instrument in Lee et al. (2006). Similarly, Böge et al. (2013) suggested a reaction pathway of 6-OH-7-OO and 7-OH-6-OO radicals to explain observed terpenylic acid in their experiments. The reaction of the other two most abundant radicals, 1-OH-2-OO and 3′-OH-3-OO, with NO would lead to the formation of HO_2 and formaldehyde together with 2-methyldiene-6-methyl-5-heptenal and 1-vinyl-5-methyl-4-hexanone, respectively (Fig. 3).

In addition to bimolecular reactions, unimolecular reactions can be of importance for specific MyO_2. Due to the similarity of the conjugated double-bond structure in myrcene and isoprene, it can be expected that H-shift reactions found to be important in isoprene (Peeters et al., 2009, 2014; Fuchs et al., 2013; Wennberg et al., 2018; Novelli et al., 2020) apply for corresponding MyO_2 radicals. Therefore, Z-3′-OH-1-OO and Z-1-OH-3′-OO radicals are expected to undergo α-OH 1,6-H migration followed by O_2 addition leading to hydroperoxy peroxy radicals (Fig. 4). As a first approximation, reaction rate constants can be assumed to be on the order of 1 s^{-1} at 298 K like for corresponding reactions in isoprene (Peeters et al., 2014). Similar products from further isomerization and decomposition reactions could be expected as predicted for isoprene (Peeters et al., 2014). This would also lead to the regeneration of HO_x radicals.

According to SAR by Vereecken and Nozière (2020), E-3′-OH-1-OO undergoes an allylic 1,7 H shift (Fig. 4). The reaction rate constant is estimated by this SAR to be high with a value of 8 s^{-1} ($T = 298$ K). In addition, E-1-OH-3′-OO can undergo an allylic 1,6-H-shift isomerization reaction with a fast isomerization reaction rate constant of 2 s^{-1} ($T = 298$ K). Products likely undergo fast ring-closure reactions on the dimethyl double bond with rates on the order of 1 s^{-1} (Luc Vereecken, personal communication, 2021).

As a consequence of the equilibration between different MyO_2 isomers that originate from the 3′-OH or 1-OH addition, a significant fraction of the MyO_2 can be removed through the H-shift reaction channels if rates of competing bimolecular reactions of all RO_2 isomers are low enough. In order to estimate effective bulk MyO_2 isomerization reaction rates, the distribution of MyO_2 isomers is estimated by using reaction rate constants for the oxygen addition and elimination reactions recommended for isoprene (Novelli et al., 2020). This results in a total bulk MyO_2 loss rate of approximately 0.21 and 0.097 s^{-1} ($T = 298$ K) for the three isomers resulting from the 3′-OH and 1-OH addition, respectively. This means that isomerization reactions are becoming competitive for nearly half of the total MyO_2 (Fig. 2) isomers for chemical conditions with NO mixing ratios lower than 1 ppbv. It is worth noting that isomerization reaction rate constants have a strong temperature dependence, so that their impact can be significantly enhanced at higher temperatures. However, all rate constants by SAR predictions also have a high uncertainty of at least a factor of 2, and the uncertainty might be as high as a factor of 10 (Vereecken and Nozière, 2020).

3 Methods

3.1 Experiments in the SAPHIR chamber

The experiments were conducted in the outdoor atmospheric simulation chamber SAPHIR. SAPHIR has a cylindrical shape with double walls made of Teflon (FEP) film (length: 18 m diameter: 5 m, volume: 270 m^3). The space between the double walls is permanently purged with clean air to avoid diffusion of impurities from ambient air into the inner cham-

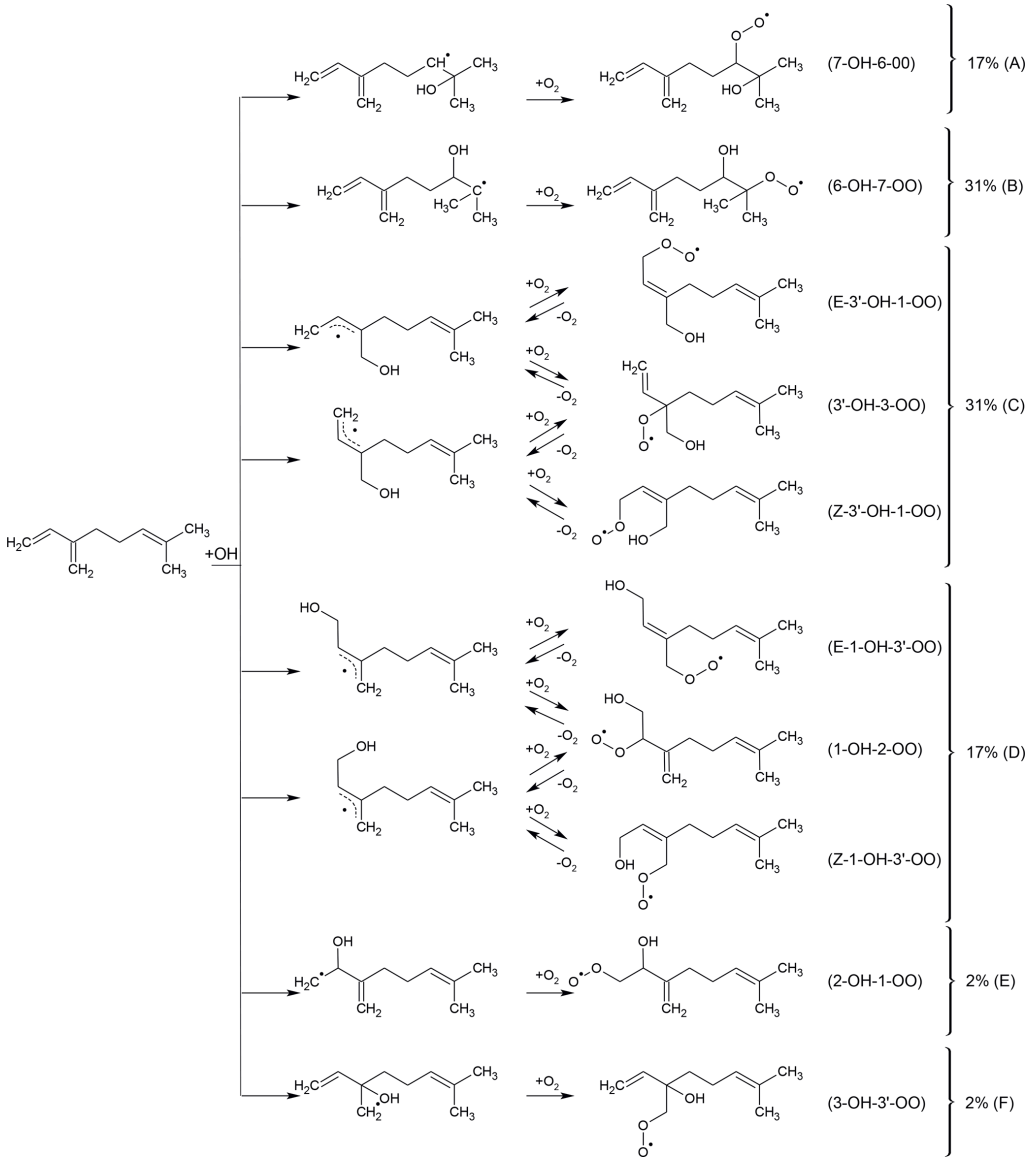

Figure 2. Peroxy radicals formed from the addition of OH to the double bonds in myrcene. MyO_2 formed from the OH addition to the isoprenyl part of myrcene leads to the formation of MyO_2 species that are expected to rapidly interconvert by oxygen abstraction and elimination like in isoprene (Peeters et al., 2014). Assuming reaction rate constants for oxygen abstraction and elimination like in isoprene, $3'-OH-3-OO$ and $1-OH-2-OO$ are expected to have the highest yields among the MyO_2 species that can interconvert. MyO_2 yields are predicted using SAR by Peeters et al. (2007).

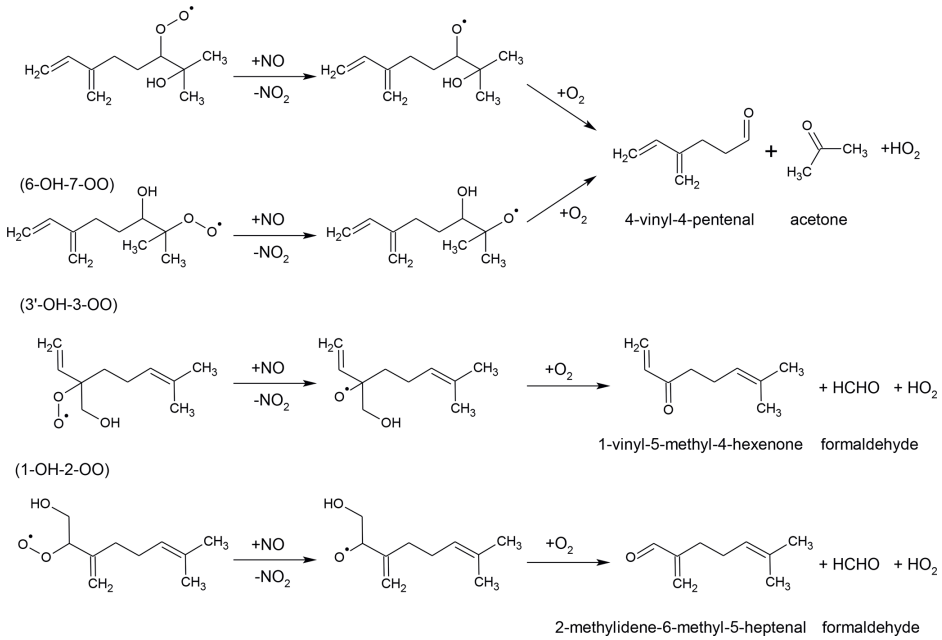

Figure 3. Reactions of the four most abundant myrcene hydroxy peroxy radicals with NO forming HO_2 and carbonyl compounds.

ber. The walls are transmissive for the entire solar UV and visible spectrum. The chamber is operated with synthetic air that is produced from evaporated liquid nitrogen and oxygen of highest purity (Linde, purity > 99.99990 %). It is kept at a slight overpressure of 35 Pa that is maintained by a replenishment flow, which compensates for leakages and the sampling flow of analytical instruments. As a consequence, trace gases are diluted with a rate constant that is equivalent to a lifetime of approximately 17 h. The air in the chamber can be exposed to sunlight by opening a shutter system. When the chamber film is exposed to solar radiation, nitrous acid (HONO), formaldehyde and acetone are released. The source strengths range between 100 and 200 pptv h^{-1}. The photolysis of HONO leads to a continuous increase in nitrogen oxide concentrations in the chamber and is a significant source for hydroxyl radicals (OH). More details of the SAPHIR can be found in previous publications (e.g. Bohn et al., 2005; Rohrer et al., 2005).

In total four experiments investigating the oxidation of myrcene by OH were performed (Table 1), two of which were done at medium levels of nitric oxide (NO) ranging from 0.1 to 0.4 ppbv (on 18 August 2012, Fuchs et al., 2021a, from 0.18 to 0.43 ppbv of NO, Fig. 5, and on 22 August 2012, Fuchs et al., 2021b, from 0.15 to 0.30 ppbv of NO, Fig. S1 in the Supplement), while lower NO mixing ratios below 0.11 ppbv were achieved in the other two experiments (17 July 2013, Fuchs et al., 2021c, Fig. S2 in the Supplement, and 18 July 2013, Fuchs et al., 2021d, Fig. S3 in the Supplement).

The experimental procedure was similar in all experiments. The chamber was cleaned in the night before the experiment by flushing the chamber with a high flow of synthetic air to remove all trace gases from previous experiments. Figure 5 shows, as an example, time series of trace gases for the experiment conducted on 22 August 2012. Experiments started in the morning with humidification of the chamber air in the dark. This was achieved by flushing evaporated Milli-Q water into the chamber together with a high flow of synthetic air. The chamber air was exposed to sunlight approximately for 1 h without the presence of any additional reactant to determine the source strengths of chamber sources for formaldehyde for the specific experiment. In the experiments in 2013, approximately 50 ppbv of ozone produced by a silent discharge ozonizer (O3onia) was injected to suppress NO in the reaction with O_3. Products from the ozonolysis of myrcene are similar to the products formed from the reaction with OH. These could lead to systematic errors in the conclusions with respect to the OH oxidation scheme. Given the typical OH concentration in this study (5×10^6 cm^{-3}), the contribution of ozonolysis to the entire

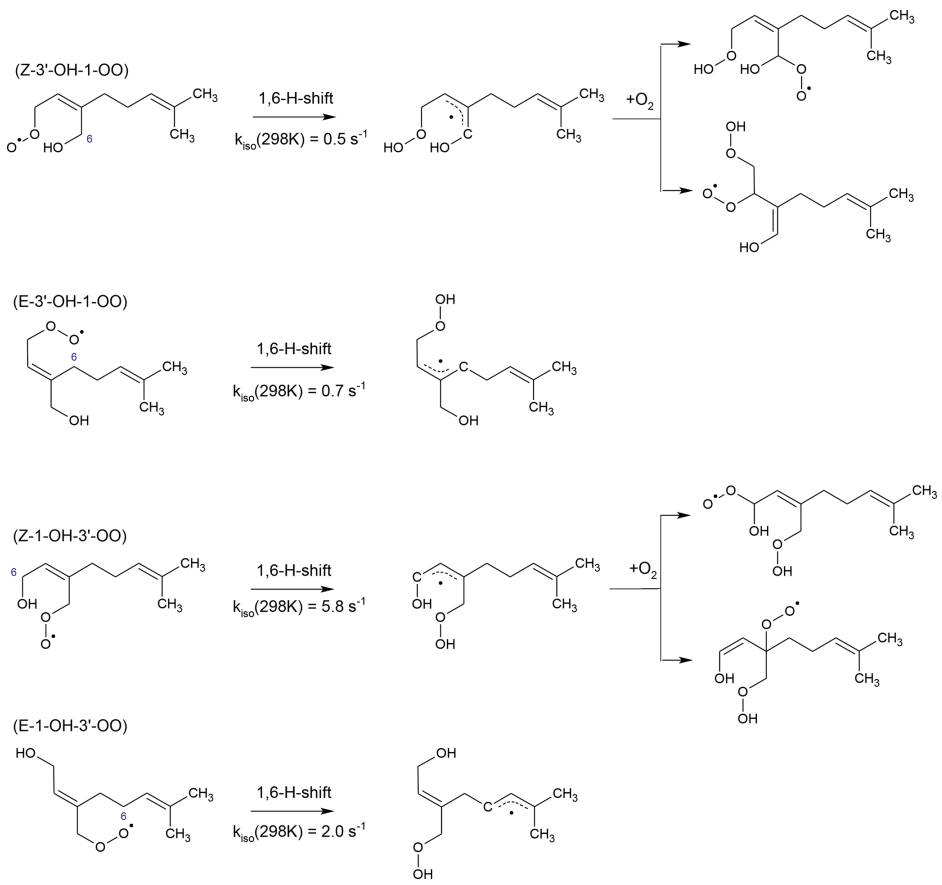

Figure 4. Fast H-shift reactions of myrcene peroxy radicals. Rate constants apply to 298 K. They are adopted for the Z−3′−OH−1−OO and Z−1−OH−3′−OO isomers from the corresponding 1,6-H-shift reactions of isoprene peroxy radicals (Peeters et al., 2014). Similar subsequent chemistry like for isoprene leads to the formation of peroxy radicals, some of which rapidly decompose. The isomerization reaction rate constants for the E−3′−OH−1−OO and E−1−OH−3′−OO peroxy radicals are calculated using SAR by Vereecken and Nozière (2020). Subsequent chemistry of products from these reactions likely undergoes fast ring-closure reactions on the dimethyl double bond (not shown here).

Table 1. Experimental conditions for the oxidation experiments. Concentrations are given for the conditions in the SAPHIR chamber at the time of the first VOC injection.

Date	Type of VOC	VOC/ppbv	NO/ppbv	O_3/ppbv	T/K	RH/%
16 August 2012	myrcene	2.3	0.2	< 20	305	30.7
22 August 2012	myrcene	2.3	0.2	< 15	310	10.1
17 July 2013	myrcene	0.8	0.06	40	305	57.7
18 July 2013	myrcene	0.8	0.09	40	308	32.0
29 May 2020	methane	140 000	0.23	60–120	303	22.1
3 September 2019	α-pinene	8.5	0.1	8	296	24.0

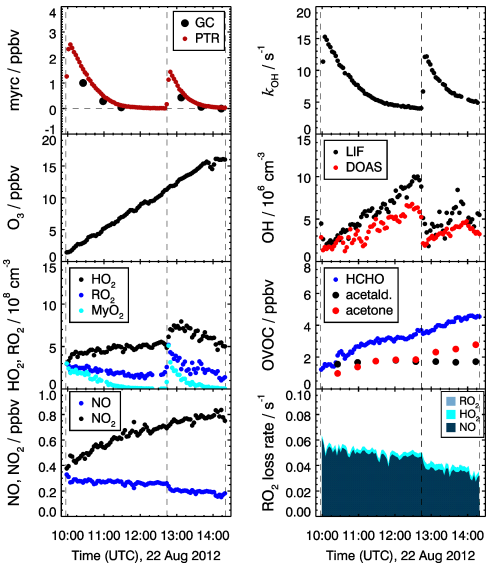

Figure 5. Trace gas and radical concentrations in the chamber experiment investigating the OH oxidation of myrcene (myrc) at NO mixing ratios between 200 and 300 pptv on 22 August 2012. Peroxy radicals from the reaction of OH with myrcene (MyO_2) and total organic peroxy radical ($RO_2 = MyO_2 + RO_{2,other}$) concentrations are calculated from observed radical concentrations as explained in Sect. 3.4. In the lowest right panel, the loss rates of total RO_2 with respect to their reaction with NO and radical recombination reactions are shown.

oxidation of myrcene is less than 20 %. The potential interfering is minimized in the medium NO cases, where ozonolysis only contributes 10 % of the myrcene oxidation.

Air mixtures of myrcene (Sigma-Aldrich, purity 99 %) were premixed in a canister (stainless steel with SilcoNert coating). The mixture was injected into the chamber air by calibrated mass flow controllers to reach myrcene mixing ratios of several parts per billion by volume. Injections were performed two times (approximately 2 ppbv each) in experiments with medium NO, and four injections with smaller concentrations (approximately 1 ppbv) were performed in the other experiments.

Additional reference experiments were performed using the same procedure like for the experiments with myrcene, but either with one injection of 140 ppmv of methane (29 May 2020, Fuchs et al., 2021f, Fig. S4 in the Supplement, and 10 July 2013) or three injections of 8.5 ppbv of α-pinene (3 September 2019, Fuchs et al., 2021e, Fig. S5 in the Supplement). These experiments were used to evaluate the accuracies of the procedures that were used to analyse the organic nitrate formation and radical budgets in the experiments with myrcene.

3.2 Measurement of trace gas concentrations

Table 2 summarizes properties of instruments used in this work. The set of instruments was similar to that used in previous experiments investigating the photochemistry of organic compounds (Kaminski et al., 2017; Fuchs et al., 2018; Novelli et al., 2018; Rolletter et al., 2019). Therefore, only a brief description is given here. Ozone was detected by a UV photometer (Ansyco). NO concentrations were measured by a chemiluminescence instrument (Eco Physics) that also detected nitrogen dioxide (NO_2) after conversion to NO in a photolytic converter. Methane, water vapour and carbon monoxide concentrations were measured by a cavity ring-down instrument (Picarro). Nitrous acid (HONO) was detected by a custom-built long-path absorption photometry (LOPAP) (Li et al., 2014). Photolysis frequencies were derived from solar actinic flux measurements by a spectroradiometer outside the chamber. Calculations take into account the reduction of radiation by the chamber construction elements and the Teflon film (Bohn and Zilken, 2005).

Myrcene was detected by gas chromatography coupled with a flame ionization detector (GC-FID) (Wegener et al., 2007) and by a proton-transfer-reaction mass spectrometer (PTR-MS, Ionicon). The PTR-MS was not calibrated for myrcene. Therefore, the signal was scaled to match the GC-FID measurements and used because of its higher time resolution (40 s) compared to that of GC-FID (30 min). Acetone and acetaldehyde were also measured by GC-FID. Formaldehyde (HCHO) measurements were performed by a Hantzsch instrument (Aerolaser) or by differential optical absorption spectrometry (DOAS). The HCHO concentrations measured by the different methods has been shown to agree within 10 % in a series of experiments in the SAPHIR chamber, in which both instruments concurrently measured (Glowania et al., 2020). OH reactivity (k_{OH}), which is the pseudo-first-order rate constant of the OH radical loss, was measured by a laser flash photolysis–laser-induced fluorescence instrument (Lou et al., 2010; Fuchs et al., 2017).

3.3 Measurement of radical concentrations

Measurements of OH radicals were performed by differential optical absorption spectrometry (DOAS) (Dorn et al., 1995) and laser-induced fluorescence (LIF) (Tan et al., 2017, and references therein). The DOAS instrument was not available in the experiment on 16 August 2012. In the experiment 6 d later (22 August 2012), OH concentrations measured by the LIF instrument were consistently 20 % higher than those measured by DOAS, which is considered to be an absolute standard. The difference is larger than the combined 1σ uncertainty (14.5 %) of the measurements and is probably caused by a calibration error of the LIF instru-

Table 2. Instrumentation for radical and trace gas detection in the experiments.

Measured quantity	Measurement technique	Time resolution	Precision ($1\,\sigma$)	Accuracy ($1\,\sigma$)
OH	differential optical absorption spectroscopy	205 s	0.6×10^6 cm^{-3}	6.5 %
OH	laser-induced fluorescence (LIF)	47 s	0.4×10^6 cm^{-3}	13 %
HO_2, RO_2	laser-induced fluorescence (LIF)	47 s	1.5×10^7 cm^{-3}	16 %
MyO_2				50 %
k_{OH}	laser photolysis + LIF	180 s	0.3 s^{-1}	10 %, $\pm$0.7 s^{-1}
myrcene, α-pinene	proton-transfer-reaction mass spectrometry	40 s	15 pptv	7 %
myrcene, acetone	gas chromatography	30 min	100 pptv	6 %
CH_4	cavity ring-down spectroscopy	60 s	1 ppbv	3 ppbv
CO	cavity ring-down spectroscopy	60 s	25 ppbv	1 ppbv
NO	chemiluminescence	180 s	13 pptv	5 %
NO_2	photolytic converter + chemiluminescence	180 s	30 pptv	7 %
HONO	long-path absorption photometry	300 s	7 pptv	20 %
O_3	UV absorption	10 s	1 ppbv	5 %
HCHO	differential optical absorption spectroscopy	100 s	20 %	10 %
HCHO	Hantzsch method (Aerolaser)	90 s	100 pptv	10 %
photolysis frequency	actinic flux spectroradiometry	60 s	10 %	10 %

ment. This assumption is supported by the observed decay of myrcene, which is caused by the reaction with OH. The decay can be accurately described with LIF data if these are reduced by 20 % in both experiments (Fig. S6 in the Supplement, Sect. 6.1). Therefore, OH measurements by LIF were scaled by a factor of 0.8 for both experiments. For the experiments in 2013, OH measurements by LIF and DOAS agreed well within 5 %. For the analysis of this work, OH measurements by the DOAS instrument are used if available. Interference could occur in OH measurements by the LIF instrument from alkene ozonolysis at exceptionally high concentrations of reactants (Fuchs et al., 2016). However, the ozone and myrcene concentrations used in this study were much lower compared to concentrations used in the characterization experiments in Fuchs et al. (2016). Therefore, it is not expected that similar interferences were significant for measurements in these experiments. Thus, the observed differences in the OH measurements of the LIF and DOAS instruments were most likely caused by calibration errors.

In addition to OH, peroxy radicals (HO_2 and RO_2) can be detected by the LIF instrument after chemical conversion to OH. The conversion of HO_2 radicals is accomplished by adding excess NO in a second low-pressure fluorescence cell, in which the sum of HO_2 and OH concentrations is measured (Fuchs et al., 2011). The measurement of RO_2 is accomplished in a two-stage system (ROxLIF) in which all atmospheric RO_x radicals are first converted to HO_2 by added NO and CO in a flow reactor (Fuchs et al., 2008). This is followed by HO_2-to-OH conversion with additionally added NO in a fluorescence cell. In this case, RO_2 is determined as the difference of RO_x and OH+HO_2. The operational parameters of the reactor are optimized to maximize the detection sensitivity for methyl peroxy radicals (CH_3O_2). However, it was found in previous studies that specific RO_2 species from other VOCs may be converted less efficiently in the reactor if their conversion to HO_2 needs more reaction steps and therefore more reaction time than in the case of CH_3O_2 (Fuchs et al., 2008). An alternative explanation for the lower sensitivity could be the reversibility of the MyO_2 formation at low O_2 in the reactor, which slow down the conversion to HO_2.

For the evaluation of data in this work, the ROxLIF instrument was calibrated for CH_3O_2 and myrcene RO_2 radicals (MyO_2) that were produced by reaction of OH with the corresponding VOC in the radical calibration source as described by Fuchs et al. (2008). The detection sensitivity was only half as high for MyO_2 compared to CH_3O_2. The lower sensitivity could hint that some specific MyO_2 isomers are not efficiently converted to HO_2 for conditions inside the conversion reactor. The difference in the detection sensitivity for MyO_2 and other RO_2 species like CH_3O_2 adds to the uncertainty of measurements, because a mixture of different peroxy radicals is present during the experiments and the exact distribution of RO_2 species is not known. For the analysis in this work, the fraction of MyO_2 is estimated as described in the next subsection, in order to account for the lower sensitivity.

3.4 VOC reactivity and RO_2 speciation in myrcene experiments

The total OH reactivity (k_{OH}) that was measured in the experiments consists of reactivity from organic and inorganic compounds. Total OH reactivity was measured by LP-LIF, while the speciated OH reactivity for individual species X was calculated from the products of concentrations of X and its reaction rate vs. OH. The reaction of OH with most of the organic compounds leads to the formation of RO_2 radicals.

Table 3. Chemical reactions considered in the radical budget analysis of OH, HO_2 and RO_2. Some reactions are only applicable in the experiment with either methane, α-pinene or myrcene, in which specific RO_2 radicals, CH_3O_2, MyO_2 or APO_2 are formed. $RO_2 + RO_2$ reactions are not listed, because they do not significantly contribute to the loss of radicals for conditions of experiments here.

	Reaction	$k(T = 298\,\mathrm{K},\ P = 1\,\mathrm{atm})$	Uncertainty[a]	Reference
Radical initiation reactions				
(R1)	$HONO + h\nu\ (< 400\,nm) \rightarrow OH + NO$	j_{HONO}	22 %	measured
(R2)	$O_3 + h\nu\ (< 340\,nm) \rightarrow O(^1D) + O_2$	$j_{O(^1D)}$	11 %	measured
	$O(^1D) + H_2O \rightarrow OH + OH$	$2.1 \times 10^{-10}\,cm^3\,s^{-1}$		IUPAC (2020)
	$O(^1D) + M \rightarrow O(^3P) + M$	$3.3 \times 10^{-11}\,cm^3\,s^{-1}$		IUPAC (2020)
(R3)	$HCHO + h\nu\ (< 335\,nm) + 2O_2 \rightarrow 2HO_2 + CO$	j_{HCHO}	11 %	measured
(R4)	$O_3 + myrc \rightarrow 0.71OH + 0.71RO_2$	$3.9 \times 10^{-16}\,cm^3\,s^{-1}$	22 %	Deng et al. (2018); Kim et al. (2011)
Radical propagation reactions				
(R5)	$HO_2 + NO \rightarrow OH + NO_2$	$8.5 \times 10^{-12}\,cm^3\,s^{-1}$	27 %	IUPAC (2020)
(R6)	$HO_2 + O_3 \rightarrow OH + 2O_2$	$2.0 \times 10^{-15}\,cm^3\,s^{-1}$	20 %	IUPAC (2020)
(R7)	$OH + VOC + O_2 \rightarrow RO_2$			
	$RO_2 = CH_3O_2$	$6.4 \times 10^{-15}\,cm^3\,s^{-1}$	17 %	IUPAC (2020)
	$RO_2 = MyO_2$	$2.3 \times 10^{-10}\,cm^3\,s^{-1}$	25 %	this work
(R8)	$OH + HCHO + O_2 \rightarrow HO_2 + CO + H_2O$	$8.4 \times 10^{-12}\,cm^3\,s^{-1}$	25 %	IUPAC (2020)
(R9)	$OH + CO + O_2 \rightarrow HO_2 + CO_2$	$2.3 \times 10^{-13}\,cm^3\,s^{-1}$	17 %	IUPAC (2020)
(R10)	$OH + O_3 \rightarrow HO_2 + O_2$	$7.3 \times 10^{-14}\,cm^3\,s^{-1}$	17 %	IUPAC (2020)
(R11)	$RO_2 + NO \rightarrow HO_2 + NO_2 + R'CHO$[c]			
	$RO_2 = CH_3O_2$	$7.7 \times 10^{-12}\,cm^3\,s^{-1}$	27 %	IUPAC (2020)
	$RO_2 = MyO_2$	$0.87 \times 9.1 \times 10^{-12}\,cm^3\,s^{-1}$	55 %	IUPAC (2020) [b]
Radical termination reactions				
(R12)	$OH + NO_2 \rightarrow HNO_3$	$1.2 \times 10^{-11}\,cm^3\,s^{-1}$	28 %	IUPAC (2020)
(R13)	$OH + NO \rightarrow HONO$	$9.8 \times 10^{-12}\,cm^3\,s^{-1}$	28 %	IUPAC (2020)
(R14)	$RO_2 + NO \rightarrow RONO_2$			
	$RO_2 = CH_3O_2$	≈ 0	–	IUPAC (2020)
	$RO_2 = APO_2$	$0.18 \times 9.1 \times 10^{-12}\,cm^3\,s^{-1}$	27 %	IUPAC (2020) [b]
	$RO_2 = MyO_2$	$0.13 \times 9.1 \times 10^{-12}\,cm^3\,s^{-1}$	55 %	IUPAC (2020) [b]
(R15)	$RO_{2,myrc} + HO_2 \rightarrow ROOH + O_2$	$9.1 \times 10^{-12}\,cm^3\,s^{-1}$	25 %	this work
(R16)	$HO_2 + HO_2 + H_2O \rightarrow H_2O_2 + O_2 + H_2O$	$4.0 \times 10^{-13}\,cm^3\,s^{-1}$[d]	25 %	IUPAC (2020)

[a] Uncertainty measurements (Table 2) and kinetic rate constants (10 % for reactions of inorganic and methyl peroxy radicals and 15 % for other). [b] Reaction rate constant: IUPAC (2020); the branching ratio of 0.87 is taken from this work. [c] The dominant reaction of alkoxy radical is to form HO_2, which is not rate limiting for RO_2-to-HO_2 conversion. [d] Effective reaction rate constant for 1 % H_2O mixing ratio.

Therefore, it is useful to distinguish between OH reactivity from those compounds unmeasured (k_{OHVOC}), and OH reactivity calculated from measured concentrations of inorganic compounds (CO, NO, NO_2) and formaldehyde:

$$k_{OHVOC} = k_{OH} - (k_8[HCHO] + k_9[CO] + k_{12}[NO_2] + k_{13}[NO]), \quad (1)$$

where k_i represents the bimolecular rate constants of reactions R_i listed in Table 3. For the reference experiment with methane, only methane contributed to the VOC reactivity, because its oxidation product is formaldehyde, which does not produce RO_2 in the reaction with OH. Therefore, methyl peroxy radicals are the only RO_2 radical expected in that experiment. For the experiments with myrcene, the VOC reactivity includes the reactivity from myrcene and from partly unmeasured oxygenated organic compounds (OVOC) that are products of the myrcene oxidation. The OH reactivity from myrcene ($k_{OH\ myrcene}$) can be calculated from measured myrcene concentrations and the rate constant of its reaction with OH (k_7, Table 3):

$$k_{OH\ myrcene} = k_7[myrcene]. \quad (2)$$

Assuming that each OH reaction with an organic compound except formaldehyde in the experiments in this work leads to the formation of one RO_2 radical and all RO_2 radicals have similar chemical lifetimes, the distribution of RO_2 species from different VOCs is similar to the distribution of the OH reactivity from the VOCs. Therefore, the concentra-

tion of RO_2 derived from myrcene (MyO_2) can be approximated by scaling the total measured organic peroxy radical concentration ($[RO_2]_m$) that is determined assuming the same instrument sensitivity for all RO_2 with the ratio of OH reactivity from myrcene ($k_{\mathrm{OH\ myrcene}}$) to the total OH reactivity from VOCs ($k_{\mathrm{OH\ VOC}}$). Taking also into account that the sensitivity of the instrument for MyO_2 ($S_{\mathrm{MyO_2}}$) is reduced compared to the sensitivity for CH_3O_2 (S_{CH3O2}), the concentration of MyO_2 can be calculated from observed quantities:

$$[\mathrm{MyO_2}] = \frac{1}{\frac{S_{\mathrm{MyO2}}}{S_{\mathrm{CH3O2}}} + \frac{k_{\mathrm{OH\ VOC}}}{k_{\mathrm{OH\ myrcene}}} - 1} [\mathrm{RO_2}]_m. \quad (3)$$

RO_2 species originating from other hydrocarbons than myrcene ($RO_{2,\mathrm{other}}$) can be calculated using the remaining fraction of the VOC reactivity:

$$[\mathrm{RO_{2,other}}] = [\mathrm{MyO_2}] \left(\frac{k_{\mathrm{OH\ VOC}}}{k_{\mathrm{OH\ myrcene}}} - 1 \right). \quad (4)$$

Equations (3) and (4) allow calculating a more realistic total RO_2 concentration by taking the sum of MyO_2 and $RO_{2,\mathrm{other}}$ instead of using the measured RO_2 concentration if the same instrument sensitivity for all RO_2 is assumed. An example of the result of this calculation is shown in Fig. 5, demonstrating that MyO_2 was the dominant RO_2 species right after each myrcene injection. However, these values have a high uncertainty that cannot easily be quantified because, for example, the detection sensitivity for RO_2 produced in the reaction of OH with oxidation products may also differ from that of methyl peroxy radicals. The uncertainty of calculated RO_2 concentrations is lowest after each injection of myrcene, because the total OH reactivity and therefore RO_2 production are dominated by myrcene. Therefore, the analysis of radical production and destruction rates in this work (Sect. 6.4) focuses on the times right after each myrcene injection.

4 Experimental determination of organic nitrate yields

The determination of organic nitrate yields from photochemical VOC oxidation makes use of a budget analysis of the sum of NO_x and HONO in the chamber air. In the following, the sum of NO, NO_2 and HONO concentrations is defined as NO_y^*, which can be calculated from measurements of these species (Table 2).

In the sunlit SAPHIR chamber, the only source of reactive nitrogen is the emission of HONO from the chamber film (Sect. 3.1). The source strength $Q(\mathrm{HONO})$ is variable and depends on solar ultraviolet radiation, temperature and relative humidity (Rohrer et al., 2005). HONO is photolysed to OH and NO (Reaction R1), which is further oxidized to NO_2 by reactions with O_3, HO_2 (Reaction R5) and RO_2 (Reaction R11). The sum of NO_y^* is chemically lost in the chamber by reactions forming nitric acid (HNO_3) (Reaction R12) and organic nitrates ($RONO_2$) (Reaction R14). In addition, the NO_y^* species are removed ($L(NO_y^*)$) by transport due to the replenishment flow that compensates for chamber leakage and gas sampling of analytical instruments with a first-order rate constant of $k_\mathrm{d} \approx 1.6 \times 10^{-5}\,\mathrm{s}^{-1}$ (Sect. 3.1):

$$L(\mathrm{NO_y^*}) = ([\mathrm{NO}] + [\mathrm{NO_2}] + [\mathrm{HONO}])\, k_\mathrm{d}. \quad (5)$$

The dilution rate is monitored by the input flow rate of synthetic air, which yields an accuracy of k_d better than 1 %. Hence, the uncertainty due to the dilution is neglected due to its small contribution. The concentration of NO_y^* at a given time is then determined by the difference between the time-integrated production and loss terms.

$$[\mathrm{NO_y^*}] = \int_t \big(Q(\mathrm{HONO}) - k_{12}[\mathrm{OH}][\mathrm{NO_2}] - k_{14}[\mathrm{RO_2}][\mathrm{NO}] - L(\mathrm{NO_y^*}) \big) \mathrm{d}t \quad (6)$$

It is assumed that the formations of HNO_3 and $RONO_2$ are effective sinks for NO_x and that reformation of NO_x by its reactions with OH or photolysis does not play a role. This assumption is justified because the low reaction rate constant with OH and small absorption cross sections of HNO_3 and $RONO_2$ (Burkholder et al., 2020; Browne et al., 2014) lead to their lifetimes in the range of several days, which is much slower than the timescale of the experiments. The loss of NO_2 due to reaction with ozone which forms nitrate radicals (NO_3) is neglected in Eq. (6), because the NO_3 radical is efficiently converted back to NO_2 by photolysis and reaction with NO in the photo-oxidation experiments in this work. The formation of other oxidized nitrogen species such as peroxy nitric acid (HNO_4) and acetyl peroxy nitrate (PAN) is also assumed to be negligible because their mixing ratios are expected to be only a few tens of parts per trillion by volume for conditions of the experiments.

The formation rate of HONO that is within the range of a few hundred parts per trillion by volume per hour in the chamber experiments can be determined from measurements of OH, NO, HONO and $j(\mathrm{HONO})$ by assuming a photostationary state for the HONO concentration:

$$\frac{\mathrm{d}[\mathrm{HONO}]}{\mathrm{d}t} = Q(\mathrm{HONO}) - j_{\mathrm{HONO}}[\mathrm{HONO}] + k_{\mathrm{OH+NO}}[\mathrm{OH}][\mathrm{NO}] = 0$$
$$Q(\mathrm{HONO}) = j_{\mathrm{HONO}}[\mathrm{HONO}] - k_{13}[\mathrm{OH}][\mathrm{NO}]. \quad (7)$$

For the experimental conditions ($j(\mathrm{HONO}) = 8 \times 10^{-4}\,\mathrm{s}^{-1}$) the photo-stationary state is reached within approximately 20 min. On this timescale, the dilution of HONO by the chamber replenishment flow is only 2 % and is therefore neglected. The uncertainty of the HONO formation rate (Eq. 7) is dominated by the uncertainty in the HONO measurement (22 %, Table 3).

Using measured concentrations of NO, NO_2 and HONO, the concentration of NO that is converted to organic nitrates

during the experiment ($\Delta RONO_2$) is determined by the balance of nitrogen oxide concentrations:

$$\begin{aligned}\Delta[\mathrm{RONO_2}] &= \int_t k_{14}[\mathrm{RO_2}][\mathrm{NO}]\mathrm{d}t \\ &= \Phi_{\mathrm{RONO2}} \int_t (k_{11}+k_{14})[\mathrm{RO_2}][\mathrm{NO}]\mathrm{d}t \\ &= \int_t \big(Q(\mathrm{HONO}) - k_{12}[\mathrm{OH}][\mathrm{NO_2}] \\ &- L(\mathrm{NO_y^*})\big)\mathrm{d}t - ([\mathrm{NO}]+[\mathrm{NO_2}]+[\mathrm{HONO}])\,. \end{aligned} \quad (8)$$

The reaction yield of organic nitrates (Φ_{RONO2}) can be then derived as slope of a linear fit (Eq. 8). The accuracy of the yield is mainly determined by the accuracy the kinetic reaction rate constants and measurements that vary between the specific experiments.

4.1 Test experiments with methane and α-pinene

In order to test the method described above, organic nitrate yields from the photo-oxidation of methane and α-pinene were experimentally determined and compared with literature values. NO mixing ratios were between 100 and 300 pptv in both experiments, so that at least 60 % of the RO_2 radicals reacted with NO.

Figure 6 shows time series of NO_y species in α-pinene and methane experiments. In the methane experiment, the total mixing ratio of NO_y species calculated from the HONO chamber source (Eq. 7) is around 1.3 ppbv and is mainly explained by measured NO_2 and NO concentrations. In the experiment with α-pinene, the calculated NO_y mixing ratio increased from 1 to 1.3 ppbv within 2 h. Approximately 1 ppbv was present as NO_2 and NO and the remaining fraction can be attributed to the formation of organic nitrates from α-pinene. The alkyl nitrate yield is derived from Eq. (8) by a linear fit as described above.

For the experiment with methane, the alkyl nitrate yield is smaller than the error of the calculation (0.00 ± 0.04, Fig. 6). This small value agrees with literature values of < 0.003 (Scholtens et al., 1995) and 0.0039 ± 0.0011 (Butkovskaya et al., 2012) at room temperature.

The alkyl nitrate yield determined from the OH oxidation experiment with α-pinene is 0.32 ± 0.06. The accuracy is mainly due to the uncertainty of RO_2 measurements. Reported literature values are 0.01 (Aschmann et al., 2002), 0.18 ± 0.09 (Noziére et al., 1999) and 0.26 ± 0.07 (Rindelaub et al., 2015). All experiments were conducted at measurement conditions where the reaction of RO_2 with NO was the dominant RO_2 reaction pathway, so that the obtained organic nitrate yields can be attributed to the yield from reaction of α-pinene-derived RO_2. The value determined in this work agrees well with values determined from direct measurements using FT-IR spectroscopy in experiments by Noziére et al. (1999) and Rindelaub et al. (2015) within the specified errors. In contrast, Aschmann et al. (2002) approximated the nitrate yield from mass spectrometer measurements with a high uncertainty that likely explains the much lower yield in their experiments compared to the other two studies and results in this work.

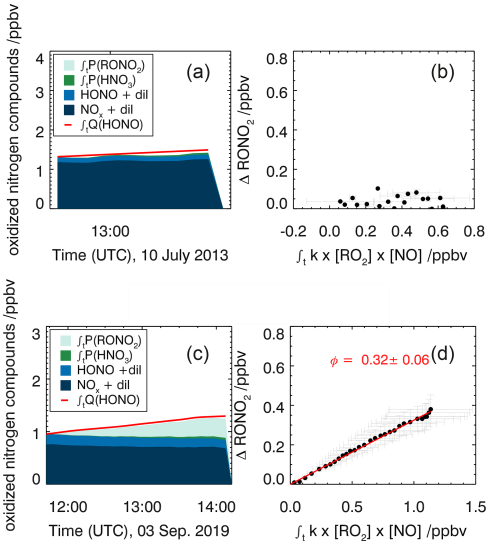

Figure 6. Time series of nitrogen oxide species in the experiments with methane (10 July 2013, **a**) and α-pinene (3 September 2019, **c**). The red lines in panels **(a)** and **(c)** are time-integrated HONO emissions calculated as described in the text. NO_x and HONO concentrations were measured; the time-integrated NO_2 loss by HNO_3 formation from the reaction of NO_2 with OH and the time-integrated NO_2 loss by $RONO_2$ formation from the reaction of RO_2 with NO were calculated as described in the text. The alkyl nitrate yield (Φ_{RONO2}) is determined from the regression analysis (red line, **d**) using Eq. (8). Errors are derived from error propagation of measurements.

The good agreement between nitrate yields determined in the experiments with methane and α-pinene with reported values in literature demonstrates that the applied method for the determination of alkyl nitrate formation in the chamber gives reliable results.

5 Experimental analysis of the chemical budgets of OH, HO_2, RO_2 and RO_x

The chamber experiments are also used to study the chemical budgets of OH, HO_2, RO_2 and RO_x during the photochemical oxidation of myrcene. Radical production and destruction rates are determined from reaction kinetic data and mea-

sured trace gas concentrations for reactions that are known to produce or consume radicals in the experiments. Because the chemical lifetime of radicals is short (seconds to minutes), the radical concentrations are expected to be in a steady state. Therefore, the total loss rates for each radical species is balanced by its total production rate. Analysing radical production and destruction rates using experimental data gives an indication if reactions taken into account can describe observations or if there are contributions from further reactions. A similar method has been used before by Tan et al. (2019, 2020) to analyse radical budgets in atmospheric air in China. Here, the method is tested for the photochemical degradation of methane and then applied to the more complex degradation mechanism of myrcene.

5.1 Radical production, destruction and regeneration reactions

In the chamber experiments, OH, HO_2 and RO_2 radicals are primarily formed from photolysis of HONO (Reaction R1), O_3 (Reaction R2), formaldehyde (Reaction R3) and from the ozonolysis of myrcene (Reaction R4). Radical termination processes include the formation of nitrates (HNO_3, HONO and $RONO_2$, Reactions R12, R13 and 14) and peroxides (ROOH and H_2O_2, Reactions R15 and R16). The contribution from RO_2 self-combination reactions is negligible and not considered here. The photolysis of peroxides that can lead to the production of radicals is neglected due to the slow photolysis frequency (typical value for example for CH_3OOH: $2 \times 10^{-6}\,s^{-1}$ at noontime). The rates for the primary production of RO_x radicals ($P(RO_x)$) and for the termination loss rate ($L(RO_x)$) can be calculated as

$$\begin{aligned} P(RO_x) = {} & j_{HONO}[HONO] + \Phi_{OH,2} j_{O(^1D)}[O_3] \\ & + 2 j_{HCHO}[HCHO] + (\Phi_{OH,4} + \Phi_{RO_2,4}) \\ & \times k_4[VOC][O_3], \end{aligned} \tag{9}$$

$$\begin{aligned} L(RO_x) = {} & (k_{12}[NO_2] + k_{13}[NO])[OH] \\ & + (k_{14}[NO] + 2k_{15}[HO_2])[RO_2] + 2k_{16}[HO_2]^2. \end{aligned} \tag{10}$$

For the calculation of $P(RO_x)$ and $L(RO_x)$, measured radical and trace gas concentrations are used. For the analysis of the myrcene experiments, total RO_2 concentrations include corrections for the reduced detection sensitivity of MyO_2 as explained in Sect. 3.4. The applied rate constants are listed in Table 3. The OH and RO_2 yields are taken from Deng et al. (2018). In their work, the yield of HO_2 is zero. The lumped rate constant for the reactions between RO_2 and HO_2 (Reaction R15) has a rather large uncertainty, because rate constants of different RO_2 species can be different by up to a factor of 4 (Jenkin et al., 2019). The uncertainty of other reaction rate constants is typically around 10 %. In addition, the accuracies of measurements (Table 2) add to the total uncertainty in the calculation of loss and production rates. In these experiments, there is a small background OH reactivity ($< 1\,s^{-1}$) which can be a permanent loss of radicals but could also regenerate HO_2 and/or RO_2. However, this background reactivity is small compared to the OH reactivity from methane and myrcene during the experiments ($> 15\,s^{-1}$), so that it does not affect the analysis.

If production and destruction rates of single RO_x species (OH, HO_2 and RO_2) are calculated, radical conversion reactions need to be additionally taken into account. The total OH loss rate ($L(OH)$) can be quantified by the product of measured OH concentrations and total OH reactivity:

$$L(OH) = [OH]k_{OH}. \tag{11}$$

The OH production rate ($P(OH)$) can be calculated from the sum of production from HONO (Reaction R1) and O_3 photolysis followed by water reaction (Reaction R2), ozonolysis of VOCs (Reaction R4) and radical regeneration from HO_2 reacting with NO (Reaction R5) or O_3 (Reaction R6):

$$\begin{aligned} P(OH) = {} & j_{HONO}[HONO] + \Phi_{OH,2} j_{O(^1D)}[O_3] \\ & + \Phi_{OH,4} k_4[VOC][O_3] \\ & + (k_5[NO] + k_6[O_3])[HO_2]. \end{aligned} \tag{12}$$

The loss of HO_2 ($L(HO_2)$) and RO_2 ($L(RO_2)$) radicals are dominated by their reactions with NO for conditions of the experiments here (Reactions R5, R11, R14) in addition to recombination of peroxy radicals including reactions of HO_2 with RO_2 (Reaction R15) and HO_2 self-reactions (Reaction R16):

$$\begin{aligned} L(HO_2) = {} & (k_5[NO] + k_6[O_3] + k_{15}[RO_2] \\ & + 2k_{16}[HO_2])[HO_2], \end{aligned} \tag{13}$$

$$L(RO_2) = ((k_{11} + k_{14})[NO] + k_{15}[HO_2])\,[RO_2]. \tag{14}$$

The HO_2 production ($P(HO_2)$) rate can be calculated from the photolysis of aldehydes, of which HCHO (Reaction R3) were measured in these experiments, and reactions that convert OH or RO_2 to HO_2. OH-to-HO_2 conversion occurs in the reaction of OH with HCHO (Reaction R6), CO (Reaction R7) and O_3 (Reaction R8). The reaction of RO_2 with NO (Reaction R9) produces either HO_2 or organic nitrates (Reaction R14). The total HO_2 production rate is then calculated as

$$\begin{aligned} P(HO_2) = {} & 2 j_{HCHO}[HCHO] + (k_6[HCHO] + k_7[CO] \\ & + k_8[O_3])[OH] + k_{11}[NO][RO_2]. \end{aligned} \tag{15}$$

RO_2 primary production consists of the ozonolysis of VOCs (Reaction R4). In addition, RO_2 is produced from radical propagation reactions via the reaction of OH with VOCs. The total production rate ($P(RO_2)$) can be calculated from the VOC reactivity, k_{OHVOC} (Eq. 1), assuming that each reaction of a VOC with OH produces one RO_2 radical:

$$P(RO_2) = \Phi_{RO2} k_4[VOC][O_3] + k_{OHVOC}[OH]. \tag{16}$$

5.2 Radical production and destruction in a test experiment with methane

The chemical radical budget analysis in SAPHIR experiments was tested in a photo-oxidation experiment with methane. The chemical oxidation mechanism of methane is much simpler than that of monoterpenes. (1) Ozonolysis reactions do not play a role. (2) Organic peroxy radicals that are formed in the chemical mechanism are methyl peroxy radicals (CH_3O_2), which can be accurately measured by the ROxLIF system. (3) There are recommendations for rate constants for reactions involving methyl peroxy radicals (IUPAC, 2020).

Reaction rates for the methane oxidation experiment (29 May 2020) are shown in Fig. 7. Since no DOAS OH measurements were available for this experiment, OH measurements by the LIF instrument were used (Fig. S4 in the Supplement). Total turnover rates are similar for all single radical species (OH, HO_2, RO_2) with values between 8 and 12 ppbv h^{-1} and do not vary much over the course of the experiment. The loss of peroxy radicals is dominated by the radical regeneration reaction with NO, whereas radical recombination reactions contribute less than 10 % to the entire loss of peroxy radicals. OH is nearly only lost by its reaction with methane and formaldehyde.

The production and destruction rates of total RO_x are significantly smaller than those of single radical species with values that rise from 2 to 4 ppbv h^{-1} over the course of the experiment as radical regeneration reactions cancel out. The increase is due to radicals from the photolysis of formaldehyde that are continuously produced from the chamber wall (Sect. 3.1) and in the reaction of OH + methane. The increase in radical production is balanced by increasing rates of peroxy radical recombination reactions and of the reaction of OH with NO_2. The latter is due to the increase in nitrogen oxide concentrations from the chamber source of nitrous acid.

Radical production and destruction rates of each radical species and of total RO_x are roughly balanced within the uncertainty of the calculation (Fig. 7). Maximum deviations are less than 0.5 ppbv h^{-1} for the production and destruction rates of RO_x and HO_2. Differences are much smaller than the accuracy of the calculation (1.5 ppbv h^{-1} for RO_x and 2 ppbv h^{-1} for HO_2). Higher deviations with values of up to 4 ppbv h^{-1} are seen for OH and RO_2 but opposite behaviour. The accuracy of OH and RO_2 radical production and destruction rates is in the range of 2 to 3 ppbv h^{-1}, which cannot explain the discrepancies. As the RO_x and HO_2 budgets are closed using measured OH concentrations, the imbalance between OH and RO_2 production and destruction indicates an unknown systematic error in the conversion rate from OH to RO_2. One possible explanation for the observed imbalances would be that the calculated reaction rate of $OH + CH_4$ is too large. This could either be caused (i) by the measured OH or CH_4 concentrations being too high or (ii) by the applied reaction rate constant k_{OH+CH_4} being too large.

The methane concentrations in the chamber were above the measurement range specified by the manufacturer (Picarro, 0–20 ppmv). However, an instrumental test of the instrument done prior to the chamber experiment showed that the stated measurement accuracy holds at the concentration (150 ppmv) used in the presented experiment. A small background reactivity of 2 s^{-1} was found before the injection of methane. The OH reactivity calculated from measured methane concentration and the reaction rate constant is about 26 s^{-1}, which is consistent with the direct OH reactivity measurement considering the contribution of background reactivity (Fig. S4 in the Supplement). This gives the confidence on the accuracy of the methane measurement.

Another reason for the imbalances could be LIF calibration errors that are larger than given in Table 2. The specification for OH in Table 2 was generally confirmed in previous intercomparisons with the OH-DOAS instrument. However, in some instances the LIF measurements were found to deviate more than expected. An example are the experiments on 16 and 22 August 2012 (Figs. 5 and S1 in the Supplement), where the LIF measurements are higher than the DOAS data by a factor 1.2 probably due to an incorrect calibration.

In the following section, radical budgets for the chemical degradation of myrcene are investigated. In these cases, also OH-DOAS data were available, which have a generally better accuracy than LIF. Therefore, the DOAS data were used for the budget analysis (Figs. 10–12). Note that LIF and DOAS showed good agreement in these experiments (Figs. S2 and S3 in the Supplement).

The rate constant for $OH + CH_4$ has an uncertainty factor of $f = 1.1$ according to NASA/JPL (Burkholder et al., 2020) and $f = 1.15$ according to IUPAC (Atkinson et al., 2004). Thus, the 10 %–15 % difference in the radical budgets would be explainable by a rate constant that is too large.

This partly unresolved discrepancy shows the limitation of the analysis of radical production and destruction rates and needs to be further investigated. The analysis of the experiment with the well-defined chemistry of methane indicates that the maximum accuracy of calculated differences between production and destruction rates for single radical species is 20 % in the chamber experiments.

6 Results and discussion of the experiments with myrcene

6.1 Reaction rate constant of the OH reaction with myrcene

The rate constant of the reaction of myrcene with OH is determined from the measured temporal decay of myrcene and the measured OH concentration. The time series of measured myrcene concentrations are compared to calculations using a chemical box model that only includes chemical loss reactions with OH and O_3 and dilution. The model is con-

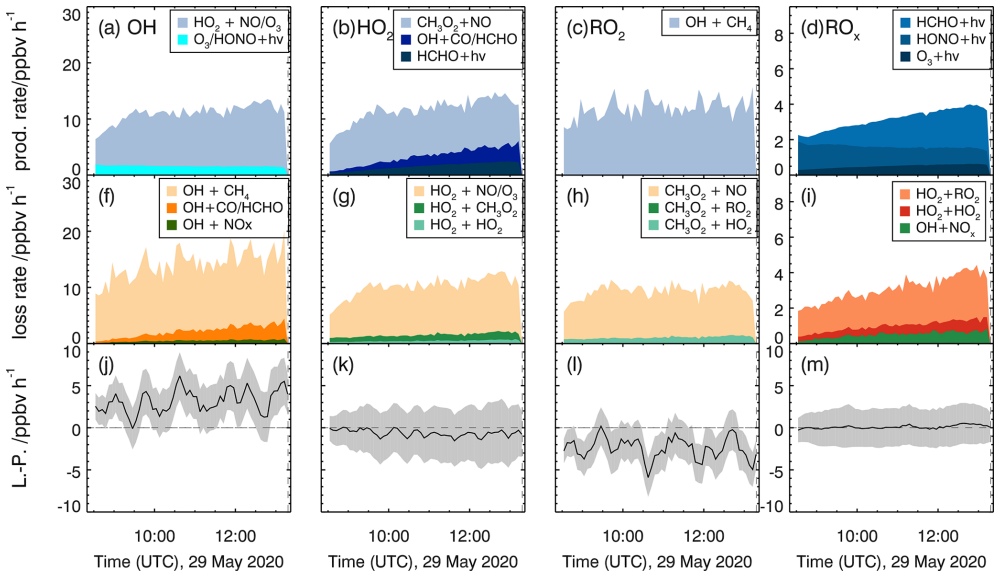

Figure 7. Calculated production and destruction rates of reactions involving radicals for the reference experiment with methane (29 May 2020). Production rates for OH, HO_2, RO_2 and total RO_x are shown in panels **(a)**–**(d)**, respectively, and loss rates for OH, HO_2, RO_2 and total RO_x are shown in panels **(f)**–**(i)**. Lower panels **(j–m)** show the differences between loss and production rates ($L-P$) with the associated accuracy (grey areas).

strained to measured values of temperature, pressure, the dilution rate constant, and OH and O_3 concentrations. The initial myrcene concentration is set to the injected amount of myrcene. The reaction rate constant for myrcene with O_3 is taken from the work by Kim et al. (2011), who measured a value of $2.21 \times 10^{-15} \exp(-(520 \pm 109)\,\mathrm{K}/T)\,\mathrm{cm^3\,s^{-1}}$ using the relative rate technique. Atkinson et al. (1986) suggested a nearly 20 % faster reaction rate constant of $4.7 \times 10^{-16}\,\mathrm{cm^3\,s^{-1}}$ ($T = 298\,\mathrm{K}$) that is still consistent with the value by Kim et al. (2011) within the experimental uncertainties. The chemical lifetime of myrcene with respect to the ozonolysis reaction was approximately 44 min in the low-NO_x experiments with O_3 concentrations of 40 ppbv but was up to 3 h in the experiments with medium NO_x and O_3 concentrations of less than 10 ppbv. In comparison, the chemical lifetime of myrcene with respect to the reaction with OH was within the range of 15 min at OH concentrations of approximately $5 \times 10^6\,\mathrm{cm^{-3}}$ observed in all experiments. Hence, the contribution of ozonolysis to the total chemical loss of myrcene in the experiments was 10 % to 26 %.

The rate constant of the reaction of myrcene with OH is optimized, such that the difference between measured and modelled myrcene concentration time series is minimized. For this optimization the OH concentration observed from DOAS is used. This procedure is applied to all three experiments, resulting in a rate constant of $(2.3 \pm 0.3) \times 10^{-10}\,\mathrm{cm^3 s^{-1}}$ ($T = 298\,\mathrm{K}$, Table 4, Fig. S6 in the Supplement). The error results mainly from the variability of values determined in the different experiments.

The rate constant determined in this study is in good agreement with those reported in the literature (Table 4). The relative rate technique was used in experiments by Atkinson et al. (1986) and Grimsrud et al. (1975). The value reported by Hites and Turner (2009) ($3.4 \times 10^{-10}\,\mathrm{cm^3\,s^{-1}}$) is higher than those of this work and reported by Atkinson et al. (1986) but has a high uncertainty of ±35 % that is explained by experimental difficulties in the handling of myrcene. The reaction rate constants calculated from structure–activity relationship (SAR) by Peeters et al. (2007) and Jenkin et al. (2018) give similar results between 1.8 and $1.9 \times 10^{-10}\mathrm{cm^3\,s^{-1}}$. Values are approximately 20 % lower than the experimentally derived reaction rate constants. However, differences are within the accuracy of SAR predictions.

6.2 Product yields of the reactions of myrcene hydroxy peroxy radicals with NO

When OH reacts with myrcene, about half (48 %) of the OH adds to the $-CH{=}C(CH_3)_2$ moiety and the other half (48 %) to the isoprenyl part (Peeters et al., 2007). In comparison,

Table 4. Rate constants of the myrcene + OH reaction at 298 K.

k cm^3 s^{-1}	Method	Reference
$(2.1 \pm 0.2) \times 10^{-10}$	relative rate technique	Atkinson et al. (1986)
$(3.4^{+1.5}_{-1.0}) \times 10^{-10}$	relative rate technique	Hites and Turner (2009)
1.8×10^{-10}	structure–activity relationship	Peeters et al. (2007)
1.9×10^{-10}	structure–activity relationship	Jenkin et al. (2018)
$(2.3 \pm 0.3) \times 10^{-10}$	direct measurement	this work

the SAR developed by Jenkin et al. (2018) predicts a branching ratio of 63 : 37 for OH addition to the $-CH=C(CH_3)_2$ and the isoprenyl part, consistent with the values reported in (Peeters et al., 2007). In this work, the branching ratio is adapted from Peeters et al. (2007) to be consistent with other studies. In the first case, 4-vinyl-4-pentenal and acetone are formed from the reaction of MyO_2 with NO (Sect. 2). In the second case, 2-methylidene-6-methyl-5-heptenal or 1-vinyl-5-methyl-4-hexenone is produced together with formaldehyde. Thus, the yields of acetone and formaldehyde are indicators for the yields of the OH addition to myrcene.

Acetone and formaldehyde yields are calculated from measured time series of product species and myrcene in the experiments on 16 and 22 August 2012, when NO mixing ratios were 200 pptv, so that > 90 % of RO_2 reacted with NO (Fig. 5). Only measurements after the first myrcene injection are used here to avoid that secondary chemistry impacts the yield determination. The two other experiments are not considered for three reasons. The large amount of ozone (up to 50 ppbv) would require considerable correction for myrcene ozonolysis. Second, due to the lower NO concentration, reactions of RO_2 with HO_2 would be competitive with the reaction of RO_2 with NO. Third, the smaller amount of injected myrcene produced fewer oxidation products.

Corrections are applied to measured myrcene, formaldehyde and acetone time series, in order to relate myrcene that reacted with OH and product species that are chemically formed from this reaction following the procedure described in previous work (Galloway et al., 2011; Kaminski et al., 2017). Product concentrations are corrected for losses due to dilution, photolysis and reaction with OH. In addition, formation of formaldehyde and acetone from chamber sources needs to be subtracted from the measured concentrations. Myrcene concentrations are also corrected for dilution and the fraction of myrcene that reacted with ozone. After corrections have been applied, the relationships between consumed myrcene and product concentrations are linear if species are mainly formed as first-generation products in the reaction of myrcene and OH. The slopes give acetone and formaldehyde yields of 0.45 ± 0.08 and 0.35 ± 0.08, respectively (Fig. 8). The error is caused by the uncertainty in the source strengths of chamber sources for acetone and formaldehyde and the accuracy of measurements.

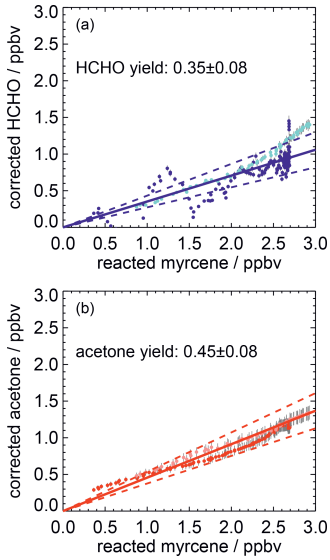

Figure 8. Corrected product concentrations vs. the myrcene that reacted away with OH for two experiments with medium NO (light colours: 16 August 2012, dark colours: 22 August 2012). Corrections are applied to account for formation of product species not connected to the oxidation of myrcene (chamber sources) and loss processes (reaction with OH, photolysis). The slopes of linear fits (solid lines) give the product yields of HCHO and acetone from the myrcene reaction with OH. The uncertainties of the yield calculations are indicated by dashed lines.

The acetone yield is in excellent agreement with SAR predictions that 48 % of the OH adds to the double bond of the $-CH=C(CH_3)_2$ moiety (Peeters et al., 2007). The formaldehyde yield of 0.35 ± 0.08 is lower than the SAR prediction for the OH attack to the isoprenyl part (0.48). One possible reason for the smaller-than-expected formaldehyde yield could be isomerization reactions of the myrcene peroxy radicals shown (Fig. 3), which may not lead to the production of HCHO. The estimated bulk isomerization rates of 0.097 and 0.21 s^{-1} (Sect. 2) are sufficiently fast to compete with the

Table 5. Products yields from the reaction of myrcene with OH. NA – not available

Product	Yield	Temperature/K	Reference
formaldehyde	0.30 ± 0.06	NA	Orlando et al. (2000)
	0.74 ± 0.08	294	Lee et al. (2006)
	0.35 ± 0.08	293–330	this work
acetone	0.36 ± 0.05	NA	Orlando et al. (2000)
	0.45 ± 0.06	296 ± 2	Reissell et al. (2002)
	0.22 ± 0.02	294	Lee et al. (2006)
	0.45 ± 0.08	293–330	this work
organic nitrate	0.10 ± 0.03	294	Lee et al. (2006)
	0.13 ± 0.03	293–330	this work

loss rate of $0.04\,s^{-1}$ for MyO_2 with 200 pptv of NO, so that the reduced formaldehyde yield could be fully explained by isomerization reaction pathways. A different explanation for the lower formaldehyde yield compared to acetone is that the nitrate yield is larger for the MyO_2 that would otherwise end up as formaldehyde. In fact, the total product yields is closed to unity (acetone (0.45 ± 0.08)+formaldehyde(0.35 ± 0.08)+ nitrate$(0.13 \pm 0.03) = 0.93 \pm 0.12$).

Acetone and formaldehyde yields agree with published results by Reissell et al. (2002) and Orlando et al. (2000) (Table 5). Lee et al. (2006) reported a smaller acetone yield of 0.22 ± 0.02 and a significantly higher HCHO yield of 0.74 ± 0.08. However, their HCHO yield carries a large uncertainty because concentrations were outside the range for which the instrument was calibrated.

The oxygenated organic compound 4-vinyl-4-pentenal has been detected in previous studies from the reaction of myrcene with OH (Reissell et al., 2002; Lee et al., 2006). Fragmentation in the PTR-MS and further oxidation of 4-vinyl-4-pentenal complicated the unambiguous yield determination. Therefore, Lee et al. (2006) reported a high yield of 0.4 but also stated a lower limit of 0.09. Acetone is the co-product of 4-vinyl-4-pentenal (Fig. 3). The high limit yield of 0.4 for 4-vinyl-4-pentenal by Lee et al. (2006) is therefore consistent with the acetone yield determined in this work. The yield of 4-vinyl-4-pentenal was also measured by Reissell et al. (2002), but a lower yield of 0.19 ± 0.04 was found. This low yield is apparently inconsistent with the yield of 0.45 ± 0.06 for the co-product acetone determined in the same experiments (Table 5). The authors suggest that there could be rearrangement of the hydroxyalkoxy radical that competes with the decomposition to 4-vinyl-4-pentenal but may still lead to acetone production, so that the yield for acetone could become higher than that of 4-vinyl-4-pentenal.

The yield of organic nitrate from reactions of MyO_2 with NO is determined from the analysis of reactive nitrogen oxides in the chamber as described in Sect. 4. This results in an organic nitrate yield of 0.13 ± 0.03 (Fig. 9). This value is consistent with the yield of 0.10 ± 0.03 reported by Lee et al. (2006), who directly measured organic nitrates by mass

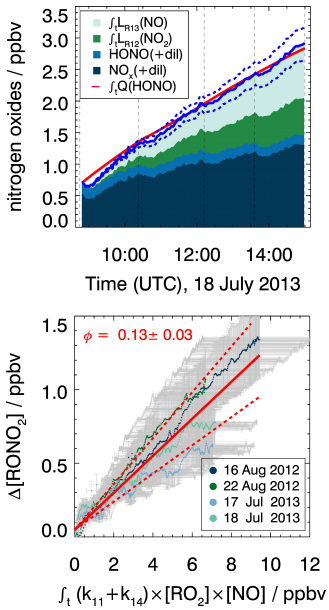

Figure 9. Determination of the organic nitrate yield from the production of nitrogen oxide species (Q(HONO)) in the chamber experiment. Upper panel: example of cumulated reactive nitrogen oxide mixing ratios over the course of the experiment on 18 July 2013. The blue line denotes the total production of nitrogen oxides including organic nitrate applying a nitrate yield (Φ_{RONO2}) of 0.13. Dashed lines show the error of the total nitrogen oxide calculation. Lower panel: scatter plot of the integrated turnover rate of the reaction of RO_2 with NO vs. the unaccounted nitrogen oxide mixing ratios (ΔNO_y, Eq. 8). Results from all four experiments are included. The organic nitrate yield is determined by the slope of regression analysis (red line, $R^2 = 0.92$). Error bars denote experimental uncertainty derived from the accuracy of the measurements (Table 2) and dashed red lines the resulting uncertainty in the slope of the regression analysis.

spectrometry. Values are lower than the yield expected from SAR described in Jenkin et al. (2019), which predicts a yield of 0.19 that would also apply for other monoterpenes, but may still be within the uncertainty of the SAR predictions. Like for the formaldehyde yield, the smaller-than-predicted organic nitrate yield may also be partly due to competing MyO_2 isomerization reactions.

6.3 Primary radical production and termination

The primary radical production is due to photolysis (Reactions R1 to R3) and ozonolysis reactions (Reaction R4). Production rates by photolysis of O_3, HONO and HCHO are calculated using measured trace gas concentrations and photol-

ysis frequencies. The calculation of the production rate from myrcene ozonolysis requires the knowledge of both the reaction rate constant (Sect. 6.1) and the yield of OH and RO_2 radicals. The uncertainty of yields is high. Values range from 0.71 determined from high-level quantum chemistry calculations and kinetic calculations (Deng et al., 2018) to experimental values of 1.15 with an uncertainty of a factor of 1.5 (Atkinson et al., 1992). It is worth noting that additional radicals could be produced from ozonolysis reactions of oxidation products at later times of the experiment because first-generation organic products from the reaction of myrcene with OH still contain C−C double bonds that can react with ozone.

The radical termination reactions include reactions with nitrogen oxides (Reactions R12–R14) and radical self-reactions (Reactions R15, R16). Loss of radicals in the reaction with NO_x and the HO_2 self-reaction contributes less than 1 ppbv h^{-1} to the total loss rate each. Contributions from RO_2 self-reactions are expected to be negligible (< 2 %) because their reaction rate constants are typically much smaller than those of $RO_2 + HO_2$ reactions (Table 3). The reaction rate constant of the $MyO_2 + HO_2$ reaction is estimated from SAR by Jenkin et al. (2019), and, therefore, the value could also have a high uncertainty.

In the experiment with medium NO concentrations (22 August 2012), the total radical production is low, with values of less than 1.5 ppbv h^{-1}, and radical production and destruction are balanced (Fig. 10). No ozone is added, so that radical production from ozonolysis plays a minor role, and radical loss by radical recombination is suppressed due to the competition of peroxy radical reactions with NO. Therefore, the uncertainties in the radical yield of myrcene ozonolysis and the reaction rate constant of the $MyO_2 + HO_2$ reaction do not impact the results.

In contrast, radical production and destruction rates in experiments performed at low NO concentrations (17 July 2013, 18 July 2013), which is achieved by suppressing NO in the reaction with O_3, are dominated by radical production from myrcene ozonolysis and radical destruction by $MyO_2 + HO_2$ reactions right after the injection of myrcene. Taking the upper limit of the radical yield from the ozonolysis reaction of 1.42 (0.71 for OH and 0.71 for MyO_2), the production is 4 ppbv h^{-1}. The radical primary production could be smaller if the unspecified radical yield of 1.15 suggested by Atkinson et al. (1992) is applied. Applying the reaction rate constant of the $MyO_2 + HO_2$ derived by SAR (Sect. 2) results in a maximum radical loss rate of 13.5 ppbv h^{-1} also right after the injection of myrcene when MyO_2 concentrations are highest. Because this high destruction rate cannot be balanced by radical production, either the reaction rate constant must be lower than SAR predictions or there are reaction pathways that do not lead to radical termination products (organic peroxide) but regenerate radicals. Due to the high uncertainty of radical production from ozonolysis in these experiments, no firm conclusion can be drawn. The reaction rate constant would need to be reduced between a factor of 0.4 and 0.7 (0.9 to 1.6×10^{-11} cm^3 s^{-1} ($T = 298$ K, Table 3) or the yield of radical products would need to be in the range of 0.3 and 0.6 to match the range of radical production.

A reduced $MyO_2 + HO_2$ reaction rate constant is significantly different from the SAR predictions by Jenkin et al. (2019). The SAR value is similar for all monoterpenes and agrees well with direct measurements for the reaction rate constant of HO_2 with RO_2 derived from α-pinene (2.1×10^{-11} cm^3 s^{-1}), γ-terpinene (2.0×10^{-11} cm^3 s^{-1}) and limonene (2.1×10^{-11} cm^3 s^{-1}) reported by Boyd et al. (2003). A high yield of radical products from the $MyO_2 + HO_2$ reaction may not be expected from analogies of isoprene and 2-methyl-2-butene (Liu et al., 2013; Paulot et al., 2009). For these reasons there is no clear conclusion on how exactly rate constants and yields need to be adjusted to balance the RO_x production and destruction rates.

6.4 RO_x radical chain propagation reactions

The total production and loss rates of OH, HO_2 and RO_2 radicals do not exhibit much variability over the course of the experiments with medium NO concentrations (Figs. 11 and S7 in the Supplement). In the experiments with low NO, the turnover rates of radical production and destruction reactions for OH, HO_2, and RO_2 exhibit peak values when myrcene is injected (Figs. 12 and S8 in the Supplement). This distinct feature is related to the elevated radical production of up to 2 ppbv h^{-1} from the ozonolysis of myrcene and peak concentrations of peroxy radical concentrations.

Production and destruction rates of OH radicals are balanced within the accuracies of the calculation in all experiments. Rates are similar in all experiments with values around 4 ppbv h^{-1}. Maximum RO_2 turnover rates are lower (2 to 3 ppbv h^{-1}) compared to those of OH and HO_2, because up to 25 % of the OH radicals are directly converted to HO_2, for example in the reaction of OH with CO or HCHO. Because myrcene is consumed within a few hours, the turnover rate of RO_2 is decreasing over time after each myrcene injection. In experiments with medium NO concentrations, HO_2 radical production and destruction rates are not balanced by 0.5 of 1.5 ppbv h^{-1} in contrast to those of OH. Discrepancies, however, are only slightly larger than the 1-σ uncertainty of the calculated values. The total uncertainty is dominated by the accuracy of RO_2 measurements because of the low detection sensitivity of the instrument for MyO_2 and the uncertainty in the sensitivity of other RO_2 formed from oxidation products that are dominant, once myrcene reacted away.

Even higher discrepancies of up to 2 ppbv h^{-1} between HO_2 and RO_2 production and destruction rates are observed in the experiments with low NO mixing ratios. Values are highest right after each myrcene injection, with the HO_2 production rate being lower than the destruction rate and the RO_2 destruction rate being higher than the production rate.

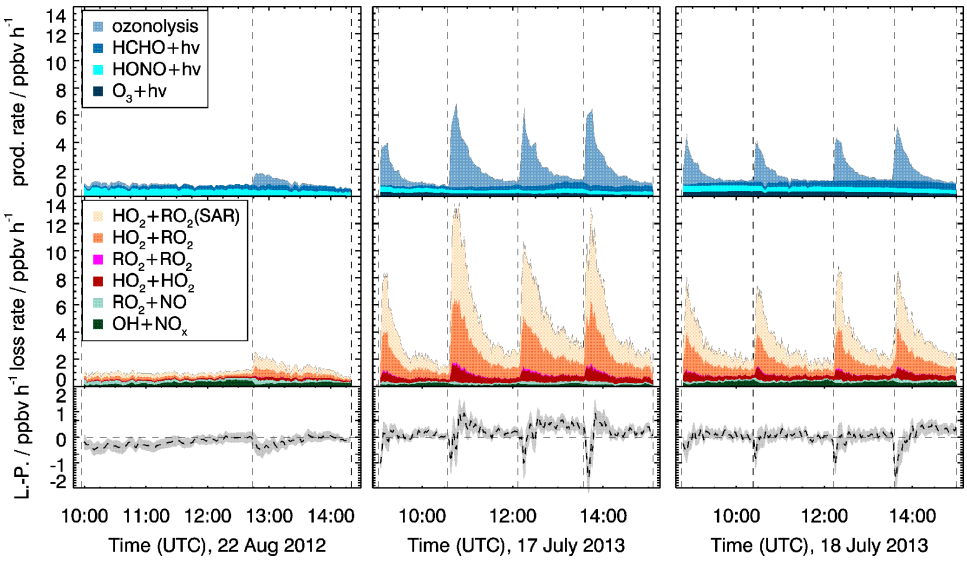

Figure 10. RO_x primary production P (upper panels), termination L (middle panels) rates and their difference (lower panels). The rate constant of the reaction of MyO_2 with HO_2 was adjusted to minimize the difference between radical production and destruction (see text for more explanation). The $HO_2 + RO_2$ (SAR) shows the additional radical loss if the unadjusted reaction rate constant is applied. In the bottom row, the lines show the difference between radical destruction and production ($L - P$), with the adjusted rate constant of the reaction of MyO_2 with HO_2. Grey areas in the lower panels give the uncertainty of $L - P$.

Because differences are highest when the chemical system is dominated by the oxidation of myrcene and therefore the presence of MyO_2, reaction pathways of MyO_2 other than reactions with NO and HO_2 could be responsible for the imbalances.

As described in Sect. 2, MyO_2 isomerization reactions can become competitive at low NO mixing ratios like in these experiments (< 0.1 ppbv). Isomerization rates derived from SAR are applied (Sect. 2). Products of the 1,6-H-shift reactions in myrcene that correspond to similar reactions in isoprene could produce radicals like in the case of isoprene (Fig. 3). Products from the two additional isomerization reactions likely undergo fast ring-closure reactions on the dimethyl double bond, and it is uncertain whether OH or HO_2 are directly produced. As an estimate for the potential impact of MyO_2 isomerization reactions on radical regeneration, production of one HO_x radical from each isomerization reaction is assumed in the following. Because the yield of OH and HO_2 from potential isomerization and decomposition reactions of MyO_2 is not known, an upper limit of one OH and one HO_2 radical for each isomerization reaction is applied. The results of this sensitivity analysis are shown in Figs. 11 and 12.

The bulk MyO_2 loss due to isomerization for the isomers that can rapidly interconvert (Fig. 2) is competitive with the reaction of MyO_2 with NO at mixing ratios of 0.5 to 1 ppbv, making these reaction very competitive for conditions of the experiments. As shown in Fig. 12, the discrepancy between RO_2 radical production and destruction rates would even be overcompensated for if isomerization rates determined by SAR are applied. Similar as for the RO_2 loss rate, potential production of OH and HO_2 from MyO_2 isomerization reactions would overcompensate for the imbalances in their production and destruction rates. A sensitivity test shows that using a bulk isomerization reaction rate constant of $0.05\,s^{-1}$ instead of $0.02\,s^{-1}$ would be sufficient to balance the RO_2 production rate. This value is a factor 2 to 4 lower than bulk reaction rates calculated by SAR but still within the uncertainty of calculations.

Although this analysis shows the potential for high contributions of MyO_2 isomerization to the total loss rate of RO_2 for conditions that are typical for forested areas, the uncertainties are high concerning the isomerization rate constants and the yield of HO_x radicals. In addition, discrepancies of radical production and destruction rates within the range of 20 % of the total rate for single radical species can be observed even for well-known chemical systems as methane as shown in Sect. 5.2. This is likely due to uncertainties in the radical concentration measurements. Unaccounted systematic errors in the analysis may therefore also explain a

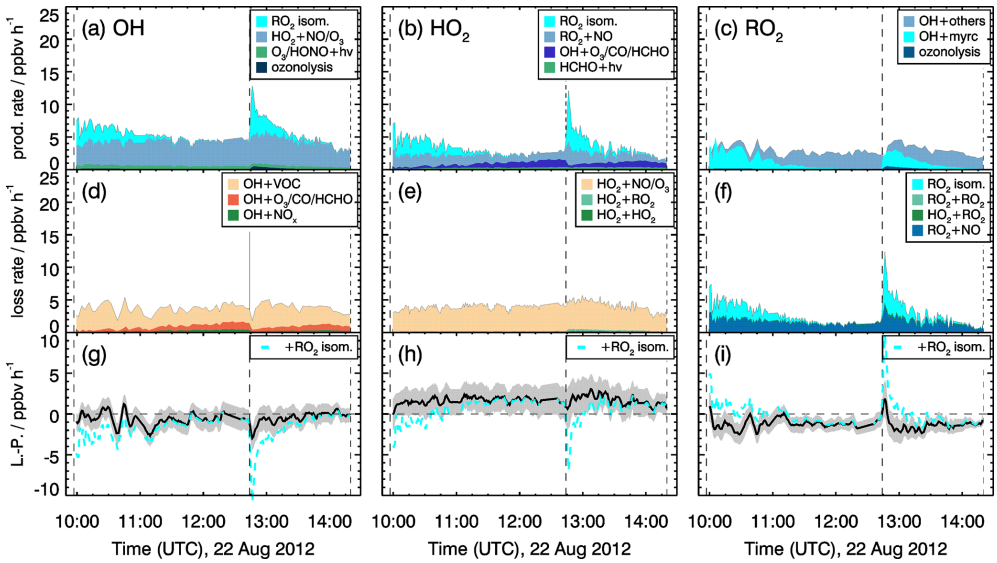

Figure 11. Rates of radical conversion reactions and imbalances between production and destruction rates ($L - P$) for the experiment with medium NO mixing ratios (0.15 to 0.30 ppbv) on 22 August 2012. Grey areas in the lower panels give the uncertainty of the calculation ($L - P$). In the bottom row, the black and cyan lines denote the radical budget with and without considering MyO_2 isomerization reactions. Upper limits for yields of OH and HO_2 radicals from MyO_2 isomerization reactions of one are assumed in the calculations of their production rates.

significant fraction of the differences in radical production and destruction rates in the experiments with myrcene.

7 Summary and conclusions

The photo-oxidation of the monoterpene myrcene was investigated at atmospheric conditions in the simulation chamber SAPHIR at two different levels of NO. The chemical mechanism of the oxidation of myrcene by OH has not been investigated in detail so far. Based on the structural similarity with isoprene (CH_2=CH−C(=CH_2)CH_2− moiety) and with 2-methyl-2-butene (−CH_2−CH=C(CH_3)$_2$ moiety) and the structure–activity relationship (Peeters et al., 2007; Jenkin et al., 2019; Vereecken and Nozière, 2020), a chemical mechanism for the first oxidation step is proposed that includes rapid RO_2 interconversion by reversible oxygen addition and H-shift reactions of RO_2 like in isoprene. In addition to RO_2 isomerization reactions similar to that of isoprene-derived RO_2, additional H-shift reactions are suggested by SAR, so that the overall impact of isomerization reactions in myrcene can be high, although only approximately half of the attack of OH to myrcene is on the isoprenyl part. Assuming that the interconversion of RO_2 is similar to that in isoprene, bulk isomerization rate constants of 0.21 and 0.097 s^{-1} ($T = 298$ K) for the three isomers resulting from the 3′-OH and 1-OH addition, respectively, are calculated using rate constants derived by SAR.

Experiments in the chamber allowed us to determine the reaction rate constant of the reaction of myrcene with OH resulting in a value of $(2.3 \pm 0.3) \times 10^{-10}$ cm^3 s^{-1}, which is in good agreement with values reported in the literature within the uncertainties (Table 4). Product yields of acetone and formaldehyde calculated from measured time series of these species were found to be 0.45 ± 0.08 and 0.35 ± 0.08, respectively. Although these values agree well with studies by Reissell et al. (2002), as well as Orlando et al. (2000) within the uncertainties, the formaldehyde yield is lower than expected for conditions of the experiment with NO mixing ratios of 200 pptv if there are no RO_2 isomerization reactions. The lower yield would be consistent with competing RO_2 isomerization reactions that may not produce formaldehyde. From the analysis of nitrogen oxides in the chamber, the yield of organic nitrates in the myrcene oxidation could be determined to be 0.13 ± 0.03, in agreement with measurements by Lee et al. (2006) (0.10 ± 0.03). Both values are lower than typical values predicted by SAR (0.19, Jenkin et al., 2019) and found for monoterpene species which often range between 0.15 and 0.25. This may impact the formation of secondary organic aerosol from the OH oxidation of myrcene compared

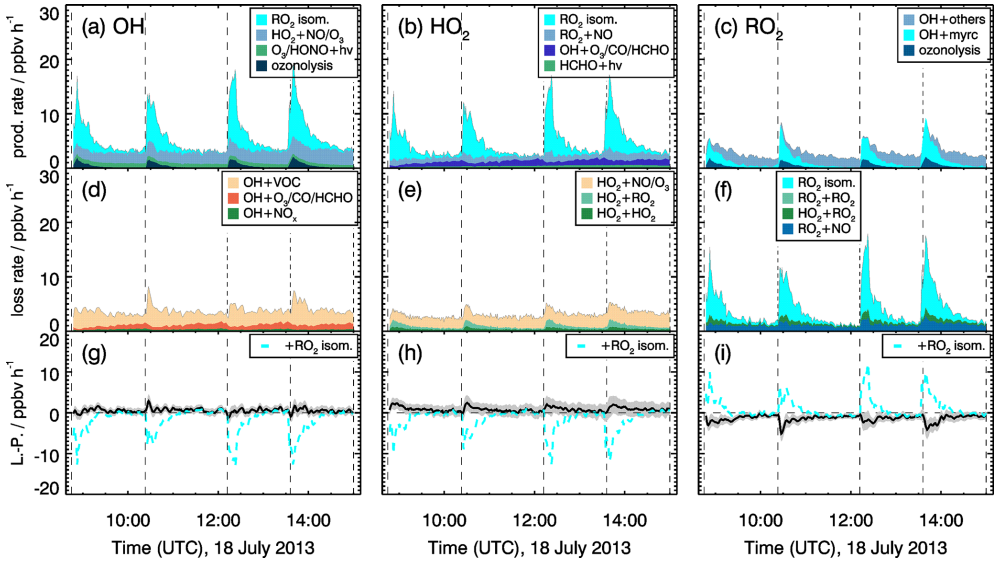

Figure 12. Rates of radical production and destruction reactions for OH, HO_2 and RO_2 for experiments at low NO mixing ratio (< 0.11 ppbv) on 18 July 2013. Grey areas in the lower panels give the uncertainty of $L - P$. In the bottom row, the black and cyan lines denote the radical budget with and without considering MyO_2 isomerization reactions. Upper limits for yields of OH and HO_2 radicals from MyO_2 isomerization reactions of one are assumed in the calculations of their production rates.

to other monoterpene species. The applicability of the procedure for the determination of the organic nitrate yield was tested in photo-oxidation experiments with methane and α-pinene, both of which resulted in organic nitrate yields that agree well with expected values. This demonstrates that the method gives reliable results and can be applied in chamber experiments.

Radical production and destruction rates can be calculated using measured radical and trace gas concentrations. Total radical (RO_x) production and destruction rates are balanced in the experiments in this work if the rate of the radical loss terminating the radical reaction chain due to recombination reactions of HO_2 and RO_2 was only 40 % of the loss expected from the reaction rate constant predicted by SAR or if this reaction would regenerate radicals instead of producing radical termination products (hydroperoxides). However, this conclusion has a high uncertainty of approximately a factor of 2 due to the uncertainty of radical production from myrcene ozonolysis.

Imbalances between radical production and destruction rates are observed for RO_2 radicals in the experiments with low NO concentrations, when the MyO_2 isomerization reaction can become competitive with bimolecular reactions. Bulk reaction rate constants around 0.05 s^{-1} for MyO_2 isomers which can quickly interconvert and which partly can isomerize are a factor of 2 to 4 lower than reaction rate constants calculated by SAR, but values are consistent regarding the high uncertainty of the determination from experiments and the uncertainty of SAR calculations.

The analysis of radical concentration measurements in field campaigns, where monoterpene emissions dominated the mix of organic compounds such as in Finland (Hens et al., 2014) and in the Rocky Mountains (Kim et al., 2013), showed that current chemical models cannot explain measured OH and HO_2 concentrations. The analysis of chamber experiments revealed that the OH oxidation of the most abundant monoterpene species α-pinene and β-pinene is not well understood (Kaminski et al., 2017; Rolletter et al., 2019). Experiments here show that also the reaction of OH with myrcene is complex due to the rapid RO_2 interconversion and H-shift RO_2 reactions. Therefore, shortcomings in the description of the photo-oxidation of myrcene could contribute to explaining model–measurement discrepancies found in field campaigns.

Data availability. Data are available from the EUROCHAMP database (16 August 2012: https://doi.org/10.25326/5XRG-Y765, Fuchs et al., 2021a; 22 August 2012: https://doi.org/10.25326/9RAV-5450, Fuchs et al., 2021b; 17 July 2013: https://doi.org/10.25326/GP2K-R926, Fuchs et al., 2021c;

18 July 2013: https://doi.org/10.25326/JJ16-1S54, Fuchs et al., 2021d; 3 September 2019: https://doi.org/10.25326/PBBV-WF18, Fuchs et al., 2021e; 29 May 2020: https://doi.org/10.25326/MG6T-TW58, Fuchs et al., 2021f).

Supplement. The supplement related to this article is available online at: https://doi.org/10.5194/acp-21-16067-2021-supplement.

Author contributions. ZT, LH and HF wrote the manuscript. MK, RW and HF designed and led the experiments in the chamber. IA (organic compounds), BB (radiation), HPD (radicals), XL (HONO), SN (OH reactivity), FR (nitrogen oxides, ozone), RT (organic compounds), AN (radicals) and CC (radicals) were responsible for measurements used in this work. All co-authors commented and discussed the manuscript and contributed to the writing of the manuscript.

Competing interests. Some authors are members of the editorial board of *Atmospheric Chemistry and Physics*. The peer-review process was guided by an independent editor, and the authors have also no other competing interests to declare.

Disclaimer. Publisher's note: Copernicus Publications remains neutral with regard to jurisdictional claims in published maps and institutional affiliations.

Special issue statement. This article is part of the special issue "Simulation chambers as tools in atmospheric research (AMT/ACP/GMD inter-journal SI)". It is not associated with a conference.

Acknowledgements. The authors thank Luc Vereecken for the discussion of the chemical mechanism.

Financial support. This research has been supported by the H2020 Excellent Science (SARLEP, grant no. 681529), the European Commission's Seventh Framework Programme (EUROCHAMP-2, grant no. 228335), and the Deutsche Forschungsgemeinschaft (grant no. 1580/3-1).

The article processing charges for this open-access publication were covered by the Forschungszentrum Jülich.

Review statement. This paper was edited by Allan Bertram and reviewed by two anonymous referees.

References

Allen, H. M., Crounse, J. D., Bates, K. H., Teng, A. P., Krawiec-Thayer, M. P., Rivera-Rios, J. C., Keutsch, F. N., St. Clair, J. M., Hanisco, T. F., Møller, K. H., Kjaergaard, H. G., and Wennberg, P. O.: Kinetics and product yields of the OH initiated oxidation of hydroxymethyl hydroperoxide, J. Phys. Chem. A, 122, 6292–6302, https://doi.org/10.1021/acs.jpca.8b04577, 2018.

Aschmann, S. M., Atkinson, R., and Arey, J.: Products of reaction of OH radicals with α-pinene, J. Geophys. Res., 107, ACH 6-1–ACH 6-7, https://doi.org/10.1029/2001JD001098, 2002.

Atkinson, R.: Gase-phase tropospheric chemistry of volatile organic compounds: 1. alkanes and alkenes, J. Phys. Chem. Ref. Data, 26, 217–290, 1997.

Atkinson, R. and Arey, J.: Atmospheric degradation of volatile organic compounds, Chem. Rev., 103, 4605–4638, https://doi.org/10.1021/cr0206420, 2003.

Atkinson, R., Aschmann, S. M., and Pitts, J. N.: Rate constants for the gas-phase reactions of the OH radical with a series of monoterpenes at 294 ± 1 K, Int. J. Chem. Kinet., 18, 287–299, https://doi.org/10.1002/kin.550180303, 1986.

Atkinson, R., Aschmann, S. M., Arey, J., and Shorees, B.: Formation of OH radicals in the gas phase reactions of O_3 with a series of terpenes, J. Geophys. Res., 97, 6065–6073, https://doi.org/10.1029/92jd00062, 1992.

Atkinson, R., Baulch, D. L., Cox, R. A., Crowley, J. N., Hampson, R. F., Hynes, R. G., Jenkin, M. E., Rossi, M. J., and Troe, J.: Evaluated kinetic and photochemical data for atmospheric chemistry: Volume I – gas phase reactions of O_x, HO_x, NO_x and SO_x species, Atmos. Chem. Phys., 4, 1461–1738, https://doi.org/10.5194/acp-4-1461-2004, 2004.

Böge, O., Mutzel, A., Iinuma, Y., Yli-Pirilä, P., Kahnt, A., Joutsensaari, J., and Herrmann, H.: Gas-phase products and secondary organic aerosol formation from the ozonolysis and photooxidation of myrcene, Atmos. Environ., 79, 553–560, https://doi.org/10.1016/j.atmosenv.2013.07.034, 2013.

Bohn, B. and Zilken, H.: Model-aided radiometric determination of photolysis frequencies in a sunlit atmosphere simulation chamber, Atmos. Chem. Phys., 5, 191–206, https://doi.org/10.5194/acp-5-191-2005, 2005.

Bohn, B., Rohrer, F., Brauers, T., and Wahner, A.: Actinometric measurements of NO_2 photolysis frequencies in the atmosphere simulation chamber SAPHIR, Atmos. Chem. Phys., 5, 493–503, https://doi.org/10.5194/acp-5-493-2005, 2005.

Boyd, A. A., Flaud, P.-M., Daugey, N., and Lesclaux, R.: Rate constants for $RO_2 + HO_2$ reactions measured under a large excess of HO_2, J. Phys. Chem. A, 107, 818–821, https://doi.org/10.1021/jp026581r, 2003.

Browne, E. C., Wooldridge, P. J., Min, K.-E., and Cohen, R. C.: On the role of monoterpene chemistry in the remote continental boundary layer, Atmos. Chem. Phys., 14, 1225–1238, https://doi.org/10.5194/acp-14-1225-2014, 2014.

Burkholder, J. B., Sander, S. P., Abbatt, J. P. D., Barker, J. R., Huie, R. E., Kolb, C. E., Kurylo, M. J., Orkin, V. L., Wilmouth, D. M., and Wine, P. H.: Chemical kinetics and photochemical data for use in atmospheric studies–evaluation number 19, available at: https://jpldataeval.jpl.nasa.gov/pdf/NASA-JPL%20Evaluation%2019-5.pdf (last access: 27 Octo-

ber 2021), Nasa panel for data evaluation technical report, 19-5, 2020.

Butkovskaya, N., Kukui, A., and Le Bras, G.: Pressure and temperature dependence of methyl nitrate formation in the $CH_3O_2 + NO$ reaction, J. Phys. Chem. A, 116, 5972–5980, https://doi.org/10.1021/jp210710d, 2012.

Crounse, J. D., Knap, H. C., Ornso, K. B., Jorgensen, S., Paulot, F., Kjaergaard, H. G., and Wennberg, P. O.: On the atmospheric fate of methacrolein: 1. Peroxy radical isomerization following addition of OH and O_2, J. Phys. Chem. A, 116, 5756–5762, https://doi.org/10.1021/jp211560u, 2012.

Crounse, J. D., Nielsen, L. B., Jørgensen, S., Kjaergaard, H. G., and Wennberg, P. O.: Autoxidation of organic compounds in the atmosphere, J. Phys. Chem. Lett., 4, 3513–3520, https://doi.org/10.1021/jz4019207, 2013.

Deng, P., Wang, L., and Wang, L.: Mechanism of gas-phase ozonolysis of β-myrcene in the atmosphere, J. Phys. Chem. A, 122, 3013–3020, https://doi.org/10.1021/acs.jpca.8b00983, 2018.

Dorn, H.-P., Brandenburger, U., Brauers, T., and Hausmann, M.: A new in-situ laser long-path absorption instrument for the measurement of tropospheric OH radicals, J. Atmos. Sci., 52, 3373–3380, 1995.

Fuchs, H., Hofzumahaus, A., and Holland, F.: Measurement of tropospheric RO_2 and HO_2 radicals by a laser-induced fluorescence instrument, Rev. Sci. Instrum., 79, 084104, https://doi.org/10.1063/1.2968712, 2008.

Fuchs, H., Bohn, B., Hofzumahaus, A., Holland, F., Lu, K. D., Nehr, S., Rohrer, F., and Wahner, A.: Detection of HO_2 by laser-induced fluorescence: calibration and interferences from RO_2 radicals, Atmos. Meas. Tech., 4, 1209–1225, https://doi.org/10.5194/amt-4-1209-2011, 2011.

Fuchs, H., Hofzumahaus, A., Rohrer, F., Bohn, B., Brauers, T., Dorn, H.-P., Häseler, R., Holland, F., Kaminski, M., Li, X., Lu, K., Nehr, S., Tillmann, R., Wegener, R., and Wahner, A.: Experimental evidence for efficient hydroxyl radical regeneration in isoprene oxidation, Nat. Geosci., 6, 1023–1026, https://doi.org/10.1038/NGEO1964, 2013.

Fuchs, H., Acir, I.-H., Bohn, B., Brauers, T., Dorn, H.-P., Häseler, R., Hofzumahaus, A., Holland, F., Kaminski, M., Li, X., Lu, K., Lutz, A., Nehr, S., Rohrer, F., Tillmann, R., Wegener, R., and Wahner, A.: OH regeneration from methacrolein oxidation investigated in the atmosphere simulation chamber SAPHIR, Atmos. Chem. Phys., 14, 7895–7908, https://doi.org/10.5194/acp-14-7895-2014, 2014.

Fuchs, H., Tan, Z., Hofzumahaus, A., Broch, S., Dorn, H.-P., Holland, F., Künstler, C., Gomm, S., Rohrer, F., Schrade, S., Tillmann, R., and Wahner, A.: Investigation of potential interferences in the detection of atmospheric RO_x radicals by laser-induced fluorescence under dark conditions, Atmos. Meas. Tech., 9, 1431–1447, https://doi.org/10.5194/amt-9-1431-2016, 2016.

Fuchs, H., Tan, Z., Lu, K., Bohn, B., Broch, S., Brown, S. S., Dong, H., Gomm, S., Häseler, R., He, L., Hofzumahaus, A., Holland, F., Li, X., Liu, Y., Lu, S., Min, K.-E., Rohrer, F., Shao, M., Wang, B., Wang, M., Wu, Y., Zeng, L., Zhang, Y., Wahner, A., and Zhang, Y.: OH reactivity at a rural site (Wangdu) in the North China Plain: contributions from OH reactants and experimental OH budget, Atmos. Chem. Phys., 17, 645–661, https://doi.org/10.5194/acp-17-645-2017, 2017.

Fuchs, H., Albrecht, S., Acir, I., Bohn, B., Breitenlechner, M., Dorn, H.-P., Gkatzelis, G. I., Hofzumahaus, A., Holland, F., Kaminski, M., Keutsch, F. N., Novelli, A., Reimer, D., Rohrer, F., Tillmann, R., Vereecken, L., Wegener, R., Zaytsev, A., Kiendler-Scharr, A., and Wahner, A.: Investigation of the oxidation of methyl vinyl ketone (MVK) by OH radicals in the atmospheric simulation chamber SAPHIR, Atmos. Chem. Phys., 18, 8001–8016, https://doi.org/10.5194/acp-18-8001-2018, 2018.

Fuchs, H., Kaminski, M., Acir, I.-H., Bohn, B., Dorn, H.-P., Nehr, S., Rohrer, F., Tillmann, R., Wegener, R., and Li, X.: Atmospheric simulation chamber study: myrcene + OH – Gas-phase oxidation – product study, AERIS [data set], https://doi.org/10.25326/5XRG-Y765, 2021a.

Fuchs, H., Kaminski, M., Acir, I.-H., Bohn, B., Dorn, H.-P., Nehr, S., Rohrer, F., Tillmann, R., Wegener, R., and Li, X.: Atmospheric simulation chamber study: myrcene + OH – Gas-phase oxidation – product study, AERIS [data set], https://doi.org/10.25326/9RAV-5450, 2021b.

Fuchs, H., Kaminski, M., Acir, I.-H., Bohn, B., Dorn, H.-P., Nehr, S., Rohrer, F., Tillmann, R., Wegener, R., and Li, X.: Atmospheric simulation chamber study: myrcene + OH – Gas-phase oxidation – product study, AERIS [data set], https://doi.org/10.25326/GP2K-R926, 2021c.

Fuchs, H., Kaminski, M., Acir, I.-H., Bohn, B., Dorn, H.-P., Nehr, S., Rohrer, F., Tillmann, R., Wegener, R., and Li, X.: Atmospheric simulation chamber study: myrcene + OH – Gas-phase oxidation – product study, AERIS [data set], https://doi.org/10.25326/JJ16-1S54, 2021d.

Fuchs, H., Bohn, B., Rohrer, F., Tillmann, R., Cho, C., and Novelli, A.: Atmospheric simulation chamber study: alpha-pinene + OH – Gas-phase oxidation – product study, AERIS [data set], https://doi.org/10.25326/PBBV-WF18, 2021e.

Fuchs, H., Rohrer, F., Bohn, B., Cho, C., and Novelli, A.: Atmospheric simulation chamber study: myrcene + OH – Reference experiment, AERIS [data set], https://doi.org/10.25326/MG6T-TW58, 2021f.

Galloway, M. M., Huisman, A. J., Yee, L. D., Chan, A. W. H., Loza, C. L., Seinfeld, J. H., and Keutsch, F. N.: Yields of oxidized volatile organic compounds during the OH radical initiated oxidation of isoprene, methyl vinyl ketone, and methacrolein under high-NO_x conditions, Atmos. Chem. Phys., 11, 10779–10790, https://doi.org/10.5194/acp-11-10779-2011, 2011.

Glowania, M., Rohrer, F., Dorn, H.-P., Hofzumahaus, A., Holland, F., Kiendler-Scharr, A., Wahner, A., and Fuchs, H.: Comparison of formaldehyde measurements by Hantzsch, CRDS and DOAS in the SAPHIR chamber, Atmos. Meas. Tech., 14, 4239–4253, https://doi.org/10.5194/amt-14-4239-2021, 2021.

Grimsrud, E. P., Westberg, H. H., and Rasmussen, R. A.: Atmospheric reactivity of monoterpene hydrocarbons, NO, photooxidation and ozonolysis, Int. J. Chem. Kinet., 7, Suppl. 1, 183–195, 1975.

Guenther, A. B., Jiang, X., Heald, C. L., Sakulyanontvittaya, T., Duhl, T., Emmons, L. K., and Wang, X.: The Model of Emissions of Gases and Aerosols from Nature version 2.1 (MEGAN2.1): an extended and updated framework for modeling biogenic emissions, Geosci. Model Dev., 5, 1471–1492, https://doi.org/10.5194/gmd-5-1471-2012, 2012.

Helmig, D., Daly, R. W., Milford, J., and Guenther, A.: Seasonal trends of biogenic terpene emissions, Chemosphere, 93, 35–46, https://doi.org/10.1016/j.chemosphere.2013.04.058, 2013.

Hens, K., Novelli, A., Martinez, M., Auld, J., Axinte, R., Bohn, B., Fischer, H., Keronen, P., Kubistin, D., Nölscher, A. C., Oswald, R., Paasonen, P., Petäjä, T., Regelin, E., Sander, R., Sinha, V., Sipilä, M., Taraborrelli, D., Tatum Ernest, C., Williams, J., Lelieveld, J., and Harder, H.: Observation and modelling of HO_X radicals in a boreal forest, Atmos. Chem. Phys., 14, 8723–8747, https://doi.org/10.5194/acp-14-8723-2014, 2014.

Hites, R. A. and Turner, A. M.: Rate constants for the gas-phase β-myrcene + OH and isoprene + OH reactions as a function of temperature, Int. J. Chem. Kinet., 41, 407–413, https://doi.org/10.1002/kin.20413, 2009.

Hofzumahaus, A., Rohrer, F., Lu, K., Bohn, B., Brauers, T., Chang, C.-C., Fuchs, H., Holland, F., Kita, K., Kondo, Y., Li, X., Lou, S., Shao, M., Zeng, L., Wahner, A., and Zhang, Y.: Amplified trace gas removal in the troposphere, Science, 324, 1702–1704, https://doi.org/10.1126/science.1164566, 2009.

IUPAC: IUPAC Task Group on Atmospheric Chemical Kinetic Data Evaluation, available at: https://iupac-aeris.ipsl.fr/, last access: 23 November 2020.

Jenkin, M. E., Valorso, R., Aumont, B., Rickard, A. R., and Wallington, T. J.: Estimation of rate coefficients and branching ratios for gas-phase reactions of OH with aliphatic organic compounds for use in automated mechanism construction, Atmos. Chem. Phys., 18, 9297–9328, https://doi.org/10.5194/acp-18-9297-2018, 2018.

Jenkin, M. E., Valorso, R., Aumont, B., and Rickard, A. R.: Estimation of rate coefficients and branching ratios for reactions of organic peroxy radicals for use in automated mechanism construction, Atmos. Chem. Phys., 19, 7691–7717, https://doi.org/10.5194/acp-19-7691-2019, 2019.

Kaminski, M., Fuchs, H., Acir, I.-H., Bohn, B., Brauers, T., Dorn, H.-P., Häseler, R., Hofzumahaus, A., Li, X., Lutz, A., Nehr, S., Rohrer, F., Tillmann, R., Vereecken, L., Wegener, R., and Wahner, A.: Investigation of the β-pinene photooxidation by OH in the atmosphere simulation chamber SAPHIR, Atmos. Chem. Phys., 17, 6631–6650, https://doi.org/10.5194/acp-17-6631-2017, 2017.

Kim, D., Stevens, P. S., and Hites, R. A.: Rate constants for the gas-phase reactions of OH and O_3 with β-ocimene, β-myrcene, and α- and β-farnesene as a function of temperature, J. Chem. Phys. A, 115, 500–506, https://doi.org/10.1021/jp111173s, 2011.

Kim, S., Wolfe, G. M., Mauldin, L., Cantrell, C., Guenther, A., Karl, T., Turnipseed, A., Greenberg, J., Hall, S. R., Ullmann, K., Apel, E., Hornbrook, R., Kajii, Y., Nakashima, Y., Keutsch, F. N., DiGangi, J. P., Henry, S. B., Kaser, L., Schnitzhofer, R., Graus, M., Hansel, A., Zheng, W., and Flocke, F. F.: Evaluation of HO_X sources and cycling using measurement-constrained model calculations in a 2-methyl-3-butene-2-ol (MBO) and monoterpene (MT) dominated ecosystem, Atmos. Chem. Phys., 13, 2031–2044, https://doi.org/10.5194/acp-13-2031-2013, 2013.

Kostiainen, R.: Volatile organic compounds in the indoor air of normal and sick houses, Atmos. Environ., 29, 693–702, https://doi.org/10.1016/1352-2310(94)00309-9, 1995.

Lee, A., Goldstein, A. H., Kroll, J. H., Ng, N. L., Varutbangkul, V., Flagan, R. C., and Seinfeld, J. H.: Gas-phase products and secondary aerosol yields from the photooxidation of 16 different terpenes, J. Geophys. Res., 111, D17305, https://doi.org/10.1029/2006JD007050, 2006.

Lelieveld, J., Butler, T. M., Crowley, J. N., Dillon, T. J., Fischer, H., Ganzeveld, L., Harder, H., Lawrence, M. G., Martinez, M., Taraborrelli, D., and Williams, J.: Atmospheric oxidation capacity sustained by a tropical forest, Nature, 452, 737–740, https://doi.org/10.1038/nature06870, 2008.

Li, X., Rohrer, F., Hofzumahaus, A., Brauers, T., Häseler, R., Bohn, B., Broch, S., Fuchs, H., Gomm, S., Holland, F., Jäger, J., Kaiser, J., Keutsch, F. N., Lohse, I., Lu, K., Tillmann, R., Wegener, R., Wolfe, G. M., Mentel, T. F., Kiendler-Scharr, A., and Wahner, A.: Missing gas-phase source of HONO inferred from Zeppelin measurements in the troposphere, Science, 344, 292–296, https://doi.org/10.1126/science.1248999, 2014.

Liu, Y. J., Herdlinger-Blatt, I., McKinney, K. A., and Martin, S. T.: Production of methyl vinyl ketone and methacrolein via the hydroperoxyl pathway of isoprene oxidation, Atmos. Chem. Phys., 13, 5715–5730, https://doi.org/10.5194/acp-13-5715-2013, 2013.

Lockhart, J., Blitz, M., Heard, D., Seakins, P., and Shannon, R.: Kinetic study of the OH + glyoxal reaction: Experimental evidence and quantification of direct OH recycling, J. Phys. Chem. A, 117, 11027–11037, https://doi.org/10.1021/jp4076806, 2013.

Lou, S., Holland, F., Rohrer, F., Lu, K., Bohn, B., Brauers, T., Chang, C. C., Fuchs, H., Häseler, R., Kita, K., Kondo, Y., Li, X., Shao, M., Zeng, L., Wahner, A., Zhang, Y., Wang, W., and Hofzumahaus, A.: Atmospheric OH reactivities in the Pearl River Delta – China in summer 2006: measurement and model results, Atmos. Chem. Phys., 10, 11243–11260, https://doi.org/10.5194/acp-10-11243-2010, 2010.

Novelli, A., Kaminski, M., Rolletter, M., Acir, I.-H., Bohn, B., Dorn, H.-P., Li, X., Lutz, A., Nehr, S., Rohrer, F., Tillmann, R., Wegener, R., Holland, F., Hofzumahaus, A., Kiendler-Scharr, A., Wahner, A., and Fuchs, H.: Evaluation of OH and HO_2 concentrations and their budgets during photooxidation of 2-methyl-3-butene-2-ol (MBO) in the atmospheric simulation chamber SAPHIR, Atmos. Chem. Phys., 18, 11409–11422, https://doi.org/10.5194/acp-18-11409-2018, 2018.

Novelli, A., Vereecken, L., Bohn, B., Dorn, H.-P., Gkatzelis, G. I., Hofzumahaus, A., Holland, F., Reimer, D., Rohrer, F., Rosanka, S., Taraborrelli, D., Tillmann, R., Wegener, R., Yu, Z., Kiendler-Scharr, A., Wahner, A., and Fuchs, H.: Importance of isomerization reactions for OH radical regeneration from the photo-oxidation of isoprene investigated in the atmospheric simulation chamber SAPHIR, Atmos. Chem. Phys., 20, 3333–3355, https://doi.org/10.5194/acp-20-3333-2020, 2020.

Noziére, B., Barnes, I., and Becker, K.-H.: Product study and mechanisms of the reactions of α-pinene and of pinonaldehyde with OH radicals, J. Geophys. Res., 104, 23645–23656, https://doi.org/10.1029/1999JD900778, 1999.

Orlando, J. J., Nozière, B., Tyndall, G. S., Orzechowska, G. E., Grazyna, E., Paulson, S. E., and Rudich Y.: Product studies of the OH- and ozone-initiated oxidation of some monoterpenes, J. Geophys. Res., 105, 11561–11572, https://doi.org/10.1029/2000JD900005, 2000.

Paulot, F., Crounse, J. D., Kjaergaard, H. G., Kroll, J. H., Seinfeld, J. H., and Wennberg, P. O.: Isoprene photooxidation: new insights into the production of acids and organic nitrates, Atmos.

Chem. Phys., 9, 1479–1501, https://doi.org/10.5194/acp-9-1479-2009, 2009.

Peeters, J., Boullart, W., Pultau, V., Vandenberk, S., and Vereecken, L.: Structure–activity relationship for the addition of OH to (poly)alkenes: site-specific and total rate constants, J. Phys. Chem. A, 111, 1618–1631, https://doi.org/10.1021/jp066973o, 2007.

Peeters, J., Nguyen, T. L., and Vereecken, L.: HO_X radical regeneration in the oxidation of isoprene, Phys. Chem. Chem. Phys., 11, 5935–5939, https://doi.org/10.1039/b908511d, 2009.

Peeters, J., Müller, J.-F., Stavrakou, T., and Nguyen, V. S.: Hydroxyl radical recycling in isoprene oxidation driven by hydrogen bonding and hydrogen tunneling: The upgraded LIM1 mechanism, J. Phys. Chem. A, 118, 8625–8643, https://doi.org/10.1021/jp5033146, 2014.

Praske, E., Otkjær, R. V., Crounse, J. D., Hethcox, J. C., Stoltz, B. M., Kjaergaard, H. G., and Wennberg, P. O.: Atmospheric autoxidation is increasingly important in urban and suburban North America, P. Natl. Acad. Sci. USA, 115, 64–69, https://doi.org/10.1073/pnas.1715540115, 2018.

Praske, E., Otkjaer, R. V., Crounse, J. D., Hethcox, J. C., Stoltz, B. M., Kjaergaard, H. G., and Wennberg, P. O.: Intramolecular hydrogen shift chemistry of hydroperoxy-substituted peroxy radicals, J. Phys. Chem. A, 123, 590–600, https://doi.org/10.1021/acs.jpca.8b09745, 2019.

Reissell, A., Aschmann, S. M., Atkinson, R., and Arey, J.: Products of the OH radical- and O_3-initiated reactions of myrcene and ocimene, J. Geophys. Res., 107, ACH 3-1–ACH 3-6, https://doi.org/10.1029/2001JD001234, 2002.

Rindelaub, J. D., McAvey, K. M., and Shepson, P. B.: The photochemical production of organic nitrates from α-pinene and loss via acid-dependent particle phase hydrolysis, Atmos. Environ., 100, 193–201, https://doi.org/10.1016/j.atmosenv.2014.11.010, 2015.

Rohrer, F., Bohn, B., Brauers, T., Brüning, D., Johnen, F.-J., Wahner, A., and Kleffmann, J.: Characterisation of the photolytic HONO-source in the atmosphere simulation chamber SAPHIR, Atmos. Chem. Phys., 5, 2189–2201, https://doi.org/10.5194/acp-5-2189-2005, 2005.

Rolletter, M., Kaminski, M., Acir, I.-H., Bohn, B., Dorn, H.-P., Li, X., Lutz, A., Nehr, S., Rohrer, F., Tillmann, R., Wegener, R., Hofzumahaus, A., Kiendler-Scharr, A., Wahner, A., and Fuchs, H.: Investigation of the α-pinene photooxidation by OH in the atmospheric simulation chamber SAPHIR, Atmos. Chem. Phys., 19, 11635–11649, https://doi.org/10.5194/acp-19-11635-2019, 2019.

Rolletter, M., Blocquet, M., Kaminski, M., Bohn, B., Dorn, H.-P., Hofzumahaus, A., Holland, F., Li, X., Rohrer, F., Tillmann, R., Wegener, R., Kiendler-Scharr, A., Wahner, A., and Fuchs, H.: Photooxidation of pinonaldehyde at ambient conditions investigated in the atmospheric simulation chamber SAPHIR, Atmos. Chem. Phys., 20, 13701–13719, https://doi.org/10.5194/acp-20-13701-2020, 2020.

Schlosser, E., Brauers, T., Dorn, H.-P., Fuchs, H., Häseler, R., Hofzumahaus, A., Holland, F., Wahner, A., Kanaya, Y., Kajii, Y., Miyamoto, K., Nishida, S., Watanabe, K., Yoshino, A., Kubistin, D., Martinez, M., Rudolf, M., Harder, H., Berresheim, H., Elste, T., Plass-Dülmer, C., Stange, G., and Schurath, U.: Technical Note: Formal blind intercomparison of OH measurements: results from the international campaign HOxComp, Atmos. Chem. Phys., 9, 7923–7948, https://doi.org/10.5194/acp-9-7923-2009, 2009.

Scholtens, K. W., Messer, B. M., Cappa, C. D., and Elrod, M. J.: Kinetics of the $CH_3O_2 + NO$ reaction: Temperature dependence of the overall rate constant and improved upper limit for the CH_3ONO_2 branching channel, J. Geophys. Res., 100, 18811–18816, https://doi.org/10.1021/jp990469k, 1995.

Schwantes, R. H., Emmons, L. K., Orlando, J. J., Barth, M. C., Tyndall, G. S., Hall, S. R., Ullmann, K., St. Clair, J. M., Blake, D. R., Wisthaler, A., and Bui, T. P. V.: Comprehensive isoprene and terpene gas-phase chemistry improves simulated surface ozone in the southeastern US, Atmos. Chem. Phys., 20, 3739–3776, https://doi.org/10.5194/acp-20-3739-2020, 2020.

Sindelarova, K., Granier, C., Bouarar, I., Guenther, A., Tilmes, S., Stavrakou, T., Müller, J.-F., Kuhn, U., Stefani, P., and Knorr, W.: Global data set of biogenic VOC emissions calculated by the MEGAN model over the last 30 years, Atmos. Chem. Phys., 14, 9317–9341, https://doi.org/10.5194/acp-14-9317-2014, 2014.

Tan, Z., Fuchs, H., Lu, K., Hofzumahaus, A., Bohn, B., Broch, S., Dong, H., Gomm, S., Häseler, R., He, L., Holland, F., Li, X., Liu, Y., Lu, S., Rohrer, F., Shao, M., Wang, B., Wang, M., Wu, Y., Zeng, L., Zhang, Y., Wahner, A., and Zhang, Y.: Radical chemistry at a rural site (Wangdu) in the North China Plain: observation and model calculations of OH, HO_2 and RO_2 radicals, Atmos. Chem. Phys., 17, 663–690, https://doi.org/10.5194/acp-17-663-2017, 2017.

Tan, Z., Lu, K., Hofzumahaus, A., Fuchs, H., Bohn, B., Holland, F., Liu, Y., Rohrer, F., Shao, M., Sun, K., Wu, Y., Zeng, L., Zhang, Y., Zou, Q., Kiendler-Scharr, A., Wahner, A., and Zhang, Y.: Experimental budgets of OH, HO_2, and RO_2 radicals and implications for ozone formation in the Pearl River Delta in China 2014, Atmos. Chem. Phys., 19, 7129–7150, https://doi.org/10.5194/acp-19-7129-2019, 2019.

Tan, Z., Hofzumahaus, A., Lu, K., Brown, S. S., Holland, F., Huey, L. G., Kiendler-Scharr, A., Li, X., Liu, X., Ma, N., Min, K.-E., Rohrer, F., Shao, M., Wahner, A., Wang, Y., Wiedensohler, A., Wu, Y., Wu, Z., Zeng, L., Zhang, Y., and Fuchs, H.: No evidence for a significant impact of heterogeneous chemistry on radical concentrations in the North China Plain in summer 2014, Environ. Sci. Technol., 54, 5973–5979, https://doi.org/10.1021/acs.est.0c00525, 2020.

Teng, A. P., Crounse, J. D., and Wennberg, P. O.: Isoprene peroxy radical dynamics, J. Am. Chem. Soc., 139, 5367–5377, https://doi.org/10.1021/jacs.6b12838, 2017.

Vereecken, L. and Peeters, J.: Decompositon of substituted alkoxy radicals – Part I: a generalized structure-activy relationship for reaction barrier heights, Phys. Chem. Chem. Phys., 11, 9062–9074, https://doi.org/10.1039/B909712K, 2009.

Vereecken, L. and Peeters, J.: A structure-activy relationship for the rate coefficients of H-migration in substituted alkoxy radicals, Phys. Chem. Chem. Phys., 12, 120608–12620, https://doi.org/10.1039/C0CP00387E, 2010.

Vereecken, L. and Nozière, B.: H migration in peroxy radicals under atmospheric conditions, Atmos. Chem. Phys., 20, 7429–7458, https://doi.org/10.5194/acp-20-7429-2020, 2020.

Vereecken, L., Carlsson, P. T. M., Novelli, A., Bernard, F., Brown, S. S., Cho, C., Crowley, J. N., Fuchs, H., Mellouki, W., Reimer, D., Shenolikar, J., Tillmann, R., Zhou, L., Kiendler-

Scharr, A., and Wahner, A.: Theoretical and experimental study of peroxy and alkoxy radicals in the NO_3-initiated oxidation of isoprene, Phys. Chem. Chem. Phys., 23, 5496–5515, https://doi.org/10.1039/D0CP06267G, 2021.

Wegener, R., Brauers, T., Koppmann, R., Bares, S. R., Rohrer, F., Tillmann, R., Wahner, A., Hansel, A., and Wisthaler, A.: Simulation chamber investigation of the reactions of ozone with short-chained alkenes, J. Geophys. Res., 112, D13301, https://doi.org/10.1029/2006JD007531, 2007.

Wennberg, P. O., Bates, K. H., Crounse, J. D., Dodson, L. G., McVay, R. C., Mertens, L. A., Nguyen, T. B., Praske, E., Schwantes, R. H., Smarte, M. D., St Clair, J. M., Teng, A. P., Zhang, X., and Seinfeld, J. H.: Gas-Phase Reactions of Isoprene and Its Major Oxidation Products, Chem. Rev., 118, 3337–3390, https://doi.org/10.1021/acs.chemrev.7b00439, 2018.

Whalley, L. K., Edwards, P. M., Furneaux, K. L., Goddard, A., Ingham, T., Evans, M. J., Stone, D., Hopkins, J. R., Jones, C. E., Karunaharan, A., Lee, J. D., Lewis, A. C., Monks, P. S., Moller, S. J., and Heard, D. E.: Quantifying the magnitude of a missing hydroxyl radical source in a tropical rainforest, Atmos. Chem. Phys., 11, 7223–7233, https://doi.org/10.5194/acp-11-7223-2011, 2011.

Xu, L., Guo, H., Boyd, C. M., Klein, M., Bougiatioti, A., Cerully, K. M., Hite, J. R., Isaacman-VanWertz, G., Kreisberg, N. M., Knote, C., Olson, K., Koss, A., Goldstein, A. H., Hering, S. V., de Gouw, J., Baumann, K., Lee, S.-H., Nenes, A., Weber, R. J., and Ng, N. L.: Effects of anthropogenic emissions on aerosol formation from isoprene and monoterpenes in the southeastern United States, P. Natl. Acad. Sci. USA, 112, 37–42, https://doi.org/10.1073/pnas.1417609112, 2015.

Zhang, H. F., Yee, L. D., Lee, B. H., Curtis, M. P., Worton, D. R., Isaacman-VanWertz, G., Offenberg, J. H., Lewandowski, M., Kleindienst, T. E., Beaver, M. R., Holder, A. L., Lonneman, W. A., Docherty, K. S., Jaoui, M., Pye, H. O. T., Hu, W. W., Day, D. A., Campuzano-Jost, P., Jimenez, J. L., Guo, H. Y., Weber, R. J., de Gouw, J., Koss, A. R., Edgerton, E. S., Brune, W., Mohr, C., Lopez-Hilfiker, F. D., Lutz, A., Kreisberg, N. M., Spielman, S. R., Hering, S. V., Wilson, K. R., Thornton, J. A., and Goldstein, A. H.: Monoterpenes are the largest source of summertime organic aerosol in the southeastern United States, P. Natl. Acad. Sci. USA, 115, 2038–2043, https://doi.org/10.1073/pnas.1717513115, 2018.

7 Photooxidation of β-pinene

7.1 β-pinene oxidation mechanism

β-pinene is the second most important monoterpene species with a global annual total emission of 18.9 Tg year^{-1} (Guenther et al. (2012)). It is a bicyclic monoterpene with an exocyclic double bond (Figure 7.1, Chapter 1). The mechanism of the oxidation of β-pinene with OH has been investigated by Vereecken and Peeters (2012) by quantum chemical calculations, structure-activity relationship and theoretical kinetics. In the following analysis, the nomenclature of the peroxy radicals formed from the oxidation of β-pinene is adapted from the MCM, version 3.3.1.

The oxidation of β-pinene by the OH radical is initiated by the addition of the OH radical to the double bond. The addition of OH happens predominantly at the least substituted C_a atom (83%, Vereecken and Peeters (2012), Figure 7.1). OH addition to the C_b atom is only of minor importance (7%, Vereecken and Peeters (2012)). H abstraction due to the OH attack is also less likely, and only occurs with a branching ratio of 10%.

After the OH addition at the least substituted C_a atom, the branching ratio for the cleavage of the four-membered ring leading to the formation of the peroxy radical BPINCO2 is 70%. The formation of the ring-closed isomer BPINAO2 has a branching ratio of 30% (Vereecken and Peeters (2012)). With respect to the initial RO_2 formation, the mechanism described by Vereecken and Peeters (2012) differs from other reported mechanisms, e.g. the widely used Master Chemical Mechanism (MCM, version 3.3.1). Lower branching ratios for the ring opened BPINCO2 peroxy radical of only 7% are assumed, and the formation of the ring-retained BPINAO2 peroxy radical is the dominant pathway. It has been shown in previous studies of the β-pinene oxidation in the SAPHIR chamber (Kaminski et al. (2017)) that using the mechanism described by Vereecken and Peeters (2012) for modelling the experimental results leads to an improved model to measurement agreement. Especially the measured yields of nopinone and acetone in the experiments by Kaminski et al. (2017) support the ratio of the formation of BPINAO2 and BPINCO2 reported in Vereecken and Peeters (2012).

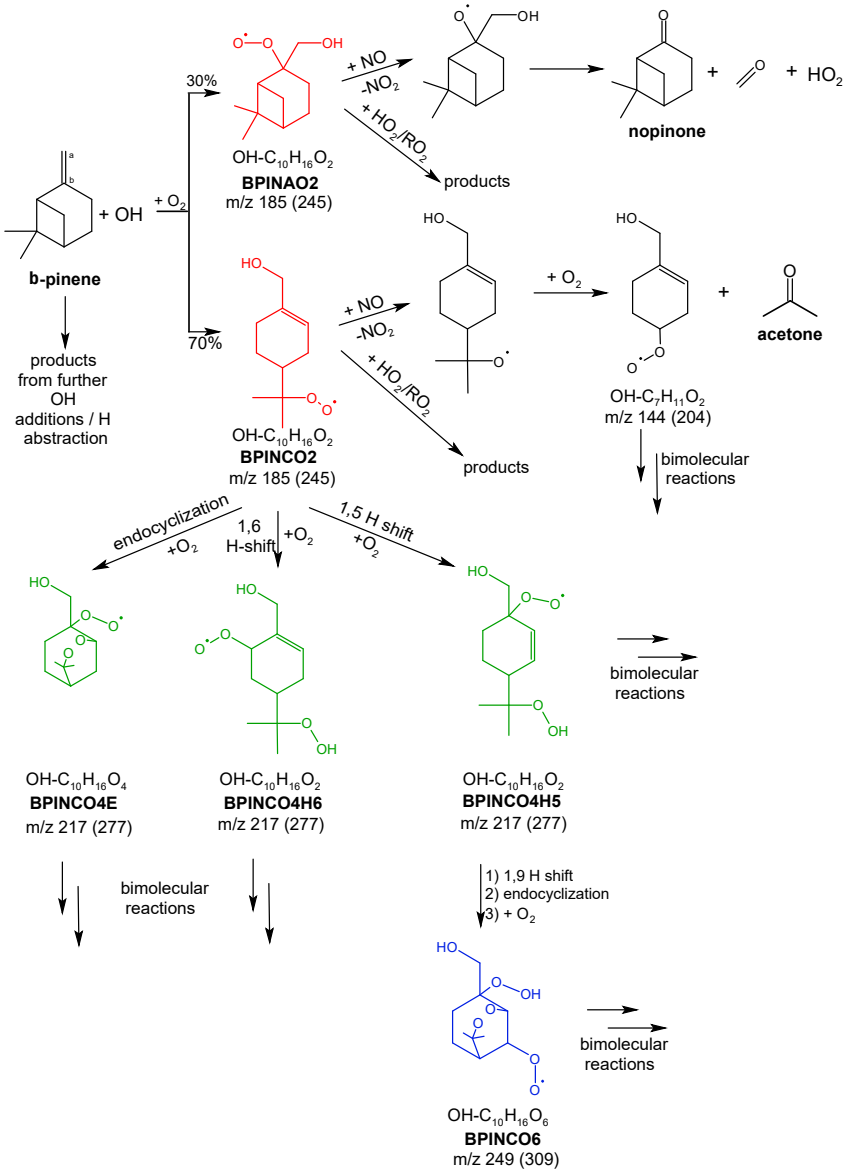

Figure 7.1: The first steps of the mechanism of the oxidation of β-pinene with OH, adapted from Kaminski et al. (2017) and Xu et al. (2019). For simplicity, the addition of OH is only shown at the C_a atom, as the branching ratio for an OH addition at C_a is 83%. The initially formed peroxy radicals with the sum formula $OH-C_{10}H_{16}O_2$ are shown in red. Peroxy radicals formed from one autoxidation step ($OH-C_{10}H_{16}O_4$) are shown in green, peroxy radicals from a second autoxidation step ($OH-C_{10}H_{16}O_6$) in blue. The mass to charge ratios are given for the respective molecule, and for the clusters of the respective peroxy radical with protonated propylamine (+ 60 Th) in brackets. Some bimolecular reaction pathways, like the formation of organic nitrates (yield: 25%) from the reactions of the peroxy radicals with NO are not shown in this scheme. The peroxy radicals can also undergo bimolecular reactions with HO_2 or RO_2 that are not shown in this scheme.

The peroxy radicals can undergo bimolecular reactions with NO, HO_2 or other RO_2 radicals. The reaction of the peroxy radicals with NO leads to the formation of an alkoxy radical. Subsequently, the alkoxy radical obtained from the BPINAO2 + NO reaction decomposes to a stable carbonyl compound, nopinone, formaldehyde and HO_2 (Figure 7.1). The reaction of the ring opened peroxy radical with NO also leads to the formation of an alkoxy radical that decomposes forming acetone and an alkyl radical (Vereecken and Peeters (2012)). This alkyl radical will subsequently quickly add oxygen, to form a peroxy radical with the sum formula $C_7H_{11}O_3$ (Vereecken and Peeters (2012)). The $C_7H_{11}O_3$ peroxy radical then undergoes bimolecular reactions with NO, HO_2 and RO_2. Potential unimolecular reactions such as endocyclizations are not competitive as the calculated energetic barriers for these reactions are too high (Vereecken and Peeters (2012)).

An alternative reaction pathway for the initially formed peroxy radicals are unimolecular reactions, leading to higher oxidized radical species. Atmospherically relevant unimolecular reactions most likely only occur for the ring-opened peroxy radical BPINCO2. For the ring-retained peroxy radical BPINAO2, rate constants of potential unimolecular reactions were calculated to be slower than $0.05\,s^{-1}$ (Xu et al. (2019)). This means that unimolecular reactions of the ring-retained peroxy radical BPINAO2 are most likely not competitive with bimolecular reactions.

Several unimolecular reactions are possible for the ring-opened peroxy radical BPINCO2. The fastest possible unimolecular reaction is an endocyclization. A hydrogen-bonding interaction between the OH group and the −OO group stabilizes the transition state of this reaction (Xu et al. (2019)). The rate of the endocyclization was calculated to be 0.62 s^{-1} by Vereecken and Peeters (2004). Xu et al. (2019) calculate a reaction rate of 4.1 s^{-1} for this reaction. The uncertainty factor given for the rate constant calculation is 10 (Xu et al. (2019)). The energetic barriers for alternative unimolecular H shift reactions were found to be too high to be competitive with the endocyclization or bimolecular reactions by Vereecken and Peeters (2012), so that it can be assumed that they have reaction rate constants in the range of $0.05\,s^{-1}$. Xu et al. (2019) calculated the reaction rates to be 1.4 s^{-1} for the 1,5-H shift and 0.28 s^{-1} for the 1,6-H shift (Figure 7.1). Xu et al. (2019) also determined the total loss rate due to unimolecular reaction of BPINCO2 experimentally by isomer-specific measurements of the organic nitrates formed in the RO_2 + NO reactions at different NO concentrations using gas chromatography coupled to a TOF-CIMS. The experimentally determined total loss rate due to unimolecular reactions was $(16\pm5)\,s^{-1}$ (Xu et al. (2019)). These unimolecular reactions lead to the formation of three peroxy radicals with the sum formula $OH-C_{10}H_{16}O_4$, BPINCO4E from the endocyclization, BPINCO4H6 from the 1,6-H shift, and BPINCO4H5 from the 1,5-H shift (Figure 7.1).

Assuming a unimolecular reaction rate of 16 s^{-1} for the autoxidation of the BPINCO2 peroxy radical as experimentally determined by Xu et al. (2019), a mixing ratio of 70 ppbv of NO would be required to obtain an equivalent loss rate of the ring-opened peroxy radical towards the bimolecular reaction with NO at 296 K. For a unimolecular reaction rate at the lower end of the reported range, of e.g. 1 s^{-1}, an equivalent loss rate of the peroxy radical towards the reaction with NO would be obtained at NO mixing ratios of 4.5 ppbv at 296 K. While NO mixing ratios of 70 ppbv are only observed in highly polluted urban environments close to emission sources, NO mixing ratios of 4.5 ppbv are possible in remote areas and are often surpassed in urban environments (e.g. Hidy et al. (2014)).

The peroxy radical from the minor 1,5-H shift reaction of BPINCO2, BPINCO4H5, can undergo several subsequent autoxidation reaction steps leading to the formation of a $OH-C_{10}H_{16}O_6$ peroxy radical (Xu et al. (2019)). It is speculated that first a 1,9-H shift occurs that is followed by a quick endocyclization (Supporting Information of Xu et al. (2019)). This reaction can be of importance as it is a possible pathway for the formation of highly oxidized molecules that contribute to the formation of new particles and growth of secondary organic aerosols (Chapter 1.2). However, it has not been investigated in detail so far. For the other two peroxy radicals, BPINCO4E formed from the endocyclization of BPINCO2 and BPINCO4H6 formed from a 1,6-H shift of BPINCO2, no pathways leading to the formation of a higher oxidized peroxy radical have been suggested in the literature so far. For the BPINCO4E radical, a 1,4-H shift followed by the addition of O_2 would be a possible pathway. However, SAR (Vereecken and Noziere (2020)) predicts a very slow reaction rate of $2.06\times10^{-5}\,s^{-1}$ for this unimolecular reaction. The BPINCO4H6 peroxy radical may undergo a 1,8-H shift followed by an endocyclization. SAR predicts a fast unimolecular reaction rate of $1.58\times10^{2}\,s^{-1}$ for this reaction.

7.2 Experiments investigating the β-pinene oxidation mechanism

Even though the mechanism reported by Vereecken and Peeters (2012) improves the agreement of model to measurement comparison in the study by Kaminski et al. (2017), the model still underpredicted the concentrations of OH and HO_2 by up to a factor of 2. The measured OH time series could only be matched by the modelled ones when the measured HO_2 time series were used as a model constraint, indicating a missing HO_2 source in both the MCM, version 3.2, and the model proposed by Vereecken and Peeters (2012) (Kaminski et al. (2017)). The discrepancies in the comparison of the measured and modelled radical concentrations indicate that unimolecular reactions and/or photolytical sources of HO_2 are missing in the model.

Additionally, the reaction rate constants of the unimolecular reactions calculated by Vereecken and Peeters (2012) and Xu et al. (2019) are yet to be proven experimentally.

Therefore, the mechanism of the oxidation of β-pinene is reinvestigated in this work with special regard to the importance and reaction rates of unimolecular reactions of the peroxy radicals. Two different chemical reactors are used, the free-jet flow system (Chapter 2.3) and the SAPHIR-STAR chamber (Chapter 2.2). In both settings, a CIMS instrument was used with protonated amines (protonated ethylamine in the free-jet flow system and protonated propylamine in the SAPHIR-STAR chamber) as primary ions for the detection of the peroxy radicals. Other reaction products, such as organic nitrates, hydroperoxides and carbonyls were also detected by the CIMS instrument. The use of the two different chemical reactors allows to investigate different aspects of the chemical mechanism. In the free-jet flow system, the peroxy radical distribution can be investigated after short reaction times of only 8 s, allowing to determine the reaction rate constants of unimolecular reactions. In the SAPHIR-STAR chamber, effects from secondary chemistry can be observed.

7.2.1 Experiments in the free-jet flow system

In total, three experiments investigating the β-pinene + OH reaction system were conducted in the free-jet flow system. In the first experiment, ozonolysis of tetramethylethylene (TME) was used as an OH source. The ozone concentration was stepwise increased from 0 to 4.3 $\times 10^{11}$ cm^{-3} to increase the OH concentration while keeping the β-pinene and TME concentrations constant at 1.5 $\times 10^{11}$ cm^{-3} and 2.0$\times 10^{10}$ cm^{-3}, respectively. The OH and HO_2 concentration were in the range of 10^5 to 10^6 cm^{-3} (Chapters 7.2.3 and 7.4). In the second experiment, isopropylnitrit (IPN) photolysis was used as an OH source. The IPN mixing ratio was 2.3$\times 10^{10}$ cm^{-3} for the whole experiment. The β-pinene mixing ratio was again kept constant at 1.5 $\times 10^{11}$ cm^{-3}. NO is formed in the photolysis of IPN, leading to the formation of organic nitrates from the RO_2 + NO reaction. The detection of the organic nitrates in the experiments is used as a confirmation of the assignment of the peroxy radical peaks (Chapter 3.4). The OH and HO_2 concentration were again in the range of 10^5 to 10^6 cm^{-3}, NO concentrations in the range of 10^8 cm^{-3}.

Table 7.1: Overview of the experimental conditions for the investigations of the β-pinene oxidation studied in the free-jet flow tube at TROPOS at a relative humidity below 0.1% and a temperature of 298 K.

Date	**OH source**	**H_2/** cm^{-3}
23 Aug. 2021	TME ozonolysis	0.0
24 Aug. 2021	IPN photolysis	0.0
26 Aug. 2021	IPN photolysis	3.7×10^{16}

In the third experiment, OH radicals were again produced from IPN photolysis. In this experiment, the IPN concentration was ramped up from 2.8×10^{10} to 4.1×10^{11} cm^{-3}. Part of the OH was converted to HO_2 by the addition of 3.7×10^{16} cm^{-3} of hydrogen to the air flow. H_2 reacts with OH producing H_2O and H that instantly reacts with O_2, forming HO_2. The reaction rate of the first reaction is 6.2×10^{-15} cm^3 s^{-1} (Orkin et al. (2006)). This is three orders of magnitude slower than the reaction of β-pinene with OH, therefore most of the OH radicals still react with β-pinene. The introduction of additional HO_2 to the system results in the formation of hydroperoxides (ROOH) from the reaction of the RO_2 radicals with HO_2. Like the organic nitrates formed in the experiment where NO was added, the detection of the hydroperoxides is used as a proof of the assignment of the peroxy radical peaks (Chapter 3.4).

7.2.2 Experiments in the SAPHIR-STAR chamber

For the study of the oxidation mechanism of β-pinene two experiments were conducted. One used O_3 photolysis in the presence of water as an OH source. In the other one, H_2O_2 photolysis was used as an OH source.

In the experiment with OH production by O_3 photolysis, 40 ppbv of O_3 was continuously added to the chamber. The relative humidity was set to 30% and the temperature was 296 K. OH concentrations in the range of 10^6 cm^{-3} were achieved. After the ozone concentration in the chamber stabilized, β-pinene was constantly injected to reach a steady state concentration of 10 ppbv. The UV-C lights (Chapter 2.2) were turned on, and the shutter system was opened stepwise from 15% to 45% to 75%. The time between each step was six hours. This time was needed to ensure that steady-state conditions in the chamber were reached. The more the shutter system was opened, the more OH was produced by photolysis reactions in the chamber.

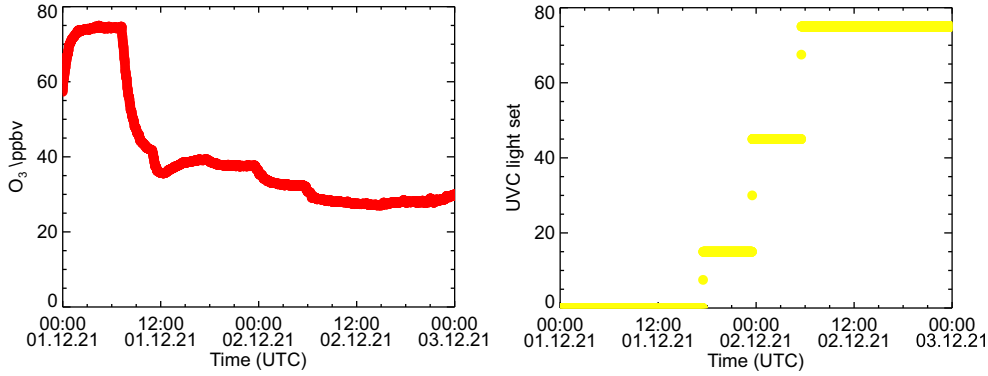

Figure 7.2: Timeseries of the O_3 mixing ratio and the opening of the shutter system of the UV-C lamps in an experiment in the SAPHIR-STAR chamber where ozone photolysis was used as an OH source. Only the time prior to the injection of NO is shown.

Then the NO addition was started at the shutter system opening of 75% of the UV-C lamps. In addition, UV-A lamps were turned on (Chapter 2.2) to ensure the reformation of NO from NO_2 formed from the reaction of the initially injected NO with O_3. In the first addition step, NO was continuously added to reach a steady state concentration of 10 ppbv. After six hours, the amount of added NO was increased to 20 ppbv that were again continuously added for six hours. In the last addition step, the amount of added NO was further increased to reach steady-state concentrations of 40 ppbv.

Finally, the NO and O_3 additions were stopped and the UV-A and UV-C lights were switched off. When no more NO and O_3 were detected in the chamber, the addition of β-pinene was stopped and the experiment concluded.

Waiting until the NO and O_3 concentrations in the chamber are zero before switching off the β-pinene addition allows to determine the exchange rate of the air in the chamber. The loss of β-pinene is then only determined by the exchange of air in the chamber.

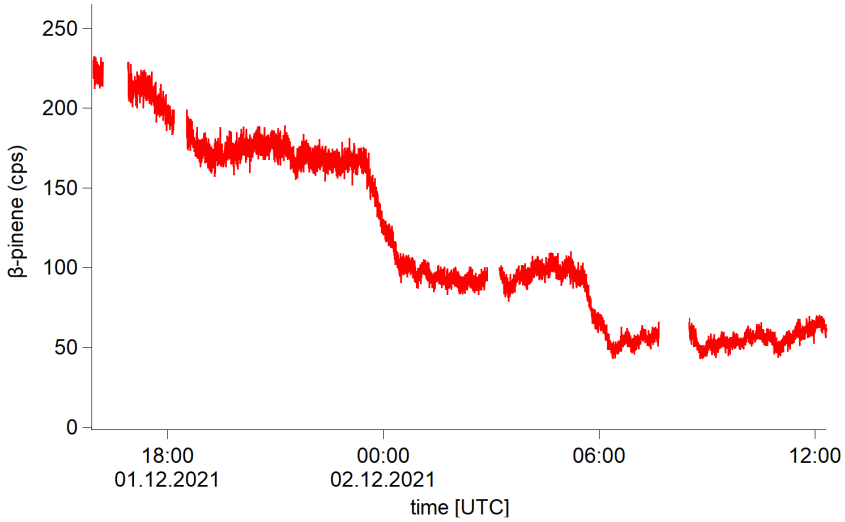

Figure 7.3: Timeseries of the β-pinene signal intensity measured by a PTR-MS instrument in an experiment in the SAPHIR-STAR chamber where ozone photolysis was used as an OH source. Only the time prior to the injection of NO is shown. Gaps in the timeseries indicate times when the sampling point of the PTR-MS was switched to the bypass line that provides the β-pinene to the chamber.

In the experiment with H_2O_2 photolysis as an OH source, 10 ppbv of β-pinene was continuously added into the chamber through the syringe pump system (Chapter 2.2). Six hours after the start of the β-pinene addition, H_2O_2 was added into the chamber by steadily bubbling 0.5 l min^{-1} of ultra-pure nitrogen through a bottle filled with a 30% H_2O_2 solution. After a waiting time of 6 hours, the H_2O_2 concentration was assumed to be stable in the chamber. The UV-C lights were switched on. Over the course of the next 12 hours, the shutter system covering the UV-C lamps was stepwise opened from 0 to 100% opening. Every step lasted three hours, to give potential reaction products enough time to stabilize. At the highest shutter system opening, 60 ppbv of NO was added to the chamber over six hours. After that, the lights were switched off, and the H_2O_2 and NO additions were stopped. The addition of β-pinene was stopped six hours later, concluding the experiment.

7.2.3 Determination of OH concentrations in the experiments

In the experiments, the OH concentration was increased stepwise. The stepwise increase of the OH concentration serves to determine whether the measured signals are actually the peroxy radicals as described in Chapter 3.4. Since no measurements of OH radical concentrations are available in either chamber, the OH concentration was modelled (Chapter 4, Figure 7.4).

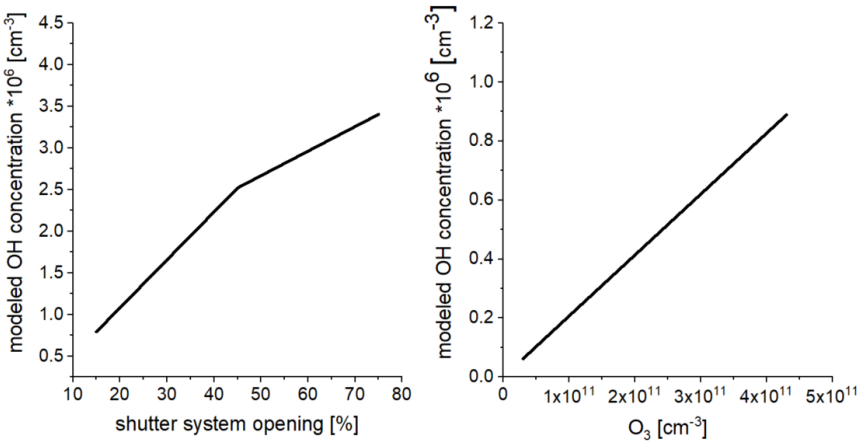

Figure 7.4: Modelled OH concentration in the SAPHIR-STAR chamber as a function of the opening of the shutter system of the UV-C lamps (left). Modelled OH concentration in the free-jet flow system as a function of the O_3 concentration during the β-pinene oxidation experiment where TME ozonolysis was used as an OH source (right). Concentrations are obtained from a box model calculation(Chapter 4.2).

In the free-jet flow system, OH radicals are produced by the ozonolysis of TME. The reaction rate and an OH yield of 0.77±0.04 for this reaction have been determined by Witter et al. (2002). An increase of the OH radical concentration can be achieved by increasing the O_3 concentration, while keeping the concentration of TME constant. This increases the oxidation rate of TME and more OH radicals are formed. The OH concentration is therefore proportional to the O_3 concentration, and the O_3 concentration is a good measure for the OH concentration (Figure 7.4).

In the experiments in the SAPHIR-STAR chamber, OH radicals are produced by the photolysis of ozone in the presence of water. The UV-C lamps are equipped with a shutter system that allows to continuously increase the light intensity. In the experiment here, the shutter was opened stepwise to increase the photolysis rate and thereby the OH concentration.

7.3 Measurement of the relative distribution of RO_2 radicals

The relative distribution of peroxy radicals derived from the oxidation of β-pinene by the OH radical at NO free, atmospherically relevant conditions were measured by a CIMS instrument in a free-jet flow system and the SAPHIR-STAR chamber.

From the peroxy radical concentrations measured by the CIMS instrument, the distribution of the three peroxy radical families with the sum formulas OH−$C_{10}H_{16}O_2$, OH−$C_{10}H_{16}O_4$ and OH−$C_{10}H_{16}O_6$ are determined. OH−$C_{10}H_{16}O_4$ peroxy radicals, BPINCO4E, BPINCO4H6 and BPINCO4H5 (Figure 7.1), are products of the autoxidation of the ring-opened OH−$C_{10}H_{16}O_2$ peroxy radical BPINCO2. The OH−$C_{10}H_{16}O_6$ peroxy radicals BPINCO6 are formed from the autoxidation of the OH−$C_{10}H_{16}O_4$ peroxy radical BPINCO4H5 (Figure 7.1). The rate constants for the formation of BPINCO4H6 calculated by both Vereecken and Peeters (2012) and Xu et al. (2019) are small in comparison to the rate constants of the formation of BPINCO4E and BPINCO4H5. Therefore, the formation of BPINCO4H6 is assumed to be negligible and not considered for the further analysis in this work.

Table 7.2: Overview of the peroxy radical families investigated in this work and their respective members .

Peroxy radical family	**member**[a]
OH−$C_{10}H_{16}O_2$	BPINAO2
	BPINCO2
OH−$C_{10}H_{16}O_4$	BPINCO4E
	BPINCO4H5
	BPINCO4H6
OH−$C_{10}H_{16}O_6$	BPINCO6

[a] nomenclature taken from Figure 7.1

The measurements are used to review the theoretically predicted oxidation mechanism of β-pinene and to redetermine reaction rate constants of the autoxidation of formed peroxy radicals.

It is not possible to distinguish between isomeric species in the CIMS measurements. Therefore, the signal intensities and ratios given for the respective mass to charge ratios of the peroxy radicals always present a sum measurement of all peroxy radicals of the same sum formula. Assuming that the sensitivity of the instrument for all peroxy radicals is similar, the relative abundance of measured signals reflects the distribution of the peroxy radicals.

In the experiments in the free-jet flow system, lower limit concentrations are determined for all peroxy radicals, using the calibration procedure described in Chapter 3.4.1. The CIMS instrument measuring at the SAPHIR-STAR chamber was not calibrated, therefore no concentrations, but normalized ion count rates measured by the mass spectrometer are given (Chapter 3.2).

7.3.1 Measurements in the free-jet flow system

In the experiments in the free-jet flow system, the OH concentration was stepwise increased by increasing the O_3 concentration (Chapters 7.2.1 and 7.2.2). Performing the experiments at different OH concentrations allowed to determine whether the signals detected by the CIMS instrument are the expected peroxy radicals, since it can be assumed that their ratios do not change with changing OH radical concentrations because the higher oxidized peroxy radicals can only be formed from BPINCO2 and not other OH induced reactions. Upon the increase of the OH radical concentration, the intensity of the peroxy radical signals measured by the CIMS instrument increased (Figure 7.5).

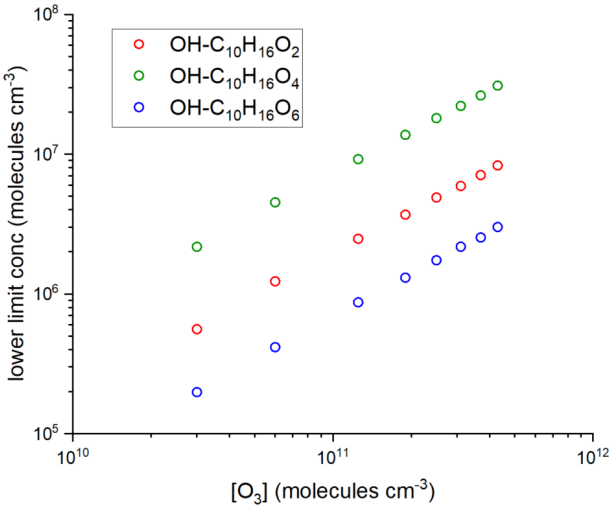

Figure 7.5: Peroxy radical concentrations at different ozone concentrations. OH was produced from TME ozonolysis in the shown experiment, so that higher O_3 concentrations are equivalent to higher OH concentrations. OH concentrations were in the range of 6×10^4 to $9\times10^5\,cm^{-3}$. The β-pinene concentration was $1.5\times10^{11}\,cm^{-3}$, the TME concentration was $2.0\times10^{10}\,cm^{-3}$.

The peroxy radicals with the sum formula $OH-C_{10}H_{16}O_4$ were the most abundant peroxy radicals at all oxidant concentrations. The peroxy radicals with the sum formula $OH-C_{10}H_{16}O_2$ have the second highest abundance, and the peroxy radicals with the sum formula $OH-C_{10}H_{16}O_6$ have the lowest abundance.

For the experiments in the free-jet flow system, all three peroxy radical families, $OH-C_{10}H_{16}O_2$, $OH-C_{10}H_{16}O_4$ and $OH-C_{10}H_{16}O_6$ showed a linear dependency on the increasing oxidant concentrations (Figure 7.5). The three peroxy radical families are formed in a constant relation independent of the OH concentration for the

reaction time of 8 s. The ratio between the OH−$C_{10}H_{16}O_2$ and the OH−$C_{10}H_{16}O_4$ peroxy radical was on average 0.26. Equally, the ratio between the OH−$C_{10}H_{16}O_2$ and the OH−$C_{10}H_{16}O_6$ peroxy radical was independent on the OH concentration with an average value of 2.8 (Figure 7.6).

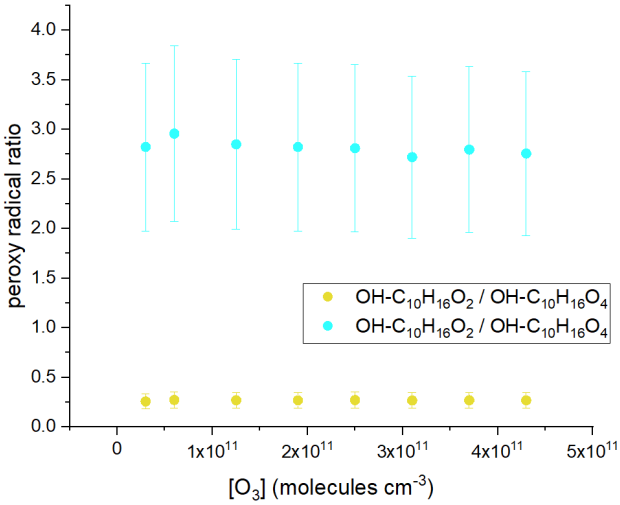

Figure 7.6: Ratio between the OH−$C_{10}H_{16}O_2$ and OH−$C_{10}H_{16}O_4$ and the OH−$C_{10}H_{16}O_2$ and OH−$C_{10}H_{16}O_6$ peroxy radicals measured in the free-jet flow system at different ozone concentrations.

An error for the experimentally determined radical ratios can be estimated from the reproducibility of the ratios for different experimental conditions. The ratio of the peroxy radicals was determined in two experiments, the one presented in this chapter, where TME ozonolysis was used as an OH source, and in experiments where IPN photolysis was used as an OH source (Chapter 7.2.1). In the two experiments, the OH−$C_{10}H_{16}O_2$ to OH−$C_{10}H_{16}O_4$ peroxy radical ratios agreed within an error of 20%. The OH−$C_{10}H_{16}O_2$ to OH−$C_{10}H_{16}O_6$ peroxy radical ratios determined in the two experiments agreed within an error of 25%. Furthermore, it has to be assumed that the three peroxy radical families are detected by the CIMS instrument with the same sensitivity. At the moment, it is not possible to determine whether this is actually the case, adding a further uncertainty to the measured peroxy radical ratios that can not be quantified. An uncertainty of 30% is therefore assumed for the experimentally determined radical ratios.

7.3.2 Measurements in the SAPHIR-STAR chamber

In the experiments in the SAPHIR-STAR chamber, the peroxy radical signal intensity also increased with increasing OH concentrations. The signal of the peroxy radicals OH−$C_{10}H_{16}O_4$ that are formed from the unimolecular reaction and following O_2 addition of the ring-opened OH−$C_{10}H_{16}O_2$ peroxy radical BPINCO2 (Figure 7.1) was highest.

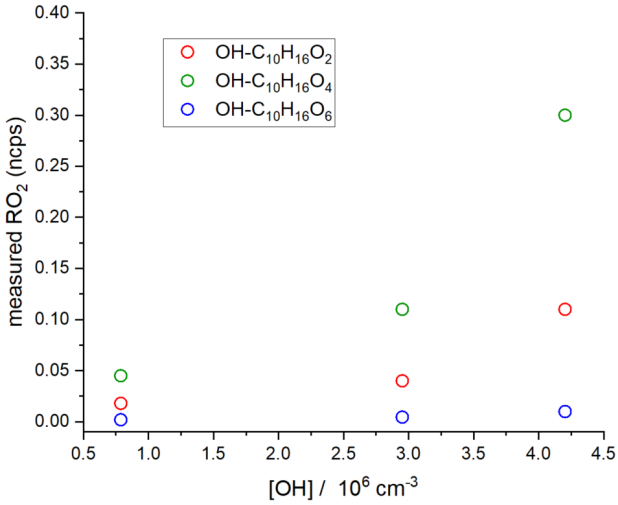

Figure 7.7: Normalized counts per second (ncps) of the measured signals for the OH−$C_{10}H_{16}O_2$, OH−$C_{10}H_{16}O_{40}$ and OH−$C_{10}H_{16}O_6$ peroxy radical families at different modelled OH concentrations in the experiments in the SAPHIR-STAR chamber. OH was produced from the photolysis of ozone in the presence of water vapour. The measured ion count rates were normalized to the protonated propylamine primary ion.

The ratio between the OH−$C_{10}H_{16}O_2$ and OH−$C_{10}H_{16}O_4$ peroxy radicals is 0.37 on average, though it decreases from 0.4 to 0.36 with increasing OH concentrations. The average radical ratio is close to the value observed in the free-jet flow system. Contrary, the ratio between the OH−$C_{10}H_{16}O_2$ and the OH−$C_{10}H_{16}O_6$ peroxy radical is on average 10.0 and increases from 9 to 11 with increasing OH concentrations. The average OH−$C_{10}H_{16}O_2$ to OH−$C_{10}H_{16}O_6$ peroxy radical ratio in the SAPHIR-STAR chamber is a factor of 3.5 higher than observed in the free-jet flow system.

Differences in the measured ratios between experiments in the free-jet flow system and the SAPHIR-STAR chamber may be related to the different chemical regimes in the two systems. In the free-jet flow system, the reaction time is only 8 s. In this short reaction time, loss of peroxy radicals by bimolecular processes do not play a significant role. Only peroxy radicals that are produced rapidly in the time scale

of 8 s are observed. Experiments in the SAPHIR-STAR chamber are conducted at steady-state conditions with a reaction time of 40 minutes. Under these conditions, the production of peroxy radicals is constant during the whole steady-state. The long lifetime of the peroxy radicals increases the probability of losses of the peroxy radicals through bimolecular reactions with NO, HO_2 or RO_2. The bimolecular reaction rates of RO_2 + NO reactions are usually similar for different kinds of peroxy radicals, however, the rate constants of the bimolecular RO_2 loss through their reactions with HO_2 and other RO_2 are highly variable. Additionally, wall losses that have not been characterized yet are expected to occur in the SAPHIR-STAR chamber. Therefore, an inclusion of all relevant loss reactions into a model is very complicated and uncertain and has not been a part of this work.

7.4 Discussion of the RO_2 formation mechanism

7.4.1 Relevance of autoxidation reactions

The short reaction time of 8 s in the free-jet flow system, the low concentration of other reaction partners such as RO_2 or HO_2 and the absence of NO in the experiment remove the influence of bimolecular reactions. The relative distribution of the peroxy radicals therefore only depends on the reaction rate constants of the autoxidation reactions. Since no NO was added to the system for the experiments described in this section, bimolecular reactions with NO do not occur. Consequently, no organic nitrates, the reaction products of the RO_2 + NO detectable by the CIMS instrument, were observed in the experiments. HO_2 can be formed in the system from radical reactions. The modelled concentrations of HO_2 were below $1\times10^5\,cm^{-3}$ after the reaction time of 8 s (Figure 7.8). The bimolecular lifetime of the RO_2 peroxy radicals for the RO_2 + HO_2 reactions for these conditions is 5 days, so that the loss of RO_2 radicals from the HO_2 + RO_2 reaction is negligible in the experiments in this work. Furthermore, hydroperoxides, a reaction product of the HO_2 + RO_2 reaction detectable by the CIMS instrument, were not observed in the experiment. Loss of the peroxy radicals to RO_2 + RO_2 reactions is also not expected for the measured RO_2 radical concentrations of $1.5\times10^7\,cm^{-3}$ at the time of measurement (Figure 7.5), because the bimolecular lifetime of the peroxy radicals for the RO_2 + RO_2 reaction is also in the range of several days.

Since formation from bimolecular reactions can be excluded, the peroxy radicals detected at mass to charge ratios corresponding to the sum formula $OH-C_{10}H_{16}O_4$ have to be a product of unimolecular reactions of the RO_2 radical formed in the first reaction step. Due to the high abundance of the $OH-C_{10}H_{16}O_4$ peroxy radicals after the reaction time of 8 s, a fast unimolecular reaction is required. Two unimolecular

reactions with subsequent O_2 addition have been suggested for the formation of $OH-C_{10}H_{16}O_4$ peroxy radicals (Xu et al. (2019), Vereecken and Peeters (2012)), an endocyclization leading to the formation of the BPINCO4E peroxy radical or a 1,5-H-shift leading to the formation of BPINCO4H5 peroxy radicals (Figure 7.1).

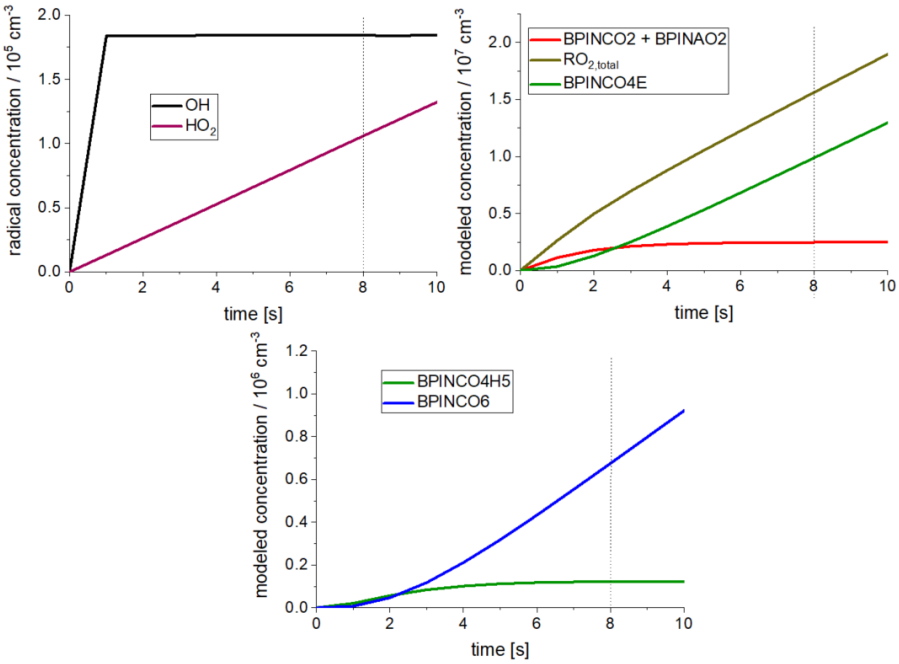

Figure 7.8: Time dependence of the modelled OH and HO_2 concentrations (upper left), the concentrations of the peroxy radicals BPINCO2, BPINCO4E and the sum of all peroxy radicals (upper right) and the concentration of the peroxy radicals BPINCO4H5 and BPINCO6 (lower panel) for the experiments in the free-jet flow system where tetramethylethylene ozonolysis was used as an OH source. The ozone concentration used in the model was $8.0\times10^{10}\,cm^{-3}$. In the model, the reaction rate constants for the unimolecular reaction of BPINCO2 leading to the formation of BPINCO4E and BPINCO4H5 were constrained to the values determined by Vereecken and Peeters (2012). The vertical dotted line represents the reaction time of 8 s in the free-jet flow system prior to the detection of the peroxy radicals by the CIMS instrument.

BPINCO4E and BPINCO4H5 have the same molecular mass, and they can therefore not be distinguished in the CIMS measurements.

The $OH-C_{10}H_{16}O_6$ must be product of an unimolecular reaction of the $OH-C_{10}H_{16}O_4$ peroxy radical with subsequent O_2 addition, since bimolecular reactions are too slow for the conditions in the experiments.

The chemical conditions of the experiment and the measured ratios of RO_2 show

that the formation of the peroxy radicals in the free-jet flow system was independent from RO_2 loss due to bimolecular reactions and is therefore only driven by rapid unimolecular reactions on the time scale of the reaction time of 8 s.

7.4.2 Determination of unimolecular rate constants

Since the relative ratios of the peroxy radicals only depend on unimolecular reactions, the observed relative distribution of RO_2 can be used to determine the rate constants of the unimolecular RO_2 reactions (Reactions R7.2 to R7.4).

$$\beta\text{−pinene} + \text{OH} \longrightarrow 0.3\,\text{BPINAO2} + 0.7\,\text{BPINCO2} \quad \text{(R7.1)}$$

$$\text{BPINCO2} + \text{O}_2 \longrightarrow \text{BPINCO4\,E} \quad \text{(R7.2)}$$

$$\text{BPINCO2} + \text{O}_2 \longrightarrow \text{BPINCO4\,H5} \quad \text{(R7.3)}$$

$$\text{BPINCO4\,H5} + \text{O}_2 \longrightarrow \text{BPINCO6} \quad \text{(R7.4)}$$

0D box model calculations were used to optimize the reaction constants of the unimolecular reactions of the peroxy radicals, such that experimentally observed ratios of radical concentrations are matched. The relative distribution of the peroxy radicals was compared at an OH concentration of $2{\times}10^{10}\,\text{cm}^{-3}$ in the free-jet flow system. In this subchapter, the OH−$C_{10}H_{16}O_2$, OH−$C_{10}H_{16}O_4$ and OH−$C_{10}H_{16}O_6$ peroxy radical families are referenced to as RO2, RO4 and RO6, respectively.

Concentration of peroxy radical species are calculated by a model (Chapter 4) using reaction rate constants for the formation of RO4 peroxy radicals from RO2 peroxy radicals by an endocyclization reaction (BPINCO4E, Reaction R7.2) or a 1,5-H shift (BPINCO4H5, Reaction R7.3) determined by Xu et al. (2019) and Vereecken and Peeters (2012). The values determined by Vereecken and Peeters (2012) and Xu et al. (2019) differ especially in the branching ratios of the BPINCO4H5 peroxy radical formation and the overall loss rate of RO2 peroxy radicals (Table 7.3). Vereecken and Peeters (2012) determined a branching ratio $k_{R7.3}/(k_{R7.2}+k_{R7.3})$ of 7.5%, whereas Xu et al. (2019) determined a branching ratio of 19.6% . Also, the value of the overall loss rate ($k_{R7.2}+k_{R7.3}$) differs significantly ($5.1\,\text{s}^{-1}$ by Xu et al. (2019), $0.67\,\text{s}^{-1}$ by Vereecken and Peeters (2012)).

Table 7.3: Comparison of the reaction rate constants at 296 K used in the modelling of the β-pinene experiments in the free-jet flow system. All values are given in s^{-1}.

	$\mathbf{k}_{R7.2}$	$\mathbf{k}_{R7.3}$	$\mathbf{k}_{R7.4,adapted}$ [a]
Xu et al.[b], original	4.1	1.0	no reasonable result
Xu et al.[b], modified	0.5	0.13	0.1 - 0.22
Vereecken et al.[c]	0.62	0.05	≥ 1
Vereecken et al.[d]	-	-	10

[a] simultaneous fitting of the RO2/RO4 and RO2/RO6 ratios within experimental uncertainty
[b] Xu et al. (2019)
[c] Vereecken and Peeters (2012)
[d] Vereecken and Noziere (2020)

For a given set of rate constants for Reactions R7.2 and R7.3 (either from Xu et al. (2019) or Vereecken and Peeters (2012)), the rate constant $k_{R7.4}$ was systematically varied, in order to obtain the best possible match between the modelled and measured RO2/RO4 and RO2/RO6 ratios.

The experimentally determined value for the RO2/RO4 ratio could not be matched with the rate constants determined by Xu et al. (2019). The modelled value for the peroxy radical ratio is about a factor of 10 lower than the experimentally determined value over the whole range of tested reaction rates (Panel A, Figure 7.9). The experimentally determined value for the RO2/RO6 ratio is matched by the value modelled with the reaction rates determined by Xu et al. (2019) for $k_{R7.4} = 0.009\,s^{-1}$ (Panel E, Figure 7.9). For all other values of the reaction rate constant $k_{R7.4}$, larger discrepancies between the modelled and measured ratios are observed. The rate constants for the unimolecular reaction of BPINCO2 leading to the formation of BPINCO4E and BPINCO4H5 are adapted to obtain a longer lifetime for the BPINCO2 peroxy radical while keeping the branching ratio for the 1,5-H shift at 20%. A good agreement with the experimentally determined RO2/RO4 ratio is obtained with unimolecular reaction rates of $0.5\,s^{-1}$ for the endocyclization reaction leading to the formation of BPINCO4E and $0.13\,s^{-1}$ for the 1,5-H shift leading to the formation of the BPINCO4H5 peroxy radical (Panel B, Figure 7.9).

These adapted reaction rates are subsequently used in the model to determine for which reaction rate $k_{R7.4}$ the experimentally determined RO2/RO6 ratio is matched. A good agreement of the modelled and experimentally determined RO2/RO6 ratio is obtained for a value of $k_{R7.4}$ between $0.08\,s^{-1}$ and $0.22\,s^{-1}$ (Panel F, Figure 7.9).

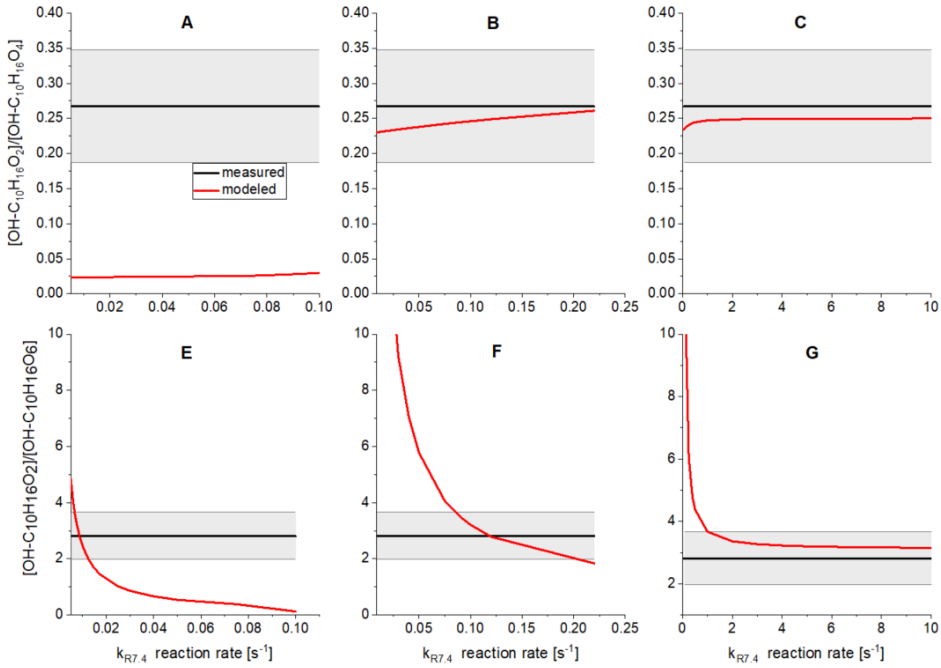

Figure 7.9: Dependence of the modelled RO2/RO4 and RO2/RO6 ratio on the reaction rate of the unimolecular reaction of BPINCO4H5 leading to the formation of the BPINCO6 peroxy radical. Model results are compared to experimental results. The gray areas indicate the uncertainty of the measured radical ratios (Chapter 7.3.1). In the modelled results shown in Panel A and E, calculated rate constants $k_{R7.2}$ and $k_{R7.3}$ by Xu et al. (2019) were used (Table 7.3). In panel B and F, the values of both reaction rate constant ($k_{R7.2}$ and $k_{R7.3}$) by Xu et al. (2019) were reduced by a factor of 8. For the results shown in panel C and G, the rate constants $k_{R7.2}$ and $k_{R7.3}$ calculated by Vereecken and Peeters (2012) were used in the model (Table 7.3).

Vereecken and Peeters (2012) determined a value of $0.62\,s^{-1}$ for the endocyclization of BPINCO2 forming BPINCO4E and a value of $0.05\,s^{-1}$ for the 1,5-H shift of BPINCO2 leading to the formation of BPINCO4H5. The sum of these unimolecular reaction rates is in good agreement with the reaction rate constants optimized from the values reported by Xu et al. (2019). With the reaction rates determined by Vereecken and Peeters (2012), a good model to measurement agreement of the RO2/RO4 peroxy radical ratio within the estimated error is obtained over the whole range of tested values of the reaction rate $k_{R7.4}$ (Panel C, Figure 7.9). From these results, it can be concluded that the sum of the unimolecular reaction rates leading to the formation of RO4 peroxy radicals from BPINCO2 has to be in the range of about $0.6\,s^{-1}$ as calculated by Vereecken and Peeters (2012). The limiting step for

the formation of RO6 peroxy radicals is most likely the 1,5-H shift of the BPINCO2 peroxy radical. For a rate of $0.05\,s^{-1}$ for the 1,5-H shift of BPINCO2 as determined by Vereecken and Peeters (2012), equivalent reactivities for the bimolecular reactions with NO and HO_2 would be achieved for mixing ratios of 0.25 ppbv and 0.1 ppbv, respectively. For the unimolecular reaction rate of $0.13\,s^{-1}$ for the 1,5-H shift of BPINCO2, mixing ratios of 0.8 ppbv (NO) and 0.25 ppbv (HO_2) would be required to obtain equivalent reactivity as for the unimolecular reaction. NO mixing ratios below 1 ppbv are regularly observed. The unimolecular formation of RO6 peroxy radicals are therefore competitive with bimolecular reactions for a wide range of atmospheric conditions.

For the RO2/RO6 ratio, a good agreement of the modelled and experimentally determined value within the given error is obtained for a reaction rate constant $k_{R7.4}$ faster than $1\,s^{-1}$ using the reaction rates determined by Vereecken and Peeters (2012). In agreement with the results obtained from the model runs using the optimized rate constants from Xu et al. (2019), it can be concluded that for a small branching ratio for the formation of BPINCO4H5 from BPINCO4E, a fast unimolecular reaction rate is required. The formation of RO6 peroxy radicals may be of importance for the formation of HOMs.

From SAR (Vereecken and Noziere (2020)), a reaction rate of $10\,s^{-1}$ is determined for a 1,9-H shift in the BPINCO4H5 peroxy radical. The subsequent endocyclization and addition of O_2 are most likely also fast. These values are close to the reaction rate $k_{R7.4}$ that is obtained from the model run with the reaction rates determined by Vereecken and Peeters (2012).

The analysis of the experiments investigating the β-pinene oxidation mechanism conducted in this work show that the combined rate constants $k_{R7.2}$ and $k_{R7.3}$ have to be fast and in the range of $0.6\,s^{-1}$. Furthermore, the reaction rate $k_{R7.4}$ optimized in the model is highly sensitive to the $k_{R7.2}/k_{R7.3}$ ratio. Using the values for $k_{R7.2}/k_{R7.3}$ modified from Xu et al. (2019), $k_{R7.4}$ cannot be faster than $0.22\,s^{-1}$. However, using the values for $k_{R7.2}/k_{R7.3}$ determined by Vereecken and Peeters (2012), $k_{R7.4}$ has to be faster than $1\,s^{-1}$.

It is not possible to finally decide which values for the unimolecular rate constants should be used in the future with the data available at the moment. However, it is not possible to reproduce the experimental observations with the rate constants originally determined by Xu et al. (2019). On the other hand, the calculated rate constants by Vereecken and Peeters (2012) give a consistent description of the β-pinene oxidation mechanism, starting with the branching ratio for the formation of the initial RO_2 radicals BPINAO2 and BPINCO2 (page 98). Additionally, the experimentally determined RO2/RO4 and RO2/RO6 ratios can be reproduced by a model using the rate constants by Vereecken and Peeters (2012). Furthermore, the

value determined for $k_{R7.4}$ is in agreement with SAR calculations (Vereecken and Noziere (2020)).

8 Summary and Conclusions

8.1 Development of a detection scheme for RO_2 based on CIMS

Berndt et al. (2018) recently developed a technique for the direct measurement of specific peroxy radicals formed in the oxidation of α-pinene, based on chemical ionization mass spectrometry. Protonated primary amines are used as primary ions that form stable clusters with the peroxy radicals. The peroxy radicals were measured during experiments conducted in a free-jet flow system.

In this work, the detection scheme initially developed by Berndt et al. (2018) was adapted to be used at the atmospheric simulation chamber SAPHIR-STAR at the Forschungszentrum Jülich. Several test experiments were conducted to obtain clean mass spectra by reducing the influence of contamination peaks. The technique was successfully applied during experiments investigating the oxidation mechanism of β-pinene in the SAPHIR-STAR chamber. This demonstrates that the detection of peroxy radicals by the CIMS-based detection scheme is possible in a larger atmospheric simulation chamber. In the future, the technique developed in this work will be used to investigate the oxidation mechanism of other atmospherically relevant VOCs.

8.2 Monoterpene oxidation

In this work, the oxidation mechanisms of the three atmospherically relevant monoterpenes β-pinene, Δ^3-carene and myrcene were performed in three different chemical reactors. The experiments aimed at clarifying understudied aspects of the oxidation mechanisms of the three respective monoterpenes, like the product yields, importance of unimolecular reactions and reaction rate constants.

8.2.1 Overview of experiments

In total, 10 experiments were conducted in the SAPHIR chamber looking into the oxidation mechanisms of myrcene and Δ^3-carene. Additionally, certain aspects of the oxidation of methane and α-pinene were studied in two separate experiments.

The experiments aimed at investigating the oxidation mechanism of biogenic VOCs at atmospheric conditions comparable to those in a boreal forest. The experiments looking into the oxidation of methane and α-pinene were conducted as proof-of-principle experiments for the determination of organic nitrate yields and the analysis of ROx radical budgets. Concerning the myrcene oxidation scheme, only OH induced oxidation was studied. Both the ozonolysis and the OH induced oxidation of Δ^3-carene as well as the photolysis and OH oxidation of caronaldehyde, one of the main daytime oxidation products of Δ^3-carene oxidation, were studied.

Experiments investigating the oxidation mechanism of β-pinene with special regard to the formation of first generation peroxy radicals were conducted in a free-jet flow system at the TROPOS institute in Leipzig, and the SAPHIR-STAR chamber at the Forschungszentrum Jülich. The peroxy radicals were measured using CIMS instruments with amines as primary ions. For the measurements at the SAPHIR-STAR chamber, the CIMS instrument was optimized for the measurement of peroxy radicals.

8.2.2 Organic nitrate yields

Organic nitrates ($RONO_2$) are formed from the reaction of peroxy radicals (RO_2) derived from the oxidation of VOCs with NO. Alternatively, an alkoxy radical and NO_2 can be formed from this reaction. Usually, the alkoxy radical formation is the dominant pathway. However, the branching ratios differ depending on the structure of the peroxy radical. As organic nitrates have lower vapour pressures than their parent compounds and are therefore prone to condense on atmospheric particles (Rollins et al. (2013)) contributing to particle growth, it is important to know the branching ratios for their formation as exactly as possible.

Jenkin et al. (2019) developed a structure-activity relationship (SAR) method that can be applied to the bimolecular reactions of peroxy radicals. For the branching ratio of the RO_2 + NO reaction, they suggest an updated calculation method originally reported by Carter and Atkinson (1989). This method takes into account the number of carbon, oxygen and nitrogen atoms in the organic group of the peroxy radical, the degree of substitution of the peroxy radical and some effects from the presence of oxygenated substituents. Assuming a primary peroxy radical from the first oxidation step of the oxidation of a monoterpene with the generic sum formula $OH-C_{10}H_{16}O_2$, the branching ratio for the formation of an organic nitrate would be 0.19 following this method (Figure 8.1).

For the experiments in the SAPHIR chamber, the organic nitrate yield of the reactions of the peroxy radicals with NO can be determined from the analysis of the concentrations of reactive nitrogen species in the chamber (Hantschke et al. (2021), Tan et al. (2021)). The organic nitrate yields for the oxidation by the OH radical of

Δ^3-carene, caronaldehyde, myrcene, α-pinene and methane were determined in the experiments in this work (Figure 8.1).

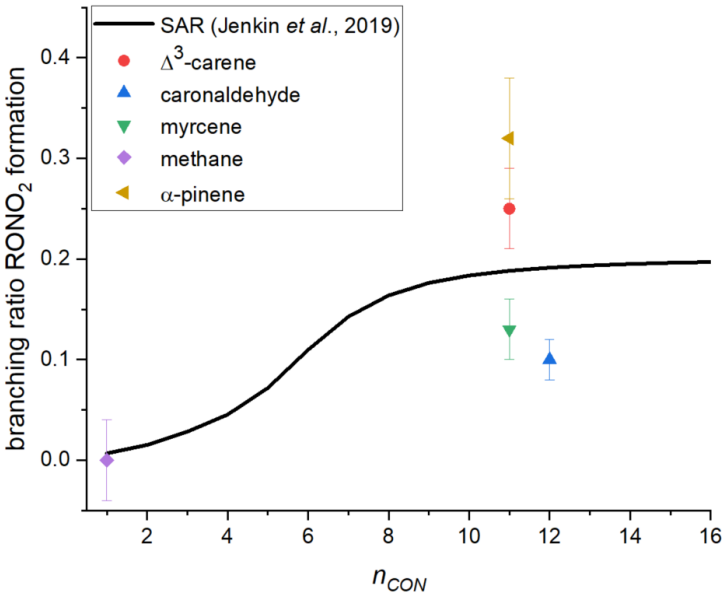

Figure 8.1: The organic nitrate yield of the RO_2 + NO calculated following the method described in Jenkin et al. (2019) for an unsubstituted primary peroxy radical for different numbers of carbon, oxygen and nitrogen (n_{CON}) in the organic rest of the peroxy radical. Coloured points show the organic nitrate yields determined in experiments in the SAPHIR chamber.

Only one peroxy radical, CH_3OO, is formed in the oxidation of methane. For the organic nitrate yield obtained for the oxidation of methane, the value predicted by the SAR and the value obtained in the experiments are in good agreement. For all other investigated species, the organic nitrate yields determined in the SAPHIR chamber represent a bulk yield for all peroxy radicals that are formed in the oxidation of the respective VOC and cannot only be assigned to the reaction of one distinguished peroxy radical with NO. For the two cyclic monoterpenes Δ^3-carene and α-pinene, the experimentally obtained values are higher than the value calculated using SAR. Assuming that not only primary, non-substituted peroxy radicals contribute to the experimental values, the SAR value could be adapted with the factors for substituted peroxy radicals given in Jenkin et al. (2019). However, this would only further reduce the organic nitrate yield predicted by SAR and would not result in a better agreement with the experimentally obtained data. The experimentally obtained organic nitrate yields for myrcene and caronaldehyde are lower than predicted by SAR. Applying the factors given in Jenkin et al. (2019) may therefore

ameliorate the agreement of the experimental values with the SAR predictions.

While the SAR predictions are useful to get a first estimate of the branching ratios of certain reactions, the result of the comparison of the SAR predictions to the experimental values obtained in this work suggests that the organic nitrate yields are highly dependent on a molecules' exact structure. Even for the structurally very similar bicyclic monoterpenes Δ^3-carene and α-pinene, the experimentally determined values for the branching ratios differ by several percent. For a better understanding of the atmospheric oxidation mechanisms of VOC, the determination of molecule-specific branching ratios is therefore important. However, direct measurements of organic nitrates are not always possible. Methods to determine organic nitrate yields without their direct measurement as presented in this work for experiments in the SAPHIR chamber are therefore useful tools.

8.2.3 ROx radical budget

By looking into radical production and destruction reactions and determining their rates, it is possible to find out whether there are radical processes occurring that are not considered in the chemical mechanisms. In this work, the radical budgets of the ROx radical family members OH, HO_2 and RO_2 are determined individually for the oxidation experiments of myrcene, and a total ROx radical budget is also determined for the oxidation experiments investigating myrcene and Δ^3-carene oxidation. During the experiments, radical production and destruction reactions must be balanced because of the short lifetime of the radicals in the range of seconds to minutes.

A chemical budget analysis was applied to determine the total ROx budgets for the experiments investigating the oxidation of Δ^3-carene in the SAPHIR chamber. It was found that the ROx budget is well balanced, so that it can be concluded that there are no primary radical formation or destruction reactions unaccounted for. The budgets of the individual OH, HO_2 and RO_2 were not determined due to missing measurements of the concentrations of some species needed in the analysis.

For the experiments investigating the oxidation mechanism of myrcene, radical destruction and production rates were calculated for OH, HO_2, RO_2 and ROx radicals. Large discrepancies were found in the radical budget analysis for the oxidation of myrcene. The ROx radical budget could only be balanced by reducing the SAR predicted HO_2 + RO_2 reaction rate by 60%. Alternatively, changing the product distribution expected from the RO_2 + HO_2 reaction also reduces the observed discrepancies. The major reaction products of the RO_2 + HO_2 reaction are usually assumed to be hydroperoxides. The formation of hydroperoxides terminates the radical chain. If it is assumed that instead of the formation of hydroperoxides, OH and HO_2 radicals are formed from the RO_2 + HO_2 reactions in yields of 0.3 to 0.6, the ROx radical budget would also be balanced. This would for example be the

case if the $RO_2 + HO_2$ reaction would yield an alkoxy radical, a hydroxy radical and oxygen (Chapter 1.2). The RO_2 radical budget is also not balanced for the experiments in the SAPHIR chamber with low NO mixing ratios. At these conditions, it can be assumed that unimolecular reactions of the peroxy radicals that lead to the formation of higher oxidized peroxy radicals, thus propagating the radical chain, are competitive with the bimolecular reactions. The radical destruction and formation reactions are better balanced if unimolecular reactions of the peroxy radicals are introduced. The peroxy radicals formed in the oxidation of myrcene have several double bonds retained in their structure, which was found to be a prerequisite for fast unimolecular reactions (Moller et al. (2020)). Additionally, the peroxy radicals bear structural similarities with peroxy radicals derived from the oxidation of isoprene that were found to be able to undergo fast unimolecular reactions competitive with bimolecular reactions at low NOx conditions (Novelli et al. (2020)). It can therefore be assumed that fast unimolecular reactions of the peroxy radicals formed in the oxidation of myrcene are possible.

Overall, the analysis of the radical budgets of the myrcene experiments point towards a fast unimolecular reaction forming HO_2 radicals. In the future, this needs to be further investigated and experimentally proven, e.g. by the measurement of the individual RO_2 radicals.

8.2.4 Product yields

The yield of caronaldehyde, the main product of the oxidation of Δ^3-carene with the OH radical and one of the reaction products of Δ^3-carene ozonolysis, was determined from the experiments in the SAPHIR chamber. The obtained results were in the range of yields reported in the literature. Additionally, the OH yield was determined for the ozonolysis of Δ^3-carene and found to be in good agreement with theoretically calculated values reported in the literature.

In the experiments investigating the oxidation of myrcene in the SAPHIR chamber, the yields of acetone and formaledehyde were determined. Since certain products can only be derived from certain mechanistic pathways, the obtained product yields reflect the branching ratios of the first reaction steps, i.a. the attack of the OH radical. The formaledehyde yield found in the myrcene oxidation experiment is lower than what would be expected for the experimental conditions from current mechanistic knowledge. From SAR, a formaldehyde yield of 0.48 would be expected. The formaldehyde yield in the experiments was 0.35 ± 0.08. The discrepancy between the value predicted by SAR and the value determined in the experiments could be fully explained by assuming a fast unimolecular isomerization pathway competing with the bimolecular reaction leading to the formation of formaldehyde. This supports the conclusion from the chemical budget analysis that fast unimolecular reactions

of the peroxy radicals occur.

8.2.5 Importance of unimolecular reactions in the oxidation mechanism of β-pinene

In the experiments in the free-jet flow system, the reaction rates of unimolecular reactions of the peroxy radicals formed in the oxidation of β-pinene were experimentally determined from the peroxy radical ratios for the first time.

The experimentally determined ratios between the peroxy radicals with the sum formulas $OH-C_{10}H_{16}O_2$, $OH-C_{10}H_{16}O_4$ and $OH-C_{10}H_{16}O_6$ were compared to ratios obtained from box model calculations using the reaction rate constants for the autoxidation reactions of RO_2 from β-pinene oxidation published by Vereecken and Peeters (2012) and Xu et al. (2019). A good agreement of the experimental and modelled ratios was achieved with the reaction rates by Vereecken and Peeters (2012). With the reaction rates published by Xu et al. (2019), the experimentally observed ratios of $OH-C_{10}H_{16}O_2$ to $OH-C_{10}H_{16}O_4$ and $OH-C_{10}H_{16}O_2$ to $OH-C_{10}H_{16}O_6$ peroxy radicals could not be matched. A correction of the reaction rates by about an order of magnitude was necessary to bring the experimental and modelled ratios into agreement. The overall reaction rate for the formation of $OH-C_{10}H_{16}O_4$ from $OH-C_{10}H_{16}O_2$ peroxy radical was in agreement with the value reported by Vereecken and Peeters (2012) after the corrections. For the first autoxidation, in which $OH-C_{10}H_{16}O_4$ peroxy radicals are formed from $OH-C_{10}H_{16}O_2$ peroxy radicals, a reaction rate in the range of $0.6\,s^{-1}$ was determined. For the second autoxidation step, where $OH-C_{10}H_{16}O_6$ peroxy radicals are formed from $OH-C_{10}H_{16}O_4$ peroxy radicals, the reaction rate depends on the branching ratio between the different $OH-C_{10}H_{16}O_4$ isomers.

8.3 Implications for atmospheric chemistry

For β-pinene, an explicit atmospheric oxidation mechanism is part of the MCM (Saunders et al. (2003), version 3.3.1 via website: http://mcm.york.ac.uk, last access January 2022). However, recent studies by Vereecken and Peeters (2004, 2012), Kaminski et al. (2017) and Xu et al. (2019) demonstrated that the mechanism in the MCM, version 3.3.1, misses key steps of the actual atmospheric oxidation of β-pinene. Specifically the disregard of unimolecular reactions of the peroxy radicals formed from the initial attack of the OH radical leads to discrepancies when comparing recent results from experiments at atmospheric conditions to the mechanism reported by the MCM (Kaminski et al. (2017)).

In the experiments in this work investigating the oxidation mechanism of β-pinene, speciated RO_2 radical concentrations and the ratios of the initially formed peroxy radical and peroxy radicals formed in further autoxidation steps were determined with a recently developed ionization scheme for a CIMS instrument. It was found that unimolecular reactions are of importance in the oxidation of β-pinene, for conditions typical for regions where the NOx mixing ratios are low, so that unimolecular reactions become competitive to bimolecular RO_2 loss reactions.

From the analysis of the data obtained in the experiments investigating the oxidation mechanisms of Δ^3-carene and myrcene in the SAPHIR chamber conducted in this work several conclusions can be drawn about the importance of unimolecular reactions in their oxidation mechanisms and the yields of products formed in bimolecular reactions of the peroxy radical derived from their oxidation. Especially the radical budget considerations contribute to clarifying whether the oxidation mechanism of the investigated monoterpenes contain unaccounted reactions leading to radical formation. Those may help to explain discrepancies found when modelling the radical concentrations measured in field studies (e.g. Hens et al. (2014), Kim et al. (2013)).

In the experiments investigating the photooxidation of Δ^3-carene, the ROx radical budget was closed. It can therefore be assumed that there are no unaccounted processes leading to radical reformation. Contrary, the experimental radical budgets in the experiments investigating the oxidation mechanism of myrcene were only balanced when fast unimolecular reactions reforming radicals were assumed. These unimolecular reaction pathways need to be considered in future investigations of the oxidation mechanism and in chemical models, so that correct values for product yields and radical regeneration can be obtained.

Kinetic data like reaction rate constants, product yields and branching ratios are required for testing modelled oxidation mechanism, the development of SAR and the correct prediction of air quality and climate by chemical models. The results obtained in this work contribute to broadening the kinetic data available.

The experiments in the SAPHIR chamber are conducted with a big set of analytical instruments, so that the concentrations of many important species such as oxidation products were measured.The data obtained in the experiments presented in Chapters 5 and 6 is available through the EUROCHAMP database (data.eurochamp.org/data-access/chamber-experiments) and can therefore be used for further testing of chemical models developed by the community in the future.

References

Albrecht, S. R., Novelli, A., Hofzumahaus, A., Kang, S., Baker, Y., Mentel, T., Wahner, A., and Fuchs, H.: Measurements of hydroperoxy radicals (HO_2) at atmospheric concentrations using bromide chemical ionisation mass spectrometry, Atmos. Meas. Tech., 12, 891–902, https://doi.org/10.5194/amt-12-891-2019, 2019.

Arey, J., Atkinson, R., and Aschmann, S. M.: Product study of the gas-phase reaction of monoterpenes with the OH radical in the presence of NOx, J. Geophys. Res.-Atmos., 95, 18 539–18 546, https://doi.org/10.1029/JD095iD11p18539, 1990.

Atkinson, R., Aschmann, S. M., Arey, J., and Shorees, B.: Formation of OH radicals in the gas-phase reaction of O_3 with a series of terpenes, J. Geophys. Res.-Atmos., 97, 6065–6073, https://doi.org/10.1029/92jd00062, 1992.

Baptista, L., Francisco, L. F., Dias, J. F., Silva, E. C. d., Santos, C. V. F. d., Simones, F., Mendonçab, G. d., and Arbillac, G.: Theoretical study of Δ-3-(+)-carene oxidation, Phys.Chem.Chem.Phys., 16, 2014.

Berndt, T.: Rapid Formation of Sulfuric Acid Particles at Near-Atmospheric Conditions, Science, 307, 698–700, https://doi.org/10.1126/science.1104054, 2005.

Berndt, T.: Peroxy Radical Processes and Product Formation in the OH Radical-Initiated Oxidation of α-Pinene for Near-Atmospheric Conditions, The Journal of Physical Chemistry A, 125, 9151–9160, https://doi.org/10.1021/acs.jpca.1c05576, 2021b.

Berndt, T., Jokinen, T., Sipilä, M., Mauldin, R. L., Herrmann, H., Stratmann, F., Junninen, H., and Kulmala, M.: H_2SO_4 formation from the gas-phase reaction of stabilized Criegee Intermediates with SO_2: Influence of water vapour content and temperature, Atmospheric Environment, 89, 603–612, https://doi.org/10.1016/j.atmosenv.2014.02.062, 2014.

Berndt, T., Kaethner, R., Voigtländer, J., Stratmann, F., Pfeifle, M., Reichle, P., Sipilä, M., Kulmala, M., and Olzmann, M.: Kinetics of the unimolecular reaction of CH2OO and the bimolecular reactions with the water monomer, acetaldehyde

and acetone under atmospheric conditions, Physical Chemistry Chemical Physics, 17, 19 862–19 873, https://doi.org/10.1039/c5cp02224j, 2015a.

Berndt, T., Richters, S., Kaethner, R., Voigtländer, J., Stratmann, F., Sipilä, M., Kulmala, M., and Herrmann, H.: Gas-Phase Ozonolysis of Cycloalkenes: Formation of Highly Oxidized RO_2 Radicals and Their Reactions with NO, NO_2, SO_2, and Other RO_2 Radicals, The Journal of Physical Chemistry A, 119, 10 336–10 348, https://doi.org/10.1021/acs.jpca.5b07295, 2015b.

Berndt, T., Richters, S., Jokinen, T., Hyttinen, N., Kurten, T., Otkjaer, R. V., Kjaergaard, H. G., Stratmann, F., Herrmann, H., Sipila, M., Kulmala, M., and Ehn, M.: Hydroxyl radical-induced formation of highly oxidized organic compounds, Nature Communications, 7, 8, https://doi.org/10.1038/ncomms13677, 2016.

Berndt, T., Mender, B., Scholz, W., Fischer, L., Herrmann, H., Kulmala, M., and Hansel, A.: Accretion Product Formation from Ozonolysis and OH Radical Reaction of alpha-Pinene: Mechanistic Insight and the Influence of Isoprene and Ethylene, Environmental Science Technology, 52, 11 069–11 077, https://doi.org/10.1021/acs.est.8b02210, 2018.

Berndt, T., Hyttinen, N., Herrmann, H., and Hansel, A.: First oxidation products from the reaction of hydroxyl radicals with isoprene for pristine environmental conditions, Communications Chemistry, 2, https://doi.org/10.1038/s42004-019-0120-9, 2019.

Berndt, T., Moller, K. H., Hermann, H., and Kjaergaard, H. G.: Trimethylamine Outruns Terpenes and Aromatics in AtmosphericAutoxidation, J. Phys. Chem. A, 125, 4454–4466, 2021a.

Berresheim, H., Elste, T., Plass-Dulmer, C., Eisele, F. L., and Tanner, D. J.: Chemical ionization mass spectrometer for long-term measurements of atmospheric OH and H_2SO_4, International Journal of Mass Spectrometry, 202, 91–109, https://doi.org/10.1016/s1387-3806(00)00233-5, 2000.

Bianchi, F., Kurten, T., Riva, M., Mohr, C., Rissanen, M. P., Roldin, P., Berndt, T., Crounse, J. D., Wennberg, P. O., Mentel, T. F., Wildt, J., Junninen, H., Jokinen, T., Kulmala, M., Worsnop, D. R., Thornton, J. A., Donahue, N., Kjaergaard, H. G., and Ehn, M.: Highly Oxygenated Organic Molecules (HOM) from Gas-Phase Autoxidation Involving Peroxy Radicals: A Key Contributor to Atmospheric Aerosol, Chemical Reviews, 119, 3472–3509, https://doi.org/10.1021/acs.chemrev.8b00395, 2019.

Boge, O., Mutzel, A., Iinuma, Y., Yli-Pirila, P., Kahnt, A., Joutsensaari, J., and Herrmann, H.: Gas-phase products and secondary organic aerosol formation from the ozonolysis and photooxidation of myrcene, Atmospheric Environment, 79, 553–560, https://doi.org/10.1016/j.atmosenv.2013.07.034, 2013.

Bohn, B. and Zilken, H.: Model-aided radiometric determination of photolysis frequencies in a sunlit atmosphere simulation chamber, Atmos. Chem. Phys., 5, 191–206, https://doi.org/10.5194/acp-5-191-2005, 2005.

Bohn, B., Rohrer, F., Brauers, T., and Wahner, A.: Actinometric measurements of NO_2 photolysis frequencies in the atmosphere simulation chamber SAPHIR, Atmos. Chem. Phys., 5, 493–503, https://doi.org/10.5194/acp-5-493-2005, 2005.

Brauers, T. and Rohrer, F.: Easy AtmoSpheric chemistrY, https://www.fz-juelich.de/iek/iek-8/EN/Expertise/Infrastructure/SAPHIR/Easy/Easypdf.pdf?blob=publicationFile, 1999.

Burkholder, J. B., Sander, S. P., Abbatt, J., Barker, J. R., Cappa, C., Crounse, J. D., Dibble, T. S., Huie, R. E., Kolb, C. E., Kurylo, M. J., Orkin, V. L., Percival, C. J., Wilmouth, D. M., and Wine, P. H.: Chemical Kinetics and Photochemical Data for Use in Atmospheric Studies, Evaluation No. 19, JPL Publication 19-5, Jet Propulsion Laboratory, Pasadena, http://jpldataeval.jpl.nasa.gov/, 2020.

Carter, W. P. L. and Atkinson, R.: Alkyl nitrate formation from the atmospheric photoxidation of alkanes; a revised estimation method, Journal of Atmospheric Chemistry, 8, 165–173, https://doi.org/10.1007/bf00053721, 1989.

Chen, H., Ren, Y., Cazaunau, M., Daële, V., Hua, Y., Chena, J., and Mellouki, A.: Rate coefficients for the reaction of ozone with 2- and 3-carene, Chem. Phys. Lett., 621, 71–77, https://doi.org/10.1016/j.cplett.2014.12.056, 2015.

Cho, C. M., Hofzumahaus, A., Fuchs, H., Dorn, H. P., Glowania, M., Holland, F., Rohrer, F., Vardhan, V., Kiendler-Scharr, A., Wahner, A., and Novelli, A.: Characterization of a chemical modulation reactor (CMR) for the measurement of atmospheric concentrations of hydroxyl radicals with a laser-induced fluorescence instrument, Atmospheric Measurement Techniques, 14, 1851–1877, https://doi.org/10.5194/amt-14-1851-2021, 2021.

Colville, C. J. and Griffin, R. J.: The roles of individual oxidants in secondary organic aerosol formation from Δ-3-carene: 1. gas-phase chemical mechanism, Atmos. Environ., 38, 4001–4012, https://doi.org/10.1016/j.atmosenv.2004.03.064, 2004.

Copeland, G., Ghosh, M. V., Shallcross, D. E., Percival, C. J., and Dyke, J. M.: A study of the alkene–ozone reactions, 2,3-dimethyl 2-butene + O3 and 2-methyl propene + O3, with photoelectron spectroscopy: measurement of product branching ratios and atmospheric implications, Physical Chemistry Chemical Physics, 13, 17 461, https://doi.org/10.1039/c1cp21922g, 2011.

Criegee, R.: Mechanism of Ozonolysis, Angewandte Chemie International Edition in English, 14, 745–752, https://doi.org/10.1002/anie.197507451, 1975.

Crounse, J. D., Nielsen, L. B., Jørgensen, S., Kjaergaard, H. G., and Wennberg, P. O.: Autoxidation of Organic Compounds in the Atmosphere, The Journal of Physical Chemistry Letters, 4, 3513–3520, https://doi.org/10.1021/jz4019207, 2013.

Dorn, H. P., Brandenburger, U., Brauers, T., and Hausmann, H.: A new in-situ long path absorption instrument for the measurement of tropospheric OH radicals, Journal of the Atmospheric Sciences, 52, 3373–3380, https://doi.org/10.1175/1520-0469(1995)052, 1995.

Edwards, G. D., Cantrell, C. A., Stephens, S., Hill, B., Goyea, O., Shetter, R. E., Mauldin, R. L., Kosciuch, E., Tanner, D. J., and Eisele, F. L.: Chemical Ionization Mass Spectrometer Instrument for the Measurement of Tropospheric HO¡sub¿2¡/sub¿ and RO¡sub¿2¡/sub¿, Analytical Chemistry, 75, 5317–5327, https://doi.org/10.1021/ac034402b, 2003.

Ehhalt, D. H.: Photooxidation of trace gases in the troposphere, Phys. Chem. Chem. Phys., 1, 5401–5408, 1999.

Ehn, M., Thornton, J. A., Kleist, E., Sipilä, M., Junninen, H., Pullinen, I., Springer, M., Rubach, F., Tillmann, R., Lee, B., Lopez-Hilfiker, F., Andres, S., Acir, I.-H., Rissanen, M., Jokinen, T., Schobesberger, S., Kangasluoma, J., Kontkanen, J., Nieminen, T., Kurtén, T., Nielsen, L. B., Jørgensen, S., Kjaergaard, H. G., Canagaratna, M., Maso, M. D., Berndt, T., Petäjä, T., Wahner, A., Kerminen, V.-M., Kulmala, M., Worsnop, D. R., Wildt, J., and Mentel, T. F.: A large source of low-volatility secondary organic aerosol, Nature, 506, 476–479, https://doi.org/10.1038/nature13032, 2014.

Eisele, F. L. and Tanner, D.: Ion-assisted tropospheric OH measurement, Journal of Geophysical Research, 96, 9295–9308, https://doi.org/10.1029/91JD00198, 1991.

Eisele, F. L. and Tanner, D. J.: MEASUREMENT OF THE GAS-PHASE CONCENTRATION OF H_2SO_4 AND METHANE SULFONIC-ACID AND ESTIMATES OF H_2SO_4 PRODUCTION AND LOSS IN THE ATMOSPHERE, J. Geophys. Res.-Atmos., 98, 9001–9010, https://doi.org/10.1029/93jd00031, 1993.

Finnlayson-Pitts, B. and Pitts, J.: Chemistry of the Upper and Lower Atmosphere: Theory, Experiments and Applications, Academic, San Diego, California, 2000.

Fuchs, H., Holland, F., and Hofzumahaus, A.: Measurement of tropospheric RO_2 and HO_2 radicals by a laser-induced fluorescence instrument, Rev. Sci. Instrum., 79, 12, https://doi.org/10.1063/1.2968712, 2008.

Fuchs, H., Dorn, H. P., Bachner, M., Bohn, B., Brauers, T., Gomm, S., Hofzumahaus, A., Holland, F., Nehr, S., Rohrer, F., Tillmann, R., and Wahner, A.: Comparison of OH concentration measurements by DOAS and LIF during SAPHIR chamber experiments at high OH reactivity and low NO concentration, Atmospheric Measurement Techniques, 5, 1611–1626, https://doi.org/10.5194/amt-5-1611-2012, 2012.

Fuchs, H., Novelli, A., Rolletter, M., Hofzumahaus, A., Pfannerstill, E. Y., Kessel, S., Edtbauer, A., Williams, J., Michoud, V., Dusanter, S., Locoge, N., Zannoni, N., Gros, V., Truong, F., Sarda-Esteve, R., Cryer, D. R., Brumby, C. A., Whalley, L. K., Stone, D., Seakins, P. W., Heard, D. E., Schoemaecker, C., Blocquet, M., Coudert, S., Batut, S., Fittschen, C., Thames, A. B., Brune, W. H., Ernest, C., Harder, H., Muller, J. B. A., Elste, T., Kubistin, D., Andres, S., Bohn, B., Hohaus, T., Holland, F., Li, X., Rohrer, F., Kiendler-Scharr, A., Tillmann, R., Wegener, R., Yu, Z. J., Zou, Q., and Wahner, A.: Comparison of OH reactivity measurements in the atmospheric simulation chamber SAPHIR, Atmos. Meas. Tech., 10, 4023–4053, https://doi.org/10.5194/amt-10-4023-2017, 2017.

Gao, Y., Jin, Y. J., Li, H. D., and Chen, H. J.: Volatile organic compounds and their roles in bacteriostasis in five conifer species, Journal of Integrative Plant Biology, 47, 499–507, https://doi.org/10.1111/j.1744-7909.2005.00081.x, 2005.

Goldman, M. J., Green, W. H., and Kroll, J. H.: Chemistry of Simple Organic Peroxy Radicals under Atmospheric through Combustion Conditions: Role of Temperature, Pressure, and NOx Level, The Journal of Physical Chemistry A, 125, 10 303–10 314, https://doi.org/10.1021/acs.jpca.1c07203, 2021.

Graßmann, J., Hippeli, S., Spitzenberger, R., and Elstner, E.: The monoterpene terpinolene from the oil of Pinus mugo L. in concert with α-tocopherol and β-carotene effectively prevents oxidation of LDL, Phytomedicine, 12, 416–423, https://doi.org/10.1016/j.phymed.2003.10.005, 2005.

Guenther, A. B., Jiang, X., Heald, C. L., Sakulyanontvittaya, T., Duhl, T., Emmons, L. K., and Wang, X.: The Model of Emissions of Gases and Aerosols from Nature version 2.1 (MEGAN2.1): an extended and updated framework for

modeling biogenic emissions, Geosci. Model Dev., 5, 1471–1492, https://doi.org/10.5194/gmd-5-1471-2012, 2012.

Hakola, H., Arey, J., Aschmann, S. M., and Atkinson, R.: Product formation from the gas-phase reactions of OH radicals and O_3 with a series of monoterpenes, J. Atmos. Chem., 18, 75–102, https://doi.org/10.1007/bf00694375, 1994.

Hakola, H., Hellen, H., Hemmila, M., Rinne, J., and Kulmala, M.: In situ measurements of volatile organic compounds in a boreal forest, Atmos. Chem. Phys., 12, 11 665–11 678, https://doi.org/10.5194/acp-12-11665-2012, 2012.

Hanke, M., Uecker, J., Reiner, T., and Arnold, F.: Atmospheric peroxy radicals: ROXMAS a new mass spectronomic methodology for speciated measurements of HO_2 and RO_2 and first results, International Journal of Mass Spectrometry, 213, 91–99, 2002.

Hantschke, L., Novelli, A., Bohn, B., Cho, C., Reimer, D., Rohrer, F., Tillmann, R., Glowania, M., Hofzumahaus, A., Kiendler-Scharr, A., Wahner, A., and Fuchs, H.: Atmospheric photooxidation and ozonolysis of Δ^3-carene and 3-caronaldehyde: rate constants and product yields, Atmospheric Chemistry and Physics, 21, 12 665–12 685, https://doi.org/10.5194/acp-21-12665-2021, 2021.

Heard, D. D.: Analytical Techniques for Atmospheric Measurement, Blackwell Publishing, Oxford, UK, 1st edn., 2006.

Hens, K., Novelli, A., Martinez, M., Auld, J., Axinte, R., Bohn, B., Fischer, H., Keronen, P., Kubistin, D., Nolscher, A. C., Oswald, R., Paasonen, P., Petaja, T., Regelin, E., Sander, R., Sinha, V., Sipila, M., Taraborrelli, D., Ernest, C. T., Williams, J., Lelieveld, J., and Harder, H.: Observation and modelling of HOx radicals in a boreal forest, Atmos. Chem. Phys., 14, 8723–8747, https://doi.org/10.5194/acp-14-8723-2014, 2014.

Hidy, G. M., Blanchard, C. L., Baumann, K., Edgerton, E., Tanenbaum, S., Shaw, S., Knipping, E., Tombach, I., Jansen, J., and Walters, J.: Chemical climatology of the southeastern United States, 1999–2013, Atmospheric Chemistry and Physics, 14, 11 893–11 914, https://doi.org/10.5194/acp-14-11893-2014, 2014.

Huey, L. G.: Measurement of trace atmospheric species by chemical ionization mass spectrometry: Speciation of reactive nitrogen and future directions, Mass Spectrometry Reviews, 26, 166–184, https://doi.org/10.1002/mas.20118, 2007.

Hyttinen, N., Kupiainen-Määttä, O., Rissanen, M. P., Muuronen, M., Ehn, M., and Kurtén, T.: Modeling the Charging of Highly Oxidized Cyclohexene Ozonoly-

sis Products Using Nitrate-Based Chemical Ionization, The Journal of Physical Chemistry A, 119, 6339–6345, https://doi.org/10.1021/acs.jpca.5b01818, 2015.

Iyer, S., Reiman, H., Møller, K. H., Rissanen, M. P., Kjaergaard, H. G., and Kurtén, T.: Computational Investigation of RO_2 + HO_2 and RO_2 + RO_2 Reactions of Monoterpene Derived First-Generation Peroxy Radicals Leading to Radical Recycling, The Journal of Physical Chemistry A, 122, 9542–9552, https://doi.org/10.1021/acs.jpca.8b09241, 2018.

Jenkin, M. E., Valorso, R., Aumont, B., Rickard, A. R., and Wallington, T. J.: Estimation of rate coefficients and branching ratios for gas-phase reactions of OH with aliphatic organic compounds for use in automated mechanism construction, Atmos. Chem. Phys., 18, 9297–9328, https://doi.org/10.5194/acp-18-9297-2018, 2018.

Jenkin, M. E., Valorso, R., Aumont, B., and Rickard, A. R.: Estimation of rate coefficients and branching ratios for reactions of organic peroxy radicals for use in automated mechanism construction, Atmos. Chem. Phys., 19, 7691–7717, https://doi.org/10.5194/acp-19-7691-2019, 2019.

Junninen, H., Ehn, M., Petäjä, T., Luosujärvi, L., Kotiaho, T., Kostiainen, R., Rohner, U., Gonin, M., Fuhrer, K., Kulmala, M., and Worsnop, D. R.: A high-resolution mass spectrometer to measure atmospheric ion composition, Atmospheric Measurement Techniques, 3, 1039–1053, https://doi.org/10.5194/amt-3-1039-2010, 2010.

Kaminski, M., Fuchs, H., Acir, I. H., Bohn, B., Brauers, T., Dorn, H. P., Haseler, R., Hofzumahaus, A., Li, X., Lutz, A., Nehr, S., Rohrer, F., Tillmann, R., Vereecken, L., Wegener, R., and Wahner, A.: Investigation of the β-pinene photooxidation by OH in the atmosphere simulation chamber SAPHIR, Atmospheric Chemistry and Physics, 17, 6631–6650, https://doi.org/10.5194/acp-17-6631-2017, 2017.

Kim, S., Wolfe, G. M., Mauldin, L., Cantrell, C., Guenther, A., Karl, T., Turnipseed, A., Greenberg, J., Hall, S. R., Ullmann, K., Apel, E., Hornbrook, R., Kajii, Y., Nakashima, Y., Keutsch, F. N., DiGangi, J. P., Henry, S. B., Kaser, L., Schnitzhofer, R., Graus, M., Hansel, A., Zheng, W., and Flocke, F. F.: Evaluation of HOx sources and cycling using measurement-constrained model calculations in a 2-methyl-3-butene-2-ol (MBO) and monoterpene (MT) dominated ecosystem, Atmos. Chem. Phys., 13, 2031–2044, https://doi.org/10.5194/acp-13-2031-2013, 2013.

Kleffmann, J.: Daytime Sources of Nitrous Acid (HONO) in the Atmospheric

Boundary Layer, ChemPhysChem, 8, 1137–1144, https://doi.org/10.1002/cphc.200700016, 2007.

Kleffmann, J., Heland, J., Kurtenbach, R., Lorzer, J., and Wiesen, P.: A new instrument (LOPAP) for the detection of nitrous acid (HONO), Environ. Sci. Pollut. Res., Special Issue 4, 48–54, 2002.

Komenda, M. and Koppmann, R.: Monoterpene emissions from Scots pine (Pinus sylvestris): Field studies of emission rate variabilities, J. Geophys. Res.-Atmos., 107, 13, https://doi.org/10.1029/2001jd000691, 2002.

Laaksonen, A., Kulmala, M., O'Dowd, C. D., Joutsensaari, J., Vaattovaara, P., Mikkonen, S., Lehtinen, K. E. J., Sogacheva, L., Dal Maso, M., Aalto, P., Petäjä, T., Sogachev, A., Yoon, Y. J., Lihavainen, H., Nilsson, D., Facchini, M. C., Cavalli, F., Fuzzi, S., Hoffmann, T., Arnold, F., Hanke, M., Sellegri, K., Umann, B., Junkermann, W., Coe, H., Allan, J. D., Alfarra, M. R., Worsnop, D. R., Riekkola, M. L., Hyötyläinen, T., and Viisanen, Y.: The role of VOC oxidation products in continental new particle formation, Atmospheric Chemistry and Physics, 8, 2657–2665, https://doi.org/10.5194/acp-8-2657-2008, 2008.

Lee, A., Goldstein, A. H., Kroll, J. H., Ng, N. L., Varutbangkul, V., Flagan, R. C., and Seinfeld, J. H.: Gas-phase products and secondary aerosol yields from the photooxidation of 16 different terpenes, Journal of Geophysical Research, 111, https://doi.org/10.1029/2006jd007050, 2006.

Li, X., Rohrer, F., Hofzumahaus, A., Brauers, T., Haseler, R., Bohn, B., Broch, S., Fuchs, H., Gomm, S., Holland, F., Jager, J., Kaiser, J., Keutsch, F. N., Lohse, I., Lu, K. D., Tillmann, R., Wegener, R., Wolfe, G. M., Mentel, T. F., Kiendler-Scharr, A., and Wahner, A.: Missing Gas-Phase Source of HONO Inferred from Zeppelin Measurements in the Troposphere, Science, 344, 292–296, https://doi.org/10.1126/science.1248999, 2014.

Lockhart, J. P. A., Gross, E. C., Sears, T. J., and Hall, G. E.: Investigating the photodissociation of H_2O_2 using frequency modulation laser absorption spectroscopy to monitor radical products, Chemical Physics Letters, 711, 148–151, https://doi.org/10.1016/j.cplett.2018.09.004, 2018.

Lopez-Hilfiker, F. D., Iyer, S., Mohr, C., Lee, B. H., apos, Ambro, E. L., Kurtén, T., and Thornton, J. A.: Constraining the sensitivity of iodide adduct chemical ionization mass spectrometry to multifunctional organic molecules using the collision limit and thermodynamic stability of iodide ion adducts, Atmospheric Measurement Techniques, 9, 1505–1512, https://doi.org/10.5194/amt-9-1505-2016, 2016.

Lou, S., Holland, F., Rohrer, F., Lu, K., Bohn, B., Brauers, T., Chang, C. C., Fuchs, H., Haseler, R., Kita, K., Kondo, Y., Li, X., Shao, M., Zeng, L., Wahner, A., Zhang, Y., Wang, W., and Hofzumahaus, A.: Atmospheric OH reactivities in the Pearl River Delta - China in summer 2006: measurement and model results, Atmos. Chem. Phys., 10, 11 243–11 260, https://doi.org/10.5194/acp-10-11243-2010, 2010.

Lüpke, M., Leuchner, M., Steinbrecher, R., and Menzel, A.: Quantification of monoterpene emission sources of a conifer species in response to experimental drought, AoB PLANTS, 9, https://doi.org/10.1093/aobpla/plx045, 2017.

Mackay, G. I. and Bohme, D. K.: Proton-transfer reactions in nitromethane at 297 K, International Journal of Mass Spectrometry and Ion Physics, 26, 327–343, https://doi.org/10.1016/0020-7381(78)80052-7, 1978.

Masson-Delmotte, V., Zhai, P., Pirani, A., Connors, S., Péan, C., Berger, S., Caud, N., Chen, Y., Goldfarb, L., Gomis, M., Huang, M., Leitzell, K., Lonnoy, E., Matthews, J., Maycock, T., Waterfield, T., Yelekçi, O., Yu, R., and (eds.), B. Z.: Climate Change 2021: The Physical Science Basis. Contribution of Working Group I to the Sixth Assessment Report of the Intergovernmental Panel on Climate Change, Report, IPCC, 2021, 2021.

McDonald, B. C., de Gouw, J. A., Gilman, J. B., Jathar, S. H., Akherati, A., Cappa, C. D., Jimenez, J. L., Lee-Taylor, J., Hayes, P. L., McKeen, S. A., Cui, Y. Y., Kim, S. W., Gentner, D. R., Isaacman-VanWertz, G., Goldstein, A. H., Harley, R. A., Frost, G. J., Roberts, J. M., Ryerson, T. B., and Trainer, M.: Volatile chemical products emerging as largest petrochemical source of urban organic emissions, Science, 359, 760–764, https://doi.org/10.1126/science.aaq0524, 2018.

Mentel, T. F., Wildt, J., Kiendler-Scharr, A., Kleist, E., Tillmann, R., Dal Maso, M., Fisseha, R., Hohaus, T., Spahn, H., Uerlings, R., Wegener, R., Griffiths, P. T., Dinar, E., Rudich, Y., and Wahner, A.: Photochemical production of aerosols from real plant emissions, Atmos. Chem. Phys., 9, 4387–4406, https://doi.org/10.5194/acp-9-4387-2009, 2009.

Moller, K. H., Otkjaer, R. V., Chen, J., and Kjaergaard, H. G.: Double Bonds Are Key to Fast Unimolecular Reactivity in First-Generation Monoterpene Hydroxy Peroxy Radicals, J. Phys. Chem. A, 124, 2885–2896, https://doi.org/10.1021/acs.jpca.0c01079, 2020.

Mumm, R. and Hilker, M.: Direct and indirect chemical defence of pine against folivorous insects, Trends in Plant Science, 11, 351–358, https://doi.org/10.1016/j.tplants.2006.05.007, 2006.

Novelli, A., Vereecken, L., Bohn, B., Dorn, H.-P., Gkatzelis, G. I., Hofzumahaus, A., Holland, F., Reimer, D., Rohrer, F., Rosanka, S., Taraborrelli, D., Tillmann, R., Wegener, R., Yu, Z., Kiendler-Scharr, A., Wahner, A., and Fuchs, H.: Importance of isomerization reactions for OH radical regeneration from the photo-oxidation of isoprene investigated in the atmospheric simulation chamber SAPHIR, Atmospheric Chemistry and Physics, 20, 3333–3355, https://doi.org/10.5194/acp-20-3333-2020, 2020.

Noziere, B., Barnes, I., and Becker, K. H.: Product study and mechanisms of the reactions of α-pinene and of pinonaldehyde with OH radicals, J. Geophys. Res.-Atmos., 104, 23 645–23 656, https://doi.org/10.1029/1999jd900778, 1999.

Nozière, B. and Hanson, D. R.: Speciated Monitoring of Gas-Phase Organic Peroxy Radicals by Chemical Ionization Mass Spectrometry: Cross-Reactions between CH3O2, CH3(CO)O2, (CH3)3CO2, and c-C6H11O2, The Journal of Physical Chemistry A, 121, 8453–8464, https://doi.org/10.1021/acs.jpca.7b06456, 2017.

Orkin, V. L., Kozlov, S. N., Poskrebyshev, G. A., and Kurylo, M. J.: Rate Constant for the Reaction of OH with H_2 between 200 and 480 K, The Journal of Physical Chemistry A, 110, 6978–6985, https://doi.org/10.1021/jp057035b, 2006.

Orlando, J. J., Noziere, B., Tyndall, G. S., Orzechowska, G. E., Paulson, S. E., and Rudich, Y.: Product studies of the OH- and ozone-initiated oxidation of some monoterpenes, J. Geophys. Res.-Atmos., 105, 11 561–11 572, https://doi.org/10.1029/2000jd900005, 2000.

Paulson, S. E. and Orlando, J. J.: The reactions of ozone with alkenes: An important source of HOx in the boundary layer, Geophysical Research Letters, 23, 3727–3730, https://doi.org/10.1029/96gl03477, 1996.

Peeters, J., Nguyen, T. L., and Vereecken, L.: HOx radical regeneration in the oxidation of isoprene, Physical Chemistry Chemical Physics, 11, 5935, https://doi.org/10.1039/b908511d, 2009.

Peeters, J., Müller, J.-F., Stavrakou, T., and Nguyen, V. S.: Hydroxyl Radical Recycling in Isoprene Oxidation Driven by Hydrogen Bonding and Hydrogen Tunneling: The Upgraded LIM1 Mechanism, The Journal of Physical Chemistry A, 118, 8625–8643, https://doi.org/10.1021/jp5033146, 2014.

Perrin, O., Heiss, A., Sahetchian, K., Kerhoas, L., and Einhorn, J.: Determination of the isomerization rate constant $HOCH_2CH_2CH_2CH(OO)CH_3$ -> $(HOCHCH_2CH_2CH)-H-(OOH)CH_3$. Importance of intramolecular hydroperoxy isomerization in tropospheric chemistry, International Journal of Chemical

Kinetics, 30, 875–887, https://doi.org/10.1002/(sici)1097-4601(1998)30:12⟨875::Aid-kin2⟩3.0.Co;2-8, 1998.

Platt, U. and Stutz, J.: Differential absorption spectroscopy, pp. 135–174, Physics of Earth and Space Environments, Springer, https://doi.org/doi.org/10.1007/978-3-540-75776-4, 2008.

Pullinen, I., Schmitt, S., Kang, S., Sarrafzadeh, M., Schlag, P., Andres, S., Kleist, E., Mentel, T. F., Rohrer, F., Springer, M., Tillmann, R., Wildt, J., Wu, C., Zhao, D. F., Wahner, A., and Kiendler-Scharr, A.: Impact of NOx on secondary organic aerosol (SOA) formation from alpha-pinene and beta-pinene photooxidation: the role of highly oxygenated organic nitrates, Atmospheric Chemistry and Physics, 20, 10 125–10 147, https://doi.org/10.5194/acp-20-10125-2020, 2020.

Reiner, T., Hanke, M., and Arnold, F.: Atmospheric peroxy radical measurements by ion molecule reaction-mass spectrometry: A novel analytical method using amplifying chemical conversion to sulfuric acid, Journal of Geophysical Research: Atmospheres, 102, 1311–1326, https://doi.org/10.1029/96jd02963, 1997.

Reissell, A., Aschmann, S. M., Atkinson, R., and Arey, J.: Products of the OH radical- and O_3initiated reactions of myrcene and ocimene, Journal of Geophysical Research, 107, https://doi.org/10.1029/2001jd001234, 2002.

Rohrer, F., Bohn, B., Brauers, T., Bruning, D., Johnen, F. J., Wahner, A., and Kleffmann, J.: Characterisation of the photolytic HONO-source in the atmosphere simulation chamber SAPHIR, Atmos. Chem. Phys., 5, 2189–2201, https://doi.org/10.5194/acp-5-2189-2005, 2005.

Rolletter, M., Blocquet, M., Kaminski, M., Bohn, B., H.-P.Dorn, Hofzumahaus, A., Holland, F., Li, X., Rohrer, F., Tillmann, R., R.Wegener, Kiendler-Scharr, A., Wahner, A., and Fuchs, H.: Photooxidation of pinonaldehyde at ambient conditions investigated in the atmospheric simulation chamber SAPHIR, Atmos. Chem. Phys., 20, 13 701–13 719, https://doi.org/doi.org/10.5194/acp-20-13701-2020, 2020.

Rollins, A. W., Smith, J. D., Wilson, K. R., and Cohen, R. C.: Real Time In Situ Detection of Organic Nitrates in Atmospheric Aerosols, Environ. Sci. Technol., 44, 5540–5545, https://doi.org/10.1021/es100926x, 2010.

Rollins, A. W., Pusede, S., Wooldridge, P., Min, K. E., Gentner, D. R., Goldstein, A. H., Liu, S., Day, D. A., Russell, L. M., Rubitschun, C. L., Surratt, J. D., and Cohen, R. C.: Gas/particle partitioning of total alkyl nitrates observed with TD-LIF in Bakersfield, J. Geophys. Res.-Atmos., 118, 6651–6662, https://doi.org/10.1002/jgrd.50522, 2013.

Sanchez, J., Tanner, D. J., Chen, D., Huey, L. G., and Ng, N. L.: A new technique for the direct detection of HO2 radicals using bromide chemical ionization mass spectrometry (Br-CIMS): initial characterization, Atmospheric Measurement Techniques, 9, 3851–3861, https://doi.org/10.5194/amt-9-3851-2016, 2016.

Sarrafzadeh, M., Wildt, J., Pullinen, I., Springer, M., Kleist, E., Tillmann, R., Schmitt, S. H., Wu, C., Mentel, T. F., Zhao, D. F., Hastie, D. R., and Kiendler-Scharr, A.: Impact of NOx and OH on secondary organic aerosol formation from beta-pinene photooxidation, Atmos. Chem. Phys., 16, 11 237–11 248, https://doi.org/10.5194/acp-16-11237-2016, 2016.

Saunders, S. M., Jenkin, M. E., Derwent, R. G., and Pilling, M. J.: Protocol for the development of the Master Chemical Mechanism, MCM v3 (Part A): tropospheric degradation of non-aromatic volatile organic compounds, Atmospheric Chemistry and Physics, 3, 161–180, https://doi.org/10.5194/acp-3-161-2003, 2003.

Schlosser, E., Bohn, B., Brauers, T., Dorn, H.-P., Fuchs, H., Häseler, R., Hofzumahaus, A., Holland, F., Rohrer, F., Rupp, L. O., Siese, M., Tillmann, R., and Wahner, A.: Intercomparison of Two Hydroxyl Radical Measurement Techniques at the Atmosphere Simulation Chamber SAPHIR, Journal of Atmospheric Chemistry, 56, 187–205, https://doi.org/10.1007/s10874-006-9049-3, 2007.

Seinfeld, J. H. and Pandis, S. N.: Atmospheric Chemistry and Physics From Air Pollution to Climate Change, John Wiley Sons, Inc., Hoboken, New Jersey, 2nd edn., 2006.

Tan, Z., **Hantschke, Luisa**, Kaminski, M., Acir, I.-H., Bohn, B., Cho, C., Dorn, H.-P., Li, X., Novelli, A., Nehr, S., Rohrer, F., Tillmann, R., Wegener, R., Hofzumahaus, A., Kiendler-Scharr, A., Wahner, A., and Fuchs, H.: Atmospheric photo-oxidation of myrcene: OH reaction rate constant, gas-phase oxidation products and radical budgets, Atmospheric Chemistry and Physics, 21, 16 067–16 091, https://doi.org/10.5194/acp-21-16067-2021, 2021.

Vereecken, L. and Noziere, B.: H migration in peroxy radicals under atmospheric conditions, Atmos. Chem. Phys., 20, 7429–7458, https://doi.org/10.5194/acp-20-7429-2020, 2020.

Vereecken, L. and Peeters, J.: Nontraditional (Per)oxy Ring-Closure Paths in the Atmospheric Oxidation of Isoprene and Monoterpenes, The Journal of Physical Chemistry A, 108, 5197–5204, https://doi.org/10.1021/jp049219g, 2004.

Vereecken, L. and Peeters, J.: Decomposition of substituted alkoxy radicals—part I: a generalized structure–activity relationship for reaction barrier heights, Physical Chemistry Chemical Physics, 11, 9062, https://doi.org/10.1039/b909712k, 2009.

Vereecken, L. and Peeters, J.: A structure–activity relationship for the rate coefficient of H-migration in substituted alkoxy radicals, Physical Chemistry Chemical Physics, 12, 12 608, https://doi.org/10.1039/c0cp00387e, 2010.

Vereecken, L. and Peeters, J.: A theoretical study of the OH-initiated gas-phase oxidation mechanism of β-pinene ($C_{10}H_{16}$): first generation products, Phy. Chem. Chem. Phys., 14, 3802–3815, https://doi.org/10.1039/c2cp23711c, 2012.

Vereecken, L., Müller, J. F., and Peeters, J.: Low-volatility poly-oxygenates in the OH-initiated atmospheric oxidation of α-pinene: impact of non-traditional peroxyl radical chemistry, Physical Chemistry Chemical Physics, 9, 5241, https://doi.org/10.1039/b708023a, 2007.

Vereecken, L., Aumont, B., Barnes, I., Bozzelli, J. W., Goldman, M. J., Green, W. H., Madronich, S., McGillen, M. R., Mellouki, A., Orlando, J. J., Picquet-Varrault, B., Rickard, A. R., Stockwell, W. R., Wallington, T. J., and Carter, W. P. L.: Perspective on Mechanism Development and Structure-Activity Relationships for Gas-Phase Atmospheric Chemistry, International Journal of Chemical Kinetics, 50, 435–469, https://doi.org/10.1002/kin.21172, 2018.

Vereecken, L., Carlsson, P. T. M., Novelli, A., Bernard, F., Brown, S. S., Cho, C., Crowley, J. N., Fuchs, H., Mellouki, W., Reimer, D., Shenolikar, J., Tillmann, R., Zhou, L., Kiendler-Scharr, A., and Wahner, A.: Theoretical and experimental study of peroxy and alkoxy radicals in the NO3-initiated oxidation of isoprene, Physical Chemistry Chemical Physics, 23, 5496–5515, https://doi.org/10.1039/d0cp06267g, 2021.

Veres, P. R., Roberts, J. M., Wild, R. J., Edwards, P. M., Brown, S. S., Bates, T. S., Quinn, P. K., Johnson, J. E., Zamora, R. J., and De Gouw, J.: Peroxynitric acid (HO_2NO_2) measurements during the UBWOS 2013 and 2014 studies using iodide ion chemical ionization mass spectrometry, Atmospheric Chemistry and Physics, 15, 8101–8114, https://doi.org/10.5194/acp-15-8101-2015, 2015.

Viggiano, A. A., Seeley, J. V., Mundis, P. L., Williamson, J. S., and Morris, R. A.: Rate Constants for the Reactions of XO3-(H2O)n (X = C, HC, and N) and NO3-(HNO3)n with H2SO4: Implications for Atmospheric Detection of H2SO4, The Journal of Physical Chemistry A, 101, 8275–8278, https://doi.org/10.1021/jp971768h, 1997.

WHO: WHO global air quality guidelines: particulate matter (PM2.5 and PM10), ozone, nitrogen dioxide, sulfur dioxide and carbon monoxide, World Health Organization, Geneva, URL https://apps.who.int/iris/handle/10665/345329, 2021.

Witter, M., Berndt, T., Boge, O., Stratmann, F., and Heintzenberg, J.: Gas-phase ozonolysis: Rate coefficients for a series of terpenes and rate coefficients and OH yields for 2-methyl-2-butene and 2,3-dimethyl-2-butene, Int. J. Chem. Kinet., 34, 394–403, https://doi.org/10.1002/kin.10063, 2002.

Xu, L., Moller, K. H., Crounse, J. D., Otkjwr, R. V., Kjaergaard, H. G., and Wennberg, P. O.: Unimolecular Reactions of Peroxy Radicals Formed in the Oxidation of alpha-Pinene and beta-Pinene by Hydroxyl Radicals, J. Phys. Chem. A, 123, 1661–1674, https://doi.org/10.1021/acs.jpca.8b11726, 2019.

Danksagung

Eine wissenschaftliche Arbeit ist nie nur das Werk einer Einzelnen, daher möchte ich die folgenden Zeilen nutzen, um all jenen zu danken, ohne die mir das Erstellen dieser Arbeit nicht möglich gewesen wäre.

Prof. Dr. Astrid Kiendler-Scharr und Prof. Dr. Andreas Wahner danke ich für die Möglichkeit, meine Arbeit am Institut für Energie- und Klimaforschung 8: Troposphäre anfertigen zu können.

Meinem Doktorvater PD Dr. Andreas Hofzumahaus danke ich für seine klugen Ratschläge und dafür, dass er sich immer die Zeit genommen hat, sich gründlich und ausgiebig mit meiner Forschung zu beschäftigen.

Prof. Dr Axel Klein danke ich für die freundliche Übernahme der Zweitkorrektur dieser Arbeit.

Die stete Unterstützung von PD Dr. Hendrik Fuchs, seine motivierenden Worte und großen und kleinen Hilfestellungen, wann immer ich nicht weiter wusste, haben mich bei dem Erstellen dieser Arbeit immer vorangebracht - danke!

Auch allen anderen Mitgliedern der LIF Gruppe bin ich zu großem Dank verpflichtet: Mathias Bachner, für seine Bereitschaft bei allen elektrischen Fragen und Problemen stets zu helfen, Dr. Frank Holland für ein offenes Ohr bei allen Fragen zu IDL und radioaktiven Quellen und besonders Dr. Anna Novelli, die nicht nur die beste Büropartnerin ist, die man sich wünschen kann, sondern auch immer bereit war, mir bei Hindernissen jeglicher Art mit Rat und Tat beiseite zu stehen.

PD Dr. Thomas Mentel und seiner gesamten Gruppe, besonders Dr Sören Zorn, Dr. Sungah Kang & Yarê Baker, danke ich für die Unterstützung bei allen Fragen rund um das Massenspektrometer, fürs Aufmuntern, wenn's Mal nicht so lief und für das gemeinsame Rätseln über mysteriöse Ausfälle des CIMS.

Dr. Torsten Berndt danke ich für die freundliche Aufnahme in seinem Labor und für die Unterstützung bei dem Versuch, die Peroxyradikal-Messungen auch an unserer Kammer zu realisieren.

Allen Beteiligten an den SAPHIR und SAPHIR-STAR Messungen gilt mein großer Dank für ihre Unterstützung bei allen Experimenten.

Ein herzliches Dankeschön auch an alle anderen Kollegen und Doktoranden, die hier aufgrund des mangelnden Platzes nicht alle aufgezählt werden können, aber ohne die meine Zeit am IEK-8 nicht dieselbe gewesen wäre.

Danke an Dilcan, Dagmar, Angie, Flo & Tom, ohne die mein Studium wohl nicht nur viel weniger spaßig, sondern auch deutlich länger gewesen wäre.
Mein größter Dank gilt meiner Familie. Danke an meine Paten Evi und Norbert und Stefan und Philipp, mit denen ich sogar unter dem Weihnachtsbaum über Wissenschaft diskutieren kann. Danke an meinen Vater Gerhard, der stets an mich und meine Fähigkeiten glaubt und mich bedingungslos unterstützt. Ohne meine Mama Petra, ohne ihre Stärke, ihren Mut, ihre Liebe und Bereitschaft, mich bei allen meinen Lebenswegen zu unterstützen wäre ich nicht die, die ich bin - ich danke dir! Meiner großen Schwester Lena, meinem Vorbild und sicheren Anker in allen Lebenslagen, danke ich für ihr Vertrauen, ihren kritischen Geist und das starke Band, das uns auch über die größte Distanz immer verbindet. Ein herzliches Danke auch an meinen Schwager Marc, der es nie versäumt uns alle zum Lachen zu bringen.
Zuletzt ein großer Dank an Thomas, für seine Fürsorglichkeit, seine Kochkünste, aber vor allem seine Liebe und den unabdingbaren Glauben an mich, auch in den schwierigsten Zeiten.

Acronyms

API	Atmospheric Pressure Interface
BSQ	Big Segmented Quadrupole
CI	Criegee Intermediate
CI-inlet	Chemical Ionization inlet
CIMS	Chemical Ionization Mass Spectrometry
cps	counts per second
DOAS	Differential Optical Absorption Spectroscopy
FEP	Fluoro-Etyhlene-Propylene
HOM	Highly Oxidized Molecules
IPN	Isopropylnitrite
JPAC	Jülich Plant Atmosphere Chamber
$\mathbf{k}_{OH}$	OH reactivity
LIF	Laser Induced Fluorescence
MCM	Master Chemical Mechanism
MCP	Multi Channel Plate
ncps	normalized counts per second
POZ	Primary Ozonide
ppbv	part per billion by volume
pptv	part per trillion by volume
PTR	Proton Transfer Reaction
RH	relative humidity

SAPHIR	Simulation of Atmospheric PHotochemistry In a large Reaction Chamber
SAPHIR-STAR	STirred Atmospheric flow Reactor
SAR	Structure-Activity Relationship
SOA	Secondary Organic Aerosol
SOZ	Secondary Ozonide
SSQ	Small Segmented Quadrupole
Th	Thomson
TME	Tetramethylethylene
TOF	Time of Flight
VOC	Volatile Organic Compounds

A Appendix

A.1 Supplementary materials to Chapter 5

Supplement of Atmos. Chem. Phys., 21, 12665–12685, 2021
https://doi.org/10.5194/acp-21-12665-2021-supplement

Atmospheric Chemistry and Physics
Open Access
EGU

Supplement of

Atmospheric photooxidation and ozonolysis of Δ^3-carene and 3-caronaldehyde: rate constants and product yields

Luisa Hantschke et al.

Correspondence to: Hendrik Fuchs (h.fuchs@fz-juelich.de)

Table S1 . Instrumentation for radical and trace gas detection in the experiments.

measured quantity	**measurement technique**	**time resolution**	**accuracy (1 σ)**	**LoD (1 σ)**
OH	laser-induced fluoresence (LIF)	47 s	13 %	$0.7\times10^{6}\,\mathrm{cm}^{-3}$
HO_2, RO_2	laser-induced fluoresence (LIF)	47 s	16 %	$0.8\times10^{7}\,\mathrm{cm}^{-3}$
k_{OH}	laser photolysis + LIF	180 s	10 %	$0.3\,\mathrm{s}^{-1}$
Δ^3-carene	proton-transfer-reaction mass-spectrometer	40 s	7 %	2 pptv
CO	cavity ring-down spectroscopy	60 s	1 ppbv	80 ppbv
NO	chemiluminescence	180 s	5 %	4 pptv
NO_2	chemiluminescence	180 s	5 %	2 pptv
HONO	long-path absorption photometry	300 s	20 %	5 pptv
O_3	UV-absorption	10 s	5 %	1 ppbv
HCHO	Hantzsch monitor	90 s	8.5 %	0.1 ppbv
HCHO	cavity ring-down spectroscopy	300 s	1.5 ppbv	0.1 ppbv
photolysis freq.	spectroradiometer	60 s	10 %	[a]

[a] several orders of magnitude lower than the maximum value at noon

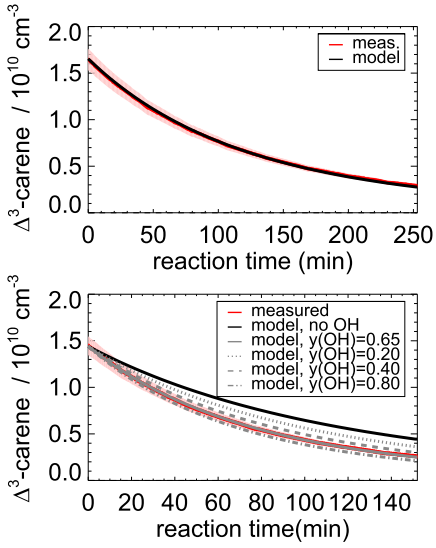

Figure S1 . Measured and modeled Δ^3-carene concentrations for the ozonolysis experiment E4. During the second part of the experiment (upper panel), $90\,\mathrm{ppmv}$ of an OH scavenger (CO) were injected to suppress OH, so that Δ^3-carene reacted only with ozone. The modeled decay is fitted with a rate constant of $(4.4 \pm 0.2) \times 10^{-17}\,\mathrm{cm^3\ s^{-1}}$. During the first part of the experiment (lower panel), when no CO was present, the measured decay of Δ^3-carene is signficantly faster than expected from ozonolysis alone. The measured time series of Δ^3-carene can be best matched, if an OH yield of 0.65 ± 0.10 from its ozonolysis reaction is assumed. OH yields of 0.20, 0.40 and 0.80 are also presented in the lower panel to demonstrate the sensitivity of the system to changes in the OH yield.

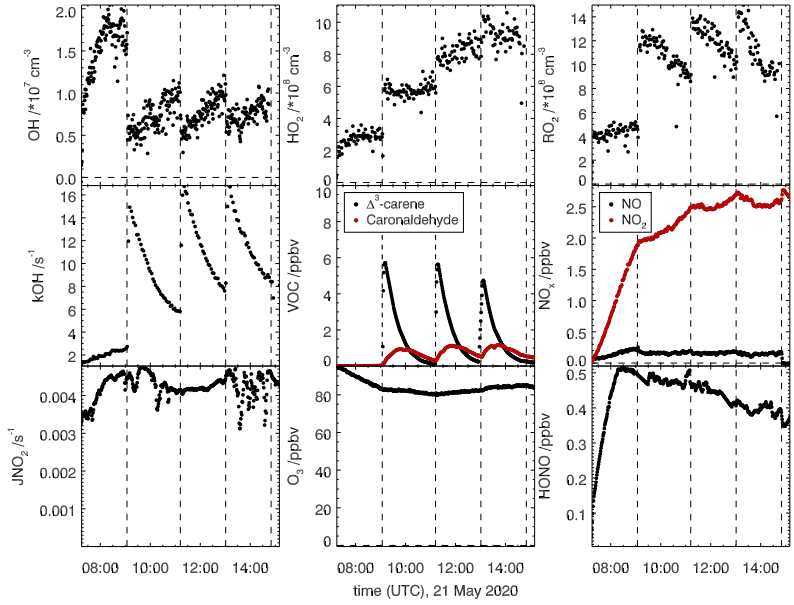

Figure S2 . Overview of measured concentrations for selected species in the SAPHIR chamber for the Δ^3-carene + OH oxidation experiment with low NOx conditions on E2. Dashed lines indicate times when Δ^3-carene was injected into the chamber.

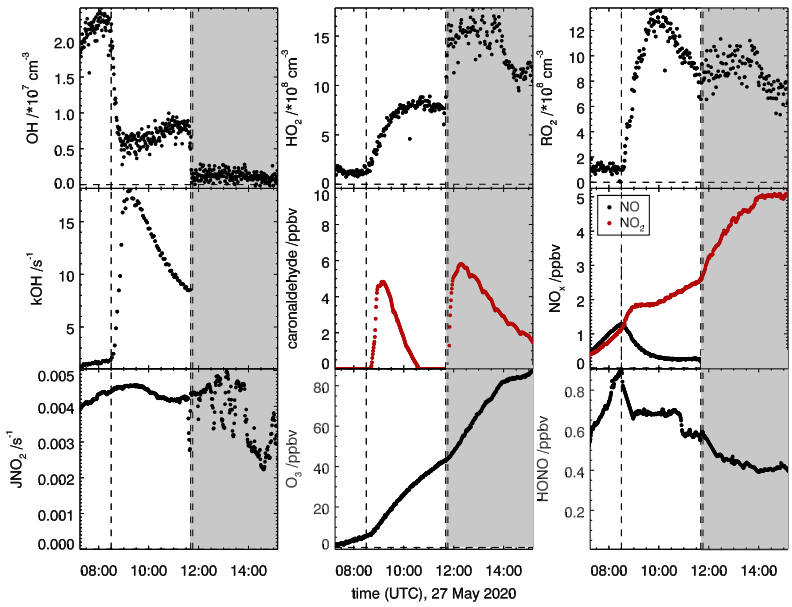

Figure S3 . Overview of measured concentrations for selected species in the SAPHIR chamber for the caronaldehyde photooxidation experiments E5. The shaded area indicates the time where CO was injected as an OH scaveger (experiment E6). Dashed lines indicate times when caronaldehyde was injected into the chamber.

5

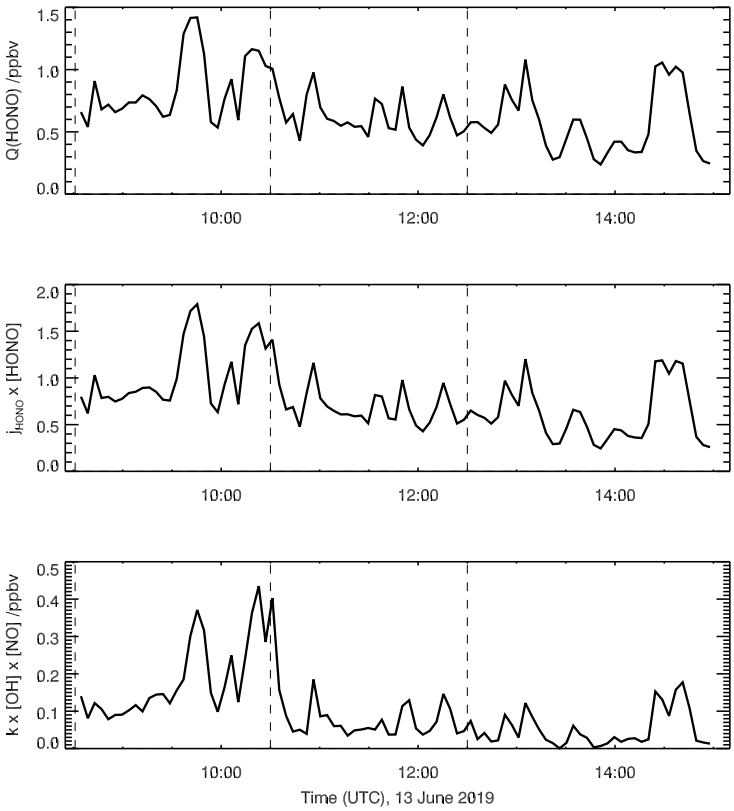

Figure S4 . Timeseries of Q(HONO), $k_{OH+NO} \times OH \times NO$ and $j_{HONO} \times HONO$ used to calculate the organic nitrate yield of the OH + Δ^3-carene in the main text (see Section 2.5).

A.2 Supplementary materials to Chapter 6

Supplement of Atmos. Chem. Phys., 21, 16067–16091, 2021
https://doi.org/10.5194/acp-21-16067-2021-supplement

Atmospheric Chemistry and Physics
Open Access
EGU

Supplement of

Atmospheric photo-oxidation of myrcene: OH reaction rate constant, gas-phase oxidation products and radical budgets

Zhaofeng Tan et al.

Correspondence to: Hendrik Fuchs (h.fuchs@fz-juelich.de)

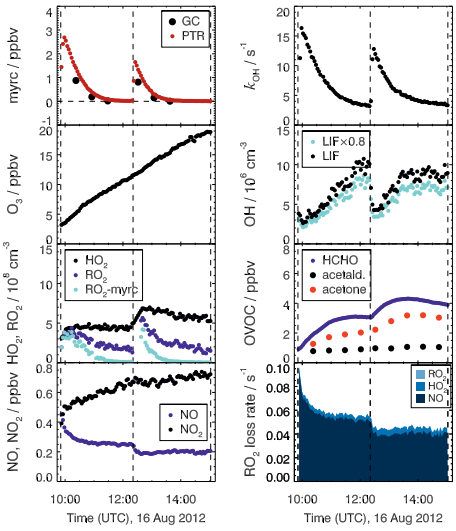

Figure S1. Overview of time series of trace gas and radical concentrations in the chamber experiment investigating the OH oxidation of myrcene (myrc) for medium NO mixing ratios on 16 August 2012. Total organic peroxy radical (RO_2) concentrations and RO_2 from the reaction of OH with myrcene were calculated from observations as explained in Section 2.4. In additions to trace gases, the loss rates of RO_2 with respect to their reaction with NO and radical recombination reactions are shown. OH measurements by LIF were scaled by a factor of 0.8 because the comparison between OH and DOAS hints to an calibration error of LIF measurements.

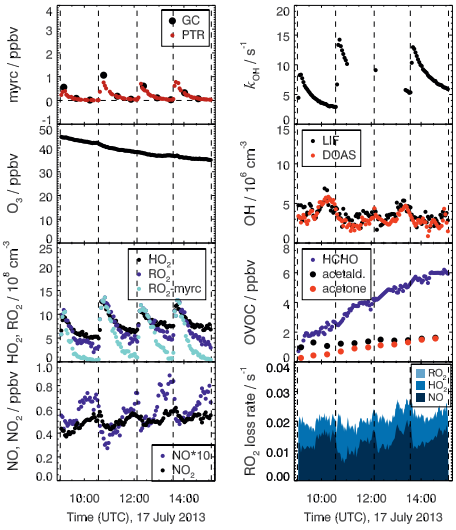

Figure S2. Same as Fig. S1, but for the experiment with myrcene at low NO conditions on 17 July 2013.

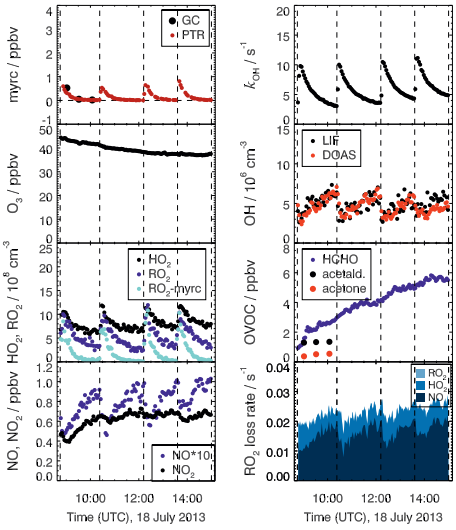

Figure S3. Same as Fig. S1, but for the experiment with myrcene at low NO conditions on 18 July 2013.

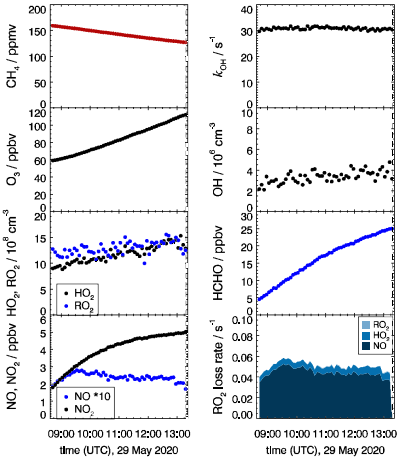

Figure S4. Same as Fig. S1, but for the experiment with methane on 29 May 2020.

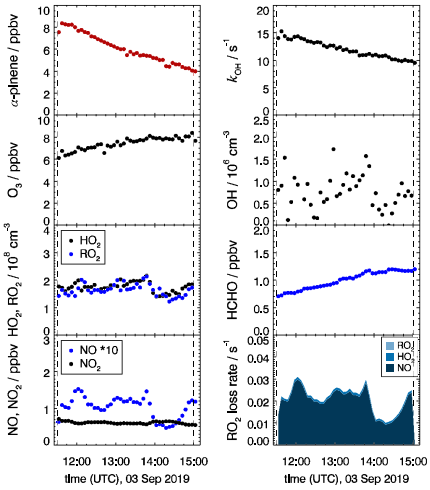

Figure S5. Same as Fig. S1, but for the experiment with α-pinene on 03 September 2019.

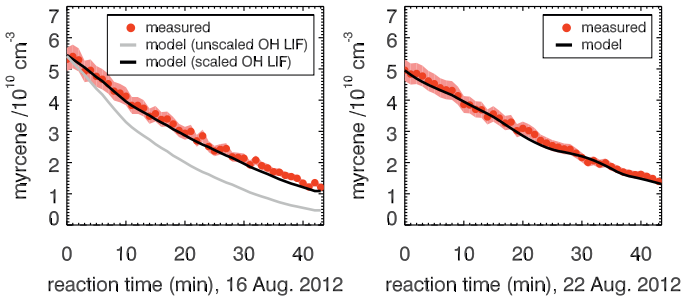

Figure S6. Comparison of the measured time series of myrcene concentrations with results from model calculations on 22 August 2012 (left panel) and 16 August 2012 (right panel). The model is constrained to measured temperature, pressure, ozone and OH concentrations and the rate constant of the reaction of myrcene with OH was optimized resulting in a value of $2.1 \times 10^{-10} molecules\,\mathrm{cm}^{-3}\mathrm{s}^{-1}$. OH was measured on 22 August by DOAS and LIF and only by LIF on 16 August. The comparison of OH and DOAS measurements on 22 August revealed that LIF measurements need to be scaled by a factor of 0.8, most likely due to a calibration error. Therefore, also measurements on 16 August are scaled by a factor of 0.8. Model results demonstrates that the scaling of the OH measurements is also required to describe the measured behaviour of myrcene in this experiment.

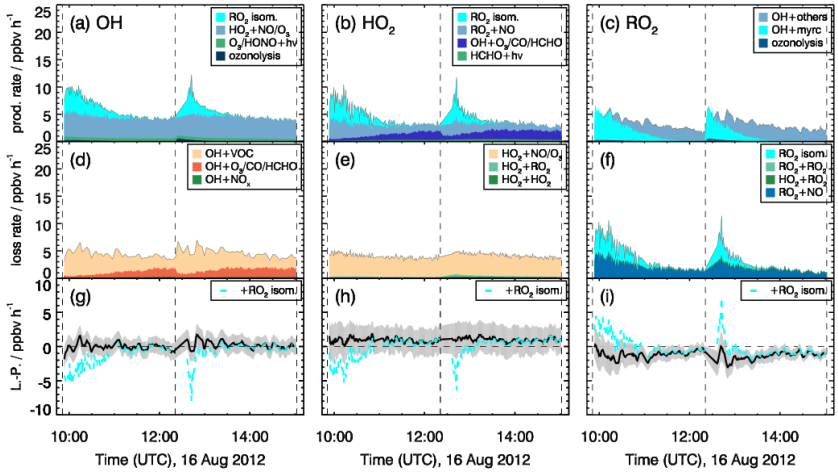

Figure S7. Rates of radical conversion reactions and imbalances between production and destruction rates ($L - P$) for the experiment with medium NO mixing ratios on 16 August 2012. Grey areas in the lower panels give the uncertainty of $L - P$. In the lowest right panel, the black and cyan lines denote RO_2 budget without and with considering MyO_2 isomerization reaction at a rate of $0.014\,s^{-1}$.

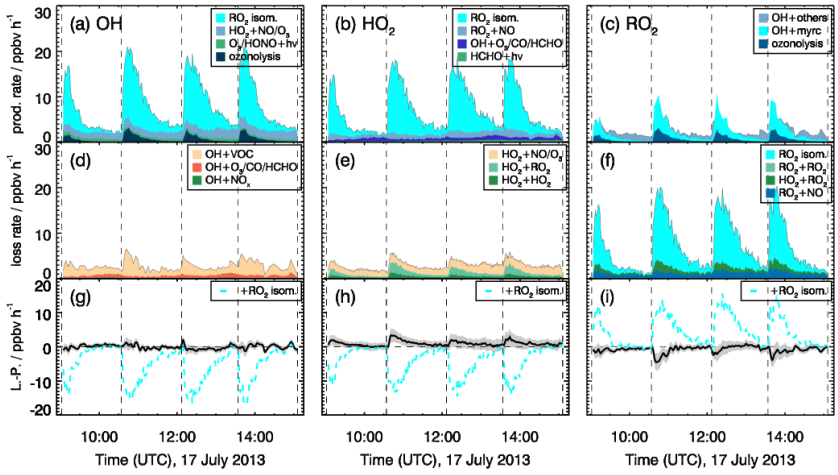

Figure S8. Same as Fig. S7, but for the experiment with myrcene at low NO conditions on 17 July 2013.

A.3 Supplementary materials to Chapter 7

A.3.1 β-pinene mechanism used in the model

```
; Source: MCM,version 3.3.1
;adapted unimolecular reaction rates from Vereecken et al., 2012
; or Xu et al., 2019
;rate constants are given in units of s^{-1}
;if not specified, rate constants are given for 298 K
;nomenclature adapted from MCM, version 3.3.1


;k's of unimolecular reaction by Vereecken et al., 2012
k[BPINCO2-->BPINCO4E]=CONST(0.62)
k[BPINCO2-->BPINCO4H5]=CONST(0.05)
k[BPINCO4H5-->BPINCO6]=CONST(10.0)
;k[BPINCO4H5-->BPINCO6] value obtained after optimization
;in this thesis

;k's of unimolecular reaction by Xu et al., 2019
k[BPINCO2-->BPINCO4E]=CONST(4.1)
k[BPINCO2-->BPINCO4H5]=CONST(1.0)

; k's from MCM
k[TME+O3-->CH3CH3CO+CH3CH3COO]=CONST(1.13D-15)
k[CH3CH3COO-->CH3COCH2+OH]=CONST(7.8D5)
k[BPINENE+O3-->NOPINONE+CH2OOF]=CONST(1.35D-15*EXP(-1270/T)*0.4)
k[BPINENE+O3-->NOPINOOA+HCHO]=CONST(1.35D-15*EXP(-1270/T)*0.6)
k[BPINENE+OH-->BPINAO2]=CONST(2.38D-11*EXP(357/T)*0.1)
k[BPINENE+OH-->BPINBO2]=CONST(2.38D-11*EXP(357/T)*0.01)
k[BPINENE+OH-->BPINCO2]=CONST(2.38D-11*EXP(357/T)*0.75)
k[NOPINONE+OH-->NOPINAO2]=CONST(1.55D-11*0.535)
k[NOPINONE+OH-->NOPINBO2]=CONST(1.55D-11*0.199)
k[NOPINONE+OH-->NOPINCO2]=CONST(1.55D-11*0.130)
k[NOPINONE+OH-->NOPINDO2]=CONST(1.55D-11*0.136)
k[CH2OOF-->CH2OO]=CONST(KDEC*0.370)
k[CH2OOF-->CO]=CONST(KDEC*0.500)
k[CH2OOF-->HO2+CO+OH]=CONST(KDEC*0.130)
k[NOPINOOA-->C8BC]=CONST(KDEC*0.330)
k[NOPINOOA-->NOPINDO2+OH]=CONST(KDEC*0.500)
```

```
k[NOPINOOA-->NOPINOO]=CONST(KDEC*0.170)
k[NO3+HCHO-->HNO3+CO+HO2]=CONST(5.5D-16)
k[OH+HCHO-->HO2+CO]=CONST(5.4D-12*EXP(135/T))
k[BPINAO2+HO2-->BPINAOOH]=CONST(KRO2HO2*0.914)
k[BPINAO2+NO-->BPINANO3]=CONST(KRO2NO*0.240)
k[BPINAO2+NO-->BPINAO+NO2]=CONST(KRO2NO*0.760)
k[BPINAO2+NO3-->BPINAO+NO2]=CONST(KRO2NO3)
k[BPINAO2-->BPINAO]=CONST(9.20D-14*RO2*0.7)
k[BPINAO2-->BPINAOH]=CONST(9.20D-14*RO2*0.3)
k[BPINBO2+HO2-->BPINBOOH]=CONST(KRO2HO2*0.914)
k[BPINBO2+NO-->BPINBNO3]=CONST(KRO2NO*0.240)
k[BPINBO2+NO-->BPINBO+NO2]=CONST(KRO2NO*0.760)
k[BPINBO2+NO3-->BPINBO+NO2]=CONST(KRO2NO3)
k[BPINBO2-->BPINAOH]=CONST(2.00D-12*RO2*0.2)
k[BPINBO2-->BPINBO]=CONST(2.00D-12*RO2*0.6)
k[BPINBO2-->C918CHO]=CONST(2.00D-12*RO2*0.2)
k[BPINCO2+HO2-->BPINCOOH]=CONST(KRO2HO2*0.914)
k[BPINCO2+NO-->BPINCNO3]=CONST(KRO2NO*0.125)
k[BPINCO2+NO-->BPINCO+NO2]=CONST(KRO2NO*0.875)
k[BPINCO2+NO3-->BPINCO+NO2]=CONST(KRO2NO3)
k[BPINCO2-->BPINCO]=CONST(6.70D-15*RO2*0.7)
k[BPINCO2-->BPINCOH]=CONST(6.70D-15*RO2*0.3)
k[BPINCO4E+NO-->BPINCNO5]=CONST(KRO2NO*0.125)
k[BPINCO4E+NO-->BPINCO3+NO2]=CONST(KRO2NO*0.875)
k[BPINCO4E-->BPINCO]=CONST(6.70D-15*RO2*0.7)
k[BPINCO4E-->BPINCOH4]=CONST(6.70D-15*RO2*0.3)
k[BPINCO4E+HO2-->BPINCOOH]=CONST(KRO2HO2*0.914)
k[BPINCO4H5+NO-->BPINCNO5]=CONST(KRO2NO*0.125)
k[BPINCO4H5+NO-->BPINCO3+NO2]=CONST(KRO2NO*0.875)
k[BPINCO4H5-->BPINCO]=CONST(6.70D-15*RO2*0.7)
k[BPINCO4H5-->BPINCOH4]=CONST(6.70D-15*RO2*0.3)
k[BPINCO4H5+HO2-->BPINCOOH]=CONST(KRO2HO2*0.914)
k[BPINCO6+NO-->BPINCNO7]=CONST(KRO2NO*0.125)
k[BPINCO6+NO-->BPINCO5+NO2]=CONST(KRO2NO*0.875)
k[BPINCO6-->BPINCO]=CONST(6.70D-15*RO2*0.7)
k[BPINCO6-->BPINCOH4]=CONST(6.70D-15*RO2*0.3)
k[BPINCO6+HO2-->BPINCOOH]=CONST(KRO2HO2*0.914)
k[BPINCNO3+OH-->NOPINONE+HCHO+NO2]=CONST(4.7D-12)
k[BPINBNO3+OH-->NOPINONE+HCHO+NO2]=CONST(4.7D-12)
```

```
k[BPINANO3+OH-->NOPINONE+HCHO+NO2]=CONST(4.7D-12)
k[BPINCNO5-->STUFF]=CONST(4.7D-12)
k[BPINCNO7-->STUFF]=CONST(4.7D-12)
k[NBPINAOOH+OH-->NBPINAO2]=CONST(9.58D-12)
k[NBPINAO-->NOPINONE+HCHO+NO2]=CONST(KDEC)
k[BPINBNO3+OH-->C918CHO+NO2]=CONST(6.12D-12)
k[NBPINBOOH+OH-->NC91CHO+OH]=CONST(9.08D-12)
k[NBPINBO-->NOPINONE+HCHO+NO2]=CONST(7.00D+03)
k[BPINANO3+OH-->NOPINONE+HCHO+NO2]=CONST(4.70D-12)
k[NC91CHO+NO3-->NC91CO3+HNO3]=CONST(KNO3AL*8.5)
k[NC91CHO+OH-->NC91CO3]=CONST(8.63D-12)
k[NOPINAO2+HO2-->NOPINAOOH]=CONST(KRO2HO2*0.890)
k[NOPINAO2+NO-->NOPINANO3]=CONST(KRO2NO*0.157)
k[NOPINAO2+NO-->NOPINAO+NO2]=CONST(KRO2NO*0.843)
k[NOPINAO2+NO3-->NOPINAO+NO2]=CONST(KRO2NO3)
k[NOPINAO2-->C9DC]=CONST(2.50D-13*RO2*0.2)
k[NOPINAO2-->NOPINAO]=CONST(2.50D-13*RO2*0.6)
k[NOPINAO2-->NOPINAOH]=CONST(2.50D-13*RO2*0.2)
k[NOPINBO2+HO2-->NOPINBOOH]=CONST(KRO2HO2*0.890)
k[NOPINBO2+NO-->NOPINBNO3]=CONST(KRO2NO*0.157)
k[NOPINBO2+NO-->NOPINBO+NO2]=CONST(KRO2NO*0.843)
k[NOPINBO2+NO3-->NOPINBO+NO2]=CONST(KRO2NO3)
k[NOPINBO2-->NOPINBCO]=CONST(2.50D-13*RO2*0.2)
k[NOPINBO2-->NOPINBO]=CONST(2.50D-13*RO2*0.6)
k[NOPINBO2-->NOPINBOH]=CONST(2.50D-13*RO2*0.2)
k[NOPINCO2+HO2-->NOPINCOOH]=CONST(KRO2HO2*0.890)
k[NOPINCO2+NO-->NOPINCNO3]=CONST(KRO2NO*0.118)
k[NOPINCO2+NO-->NOPINCO+NO2]=CONST(KRO2NO*0.882)
k[NOPINCO2+NO3-->NOPINCO+NO2]=CONST(KRO2NO3)
k[NOPINCO2-->NOPINCO]=CONST(6.70D-15*RO2*0.7)
k[NOPINCO2-->NOPINCOH]=CONST(6.70D-15*RO2*0.3)
k[NOPINDO2+HO2-->NOPINDOOH]=CONST(KRO2HO2*0.890)
k[NOPINDO2+NO-->NOPINDO+NO2]=CONST(KRO2NO)
k[NOPINDO2+NO3-->NOPINDO+NO2]=CONST(KRO2NO3)
k[NOPINDO2-->NOPINDCO]=CONST(2.00D-12*RO2*0.05)
k[NOPINDO2-->NOPINDO]=CONST(2.00D-12*RO2*0.9)
k[NOPINDO2-->NOPINDOH]=CONST(2.00D-12*RO2*0.05)
k[CH2OO+CO-->HCHO]=CONST(1.20D-15)
k[CH2OO+NO-->HCHO+NO2]=CONST(1.00D-14)
```

```
k[CH2OO+NO2-->HCHO+NO3]=CONST(1.00D-15)
k[CH2OO+SO2-->HCHO+SO3]=CONST(7.00D-14)
k[CH2OO-->HCHO+H2O2]=CONST(6.00D-18*H2O)
k[CH2OO-->HCOOH]=CONST(1.00D-17*H2O)
k[C8BC+OH-->C8BCO2]=CONST(3.04D-12)
k[NOPINOO+CO-->NOPINONE]=CONST(1.20D-15)
k[NOPINOO+NO-->NOPINONE+NO2]=CONST(1.00D-14)
k[NOPINOO+NO2-->NOPINONE+NO3]=CONST(1.00D-15)
k[NOPINOO+SO2-->NOPINONE+SO3]=CONST(7.00D-14)
k[NOPINOO-->NOPINONE+H2O2]=CONST(6.00D-18*H2O)
k[BPINAOOH+OH-->BPINAO2]=CONST(1.33D-11)
k[BPINAO-->NOPINONE+HCHO+HO2]=CONST(KDEC)
k[BPINAOH+OH-->C918CHO+HO2]=CONST(9.88D-12)
k[BPINBOOH+OH-->C918CHO+OH]=CONST(1.90D-11)
k[BPINBO-->NOPINONE+HCHO+HO2]=CONST(KDEC)
k[C918CHO+NO3-->C918CO3+HNO3]=CONST(KNO3AL*8.5)
k[C918CHO+OH-->C918CO3]=CONST(3.17D-11)
k[BPINCOOH+OH-->BPINCO2]=CONST(9.72D-11)
k[BPINCNO3+OH-->HCC7CO+CH3COCH3+NO2]=CONST(9.38D-11)
k[BPINCO-->C720O2+CH3COCH3]=CONST(KDEC)
k[BPINCOH+OH-->BPINCO]=CONST(9.37D-11)
k[NC91CO3+HO2-->NC91CO3H]=CONST(KAPHO2*0.56)
k[NC91CO3+HO2-->NOPINONE+NO2+OH]=CONST(KAPHO2*0.44)
k[NC91CO3+NO-->NOPINONE+NO2+NO2]=CONST(KAPNO)
k[NC91CO3+NO2-->NC91PAN]=CONST(KFPAN)
k[NC91CO3+NO3-->NOPINONE+NO2+NO2]=CONST(KRO2NO3*1.74)
k[NC91CO3-->NOPINONE+NO2]=CONST(1.00D-11*RO2)
k[NOPINAOOH+OH-->C9DC+OH]=CONST(8.59D-11)
k[NOPINANO3+OH-->C9DC+NO2]=CONST(3.24D-12)
k[NOPINAO-->C918O2]=CONST(2.70D+14*EXP(-6643/T))
k[NOPINAO-->C9DC+HO2]=CONST(KROSEC*O2)
k[C9DC+OH-->C9DCO2]=CONST(6.07D-12)
k[NOPINAOH+OH-->C9DC+HO2]=CONST(3.68D-11)
k[NOPINBOOH+OH-->NOPINBCO+OH]=CONST(3.44D-11)
k[NOPINBNO3+OH-->NOPINBCO+NO2]=CONST(6.05D-12)
k[NOPINBO-->C915O2]=CONST(KDEC)
k[NOPINBCO+OH-->C915O2]=CONST(1.64D-11)
k[NOPINBOH+OH-->NOPINBCO+HO2]=CONST(1.81D-11)
k[NOPINCOOH+OH-->NOPINCO2]=CONST(1.11D-11)
```

```
k[NOPINCNO3+OH-->CH3COCH3+C619CO+NO2]=CONST(6.37D-12)
k[NOPINCO-->C917O2]=CONST(KDEC)
k[NOPINCOH+OH-->NOPINCO]=CONST(7.69D-12)
k[NOPINDOOH+OH-->NOPINDCO+OH]=CONST(2.63D-11)
k[NOPINDO-->C89CO3]=CONST(KDEC)
k[NOPINDCO+OH-->C89CO3]=CONST(3.07D-12)
k[NOPINDOH+OH-->NOPINDCO+HO2]=CONST(1.41D-11)
k[HCOOH+OH-->HO2]=CONST(4.5D-13)
k[C8BCO2+HO2-->C8BCOOH]=CONST(KRO2HO2*0.859)
k[C8BCO2+NO-->C8BCNO3]=CONST(KRO2NO*0.138)
k[C8BCO2+NO-->C8BCO+NO2]=CONST(KRO2NO*0.862)
k[C8BCO2+NO3-->C8BCO+NO2]=CONST(KRO2NO3)
k[C8BCO2-->C8BCCO]=CONST(2.50D-13*RO2*0.2)
k[C8BCO2-->C8BCO]=CONST(2.50D-13*RO2*0.6)
k[C8BCO2-->C8BCOH]=CONST(2.50D-13*RO2*0.2)
k[C918CO3+HO2-->C918CO3H]=CONST(KAPHO2*0.56)
k[C918CO3+HO2-->NOPINONE+HO2+OH]=CONST(KAPHO2*0.44)
k[C918CO3+NO-->NOPINONE+HO2+NO2]=CONST(KAPNO)
k[C918CO3+NO2-->C918PAN]=CONST(KFPAN)
k[C918CO3+NO3-->NOPINONE+HO2+NO2]=CONST(KRO2NO3*1.74)
k[C918CO3-->NOPINONE+HO2]=CONST(1.00D-11*RO2)
k[HCC7CO+OH-->C719O2]=CONST(1.19D-10)
k[CH3COCH3+OH-->CH3COCH2O2]=CONST(8.8D-12*EXP(-1320/T)+1.7D-14*EXP(423/T))
k[C720O2+HO2-->C720OOH]=CONST(KRO2HO2*0.820)
k[C720O2+NO-->C720NO3]=CONST(KRO2NO*0.278)
k[C720O2+NO-->C720O+NO2]=CONST(KRO2NO*0.722)
k[C720O2+NO3-->C720O+NO2]=CONST(KRO2NO3)
k[C720O2-->C720O]=CONST(2.50D-13*RO2*0.6)
k[C720O2-->C720OH]=CONST(2.50D-13*RO2*0.2)
k[C720O2-->HCC7CO]=CONST(2.50D-13*RO2*0.2)
k[NC91CO3H+OH-->NC91CO3]=CONST(8.85D-12)
k[NC91PAN+OH-->NOPINONE+CO+NO2+NO2]=CONST(4.90D-12)
k[NC91PAN-->NC91CO3+NO2]=CONST(KBPAN)
k[C918O2+HO2-->C918OOH]=CONST(KRO2HO2*0.890)
k[C918O2+NO-->C918NO3]=CONST(KRO2NO*0.047)
k[C918O2+NO-->C918O+NO2]=CONST(KRO2NO*0.953)
k[C918O2+NO3-->C918O+NO2]=CONST(KRO2NO3)
k[C918O2-->C918O]=CONST(6.70D-15*RO2*0.7)
k[C918O2-->C918OH]=CONST(6.70D-15*RO2*0.3)
```

```
k[C9DCO2+HO2-->C9DCOOH]=CONST(KRO2HO2*0.890)
k[C9DCO2+NO-->C9DCNO3]=CONST(KRO2NO*0.157)
k[C9DCO2+NO-->C9DCO+NO2]=CONST(KRO2NO*0.843)
k[C9DCO2+NO3-->C9DCO+NO2]=CONST(KRO2NO3)
k[C9DCO2-->C9DCCO]=CONST(2.50D-13*RO2*0.2)
k[C9DCO2-->C9DCO]=CONST(2.50D-13*RO2*0.6)
k[C9DCO2-->C9DCOH]=CONST(2.50D-13*RO2*0.2)
k[C915O2+HO2-->C915OOH]=CONST(KRO2HO2*0.890)
k[C915O2+NO-->C915NO3]=CONST(KRO2NO*0.157)
k[C915O2+NO-->C915O+NO2]=CONST(KRO2NO*0.843)
k[C915O2+NO3-->C915O+NO2]=CONST(KRO2NO3)
k[C915O2-->C88CHO]=CONST(8.80D-13*RO2*0.2)
k[C915O2-->C915O]=CONST(8.80D-13*RO2*0.6)
k[C915O2-->C915OH]=CONST(8.80D-13*RO2*0.2)
k[C619CO+OH-->C512CO3]=CONST(5.99D-12)
k[C917O2+HO2-->C917OOH]=CONST(KRO2HO2*0.890)
k[C917O2+NO-->C917NO3]=CONST(KRO2NO*0.118)
k[C917O2+NO-->C917O+NO2]=CONST(KRO2NO*0.882)
k[C917O2+NO3-->C917O+NO2]=CONST(KRO2NO3)
k[C917O2-->C917O]=CONST(6.70D-15*RO2*0.7)
k[C917O2-->C917OH]=CONST(6.70D-15*RO2*0.3)
k[C89CO3+HO2-->C89CO2+OH]=CONST(KAPHO2*0.44)
k[C89CO3+HO2-->C89CO2H+O3]=CONST(KAPHO2*0.15)
k[C89CO3+HO2-->C89CO3H]=CONST(KAPHO2*0.41)
k[C89CO3+NO-->C89CO2+NO2]=CONST(KAPNO)
k[C89CO3+NO2-->C89PAN]=CONST(KFPAN)
k[C89CO3+NO3-->C89CO2+NO2]=CONST(KRO2NO3*1.74)
k[C89CO3-->C89CO2]=CONST(1.00D-11*RO2*0.7)
k[C89CO3-->C89CO2H]=CONST(1.00D-11*RO2*0.3)
k[C8BCOOH+OH-->C8BCCO+OH]=CONST(1.62D-11)
k[C8BCNO3+OH-->C8BCCO+NO2]=CONST(1.84D-12)
k[C8BCO-->C89O2]=CONST(KDEC)
k[C8BCCO+OH-->C89O2]=CONST(3.94D-12)
k[C8BCOH+OH-->C8BCCO+HO2]=CONST(6.81D-12)
k[C918CO3H+OH-->C918CO3]=CONST(1.46D-11)
k[C918PAN+OH-->NOPINONE+CO+NO2]=CONST(5.71D-12)
k[C918PAN-->C918CO3+NO2]=CONST(KBPAN)
k[C719O2+HO2-->C719OOH]=CONST(KRO2HO2*0.820)
k[C719O2+NO-->C719NO3]=CONST(KRO2NO*0.042)
```

```
k[C719O2+NO-->C719O+NO2]=CONST(KRO2NO*0.958)
k[C719O2+NO3-->C719O+NO2]=CONST(KRO2NO3)
k[C719O2-->C719O]=CONST(9.20D-14*RO2*0.7)
k[C719O2-->C719OH]=CONST(9.20D-14*RO2*0.3)
k[CH3COCH2O2+HO2-->CH3COCH2O+OH]=CONST(1.36D-13*EXP(1250/T)*0.15)
k[CH3COCH2O2+HO2-->HYPERACET]=CONST(1.36D-13*EXP(1250/T)*0.85)
k[CH3COCH2O2+NO-->CH3COCH2O+NO2]=CONST(KRO2NO)
k[CH3COCH2O2+NO3-->CH3COCH2O+NO2]=CONST(KRO2NO3)
k[CH3COCH2O2-->ACETOL]=CONST(2*(K298CH3O2*8.0D-12)@0.5*RO2*0.2)
k[CH3COCH2O2-->CH3COCH2O]=CONST(2*(K298CH3O2*8.0D-12)@0.5*RO2*0.6)
k[CH3COCH2O2-->MGLYOX]=CONST(2*(K298CH3O2*8.0D-12)@0.5*RO2*0.2)
k[CH3CO3+HO2-->CH3CO2H+O3]=CONST(KAPHO2*0.15)
k[CH3CO3+HO2-->CH3CO3H]=CONST(KAPHO2*0.41)
k[CH3CO3+HO2-->CH3O2+OH]=CONST(KAPHO2*0.44)
k[CH3CO3+NO-->NO2+CH3O2]=CONST(7.5D-12*EXP(290/T))
k[CH3CO3+NO2-->PAN]=CONST(KFPAN)
k[CH3CO3+NO3-->NO2+CH3O2]=CONST(4.0D-12)
k[CH3CO3-->CH3CO2H]=CONST(1.00D-11*0.3*RO2)
k[CH3CO3-->CH3O2]=CONST(1.00D-11*0.7*RO2)
k[CH3O2+HO2-->CH3OOH]=CONST(3.8D-13*EXP(780/T)*(1-1/(1+498*EXP(-1160/T))))
k[CH3O2+HO2-->HCHO]=CONST(3.8D-13*EXP(780/T)*(1/(1+498*EXP(-1160/T))))
k[CH3O2+NO-->CH3NO3]=CONST(2.3D-12*EXP(360/T)*0.001)
k[CH3O2+NO-->CH3O+NO2]=CONST(2.3D-12*EXP(360/T)*0.999)
k[CH3O2+NO2-->CH3O2NO2]=CONST(KMT13)
k[CH3O2+NO3-->CH3O+NO2]=CONST(1.2D-12)
k[CH3O2-->CH3O]=CONST(2*KCH3O2*RO2*7.18*EXP(-885/T))
k[CH3O2-->CH3OH]=CONST(2*KCH3O2*RO2*0.5*(1-7.18*EXP(-885/T)))
k[CH3O2-->HCHO]=CONST(2*KCH3O2*RO2*0.5*(1-7.18*EXP(-885/T)))
k[C720OOH+OH-->HCC7CO+OH]=CONST(1.27D-10)
k[C720NO3+OH-->HCC7CO+NO2]=CONST(9.60D-11)
k[C720O-->HCC7CO+HO2]=CONST(KROSEC*O2)
k[C720OH+OH-->HCC7CO+HO2]=CONST(1.09D-10)
k[C918OOH+OH-->C918O2]=CONST(7.91D-11)
k[C918NO3+OH-->HCOCH2CHO+HCOCH2CHO+CH3COCH3+NO2]=CONST(6.79D-11)
k[C918O-->C919O2]=CONST(KDEC)
k[C918OH+OH-->C918O]=CONST(7.16D-11)
k[C9DCOOH+OH-->C9DCCO+OH]=CONST(7.50D-11)
k[C9DCNO3+OH-->C9DCCO+NO2]=CONST(1.58D-12)
k[C9DCO-->C914O2]=CONST(KDEC)
```

```
k[C9DCCO+OH-->C914O2]=CONST(1.32D-12)
k[C9DCOH+OH-->C9DCCO+HO2]=CONST(3.11D-11)
k[C915OOH+OH-->C88CHO+OH]=CONST(1.01D-10)
k[C915NO3+OH-->C88CHO+NO2]=CONST(6.96D-11)
k[C915O-->C88CHO+HO2]=CONST(KROSEC*O2)
k[C915O-->C916O2]=CONST(2.70D+14*EXP(-6643/T))
k[C88CHO+NO3-->C88CO3+HNO3]=CONST(KNO3AL*8.5)
k[C88CHO+OH-->C88CO3]=CONST(7.30D-11)
k[C915OH+OH-->C88CHO+HO2]=CONST(8.33D-11)
k[C512CO3+HO2-->C512CO2H+O3]=CONST(KAPHO2*0.15)
k[C512CO3+HO2-->C512CO3H]=CONST(KAPHO2*0.41)
k[C512CO3+HO2-->C512O2+OH]=CONST(KAPHO2*0.44)
k[C512CO3+NO-->C512O2+NO2]=CONST(KAPNO)
k[C512CO3+NO2-->C512PAN]=CONST(KFPAN)
k[C512CO3+NO3-->C512O2+NO2]=CONST(KRO2NO3*1.74)
k[C512CO3-->C512CO2H]=CONST(1.00D-11*RO2*0.3)
k[C512CO3-->C512O2]=CONST(1.00D-11*RO2*0.7)
k[C917OOH+OH-->C917O2]=CONST(1.91D-11)
k[C917NO3+OH-->CH3COCH3+C619CO+NO2]=CONST(9.97D-12)
k[C917O-->C619O2+CH3COCH3]=CONST(KDEC)
k[C917OH+OH-->C917O]=CONST(1.56D-11)
k[C89CO2-->C811CO3]=CONST(KDEC*0.80)
k[C89CO2-->C89O2]=CONST(KDEC*0.20)
k[C89CO2H+OH-->C89CO2]=CONST(2.69D-11)
k[C89CO3H+OH-->C89CO3]=CONST(3.00D-11)
k[C89PAN+OH-->CH3COCH3+CO13C4CHO+CO+NO2]=CONST(2.52D-11)
k[C89PAN-->C89CO3+NO2]=CONST(KBPAN)
k[C89O2+HO2-->C89OOH]=CONST(KRO2HO2*0.859)
k[C89O2+NO-->C89NO3]=CONST(KRO2NO*0.104)
k[C89O2+NO-->C89O+NO2]=CONST(KRO2NO*0.896)
k[C89O2+NO3-->C89O+NO2]=CONST(KRO2NO3)
k[C89O2-->C89O]=CONST(6.70D-15*RO2*0.7)
k[C89O2-->C89OH]=CONST(6.70D-15*RO2*0.3)
k[C719OOH+OH-->C719O2]=CONST(7.06D-11)
k[C719NO3+OH-->C716OH+NO2]=CONST(1.26D-11)
k[C719O-->C716OH+HO2]=CONST(KDEC)
k[C719OH+OH-->C719O]=CONST(6.72D-11)
k[CH3COCH2O-->CH3CO3+HCHO]=CONST(KDEC)
k[HYPERACET+OH-->CH3COCH2O2]=CONST(1.90D-12*EXP(190/T))
```

```
k[HYPERACET+OH-->MGLYOX+OH]=CONST(8.39D-12)
k[ACETOL+OH-->MGLYOX+HO2]=CONST(1.6D-12*EXP(305/T))
k[NO3+MGLYOX-->CH3CO3+CO+HNO3]=CONST(KNO3AL*2.4)
k[OH+MGLYOX-->CH3CO3+CO]=CONST(1.9D-12*EXP(575/T))
k[CH3CO2H+OH-->CH3O2]=CONST(8.00D-13)
k[CH3CO3H+OH-->CH3CO3]=CONST(3.70D-12)
k[PAN+OH-->HCHO+CO+NO2]=CONST(3D-14)
k[PAN-->CH3CO3+NO2]=CONST(KBPAN)
k[OH+CH3OOH-->CH3O2]=CONST(5.3D-12*EXP(190/T)*0.6)
k[OH+CH3OOH-->HCHO+OH]=CONST(5.3D-12*EXP(190/T)*0.4)
k[OH+CH3NO3-->HCHO+NO2]=CONST(4.0D-13*EXP(-845/T))
k[CH3O-->HCHO+HO2]=CONST(7.2D-14*EXP(-1080/T)*O2)
k[CH3O2NO2-->CH3O2+NO2]=CONST(KMT14)
k[CH3OH+OH-->HO2+HCHO]=CONST(2.85D-12*EXP(-345/T))
k[NO3+HCOCH2CHO-->HCOCH2CO3+HNO3]=CONST(2*KNO3AL*2.4)
k[OH+HCOCH2CHO-->HCOCH2CO3]=CONST(4.29D-11)
k[C919O2+HO2-->C919OOH]=CONST(KRO2HO2*0.890)
k[C919O2+NO-->C919NO3]=CONST(KRO2NO*0.118)
k[C919O2+NO-->C919O+NO2]=CONST(KRO2NO*0.882)
k[C919O2+NO3-->C919O+NO2]=CONST(KRO2NO3)
k[C919O2-->C919O]=CONST(6.70D-15*RO2*0.7)
k[C919O2-->C919OH]=CONST(6.70D-15*RO2*0.3)
k[C914O2+HO2-->C914OOH]=CONST(KRO2HO2*0.890)
k[C914O2+NO-->C914O+NO2]=CONST(KRO2NO)
k[C914O2+NO3-->C914O+NO2]=CONST(KRO2NO3)
k[C914O2-->C914CO]=CONST(8.80D-13*RO2*0.2)
k[C914O2-->C914O]=CONST(8.80D-13*RO2*0.6)
k[C914O2-->C914OH]=CONST(8.80D-13*RO2*0.2)
k[C916O2+HO2-->C916OOH]=CONST(KRO2HO2*0.890)
k[C916O2+NO-->C916NO3]=CONST(KRO2NO*0.118)
k[C916O2+NO-->C916O+NO2]=CONST(KRO2NO*0.882)
k[C916O2+NO3-->C916O+NO2]=CONST(KRO2NO3)
k[C916O2-->C916O]=CONST(6.70D-15*RO2*0.7)
k[C916O2-->C916OH]=CONST(6.70D-15*RO2*0.3)
k[C88CO3+HO2-->C88CO2H+O3]=CONST(KAPHO2*0.15)
k[C88CO3+HO2-->C88CO3H]=CONST(KAPHO2*0.41)
k[C88CO3+HO2-->C88O2+OH]=CONST(KAPHO2*0.44)
k[C88CO3+NO-->C88O2+NO2]=CONST(KAPNO)
k[C88CO3+NO2-->C88PAN]=CONST(KFPAN)
```

```
k[C88CO3+NO3-->C88O2+NO2]=CONST(KRO2NO3*1.74)
k[C88CO3-->C88CO2H]=CONST(1.00D-11*0.3*RO2)
k[C88CO3-->C88O2]=CONST(1.00D-11*0.7*RO2)
k[C88O2+HO2-->C88OOH]=CONST(KRO2HO2*0.859)
k[C88O2+NO-->C88O+NO2]=CONST(KRO2NO)
k[C88O2+NO3-->C88O+NO2]=CONST(KRO2NO3)
k[C88O2-->C88CO]=CONST(8.80D-13*RO2*0.2)
k[C88O2-->C88O]=CONST(8.80D-13*RO2*0.6)
k[C88O2-->C88OH]=CONST(8.80D-13*RO2*0.2)
k[C512CO2H+OH-->C512O2]=CONST(7.23D-11)
k[C512CO3H+OH-->C512CO3]=CONST(7.54D-11)
k[C512O2+HO2-->C512OOH]=CONST(KRO2HO2*0.706)
k[C512O2+NO-->C512NO3]=CONST(KRO2NO*0.052)
k[C512O2+NO-->C512O+NO2]=CONST(KRO2NO*0.948)
k[C512O2+NO3-->C512O+NO2]=CONST(KRO2NO3)
k[C512O2-->C512O]=CONST(1.30D-12*RO2*0.6)
k[C512O2-->C512OH]=CONST(1.30D-12*RO2*0.2)
k[C512O2-->CO13C4CHO]=CONST(1.30D-12*RO2*0.2)
k[C512PAN+OH-->CO13C4CHO+CO+NO2]=CONST(6.76D-11)
k[C512PAN-->C512CO3+NO2]=CONST(KBPAN)
k[C619O2+HO2-->C619OOH]=CONST(KRO2HO2*0.770)
k[C619O2+NO-->C619O+NO2]=CONST(KRO2NO)
k[C619O2+NO3-->C619O+NO2]=CONST(KRO2NO3)
k[C619O2-->C619CO]=CONST(8.80D-13*RO2*0.2)
k[C619O2-->C619O]=CONST(8.80D-13*RO2*0.6)
k[C619O2-->C619OH]=CONST(8.80D-13*RO2*0.2)
k[C811CO3+HO2-->C811CO3H]=CONST(KAPHO2*0.41)
k[C811CO3+HO2-->C811O2+OH]=CONST(KAPHO2*0.44)
k[C811CO3+HO2-->PINIC+O3]=CONST(KAPHO2*0.15)
k[C811CO3+NO-->C811O2+NO2]=CONST(KAPNO)
k[C811CO3+NO2-->C811PAN]=CONST(KFPAN)
k[C811CO3+NO3-->C811O2+NO2]=CONST(KRO2NO3*1.74)
k[C811CO3-->C811O2]=CONST(1.00D-11*RO2*0.7)
k[C811CO3-->PINIC]=CONST(1.00D-11*RO2*0.3)
k[CO13C4CHO+NO3-->CHOC3COCO3+HNO3]=CONST(2*KNO3AL*5.5)
k[CO13C4CHO+OH-->CHOC3COCO3]=CONST(1.33D-10)
k[C89OOH+OH-->C89O2]=CONST(3.61D-11)
k[C89NO3+OH-->CH3COCH3+CO13C4CHO+NO2]=CONST(2.56D-11)
k[C89O-->C810O2]=CONST(2.70D+14*EXP(-6643/T))
```

```
k[C89OH+OH-->C89O]=CONST(2.86D-11)
k[C716OH+NO3-->H3C25C6CO3+HNO3]=CONST(KNO3AL*5.5)
k[C716OH+OH-->CO235C6CHO+HO2]=CONST(8.92D-11*0.232)
k[C716OH+OH-->H3C25C6CO3]=CONST(8.92D-11*0.768)
k[HCOCH2O2+HO2-->HCOCH2OOH]=CONST(KRO2HO2*0.387)
k[HCOCH2O2+NO-->NO2+HCOCH2O]=CONST(KRO2NO)
k[HCOCH2O2+NO3-->HCOCH2O+NO2]=CONST(KRO2NO3)
k[HCOCH2O2-->GLYOX]=CONST(2.00D-12*0.2*RO2)
k[HCOCH2O2-->HCOCH2O]=CONST(2.00D-12*0.6*RO2)
k[HCOCH2O2-->HOCH2CHO]=CONST(2.00D-12*0.2*RO2)
k[HCOCH2CO3+HO2-->HCOCH2CO2H+O3]=CONST(KAPHO2*0.15)
k[HCOCH2CO3+HO2-->HCOCH2CO3H]=CONST(KAPHO2*0.41)
k[HCOCH2CO3+HO2-->HCOCH2O2+OH]=CONST(KAPHO2*0.44)
k[HCOCH2CO3+NO-->HCOCH2O2+NO2]=CONST(KAPNO)
k[HCOCH2CO3+NO2-->C3PAN2]=CONST(KFPAN)
k[HCOCH2CO3+NO3-->HCOCH2O2+NO2]=CONST(KRO2NO3*1.74)
k[HCOCH2CO3-->HCOCH2CO2H]=CONST(1.00D-11*0.3*RO2)
k[HCOCH2CO3-->HCOCH2O2]=CONST(1.00D-11*0.7*RO2)
k[C919OOH+OH-->C919O2]=CONST(1.01D-10)
k[C919NO3+OH-->HCOCH2CHO+HCOCH2CHO+CH3COCH3+NO2]=CONST(9.14D-11)
k[C919O-->C62OO2+CH3COCH3]=CONST(KDEC)
k[C919OH+OH-->C919O]=CONST(9.73D-11)
k[C914OOH+OH-->C914CO+OH]=CONST(8.67D-11)
k[C914O-->C87CO3]=CONST(KDEC)
k[C914CO+OH-->C87CO3]=CONST(7.09D-11)
k[C914OH+OH-->C914CO+HO2]=CONST(7.44D-11)
k[C916OOH+OH-->C916O2]=CONST(9.73D-11)
k[C916NO3+OH-->CH3COCH3+CO123C5CHO+NO2]=CONST(9.23D-11)
k[C916O-->CH3COCH3+C616O2]=CONST(KDEC)
k[C916OH+OH-->C916O]=CONST(9.03D-11)
k[C88CO2H+OH-->C88O2]=CONST(1.02D-11)
k[C88CO3H+OH-->C88CO3]=CONST(1.37D-11)
k[C88PAN+OH-->C88CO+CO+NO2]=CONST(7.50D-12)
k[C88PAN-->C88CO3+NO2]=CONST(KBPAN)
k[C88OOH+OH-->C88CO+OH]=CONST(5.71D-11)
k[C88O-->C718CO3]=CONST(KDEC)
k[C88CO+OH-->C718CO3]=CONST(5.80D-12)
k[C88OH+OH-->C88CO+HO2]=CONST(2.58D-11)
k[C512OOH+OH-->CO13C4CHO+OH]=CONST(1.01D-10)
```

```
k[C512NO3+OH-->CO13C4CHO+NO2]=CONST(6.65D-11)
k[C512O-->C513O2]=CONST(8.40D+10*EXP(-2567/T))
k[C512O-->CO13C3CO2H+HCHO+HO2]=CONST(KDEC)
k[C512OH+OH-->CO13C4CHO+HO2]=CONST(7.96D-11)
k[C619OOH+OH-->C619CO+OH]=CONST(5.95D-11)
k[C619O-->C512CO3]=CONST(KDEC)
k[C619OH+OH-->C619CO+HO2]=CONST(2.82D-11)
k[C811CO3H+OH-->C811CO3]=CONST(1.04D-11)
k[C811O2+HO2-->C811OOH]=CONST(KRO2HO2*0.859)
k[C811O2+NO-->C811NO3]=CONST(KRO2NO*0.138)
k[C811O2+NO-->C811O+NO2]=CONST(KRO2NO*0.862)
k[C811O2+NO3-->C811O+NO2]=CONST(KRO2NO3)
k[C811O2-->C721CHO]=CONST(1.30D-12*RO2*0.2)
k[C811O2-->C811O]=CONST(1.30D-12*RO2*0.6)
k[C811O2-->C811OH]=CONST(1.30D-12*RO2*0.2)
k[PINIC+OH-->C811O2]=CONST(7.29D-12)
k[C811PAN+OH-->C721CHO+CO+NO2]=CONST(6.77D-12)
k[C811PAN-->C811CO3+NO2]=CONST(KBPAN)
k[CHOC3COCO3+HO2-->CHOC3COO2+OH]=CONST(KAPHO2*0.44)
k[CHOC3COCO3+HO2-->CHOC3COOOH]=CONST(KAPHO2*0.56)
k[CHOC3COCO3+NO-->CHOC3COO2+NO2]=CONST(KAPNO)
k[CHOC3COCO3+NO2-->CHOC3COPAN]=CONST(KFPAN)
k[CHOC3COCO3+NO3-->CHOC3COO2+NO2]=CONST(KRO2NO3*1.74)
k[CHOC3COCO3-->CHOC3COO2]=CONST(1.00D-11*RO2)
k[CHOC3COO2+HO2-->C413COOOH]=CONST(KRO2HO2*0.625)
k[CHOC3COO2+NO-->CHOC3COO+NO2]=CONST(KRO2NO)
k[CHOC3COO2+NO3-->CHOC3COO+NO2]=CONST(KRO2NO3)
k[CHOC3COO2-->CHOC3COO]=CONST(2.00D-12*RO2)
k[C810O2+HO2-->C810OOH]=CONST(KRO2HO2*0.914)
k[C810O2+NO-->C810NO3]=CONST(KRO2NO*0.104)
k[C810O2+NO-->C810O+NO2]=CONST(KRO2NO*0.896)
k[C810O2+NO3-->C810O+NO2]=CONST(KRO2NO3)
k[C810O2-->C810O]=CONST(6.70D-15*RO2*0.7)
k[C810O2-->C810OH]=CONST(6.70D-15*RO2*0.3)
k[H3C25C6CO3+HO2-->H3C25C6O2+OH]=CONST(KAPHO2*0.44)
k[H3C25C6CO3+HO2-->H3C25CCO2H+O3]=CONST(KAPHO2*0.15)
k[H3C25C6CO3+HO2-->H3C25CCO3H]=CONST(KAPHO2*0.41)
k[H3C25C6CO3+NO-->H3C25C6O2+NO2]=CONST(KAPNO)
k[H3C25C6CO3+NO2-->H3C25C6PAN]=CONST(KFPAN)
```

```
k[H3C25C6CO3+NO3-->H3C25C6O2+NO2]=CONST(KRO2NO3*1.74)
k[H3C25C6CO3-->H3C25C6O2]=CONST(1.00D-11*RO2*0.7)
k[H3C25C6CO3-->H3C25CCO2H]=CONST(1.00D-11*RO2*0.3)
k[CO235C6CHO+NO3-->CO235C6CO3+HNO3]=CONST(KNO3AL*5.5)
k[CO235C6CHO+OH-->CO235C6CO3]=CONST(6.70D-11)
k[H3C25C6O2+HO2-->H3C25C6OOH]=CONST(KRO2HO2*0.770)
k[H3C25C6O2+NO-->H3C25C6O+NO2]=CONST(KRO2NO)
k[H3C25C6O2+NO3-->H3C25C6O+NO2]=CONST(KRO2NO3)
k[H3C25C6O2-->H3C25C5CHO]=CONST(2.00D-12*RO2*0.2)
k[H3C25C6O2-->H3C25C6O]=CONST(2.00D-12*RO2*0.6)
k[H3C25C6O2-->H3C25C6OH]=CONST(2.00D-12*RO2*0.2)
k[HCOCH2OOH+OH-->GLYOX+OH]=CONST(2.91D-11)
k[HCOCH2OOH+OH-->HCOCH2O2]=CONST(1.90D-12*EXP(190/T))
k[HCOCH2O-->HCHO+CO+HO2]=CONST(KDEC)
k[NO3+GLYOX-->HCOCO+HNO3]=CONST(KNO3AL)
k[OH+GLYOX-->HCOCO]=CONST(3.1D-12*EXP(340/T))
k[HOCH2CHO+NO3-->HOCH2CO3+HNO3]=CONST(KNO3AL)
k[HOCH2CHO+OH-->GLYOX+HO2]=CONST(1.00D-11*0.200)
k[HOCH2CHO+OH-->HOCH2CO3]=CONST(1.00D-11*0.800)
k[OH+HCOCH2CO2H-->HCOCH2O2]=CONST(2.14D-11)
k[OH+HCOCH2CO3H-->HCOCH2CO3]=CONST(2.49D-11)
k[C3PAN2-->HCOCH2CO3+NO2]=CONST(KBPAN)
k[OH+C3PAN2-->GLYOX+CO+NO2]=CONST(2.10D-11)
k[C620O2+HO2-->C620OOH]=CONST(KRO2HO2*0.770)
k[C620O2+NO-->C620O+NO2]=CONST(KRO2NO)
k[C620O2+NO3-->C620O+NO2]=CONST(KRO2NO3)
k[C620O2-->C515CHO]=CONST(8.80D-13*RO2*0.2)
k[C620O2-->C620O]=CONST(8.80D-13*RO2*0.6)
k[C620O2-->C620OH]=CONST(8.80D-13*RO2*0.2)
k[C87CO3+HO2-->C87CO2H+O3]=CONST(KAPHO2*0.15)
k[C87CO3+HO2-->C87CO3H]=CONST(KAPHO2*0.41)
k[C87CO3+HO2-->C87O2+OH]=CONST(KAPHO2*0.44)
k[C87CO3+NO-->C87O2+NO2]=CONST(KAPNO)
k[C87CO3+NO2-->C87PAN]=CONST(KFPAN)
k[C87CO3+NO3-->C87O2+NO2]=CONST(KRO2NO3*1.74)
k[C87CO3-->C87CO2H]=CONST(1.00D-11*RO2*0.3)
k[C87CO3-->C87O2]=CONST(1.00D-11*RO2*0.7)
k[CO123C5CHO+NO3-->CHOC2CO3+CO+CO+HNO3]=CONST(2*KNO3AL*5.5)
k[CO123C5CHO+OH-->CHOC2CO3+CO+CO]=CONST(3.89D-11)
```

```
k[C616O2+HO2-->C616OOH]=CONST(KRO2HO2*0.770)
k[C616O2+NO-->C616O+NO2]=CONST(KRO2NO)
k[C616O2+NO3-->C616O+NO2]=CONST(KRO2NO3)
k[C616O2-->C616O]=CONST(8.80D-13*RO2*0.6)
k[C616O2-->C616OH]=CONST(8.80D-13*RO2*0.2)
k[C616O2-->CO123C5CHO]=CONST(8.80D-13*RO2*0.2)
k[C718CO3+HO2-->C718CO2H+O3]=CONST(KAPHO2*0.15)
k[C718CO3+HO2-->C718CO3H]=CONST(KAPHO2*0.41)
k[C718CO3+HO2-->C718O2+OH]=CONST(KAPHO2*0.44)
k[C718CO3+NO-->C718O2+NO2]=CONST(KAPNO)
k[C718CO3+NO2-->C718PAN]=CONST(KFPAN)
k[C718CO3+NO3-->C718O2+NO2]=CONST(KRO2NO3*1.74)
k[C718CO3-->C718CO2H]=CONST(1.00D-11*0.3*RO2)
k[C718CO3-->C718O2]=CONST(1.00D-11*0.7*RO2)
k[C513O2+HO2-->C513OOH]=CONST(KRO2HO2*0.706)
k[C513O2+NO-->C513O+NO2]=CONST(KRO2NO)
k[C513O2+NO3-->C513O+NO2]=CONST(KRO2NO3)
k[C513O2-->C513CO]=CONST(8.80D-13*RO2*0.2)
k[C513O2-->C513O]=CONST(8.80D-13*RO2*0.6)
k[C513O2-->C513OH]=CONST(8.80D-13*RO2*0.2)
k[CO13C3CO2H+OH-->HCOCH2CO3]=CONST(6.69D-11)
k[C811OOH+OH-->C721CHO+OH]=CONST(1.70D-11)
k[C811NO3+OH-->C721CHO+NO2]=CONST(3.29D-12)
k[C811O-->C812O2]=CONST(KDEC)
k[C721CHO+NO3-->C721CO3+HNO3]=CONST(KNO3AL*8.5)
k[C721CHO+OH-->C721CO3]=CONST(2.63D-11)
k[C811OH+OH-->C721CHO+HO2]=CONST(7.89D-12)
k[CHOC3COOOH+OH-->CHOC3COCO3]=CONST(7.55D-11)
k[CHOC3COPAN+OH-->C4CODIAL+CO+NO2]=CONST(7.19D-11)
k[CHOC3COPAN-->CHOC3COCO3+NO2]=CONST(KBPAN)
k[C413COOOH+OH-->CHOC3COO2]=CONST(8.33D-11)
k[CHOC3COO-->HCOCH2CO3+HCHO]=CONST(KDEC)
k[C810OOH+OH-->C810O2]=CONST(8.35D-11)
k[C810NO3+OH-->CH3COCH3+CO13C4CHO+NO2]=CONST(4.96D-11)
k[C810O-->CH3COCH3+C514O2]=CONST(2.70D+14*EXP(-6643/T))
k[C810OH+OH-->C810O]=CONST(8.00D-11)
k[H3C25CCO2H+OH-->H3C25C6O2]=CONST(2.39D-11)
k[H3C25CCO3H+OH-->H3C25C6CO3]=CONST(2.70D-11)
k[H3C25C6PAN+OH-->H3C25C5CHO+CO+NO2]=CONST(2.29D-11)
```

```
k[H3C25C6PAN-->H3C25C6CO3+NO2]=CONST(KBPAN)
k[CO235C6CO3+HO2-->C235C6CO3H]=CONST(KAPHO2*0.56)
k[CO235C6CO3+HO2-->CO235C6O2+OH]=CONST(KAPHO2*0.44)
k[CO235C6CO3+NO-->CO235C6O2+NO2]=CONST(KAPNO)
k[CO235C6CO3+NO2-->C7PAN3]=CONST(KFPAN)
k[CO235C6CO3+NO3-->CO235C6O2+NO2]=CONST(KRO2NO3*1.74)
k[CO235C6CO3-->CO235C6O2]=CONST(1.00D-11*RO2)
k[H3C25C6OOH+OH-->H3C25C5CHO+OH]=CONST(3.23D-11)
k[H3C25C6O-->H3C2C4CO3+HCHO]=CONST(KDEC)
k[H3C25C5CHO+OH-->H3C2C4CO3+CO]=CONST(3.55D-11)
k[H3C25C6OH+OH-->C614CO+HO2]=CONST(2.54D-11*0.890)
k[H3C25C6OH+OH-->H3C25C5CHO+HO2]=CONST(2.54D-11*0.110)
k[HCOCO-->CO+CO+HO2] = CONST( 7.00D11*EXP(-3160/T) + 5.00D-12*O2 )
k[HCOCO-->CO+OH]=CONST(5.00D-12*O2*3.2*(1-EXP(-550/T)))
k[HCOCO-->HCOCO3]=CONST(5.00D-12*O2*3.2*EXP(-550/T))
k[HOCH2CO3+HO2-->HO2+HCHO+OH]=CONST(KAPHO2*0.44)
k[HOCH2CO3+HO2-->HOCH2CO2H+O3]=CONST(KAPHO2*0.15)
k[HOCH2CO3+HO2-->HOCH2CO3H]=CONST(KAPHO2*0.41)
k[HOCH2CO3+NO-->NO2+HO2+HCHO]=CONST(KAPNO)
k[HOCH2CO3+NO2-->PHAN]=CONST(KFPAN)
k[HOCH2CO3+NO3-->NO2+HO2+HCHO]=CONST(KRO2NO3*1.74)
k[HOCH2CO3-->HCHO+HO2]=CONST(1.00D-11*0.7*RO2)
k[HOCH2CO3-->HOCH2CO2H]=CONST(1.00D-11*0.3*RO2)
k[C620OOH+OH-->C515CHO+OH]=CONST(1.15D-10)
k[C620O-->HCOCH2CHO+HCOCH2CO3]=CONST(KDEC)
k[C515CHO+OH-->C515CO3]=CONST(1.33D-10)
k[C620OH+OH-->C515CHO+HO2]=CONST(9.44D-11)
k[C87CO2H+OH-->C87O2]=CONST(9.19D-11)
k[C87CO3H+OH-->C87CO3]=CONST(9.50D-11)
k[C87O2+HO2-->C87OOH]=CONST(KRO2HO2*0.859)
k[C87O2+NO-->C87O+NO2]=CONST(KRO2NO)
k[C87O2+NO3-->C87O+NO2]=CONST(KRO2NO3)
k[C87O2-->C87CO]=CONST(2.00D-12*RO2*0.2)
k[C87O2-->C87O]=CONST(2.00D-12*RO2*0.6)
k[C87O2-->C87OH]=CONST(2.00D-12*RO2*0.2)
k[C87PAN+OH-->C87CO+CO+NO2]=CONST(9.11D-11)
k[C87PAN-->C87CO3+NO2]=CONST(KBPAN)
k[CHOC2CO3+HO2-->CHOC2CO2H+O3]=CONST(KAPHO2*0.15)
k[CHOC2CO3+HO2-->CHOC2CO3H]=CONST(KAPHO2*0.41)
```

```
k[CHOC2CO3+HO2-->CHOC2H4O2+OH]=CONST(KAPHO2*0.44)
k[CHOC2CO3+NO-->CHOC2H4O2+NO2]=CONST(KAPNO)
k[CHOC2CO3+NO2-->CHOC2PAN]=CONST(KFPAN)
k[CHOC2CO3+NO3-->CHOC2H4O2+NO2]=CONST(KRO2NO3*1.74)
k[CHOC2CO3-->CHOC2CO2H]=CONST(1.00D-11*RO2*0.3)
k[CHOC2CO3-->CHOC2H4O2]=CONST(1.00D-11*RO2*0.7)
k[C616OOH+OH-->CO123C5CHO+OH]=CONST(1.02D-10)
k[C616O-->CHOC2CO3+GLYOX]=CONST(KDEC*0.5)
k[C616O-->CO12C4CHO+HO2+CO]=CONST(KDEC*0.5)
k[C616OH+OH-->CO123C5CHO+HO2]=CONST(9.27D-11)
k[C718CO2H+OH-->C718O2]=CONST(7.21D-11)
k[C718CO3H+OH-->C718CO3]=CONST(7.52D-11)
k[C718O2+HO2-->C718OOH]=CONST(KRO2HO2*0.820)
k[C718O2+NO-->C718NO3]=CONST(KRO2NO*0.138)
k[C718O2+NO-->C718O+NO2]=CONST(KRO2NO*0.862)
k[C718O2+NO3-->C718O+NO2]=CONST(KRO2NO3)
k[C718O2-->C617CHO]=CONST(1.30D-12*RO2*0.2)
k[C718O2-->C718O]=CONST(1.30D-12*RO2*0.6)
k[C718O2-->C718OH]=CONST(1.30D-12*RO2*0.2)
k[C718PAN+OH-->C617CHO+CO+NO2]=CONST(6.81D-11)
k[C718PAN-->C718CO3+NO2]=CONST(KBPAN)
k[C513OOH+OH-->C513CO+OH]=CONST(9.23D-11)
k[C513O-->GLYOX+HOC2H4CO3]=CONST(KDEC)
k[C513CO+OH-->HOC2H4CO3+CO+CO]=CONST(2.64D-11)
k[C513OH+OH-->C513CO+HO2]=CONST(8.35D-11)
k[C812O2+HO2-->C812OOH]=CONST(KRO2HO2*0.859)
k[C812O2+NO-->C812O+NO2]=CONST(KRO2NO)
k[C812O2+NO3-->C812O+NO2]=CONST(KRO2NO3)
k[C812O2-->C812O]=CONST(9.20D-14*RO2*0.7)
k[C812O2-->C812OH]=CONST(9.20D-14*RO2*0.3)
k[C721CO3+HO2-->C721CO3H]=CONST(KAPHO2*0.41)
k[C721CO3+HO2-->C721O2+OH]=CONST(KAPHO2*0.44)
k[C721CO3+HO2-->NORPINIC+O3]=CONST(KAPHO2*0.15)
k[C721CO3+NO-->C721O2+NO2]=CONST(KAPNO)
k[C721CO3+NO2-->C721PAN]=CONST(KFPAN)
k[C721CO3+NO3-->C721O2+NO2]=CONST(KRO2NO3*1.74)
k[C721CO3-->C721O2]=CONST(1.00D-11*RO2*0.7)
k[C721CO3-->NORPINIC]=CONST(1.00D-11*RO2*0.3)
k[C721O2+HO2-->C721OOH]=CONST(KRO2HO2*0.820)
```

```
k[C721O2+NO-->C721O+NO2]=CONST(KRO2NO)
k[C721O2+NO3-->C721O+NO2]=CONST(KRO2NO3)
k[C721O2-->C721O]=CONST(1.30D-12*RO2)
k[C4CODIAL+NO3-->C312COCO3+HNO3]=CONST(2*KNO3AL*4.0)
k[C4CODIAL+OH-->C312COCO3]=CONST(3.39D-11)
k[C514O2+HO2-->C514OOH]=CONST(KRO2HO2*0.706)
k[C514O2+NO-->C514NO3]=CONST(KRO2NO*0.129)
k[C514O2+NO-->C514O+NO2]=CONST(KRO2NO*0.871)
k[C514O2+NO3-->C514O+NO2]=CONST(KRO2NO3)
k[C514O2-->C514O]=CONST(2.50D-13*RO2*0.6)
k[C514O2-->C514OH]=CONST(2.50D-13*RO2*0.2)
k[C514O2-->CO13C4CHO]=CONST(2.50D-13*RO2*0.2)
k[C235C6CO3H+OH-->CO235C6CO3]=CONST(4.75D-12)
k[CO235C6O2+HO2-->CO235C6OOH]=CONST(KRO2HO2*0.770)
k[CO235C6O2+NO-->CO235C6O+NO2]=CONST(KRO2NO)
k[CO235C6O2+NO3-->CO235C6O+NO2]=CONST(KRO2NO3)
k[CO235C6O2-->CO235C6O]=CONST(2.00D-12*RO2)
k[C7PAN3+OH-->CO235C5CHO+CO+NO2]=CONST(8.83D-13)
k[C7PAN3-->CO235C6CO3+NO2]=CONST(KBPAN)
k[H3C2C4CO3+HO2-->H3C2C4CO2H+O3]=CONST(KAPHO2*0.15)
k[H3C2C4CO3+HO2-->H3C2C4CO3H]=CONST(KAPHO2*0.41)
k[H3C2C4CO3+HO2-->HMVKAO2+OH]=CONST(KAPHO2*0.44)
k[H3C2C4CO3+NO-->HMVKAO2+NO2]=CONST(KAPNO)
k[H3C2C4CO3+NO2-->H3C2C4PAN]=CONST(KFPAN)
k[H3C2C4CO3+NO3-->HMVKAO2+NO2]=CONST(KRO2NO3*1.74)
k[H3C2C4CO3-->H3C2C4CO2H]=CONST(1.00D-11*RO2*0.3)
k[H3C2C4CO3-->HMVKAO2]=CONST(1.00D-11*RO2*0.7)
k[C614CO+OH-->CO235C5CHO+HO2]=CONST(3.22D-12)
k[HMVKAO2+HO2-->HMVKAOOH]=CONST(KRO2HO2*0.625)
k[HMVKAO2+NO-->HMVKANO3]=CONST(KRO2NO*0.017)
k[HMVKAO2+NO-->HMVKAO+NO2]=CONST(KRO2NO*0.983)
k[HMVKAO2+NO3-->HMVKAO+NO2]=CONST(KRO2NO3)
k[HMVKAO2-->CO2H3CHO]=CONST(2.00D-12*0.2*RO2)
k[HMVKAO2-->HMVKAO]=CONST(2.00D-12*0.6*RO2)
k[HMVKAO2-->HO12CO3C4]=CONST(2.00D-12*0.2*RO2)
k[HCOCO3+HO2-->HCOCO2H+O3]=CONST(KAPHO2*0.15)
k[HCOCO3+HO2-->HCOCO3H]=CONST(KAPHO2*0.41)
k[HCOCO3+HO2-->HO2+CO+OH]=CONST(KAPHO2*0.44)
k[HCOCO3+NO-->HO2+CO+NO2]=CONST(KAPNO)
```

```
k[HCOCO3+NO2-->HO2+CO+NO3]=CONST(KFPAN)
k[HCOCO3+NO3-->HO2+CO+NO2]=CONST(KRO2NO3*1.74)
k[HCOCO3-->CO+HO2]=CONST(1.00D-11*0.7*RO2)
k[HCOCO3-->HCOCO2H]=CONST(1.00D-11*0.3*RO2)
k[HOCH2CO2H+OH-->HCHO+HO2]=CONST(2.73D-12)
k[HOCH2CO3H+OH-->HOCH2CO3]=CONST(6.19D-12)
k[PHAN+OH-->HCHO+CO+NO2]=CONST(1.12D-12)
k[PHAN-->HOCH2CO3+NO2]=CONST(KBPAN)
k[C515CO3+HO2-->C515CO3H]=CONST(KAPHO2*0.56)
k[C515CO3+HO2-->C515O2+OH]=CONST(KAPHO2*0.44)
k[C515CO3+NO-->C515O2+NO2]=CONST(KAPNO)
k[C515CO3+NO2-->C515PAN]=CONST(KFPAN)
k[C515CO3+NO3-->C515O2+NO2]=CONST(KRO2NO3*1.74)
k[C515CO3-->C515O2]=CONST(1.00D-11*RO2)
k[C515O2+HO2-->C515OOH]=CONST(KRO2HO2*0.706)
k[C515O2+NO-->C515O+NO2]=CONST(KRO2NO)
k[C515O2+NO3-->C515O+NO2]=CONST(KRO2NO3)
k[C515O2-->C515O]=CONST(2.00D-12*RO2)
k[C87OOH+OH-->C87CO+OH]=CONST(1.00D-10)
k[C87O-->C615CO3+HCHO]=CONST(KDEC)
k[C87CO+OH-->C615CO3+CO]=CONST(1.03D-10)
k[C87OH+OH-->C87CO+HO2]=CONST(9.34D-11)
k[CHOC2CO2H+OH-->CHOC2H4O2]=CONST(2.64D-11)
k[CHOC2CO3H+OH-->CHOC2CO3]=CONST(3.00D-11)
k[CHOC2H4O2+HO2-->CHOC2H4OOH]=CONST(KRO2HO2*0.520)
k[CHOC2H4O2+NO-->CHOC2H4O+NO2]=CONST(KRO2NO)
k[CHOC2H4O2+NO3-->CHOC2H4O+NO2]=CONST(KRO2NO3)
k[CHOC2H4O2-->CHOC2H4O]=CONST(6.00D-13*RO2)
k[CHOC2PAN+OH-->HCOCH2CHO+CO+NO2]=CONST(2.64D-11)
k[CHOC2PAN-->CHOC2CO3+NO2]=CONST(KBPAN)
k[CO12C4CHO+NO3-->CHOC2CO3+CO+HNO3]=CONST(2*KNO3AL*5.5)
k[CO12C4CHO+OH-->CHOC2CO3+CO]=CONST(3.89D-11)
k[C718OOH+OH-->C617CHO+OH]=CONST(1.01D-10)
k[C718NO3+OH-->C617CHO+NO2]=CONST(6.65D-11)
k[C718O-->C617CHO+HO2]=CONST(KDEC)
k[C617CHO+NO3-->C617CO3+HNO3]=CONST(KNO3AL*8.5)
k[C617CHO+NO3-->C618CO3+HNO3]=CONST(KNO3AL*8.5)
k[C617CHO+OH-->C617CO3]=CONST(1.33D-10*0.5)
k[C617CHO+OH-->C618CO3]=CONST(1.33D-10*0.5)
```

```
k[C718OH+OH-->C617CHO+HO2]=CONST(7.96D-11)
k[HOC2H4CO3+HO2-->HOC2H4CO2H+O3]=CONST(KAPHO2*0.15)
k[HOC2H4CO3+HO2-->HOC2H4CO3H]=CONST(KAPHO2*0.41)
k[HOC2H4CO3+HO2-->HOCH2CH2O2+OH]=CONST(KAPHO2*0.44)
k[HOC2H4CO3+NO-->HOCH2CH2O2+NO2]=CONST(KAPNO)
k[HOC2H4CO3+NO2-->C3PAN1]=CONST(KFPAN)
k[HOC2H4CO3+NO3-->HOCH2CH2O2+NO2]=CONST(KRO2NO3*1.74)
k[HOC2H4CO3-->HOC2H4CO2H]=CONST(1.00D-11*0.3*RO2)
k[HOC2H4CO3-->HOCH2CH2O2]=CONST(1.00D-11*0.7*RO2)
k[C812OOH+OH-->C812O2]=CONST(1.09D-11)
k[C812O-->C813O2]=CONST(KDEC)
k[C812OH+OH-->C812O]=CONST(7.42D-12)
k[C721CO3H+OH-->C721CO3]=CONST(9.65D-12)
k[NORPINIC+OH-->C721O2]=CONST(6.57D-12)
k[C721PAN+OH-->C721OOH+CO+NO2]=CONST(2.96D-12)
k[C721PAN-->C721CO3+NO2]=CONST(KBPAN)
k[C721OOH+OH-->C721O2]=CONST(1.27D-11)
k[C721O-->C722O2]=CONST(KDEC)
k[C312COCO3+HO2-->C312COCO3H]=CONST(KAPHO2*0.56)
k[C312COCO3+HO2-->CHOCOCH2O2+OH]=CONST(KAPHO2*0.44)
k[C312COCO3+NO-->CHOCOCH2O2+NO2]=CONST(KAPNO)
k[C312COCO3+NO2-->C312COPAN]=CONST(KFPAN)
k[C312COCO3+NO3-->CHOCOCH2O2+NO2]=CONST(KRO2NO3*1.74)
k[C312COCO3-->CHOCOCH2O2]=CONST(1.00D-11*RO2)
k[CHOCOCH2O2+HO2-->ALCOCH2OOH]=CONST(KRO2HO2*0.520)
k[CHOCOCH2O2+NO-->CHOCOCH2O+NO2]=CONST(KRO2NO)
k[CHOCOCH2O2+NO3-->CHOCOCH2O+NO2]=CONST(KRO2NO3)
k[CHOCOCH2O2-->CHOCOCH2O]=CONST(2.00D-12*RO2)
k[C514OOH+OH-->CO13C4CHO+OH]=CONST(1.10D-10)
k[C514NO3+OH-->CO13C4CHO+NO2]=CONST(4.33D-11)
k[C514O-->CO13C4CHO+HO2]=CONST(1.80D-14*EXP(-260/T)*O2)
k[C514OH+OH-->CO13C4CHO+HO2]=CONST(6.99D-11)
k[CO235C6OOH+OH-->CO235C6O2]=CONST(1.01D-11)
k[CO235C6O-->CO23C4CO3+HCHO]=CONST(KDEC)
k[CO235C5CHO+NO3-->CO23C4CO3+CO+HNO3]=CONST(KNO3AL*5.5)
k[CO235C5CHO+OH-->CO23C4CO3+CO]=CONST(1.33D-11)
k[H3C2C4CO2H+OH-->HMVKAO2]=CONST(2.34D-11)
k[H3C2C4CO3H+OH-->H3C2C4CO3]=CONST(2.65D-11)
k[H3C2C4PAN+OH-->CO2H3CHO+CO+NO2]=CONST(7.60D-12)
```

```
k[H3C2C4PAN-->H3C2C4CO3+NO2]=CONST(KBPAN)
k[BIACETO2+HO2-->BIACETOOH]=CONST(KRO2HO2*0.625)
k[BIACETO2+NO-->BIACETO+NO2]=CONST(KRO2NO)
k[BIACETO2+NO3-->BIACETO+NO2]=CONST(KRO2NO3)
k[BIACETO2-->BIACETO]=CONST(2.00D-12*0.6*RO2)
k[BIACETO2-->BIACETOH]=CONST(2.00D-12*0.2*RO2)
k[BIACETO2-->CO23C3CHO]=CONST(2.00D-12*0.2*RO2)
k[OH+HMVKAOOH-->CO2H3CHO+OH]=CONST(5.77D-11)
k[OH+HMVKANO3-->CO2H3CHO+NO2]=CONST(2.23D-12)
k[HMVKAO-->MGLYOX+HCHO+HO2]=CONST(KDEC)
k[NO3+CO2H3CHO-->CO2H3CO3+HNO3]=CONST(KNO3AL*4.0)
k[OH+CO2H3CHO-->CO2H3CO3]=CONST(2.45D-11)
k[OH+HO12CO3C4-->BIACETOH+HO2]=CONST(1.88D-11)
k[OH+HCOCO2H-->CO+HO2]=CONST(1.23D-11)
k[OH+HCOCO3H-->HCOCO3]=CONST(1.58D-11)
k[C515CO3H+OH-->C515CO3]=CONST(7.05D-11)
k[C515PAN+OH-->C515CO+CO+NO2]=CONST(6.69D-11)
k[C515PAN-->C515CO3+NO2]=CONST(KBPAN)
k[C515OOH+OH-->C515CO+OH]=CONST(7.91D-11)
k[C515O-->HCHO+CO+HCOCH2CO3]=CONST(KDEC)
k[C615CO3+HO2-->C615CO2H+O3]=CONST(KAPHO2*0.15)
k[C615CO3+HO2-->C615CO3H]=CONST(KAPHO2*0.41)
k[C615CO3+HO2-->C615O2+OH]=CONST(KAPHO2*0.44)
k[C615CO3+NO-->C615O2+NO2]=CONST(KAPNO)
k[C615CO3+NO2-->C615PAN]=CONST(KFPAN)
k[C615CO3+NO3-->C615O2+NO2]=CONST(KRO2NO3*1.74)
k[C615CO3-->C615CO2H]=CONST(1.00D-11*RO2*0.3)
k[C615CO3-->C615O2]=CONST(1.00D-11*RO2*0.7)
k[CHOC2H4OOH+OH-->CHOC2H4O2]=CONST(7.31D-11)
k[CHOC2H4O-->HCOCH2CHO+HO2]=CONST(KROPRIM*O2)
k[C617CO3+HO2-->C617CO2H+O3]=CONST(KAPHO2*0.15)
k[C617CO3+HO2-->C617CO3H]=CONST(KAPHO2*0.41)
k[C617CO3+HO2-->C617O2+OH]=CONST(KAPHO2*0.44)
k[C617CO3+NO-->C617O2+NO2]=CONST(KAPNO)
k[C617CO3+NO2-->C617PAN]=CONST(KFPAN)
k[C617CO3+NO3-->C617O2+NO2]=CONST(KRO2NO3*1.74)
k[C617CO3-->C617CO2H]=CONST(1.00D-11*RO2*0.3)
k[C617CO3-->C617O2]=CONST(1.00D-11*RO2*0.7)
k[C618CO3+HO2-->C618CO2H+O3]=CONST(KAPHO2*0.15)
```

```
k[C618CO3+HO2-->C618CO3H]=CONST(KAPHO2*0.41)
k[C618CO3+HO2-->C618O2+OH]=CONST(KAPHO2*0.44)
k[C618CO3+NO-->C618O2+NO2]=CONST(KAPNO)
k[C618CO3+NO2-->C618PAN]=CONST(KFPAN)
k[C618CO3+NO3-->C618O2+NO2]=CONST(KRO2NO3*1.74)
k[C618CO3-->C618CO2H]=CONST(1.00D-11*RO2*0.3)
k[C618CO3-->C618O2]=CONST(1.00D-11*RO2*0.7)
k[C617O2+HO2-->C617OOH]=CONST(KRO2HO2*0.770)
k[C617O2+NO-->C617O+NO2]=CONST(KRO2NO)
k[C617O2+NO3-->C617O+NO2]=CONST(KRO2NO3)
k[C617O2-->C615CO]=CONST(2.00D-12*RO2*0.2)
k[C617O2-->C617O]=CONST(2.00D-12*RO2*0.6)
k[C617O2-->C617OH]=CONST(2.00D-12*RO2*0.2)
k[C618O2+HO2-->C618OOH]=CONST(KRO2HO2*0.770)
k[C618O2+NO-->C618O+NO2]=CONST(KRO2NO)
k[C618O2+NO3-->C618O+NO2]=CONST(KRO2NO3)
k[C618O2-->C618O]=CONST(9.20D-14*RO2*0.7)
k[C618O2-->C67CHO]=CONST(9.20D-14*RO2*0.3)
k[OH+HOC2H4CO2H-->HOCH2CH2O2]=CONST(1.39D-11)
k[OH+HOC2H4CO3H-->HOC2H4CO3]=CONST(1.73D-11)
k[HOCH2CH2O2+HO2-->HYETHO2H]=CONST(1.53D-13*EXP(1300/T))
k[HOCH2CH2O2+NO-->ETHOHNO3]=CONST(KRO2NO*0.005)
k[HOCH2CH2O2+NO-->HOCH2CH2O+NO2]=CONST(KRO2NO*0.995)
k[HOCH2CH2O2+NO3-->HOCH2CH2O+NO2]=CONST(KRO2NO3)
k[HOCH2CH2O2-->ETHGLY]=CONST(2*(KCH3O2*7.8D-14*EXP(1000/T))@0.5*RO2*0.2)
k[HOCH2CH2O2-->HOCH2CH2O]=CONST(2*(KCH3O2*7.8D-14*EXP(1000/T))@0.5*RO2*0.6)
k[HOCH2CH2O2-->HOCH2CHO]=CONST(2*(KCH3O2*7.8D-14*EXP(1000/T))@0.5*RO2*0.2)
k[C3PAN1-->HOC2H4CO3+NO2]=CONST(KBPAN)
k[OH+C3PAN1-->HOCH2CHO+CO+NO2]=CONST(4.51D-12)
k[C813O2+HO2-->C813OOH]=CONST(KRO2HO2*0.859)
k[C813O2+NO-->C813NO3]=CONST(KRO2NO*0.104)
k[C813O2+NO-->C813O+NO2]=CONST(KRO2NO*0.896)
k[C813O2+NO3-->C813O+NO2]=CONST(KRO2NO3)
k[C813O2-->C813O]=CONST(6.70D-15*RO2*0.7)
k[C813O2-->C813OH]=CONST(6.70D-15*RO2*0.3)
k[C722O2+HO2-->C722OOH]=CONST(KRO2HO2*0.820)
k[C722O2+NO-->C722O+NO2]=CONST(KRO2NO)
k[C722O2+NO3-->C722O+NO2]=CONST(KRO2NO3)
k[C722O2-->C722O]=CONST(6.70D-15*RO2)
```

```
k[C312COCO3H+OH-->C312COCO3]=CONST(1.63D-11)
k[C312COPAN+OH-->C33CO+CO+NO2]=CONST(1.27D-11)
k[C312COPAN-->C312COCO3+NO2]=CONST(KBPAN)
k[ALCOCH2OOH+OH-->CHOCOCH2O2]=CONST(2.41D-11)
k[CHOCOCH2O-->HCHO+HCOCO]=CONST(KDEC)
k[CO23C4CO3+HO2-->BIACETO2+OH]=CONST(KAPHO2*0.44)
k[CO23C4CO3+HO2-->CO23C4CO3H]=CONST(KAPHO2*0.56)
k[CO23C4CO3+NO-->BIACETO2+NO2]=CONST(KAPNO)
k[CO23C4CO3+NO2-->C5PAN9]=CONST(KFPAN)
k[CO23C4CO3+NO3-->BIACETO2+NO2]=CONST(KRO2NO3*1.74)
k[CO23C4CO3-->BIACETO2]=CONST(1.00D-11*RO2)
k[OH+BIACETOOH-->BIACETO2]=CONST(1.90D-12*EXP(190/T))
k[OH+BIACETOOH-->CO23C3CHO+OH]=CONST(5.99D-12)
k[BIACETO-->CH3CO3+HCHO+CO]=CONST(KDEC)
k[OH+BIACETOH-->CO23C3CHO+HO2]=CONST(2.69D-12)
k[NO3+CO23C3CHO-->CH3CO3+CO+CO+HNO3]=CONST(KNO3AL*4.0)
k[OH+CO23C3CHO-->CH3CO3+CO+CO]=CONST(1.23D-11)
k[CO2H3CO3+HO2-->CO2H3CO3H]=CONST(KAPHO2*0.56)
k[CO2H3CO3+HO2-->MGLYOX+HO2+OH]=CONST(KAPHO2*0.44)
k[CO2H3CO3+NO-->MGLYOX+HO2+NO2]=CONST(KAPNO)
k[CO2H3CO3+NO2-->C4PAN6]=CONST(KFPAN)
k[CO2H3CO3+NO3-->MGLYOX+HO2+NO2]=CONST(KRO2NO3*1.74)
k[CO2H3CO3-->MGLYOX+HO2]=CONST(1.00D-11*RO2)
k[C515CO+OH-->CO+CO+HCOCH2CO3]=CONST(7.90D-11)
k[C615CO2H+OH-->C615O2]=CONST(9.13D-11)
k[C615CO3H+OH-->C615CO3]=CONST(9.44D-11)
k[C615O2+HO2-->C615OOH]=CONST(KRO2HO2*0.770)
k[C615O2+NO-->C615O+NO2]=CONST(KRO2NO)
k[C615O2+NO3-->C615O+NO2]=CONST(KRO2NO3)
k[C615O2-->C615CO]=CONST(8.80D-13*RO2*0.2)
k[C615O2-->C615O]=CONST(8.80D-13*RO2*0.6)
k[C615O2-->C615OH]=CONST(8.80D-13*RO2*0.2)
k[C615PAN+OH-->C615CO+CO+NO2]=CONST(8.47D-11)
k[C615PAN-->C615CO3+NO2]=CONST(KBPAN)
k[C617CO2H+OH-->C617O2]=CONST(6.72D-11)
k[C617CO3H+OH-->C617CO3]=CONST(7.03D-11)
k[C617PAN+OH-->C615CO+CO+NO2]=CONST(6.74D-11)
k[C617PAN-->C617CO3+NO2]=CONST(KBPAN)
k[C618CO2H+OH-->C618O2]=CONST(6.72D-11)
```

```
k[C618CO3H+OH-->C618CO3]=CONST(7.03D-11)
k[C618PAN+OH-->CH3COCH3+HCOCH2CHO+CO+NO2]=CONST(6.67D-11)
k[C618PAN-->C618CO3+NO2]=CONST(KBPAN)
k[C617OOH+OH-->C615CO+OH]=CONST(7.56D-11)
k[C617O-->CO1M22CO3+HCHO]=CONST(KDEC)
k[C615CO+OH-->CO1M22CO3+CO]=CONST(7.88D-11)
k[C617OH+OH-->C615CO+HO2]=CONST(6.89D-11)
k[C618OOH+OH-->C618O2]=CONST(7.03D-11)
k[C618O-->HCOCH2CO3+CH3COCH3]=CONST(KDEC)
k[NO3+C67CHO-->C67CO3+HNO3]=CONST(KNO3AL*8.5)
k[OH+C67CHO-->C67CO3]=CONST(6.76D-11)
k[HYETHO2H+OH-->HOCH2CH2O2]=CONST(1.90D-12*EXP(190/T))
k[HYETHO2H+OH-->HOCH2CHO+OH]=CONST(1.38D-11)
k[ETHOHNO3+OH-->HOCH2CHO+NO2]=CONST(8.40D-13)
k[HOCH2CH2O-->HO2+HCHO+HCHO]=CONST(9.50D+13*EXP(-5988/T))
k[HOCH2CH2O-->HO2+HOCH2CHO]=CONST(KROPRIM*O2)
k[ETHGLY+OH-->HOCH2CHO+HO2]=CONST(1.45D-11)
k[C813OOH+OH-->C813O2]=CONST(1.86D-11)
k[C813NO3+OH-->CH3COCH3+CO13C3CO2H+HCHO+NO2]=CONST(7.82D-12)
k[C813O-->CH3COCH3+C516O2]=CONST(KDEC)
k[C813OH+OH-->C813O]=CONST(1.75D-11)
k[C722OOH+OH-->C722O2]=CONST(3.31D-11)
k[C722O-->CH3COCH3+C44O2]=CONST(KDEC)
k[C33CO+OH-->CO+CO+CO+HO2]=CONST(5.77D-11)
k[OH+CO23C4CO3H-->CO23C4CO3]=CONST(4.23D-12)
k[C5PAN9-->CO23C4CO3+NO2]=CONST(KBPAN)
k[OH+C5PAN9-->CO23C3CHO+CO+NO2]=CONST(3.12D-13)
k[OH+CO2H3CO3H-->CO2H3CO3]=CONST(7.34D-12)
k[C4PAN6-->CO2H3CO3+NO2]=CONST(KBPAN)
k[OH+C4PAN6-->MGLYOX+CO+NO2]=CONST(3.74D-12)
k[C615OOH+OH-->C615CO+OH]=CONST(9.31D-11)
k[C615O-->CO1M22CHO+HO2+CO]=CONST(KDEC)
k[C615OH+OH-->C615CO+HO2]=CONST(6.15D-11)
k[CO1M22CO3+HO2-->CO1M22CO2H+O3]=CONST(KAPHO2*0.15)
k[CO1M22CO3+HO2-->CO1M22CO3H]=CONST(KAPHO2*0.41)
k[CO1M22CO3+HO2-->IBUTALCO2+OH]=CONST(KAPHO2*0.44)
k[CO1M22CO3+NO-->IBUTALCO2+NO2]=CONST(KAPNO)
k[CO1M22CO3+NO2-->CO1M22PAN]=CONST(KFPAN)
k[CO1M22CO3+NO3-->IBUTALCO2+NO2]=CONST(KRO2NO3*1.74)
```

```
k[CO1M22CO3-->CO1M22CO2H]=CONST(1.00D-11*RO2*0.3)
k[CO1M22CO3-->IBUTALCO2]=CONST(1.00D-11*RO2*0.7)
k[C55O2+HO2-->C55OOH]=CONST(KRO2HO2*0.706)
k[C55O2+NO-->C55O+NO2]=CONST(KRO2NO)
k[C55O2+NO3-->C55O+NO2]=CONST(KRO2NO3)
k[C55O2-->C55O]=CONST(2.00D-12*RO2)
k[C67CO3+HO2-->C55O2+OH]=CONST(KAPHO2*0.44)
k[C67CO3+HO2-->C67CO3H]=CONST(KAPHO2*0.56)
k[C67CO3+NO-->C55O2+NO2]=CONST(KAPNO)
k[C67CO3+NO2-->C6PAN9]=CONST(KFPAN)
k[C67CO3+NO3-->C55O2+NO2]=CONST(KRO2NO3*1.74)
k[C67CO3-->C55O2]=CONST(1.00D-11*RO2)
k[C516O2+HO2-->C516OOH]=CONST(KRO2HO2*0.706)
k[C516O2+NO-->C516O+NO2]=CONST(KRO2NO)
k[C516O2+NO3-->C516O+NO2]=CONST(KRO2NO3)
k[C516O2-->C516O]=CONST(8.8D-13*RO2)
k[C44O2+HO2-->C44OOH]=CONST(KRO2HO2*0.625)
k[C44O2+NO-->C44O+NO2]=CONST(KRO2NO)
k[C44O2+NO3-->C44O+NO2]=CONST(KRO2NO3)
k[C44O2-->C44O]=CONST(8.80D-13*RO2)
k[CO1M22CHO+NO3-->CO1M22CO3+HNO3]=CONST(2*KNO3AL*8.5)
k[CO1M22CHO+OH-->CO1M22CO3]=CONST(1.32D-10)
k[CO1M22CO2H+OH-->IBUTALCO2]=CONST(6.67D-11)
k[CO1M22CO3H+OH-->CO1M22CO3]=CONST(6.98D-11)
k[IBUTALCO2+HO2-->IBUTALO2H]=CONST(KRO2HO2*0.625)
k[IBUTALCO2+NO-->M2PROPAL2O+NO2]=CONST(KRO2NO)
k[IBUTALCO2+NO3-->M2PROPAL2O+NO2]=CONST(KRO2NO3)
k[IBUTALCO2-->IBUTALOH]=CONST(9.20D-14*0.3*RO2)
k[IBUTALCO2-->M2PROPAL2O]=CONST(9.20D-14*0.7*RO2)
k[CO1M22PAN+OH-->CH3COCH3+CO+NO2]=CONST(2.11D-11)
k[CO1M22PAN-->CO1M22CO3+NO2]=CONST(KBPAN)
k[OH+C55OOH-->C55O2]=CONST(1.32D-11)
k[C55O-->HCHO+IPRHOCO3]=CONST(KDEC)
k[OH+C67CO3H-->C67CO3]=CONST(5.33D-12)
k[C6PAN9-->C67CO3+NO2]=CONST(KBPAN)
k[OH+C6PAN9-->MIBKHO4CHO+CO+NO2]=CONST(1.41D-12)
k[OH+C516OOH-->C516O2+OH]=CONST(3.38D-11)
k[C516O-->CO13C3CO2H+HCHO+HO2]=CONST(KDEC)
k[C44OOH+OH-->C44O2]=CONST(7.46D-11)
```

```
k[C44O-->HCOCH2CHO+HO2]=CONST(KDEC)
k[IBUTALO2H+OH-->IBUTALCO2]=CONST(2.57D-11)
k[M2PROPAL2O-->CH3COCH3+HO2+CO]=CONST(KDEC)
k[IBUTALOH+OH-->IPRHOCO3]=CONST(1.4D-11)
k[IPRHOCO3+HO2-->CH3COCH3+HO2+OH]=CONST(KAPHO2*0.44)
k[IPRHOCO3+HO2-->IPRHOCO2H+O3]=CONST(KAPHO2*0.15)
k[IPRHOCO3+HO2-->IPRHOCO3H]=CONST(KAPHO2*0.41)
k[IPRHOCO3+NO-->CH3COCH3+HO2+NO2]=CONST(KAPNO)
k[IPRHOCO3+NO2-->C4PAN5]=CONST(KFPAN)
k[IPRHOCO3+NO3-->CH3COCH3+HO2+NO2]=CONST(KRO2NO3*1.74)
k[IPRHOCO3-->CH3COCH3+HO2]=CONST(1.00D-11*RO2*0.7)
k[IPRHOCO3-->IPRHOCO2H]=CONST(1.00D-11*RO2*0.3)
k[MIBKHO4CHO+NO3-->TBUTOLO2+CO+CO+HNO3]=CONST(KNO3AL*8.5)
k[MIBKHO4CHO+OH-->TBUTOLO2+CO+CO]=CONST(1.34D-11)
k[IPRHOCO2H+OH-->CH3COCH3+HO2]=CONST(1.72D-12)
k[OH+IPRHOCO3H-->IPRHOCO3]=CONST(4.80D-12)
k[C4PAN5-->IPRHOCO3+NO2]=CONST(KBPAN)
k[OH+C4PAN5-->CH3COCH3+CO+NO2]=CONST(4.75D-13)
k[TBUTOLO2+HO2-->TBUTOLOOH]=CONST(5.60D-14*EXP(1650/T))
k[TBUTOLO2+NO-->TBUTOLNO3]=CONST(KRO2NO*0.017)
k[TBUTOLO2+NO-->TBUTOLO+NO2]=CONST(KRO2NO*0.983)
k[TBUTOLO2+NO3-->NO2+TBUTOLO]=CONST(KRO2NO3)
k[TBUTOLO2-->IBUTALOH]=CONST(2.00D-13*0.2*RO2)
k[TBUTOLO2-->IBUTOLOHB]=CONST(2.00D-13*0.2*RO2)
k[TBUTOLO2-->TBUTOLO]=CONST(2.00D-13*0.6*RO2)
k[H2M2C3CO3+HO2-->H2M2C3CO3H]=CONST(KAPHO2*0.56)
k[H2M2C3CO3+HO2-->TBUTOLO2+OH]=CONST(KAPHO2*0.44)
k[H2M2C3CO3+NO-->TBUTOLO2+NO2]=CONST(KAPNO)
k[H2M2C3CO3+NO2-->C5PAN11]=CONST(KFPAN)
k[H2M2C3CO3+NO3-->TBUTOLO2+NO2]=CONST(KRO2NO3*1.74)
k[H2M2C3CO3-->TBUTOLO2]=CONST(1.00D-11*RO2)
k[TBUTOLOOH+OH-->IBUTALOH+OH]=CONST(9.98D-12)
k[TBUTOLOOH+OH-->TBUTOLO2]=CONST(1.90D-12*EXP(190/T))
k[TBUTOLNO3+OH-->IBUTALOH+NO2]=CONST(5.21D-13)
k[TBUTOLO-->CH3COCH3+HCHO+HO2]=CONST(2.00D+14*EXP(-4909/T))
k[IBUTOLOHB+OH-->IBUTALOH+HO2]=CONST(4.64D-12)
k[OH+H2M2C3CO3H-->H2M2C3CO3]=CONST(4.83D-12)
k[C5PAN11-->H2M2C3CO3+NO2]=CONST(KBPAN)
k[OH+C5PAN11-->IBUTALOH+CO+NO2]=CONST(1.23D-12)
```

B Anhänge gemäß Prüfungsordnung

B.1 Own contributions to publications

The two publications building the base of Chapters 5 and 6 both contain an author contribution section. To make this information more accesible, they are copied to the list below.

1.) **Hantschke, L.**, Novelli, A., Bohn, B., Cho, C., Reimer, D., Rohrer, F., Tillmann, R., Glowania, M., Hofzumahaus, A., Kiendler-Scharr, A., Wahner, A., and Fuchs, H.: Atmospheric photooxidation and ozonolysis of Δ3-carene and 3-caronaldehyde: rate constants and product yields, Atmospheric Chemistry and Physics, 21, 12 665–12 685, https://doi.org/10.5194/acp-21-12665-2021, 2021.

LH and HF designed the experiments. AN and CC conducted the ROx radical measurements and the OH reactivity measurements. MG conducted the HONO measurements. RT, DR and SW were responsible for the PTR-TOF-MS and VOCUS measurements. BB conducted the radiation measurements. FR was responsible for the NOx and O3 data. LH analyzed the data and wrote the paper with the help of HF. All co-authors commented and discussed the article.

2.) Tan, Z., **Hantschke, L.**, Kaminski, M., Acir, I.-H., Bohn, B., Cho, C., Dorn, H.-P., Li, X., Novelli, A., Nehr, S., Rohrer, F., Tillmann, R., Wegener, R., Hofzumahaus, A., Kiendler-Scharr, A., Wahner, A., and Fuchs, H.: Atmospheric photo-oxidation of myrcene: OH reaction rate constant, gas-phase oxidation products and radical budgets, Atmospheric Chemistry and Physics, 21, 16 067–16 091, https://doi.org/10.5194/acp-21-16067-2021, 2021.

ZT, LH and HF wrote the manuscript. MK, RW and HF designed and led the experiments in the chamber. IA (organic compounds), BB (radiation), HPD (radicals), XL (HONO), SN (OH reactivity), FR (nitrogen oxides, ozone), RT (organic compounds), AN (radicals) and CC (radicals) were responsible for measurements used in this work. All co-authors commented and discussed the manuscript and contributed to the writing of the manuscript.

B.2 Erklärung zur Dissertation

Hiermit versichere ich an Eides statt, dass ich die vorliegende Dissertation selbstständig und ohne die Benutzung anderer als der angegebenen Hilfsmittel und Literatur angefertigt habe. Alle Stellen, die wörtlich oder sinngemäß aus veröffentlichten und nicht veröffentlichten Werken dem Wortlaut oder dem Sinn nach entnommen wurden, sind als solche kenntlich gemacht. Ich versichere an Eides statt, dass diese Dissertation noch keiner anderen Fakultät oder Universität zur Prüfung vorgelegen hat; dass sie - abgesehen von unten angegebenen Teilpublikationen und eingebundenen Artikeln und Manuskripten - noch nicht veröffentlicht worden ist sowie, dass ich eine Veröffentlichung der Dissertation vor Abschluss der Promotion nicht ohne Genehmigung des Promotionsausschusses vornehmen werde. Die Bestimmungen dieser Ordnung sind mir bekannt. Darüber hinaus erkläre ich hiermit, dass ich die Ordnung zur Sicherung guter wissenschaftlicher Praxis und zum Umgang mit wissenschaftlichem Fehlverhalten der Universität zu Köln gelesen und sie bei der Durchführung der Dissertation zugrundeliegenden Arbeiten und der schriftlich verfassten Dissertation beachtet habe und verpflichte mich hiermit, die dort genannten Vorgaben bei allen wissenschaftlichen Tätigkeiten zu beachten und umzusetzen. Ich versichere, dass die eingereichte elektronische Fassung der eingereichten Druckfassung vollständig entspricht.

Jülich den 30.05.2022

Teilpublikationen:

1) **Hantschke, L.**, Novelli, A., Bohn, B., Cho, C., Reimer, D., Rohrer, F., Tillmann, R., Glowania, M., Hofzumahaus, A., Kiendler-Scharr, A., Wahner, A., and Fuchs, H.: Atmospheric photooxidation and ozonolysis of $\Delta 3$-carene and 3-caronaldehyde: rate constants and product yields, Atmospheric Chemistry and Physics, 21, 12 665–12 685, https://doi.org/10.5194/acp-21-12665-2021, 2021.

2) Tan, Z., **Hantschke, L.**, Kaminski, M., Acir, I.-H., Bohn, B., Cho, C., Dorn, H.-P., Li, X., Novelli, A., Nehr, S., Rohrer, F., Tillmann, R., Wegener, R., Hofzumahaus, A., Kiendler-Scharr, A., Wahner, A., and Fuchs, H.: Atmospheric photo-oxidation of myrcene: OH reaction rate constant, gas-phase oxidation products and radical budgets, Atmospheric Chemistry and Physics, 21, 16 067–16 091, https://doi.org/10.5194/acp-21-16067-2021, 2021.

Band / Volume 577
Neue Ziele auf alten Wegen?
Strategien für eine treibhausgasneutrale Energieversorgung bis zum Jahr 2045
D. Stolten, P. Markewitz, T. Schöb, F. Kullmann, S. Risch, T. Groß, M. Hoffmann, D. Franzmann, T. Triesch, S. Kraus, R. Maier, B. Gillessen, H. Heinrichs, N. Pflugradt, T. Grube, J. Linssen, L. Kotzur (2022), VI, 81 pp
ISBN: 978-3-95806-627-4

Band / Volume 578
Improving stationary and mobile cosmic ray neutron soil moisture measurements
Assessment of the cosmic ray neutron uncertainty and the potential of the thermal neutron signal
J. C. Jakobi (2022), xxiii, 137 pp
ISBN: 978-3-95806-628-1

Band / Volume 579
Application-Specific Calibration of Condensation Particle Counters under Low Pressure Conditions
O. B. F. Bischof (2022), ix, 137 pp
ISBN: 978-3-95806-629-8

Band / Volume 580
Konzepte und Potenziale von Demonstrationsanlagen für die Produktion von erneuerbarem synthetischen Flugzeugtreibstoff als Beitrag zur Transformation der Reviere in NRW – Abschlussbericht
S. Weiske, F. Schorn, J. L. Breuer, L. Becka, N. Beltermann, N. Wegener, R. C. Samsun, P. Moser, S. Schmidt, C. Götte, E. Rietmann, U. Balfanz, A. Spieckermann, D. Beckmann, J. Edler-Krupp, F. Steffen und R. Peters (2022), 167 pp
ISBN: 978-3-95806-630-4

Band / Volume 581
Schlussbericht
Accelerating Low- carbon Industrial Growth through CCUS (ALIGN-CCUS)
S. Weiske, S. Schemme, R. C. Samsun, R. Peters, S. Troy, S. Morgenthaler, D. Schumann, P. Zapp (2022), 216 pp
ISBN: 978-3-95806-632-8

Band / Volume 582
Closed Carbon Cycle Mobility –
Klimaneutrale Kraftstoffe für den Verkehr der Zukunft
F. Schorn, J. Häusler, J. L. Breuer, S. Weiske, J. Pasel, R. C. Samsun, R. Peters (2022), 220 pp
ISBN: 978-3-95806-636-6

Band / Volume 583
Machine learning for monitoring groundwater resources over Europe
Y. Ma (2022), viii, 125 pp
ISBN: 978-3-95806-638-0

Band / Volume 584
Mechanical properties of single and dual phase proton conducting membranes
W. Zhou (2022), IV, VI, 133 pp
ISBN: 978-3-95806-645-8

Band / Volume 585
Improvements to gravity wave physics from an observational perspective
M. Geldenhuys (2022), vii, 136 pp
ISBN: 978-3-95806-647-2

Band / Volume 586
Impact of severe convection on the water vapor mixing ratio in the extra-tropical stratosphere
D. Khordakova (2022), ii, 136 pp
ISBN: 978-3-95806-648-9

Band / Volume 587
Effects of salt precipitation during evaporation on porosity and permeability of porous media
J. Piotrowski (2022), xxvii, 139 pp
ISBN: 978-3-95806-650-2

Band / Volume 588
IEK-14 Report 2022
Forschung für die Energiewende und den Wandel im Rheinischen Revier
B. Emonts (Hrsg.) (2022)
ISBN: 978-3-95806-652-6

Band / Volume 589
Oxidation of monoterpenes studied in atmospheric simulation chambers
L. L. Hantschke (2022), 188 pp
ISBN: 978-3-95806-653-3

Energie & Umwelt / Energy & Environment
Band / Volume 589
ISBN 978-3-95806-653-3

Mitglied der Helmholtz-Gemeinschaft

JÜLICH
Forschungszentrum